TIME-DEPENDENT INACTIVATION OF INTESTINAL CYTOCHROME P450S AND ITS IMPACT ON SYSTEMIC BIOAVAILABILITY

A Dissertation

Submitted to

the Temple University Graduate Board

In Partial Fulfillment

of the Requirements for the Degree

DOCTOR OF PHILOSOPHY

---

by

Tirtha Nandi

December 2022

Examining Committee Members:

Dr. Swati Nagar, Advisory Chair, Department of Pharmaceutical Sciences
Dr. Reza Fassihi, Department of Pharmaceutical Sciences
Dr. Carlos Barrero, Department of Pharmaceutical Sciences
Dr. Chris Bode, External Member, Absorption Systems, Exton, PA

©

Copyright

2022

by

Tirtha Nandi

All Rights Reserved

ABSTRACT

The oral route of administration is the most widely used mode of drug administration due to advantages such as the convenience of oral drug administration, patient choice, cost-effectiveness, and ease of generating oral dosage forms on a large scale. How effectively an oral drug is absorbed and made accessible to the target organ depends on a variety of factors. Poor absorption from the absorption site, excessive metabolism in the gut and liver, and pharmacokinetic drug-drug (PK-DDI) interactions can all contribute to inadequate therapy. The PK-DDI may result in greater than anticipated bioavailability and toxicity due to irreversible enzyme inhibition including time-dependent inactivation (TDI) of the intestinal enzymes.

There are different *in vitro* models available to predict the fraction escaping gut metabolism (F_g), which is a major determinant of intestinal bioavailability. On the other hand, using pre-clinical species, F_g can be extrapolated in humans using allometric scaling, but there has been significant discordance due to the variable intestinal metabolism in humans vs. pre-clinical species. A number of absorption models have been developed over the years to predict oral drug absorption, and intestinal TDI can be incorporated into many of those models. In this study, the continuous intestinal absorption model has been refined, including the intestinal metabolism model, to predict the oral absorption of midazolam and nicardipine in both humans and rats. This absorption model was also used to predict the F_g of these drugs in those two species.

The *in vitro* metabolic characteristics of the model drugs were investigated using both human and rat microsomes. The kinetic profiles of their metabolic conversion in rats and humans were developed using numerical techniques. The continuous absorption model

explains how drug concentration changes with time and distance. A physiologically based pharmacokinetic (PBPK) model describes the intestine. The physiological inputs to the model, as well as the structure of the gastrointestinal tract, vary depending on the species. Rats and humans have different lengths of the small intestine's regions, such as the jejunum, and absorptive surface area amplifiers, such as the villi and microvilli. Along with the metabolic characteristics established through *in vitro* metabolic investigations, physiological aspects (applied to both rats and humans) and physicochemical drug characteristics were also added to the model. To estimate the absorption characteristics of midazolam and nicardipine, this model was further connected to the traditional compartmental model that represents the rest of the body.

Chapter one details the background and importance concerning this project, along with the hypothesis and goals. Chapter two involves developing and validating bioanalytical methods for the drugs of interest. Chapters three and four detail the *in vitro* metabolic studies in rat and human microsomes (both intestinal and liver). Chapter five represents the TDI studies which were finally excluded from the absorption modeling in this thesis. Finally, chapter six illustrates the prediction of the oral PK profile of midazolam and nicardipine in rats and humans, rendering predicted values of F_g of these drugs in both species. Finally, chapter seven presents the significance, summary, and some directions to take this research further down the future.

DEDICATION

Dedicated to

My wife and love of my life Moumita

and

My parents

ACKNOWLEDGEMENTS

“Life is like a box of chocolates; you never know what you are going to get”- Forrest Gump’s mother said this to him, but this has been one of my life's most influential statements. I have always seen my life as a journey of uncertainty in a positive way. I do not want to know what is there for me in the future, but I want to be prepared for every situation in my life, whatever the circumstance is. When I graduated from the University of Dhaka as a topper, I wanted to join there as a faculty, but my destiny decided something else. In 2017, I ended up at Temple University School of Pharmacy to pursue my Ph.D., but I did not know this journey would be fascinating. When I am about to end this journey, many people deserve to be mentioned for their unconditional love, support, and encouragement.

I would love to start my gratitude by saying thanks to my Ph.D. mentor Dr. Swati Nagar. I would never understand how knowledgeable she is if I were not working under her. It was a learning experience that will be helpful for my whole lifetime. She taught me how to think as an independent researcher. Since I joined her lab, I have seen her to promote to a full professor from associate professor. At the same time, she had taken the responsibility of being the director of graduate service (DGS). Despite all these priorities, she never forgot to meet and check from time to time how my Ph.D. journey was progressing. She was the one who supported me during Covid-19 when I was feeling helpless thousand miles away from home. She also supported me when I wanted to do an internship. I am also thankful for all the finances given to me during the research assistantship and the conferences I have attended. I think it would take pages to point out everything for which I am super grateful to her.

Next, I want to thank Dr. Ken Korzekwa. I cannot express how much I am impressed by his knowledge. Sometimes, I just think there is nothing that he does not know. He is the one for whom I grew up my interest in simulation. Unfortunately, I could not finish all the work I proposed in my thesis proposal due to different circumstances. Nevertheless, later, I added so much simulation work just because I got that learning from Ken.

I want to extend my gratitude to Dr. Fassihi and Dr. Barrero for being on my thesis committee. Their suggestions in my thesis proposal have been a key direction for completing my thesis work successfully. I also want to thank Dr. Chris Bode for being the external reader of my thesis. I appreciate his time. Dr. Canney was the DGS when I was enrolled in TUSP, and Dr. Walker has been the department chair for the whole time of my Ph.D. life. I am truly grateful to them for their continuous support and encouragement. I would also like to thank Dr. Lebo and Andy for my teaching assistantship experience with them. Finally, I am thankful to Mira and Sophon for all the administrative work.

It was truly an honor to collaborate with a wonderful team of lab members in this lab. My previous lab members, including Jaydeep, Kim, John, Casey, and Erickson, were so nice to me and helpful with any information or lab help. I am also thankful to the current lab members, Min, Leo, Yifan, and Yousuf, for the fun we always have in the lab.

Last but not least is my wife. From day one, she has been with me in my Ph.D. journey. Probably this one sentence was enough to explain what she has been through with me. I am also thankful to my parents for being my parents. It was not so easy to bring me up. I am here for so many people whom I could not mention. I am also thanking everyone who loved me for who I am.

TABLE OF CONTENTS

ABSTRACT iii

DEDICATION v

ACKNOWLEDGEMENTS vi

LIST OF TABLES xvii

LIST OF FIGURES xxi

ABBREVIATIONS xxxii

CHAPTER ONE: INTRODUCTION 1

1.1 Bioavailability and Oral Drug Administration: 1

1.2 Pharmacokinetics of Oral Drug Absorption 4

1.3 Biopharmaceutic Classification System (BCS) 8

1.4 Anatomy and Physiology of Gastrointestinal Tract of Human and Rat 10

1.5 Mechanisms of Drug Absorption from Gastrointestinal Tract (GIT): 18

1.6 Drug-Drug Interaction and Impact on Bioavailability: Focus on Time-Dependent Inactivation (TDI) 20

1.7 Cytochrome P450 Enzymes (CYPs) 25

1.8 Fundamentals of Cytochrome P450 Enzyme Kinetics: 28

1.9 Hepatic and Intestinal Transporters 31

1.10 *In Vitro-In Vivo* Extrapolation (IVIVE) for DDI: 32

1.11 *In Vitro* Models for Intestinal Epithelium Permeation 36

1.12 Animal Models in Pharmacokinetics and Use of Rats 39

1.13 Absorption Models 42

Dispersion Model: 43

Compartmental Absorption and Transit (CAT) Model: 43

Advanced Compartmental Absorption and Transit (ACAT) Model: 44

ADAM Model: 46

Continuous Intestinal Absorption Model (CIAM): 46

1.14 Drugs of Interest: 48

Midazolam (MDZ): 49

Nicardipine (NCD) 50

1.15 Goal of This Thesis 51

1.16 Hypothesis 52

1.17 Specific Aims 53

CHAPTER TWO: DEVELOPMENT AND VALIDATION OF LC-MS/MS METHOD FOR QUANTIFICATION OF VARIOUS COMPOUNDS 56

2.1 Rationale 56

2.2 Materials 57

2.3 Assay Development 57

2.3.1 Preparation of the Stock Solutions, Calibration Standard Samples, and Quality Control (QC) Sample 57

2.3.2 LC-MS/MS 59

2.4 Assay Validation 60

2.5 Results 61

2.6 Discussion and Conclusions 69

CHAPTER THREE: *IN VITRO* ENZYME KINETICS OF MIDAZOLAM AND NICARDIPINE USING RAT INTESTINAL MICROSOMES (RIM) AND RAT LIVER MICROSOMES (RLM) 71

3.1 Rationale 71

3.1.1 *In Vitro* Tools for Metabolic Studies: 71

3.1.2 Fundamentals of Cytochrome P450 Enzyme Kinetics: 73

3.1.3 Midazolam (MDZ) CYP-Mediated Metabolic Pathway: 77

3.1.4 Nicardipine (NCD) CYP-Mediated Metabolic Pathway: 78

3.2 Materials 80

3.3 Methods 81

3.3.1 Equilibrium Dialysis Assay to Determine the Fraction Unbound in Microsomes (f_{um}) using RLM and HIM 81

3.3.2 *In Vitro* Enzyme Kinetics of Midazolam (MDZ) 84

3.3.2.1 *In Vitro* Metabolic Conversion of Midazolam (MDZ) to 1’-hydroxymidazolam (1’-OH MDZ) and 4-hydroxymidazolam (4-OH MDZ) Using RLM 84

3.3.2.2 *In Vitro* Metabolic Conversion of Midazolam (MDZ) to 1'-hydroxymidazolam (1'-OH MDZ) and 4-hydroxymidazolam (4-OH MDZ) Using RIM 85

3.3.3 *In Vitro* Enzyme Kinetics of Nicardipine (NCD) 86

3.3.3.1 *In Vitro* Metabolism of Nicardipine (NCD) Using RLM 87

3.3.3.2 *In Vitro* Metabolism of Nicardipine (NCD) Using RIM 88

3.4 Results 90

3.4.1 Equilibrium Dialysis Assay to Determine the Fraction Unbound in Microsomes (f_{um}) using RLM and HIM 90

3.4.2 *In Vitro* Enzyme Kinetics of Midazolam (MDZ) 90

3.4.2.1 *In Vitro* Metabolic Conversion of Midazolam (MDZ) to 1'-hydroxymidazolam (1'-OH MDZ) and 4-hydroxymidazolam (4-OH MDZ) Using RLM 91

3.4.2.2 *In Vitro* metabolic Conversion of Midazolam (MDZ) to 1'-hydroxymidazolam (1'-OH MDZ) and 4-hydroxymidazolam (4-OH MDZ) Using RIM 96

3.4.3 *In Vitro* Enzyme Kinetics of Nicardipine (NCD) 101

3.4.3.1 *In Vitro* Metabolism of Nicardipine (NCD) using RLM 102

3.4.3.2 *In Vitro* Metabolism of Nicardipine (NCD) using RIM 106

3.5 Discussion and Conclusions 111

CHAPTER FOUR: *IN VITRO* ENZYME KINETICS OF MIDAZOLAM AND NICARDIPINE USING HUMAN INTESTINAL MICROSOMES (HIM) and HUMAN LIVER MICROSOMES (HLM) 119

4.1 Rationale 119

4.1.1 IVIVE for Predicting Human F_h 120

4.1.2 IVIVE for Predicting Human F_g 125

4.2 Materials 130

4.3 Methods 130

4.3.1 *In Vitro* Enzyme Kinetics of Midazolam (MDZ) 130

4.3.1.1 *In Vitro* Metabolism of Midazolam (MDZ) Using HLM 131

4.3.1.2 *In Vitro* Metabolism of Midazolam (MDZ) Using HIM 133

4.3.2 *In Vitro* Enzyme Kinetics of Nicardipine (NCD) 134

4.3.2.1 *In Vitro* Metabolism of Nicardipine (NCD) Using HLM 134

4.3.2.2 *In Vitro* Metabolism of Nicardipine (NCD) Using HIM 135

4.3.3 *In Vitro-In Vivo* Extrapolation of Midazolam (MDZ) and Nicardipine (NCD) 137

4.4 Results 137

4.4.1 *In Vitro* Enzyme Kinetics of Midazolam (MDZ) 137

4.4.1.1 *In Vitro* Metabolism of Midazolam (MDZ) Using HLM 137

4.4.1.2 *In Vitro* Metabolism of Midazolam (MDZ) Using HIM 149

4.4.2 *In Vitro* Enzyme Kinetics of Nicardipine (NCD) 160

4.4.2.1 *In Vitro* Metabolism of Nicardipine (NCD) Using HLM 160

4.4.2.2 *In vitro* metabolism of nicardipine (NCD) using HIM 165

4.4.3 *In Vitro-In Vivo* Extrapolation of Midazolam (MDZ) and Nicardipine (NCD) 170

4.5 Discussion and Conclusions 171

CHAPTER FIVE: *IN VITRO* TIME-DEPENDENT INACTIVATION (TDI) ASSAYS USING RAT INTESTINAL MICROSOMES (RIM) AND RAT LIVER MICROSOMES (RLM) AND MODELING OF TDI DATA 179

5.1 Background and Significance 179

5.1.1 Kinetics of Time-Dependent Inactivation (TDI): 183

5.1.2 Screening Assays 184

5.1.2.1 Two-Time Points Analysis 185

5.1.2.2 One-Concentration Approach 185

5.1.2.3 IC_{50} Shift Assay 187

5.1.3 Determination of TDI Kinetic Constants (K_I and k_{inact}) 188

5.1.3.1 One-step Incubation for the Progress Curve 188

5.1.3.2 Two-Step Incubation with Dilution or Non-Dilution 189

5.1.4.3 TDI Data Analysis: 189

5.2 Materials 191

5.3 Methods 192

5.3.1 Pilot Assays to Determine Time-Dependent Inactivation (TDI) 192

5.3.1.1 Determination of TDI Liability of ABT on MDZ Metabolism Using RLM/RIM 193

5.3.1.2 Determination of TDI Liability of NCD on MDZ Metabolism Using RLM/RIM 194

5.3.1.3 Determination of TDI Liability of ABT on NCD Metabolism Using RLM 194

5.3.2 Full TDI Assay to Determine K_I and k_{inact} 196

5.4 Results 200

5.4.1 Pilot Assays to Determine Time-Dependent Inactivation (TDI) 200

5.4.1.1 Determination of TDI Liability of ABT on MDZ Metabolism Using RLM/RIM 200

5.4.1.2 Determination of TDI Liability of NCD on MDZ Metabolism Using RLM/RIM 201

5.4.1.3 Determination of TDI Liability of ABT on NCD Metabolism Using RLM 202

5.4.2 Full TDI Assay to Determine K_I and k_{inact} 203

5.4.2.1 Determination of K_I and k_{inact} of ABT Using MDZ as the Probe Substrate in RLM 203

5.4.2.2 Determination of K_I and k_{inact} of NCD Using MDZ as the Probe Substrate in RLM 210

5.5 Discussion and Conclusions 215

CHAPTER SIX: INCORPORATION OF INTESTINAL METABOLISM IN THE PRESENT HUMAN AND RAT CONTINUOUS INTESTINAL ABSORPTION MODEL 224

6.1 Rationale 224

6.2 Methods 229

6.2.1 Input Parameters 230

6.2.1.1 Physiologic Input Parameters 231

6.2.1.2 Drug-Specific Input Parameters 233

6.2.1.3 Formulation Input Parameters 234

6.2.2 Solution Dosing Partial Differential Equations (PDEs): 235

6.2.3 Disposition Functions from the IV Data 237

6.2.4 Data Analysis 238

6.3 Results 239

6.3.1 Simulation of Oral PK of MDZ in Humans 239

6.3.1.1 Simulation of Oral MDZ Without Regional Expression of CYP3A4 and Atypical Kinetics: 241

6.3.1.2 Simulation of Oral MDZ with Regional Expression of CYP3A4 and Atypical kinetics: 246

6.3.2 Simulation of Oral PK of MDZ in SD Rats ... 249

6.3.3 Simulation of Oral PK of NCD in Humans ... 255

6.3.4 Simulation of Oral PK of NCD in SD Rats ... 262

6.4 Discussion and Conclusions ... 268

CHAPTER SEVEN: FUTURE DIRECTIONS AND SUMMARY ... 278

7.1 Regional Expression of CYPs Along the SD Rat Intestine ... 278

7.2 Inclusion of BCS Class III and IV Drugs for the Absorption Modeling Incorporating Intestinal Metabolism and Transporters ... 279

7.3 Time-Dependent Inactivation Assay Using Recombinant CYP Enzymes and Translating to the Intestinal DDI Scenario ... 281

7.4 Summary and Significance of this Thesis ... 282

BIBLIOGRAPHY ... 288

APPENDIX A: EQUIIBRIUM DIALYSIS OF NICARDIPINE ADDING DRUG IN THE RECEIVER COMPARTMENT ... 330

LIST OF TABLES

Table 1.1: Intestinal tract dimensions for human and rat.. 13

Table 1.2: Major static models to predict oral DDI.. 34

Table 2.1: List of compounds and respective biological matrices for LC-MS/MS method development and validation.. 56

Table 2.2 MS/MS parameters for compounds evaluated... 61

Table 2.3: HPLC gradients for all the compounds 62

Table 2.4 HPLC parameters for various compounds studied 63

Table 2.5 Validation results of different compounds.. 68

Table 3.1: Unbound fraction in microsomes (f_{um}) of different compounds (scaled to 1 mg/mL). Data presented as parameter estimate ± S.E. 90

Table 3.2. Statistical functions for model comparison 94

Table 3.3. Comparison of estimates of kinetic parameters from ESP1P2 model and ESSP1P2 model. Data presented as parameter estimate ± S.E................................ 95

Table 3.4. Statistical matrices for model comparison.. 98

Table 3.5. Comparison of estimates of kinetic parameters from ESP1P2 model and ESSP1P2 model. Data presented as parameter estimate ± S.E.............................. 100

Table 3.6. Statistical matrices for model comparison.. 103

Table 3.7. Comparison of estimates of kinetic parameters from ESP model and ESSP model. Data presented as parameter estimate ± S.E. 105

Table 3.8. Statistical matrices for model comparison.. 108

Table 3.9. Comparison of estimates of kinetic parameters from ESP model and ESSP model. Data presented as parameter estimate ± S.E. 110

Table 4.1. Statistical functions for model comparison 140

Table 4.2. Comparison of estimates of kinetic parameters from ESP model and ESSP model. Data presented as parameter estimate ± S.E. 141

Table 4.3. Statistical functions for model comparison 143

Table 4.4. Comparison of estimates of kinetic parameters from ESP model and ESSP model. Data presented as parameter estimate ± S.E. 145

Table 4.5. Kinetic parameters from ESSP1P2 model. Data presented as parameter estimate ± S.E. 148

Table 4.6. Statistical functions for model comparison 151

Table 4.7. Comparison of estimates of kinetic parameters from ESP model and ESSP model. Data presented as parameter estimate ± S.E. 152

Table 4.8. Statistical functions for model comparison 154

Table 4.9. Comparison of estimates of kinetic parameters from ESP model and ESSP model. Data presented as parameter estimate ± S.E. 156

Table 4.10. Kinetic parameters from ESSP1P2 model. Data presented as parameter estimate ± S.E. 159

Table 4.11. Statistical functions for model comparison 162

Table 4.12. Comparison of estimates of kinetic parameters from ESP model and ESSP model. Data presented as parameter estimate ± S.E. 164

Table 4.13. Statistical functions for model comparison 167

Table 4.14. Comparison of estimates of kinetic parameters from ESP model and ESSP model. Data presented as parameter estimate ± S.E. 169

Table 4.15: Predicted F_h and F_g obtained from the IVIVE 170

Table 5.1. Results of different model fittings 207

Table 5.2: Micro-rate constants associated with all the models. Data presented as parameter estimates (SD) 207

Table 5.3. TDI parameters of ABT with MDZ using RLM... 209

Table 5.4. Statistical functions of different model fittings for model comparison 212

Table 5.5: Micro-rate constants associated with all the models. Data presented as parameter estimates (SD) 213

Table 5.6. TDI parameters of NCD with MDZ using RLM 214

Table 6.1: Length and radii of the intestinal segments of humans 229

Table 6.2: Length and radii of the intestinal segments of SD rats................................. 230

Table 6.3 Physiologic input parameters to develop physiologic expression as a function of intestinal length (x) 231

Table 6.4. Physicochemical properties of MDZ and NCD used for the continuous intestinal absorption model 233

Table 6.5: Drug-specific input parameters to generate input expressions as a function of x 234

Table 6.6. Model comparison functions for IV bolus data 240

Table 6.7. Kinetic parameters as disposition function. Data presented as the parameter estimates (S.E.) 241

Table 6.8. Sensitivity analysis changing the stomach lag time (t_{lag}) and empirical scaling factor (f_{CYP}) and their impact on EOC, Fa, F_g, t_{max}, and C_{max}. Grey values are the finalized values for model finalization. 244

Table 6.9. Sensitivity analysis changing the stomach lag time (t_{lag}) and empirical scaling factor (f_{CYP}) and their impact on EOC, Fa, F_g, t_{max}, and C_{max}. Grey values are the finalized values for model finalization. 248

Table 6.10. Model comparison functions for IV bolus data 250

Table 6.11. Kinetic parameters as disposition function. Data presented as the parameter estimates (S.E.) 251

Table 6.12. Sensitivity analysis changing the stomach lag time (t_{lag}) and empirical scaling factor (f_{CYP}) and their impact on EOC, Fa, F_g, t_{max}, and C_{max}. Grey values are the finalized values for model finalization. 254

Table 6.13. Model comparison functions for IV bolus data 256

Table 6.14. Kinetic parameters as disposition function. Data presented as the parameter estimates (S.E.) 257

Table 6.15. Sensitivity analysis changing the cytosolic lipid volume, stomach lag time (t_{lag}) and empirical scaling factor (f_{CYP}) and their impact on EOC, Fa, F_g, t_{max}, and C_{max}. Grey values are the finalized values for model finalization. 259

Table 6.16. Model comparison functions for IV bolus data 263

Table 6.17. Kinetic parameters as disposition function. Data presented as the parameter estimates (S.E.) 264

Table 6.18. Sensitivity analysis changing the cytosolic lipid volume, stomach lag time (t_{lag}) and empirical scaling factor (f_{CYP}) and their impact on EOC, Fa, F_g, t_{max}, and C_{max}. Grey values are the finalized values for model finalization. 266

Table A1: Equilibrium dialysis of NCD (Repeat experiment) 330

LIST OF FIGURES

Figure 1.1. A representative C-t profile 6

Figure 1.2 Biopharmaceutics Classification System (BCS) of drugs 9

Figure 1.3. Biopharmaceutics Drug Disposition Classification System (BDDCS) 10

Figure 1.4: Scheme of TDI 23

Figure 1.5: (A) A single-substrate binding (ES model) (B) A two-substrate binding (ESS model). (Figure reproduced from (Paragas et al., 2021; Wang et al., 2021)) 28

Figure 1.6: Representation of same AUC but different absorption profile 35

Figure 1.7: Chemical structure of midazolam 49

Figure 1.8: Chemical structure of nicardipine 50

Figure 2.1 Representative calibration curve for 1'-OH MDZ 64

Figure 2.2 Representative chromatogram of 1'-OH MDZ (red) with IS phenacetin (blue) 64

Figure 2.3 Representative calibration curve for 4-OH MDZ 65

Figure 2.4 Representative chromatogram of 4-OH MDZ (red) with IS phenacetin (blue) 65

Figure 2.5: Representative calibration curve for NCD in RLM 66

Figure 2.6: Representative calibration curve for NCD in SD rat plasma 66

Figure 2.7: Representative chromatogram of NCD (blue) with IS phenacetin (green) 67

Figure 2.8 Representative calibration curve for DHD NCD 67

Figure 2.9: Representative chromatogram of DHD NCD (red) with IS phenacetin (blue) 68

Figure 3.1: (A) A single-substrate binding (ES model) (B) A two-substrate binding (ESS model). (Figure reproduced from (Paragas et al., 2021; Wang et al., 2021)) 74

Figure 3.2: Midazolam metabolic pathway in human (Reproduced from (Christensen et al., 2009) 78

Figure 3.3: Nicardipine metabolic pathway in human (Reproduced from (Graham et al., 1985)) 79

Figure 3.4: Time and protein linearity assay of MDZ with RLM (n=1). 91

Figure 3.5. MDZ saturation curve for the incubation with RLM (Red:1’-OH MDZ & Blue: 4-OH MDZ). Plots represent mean data (n=3). 91

Figure 3.6. Diagnostic plots for the MDZ incubation with RLM (Left: EH plot for MDZ→1’-OH MDZ, middle: EH plot for MDZ→4-OH MDZ, and right: Metabolite formation ratio plot). Plots represents mean data ± standard errors (n=3). 92

Figure 3.7. Schemes for multiple product formation. (A) A one-substrate binding, two-metabolite formation (ESP1P2) scheme. (B) A two-substrate binding, two-metabolite formation (ESSP1P2) scheme (Reproduced from (Paragas et al., 2021; Wang et al., 2021)) 93

Figure 3.8. ESSP1P2 model fitting with the observed data for the MDZ incubation with RLM (Left: Saturation curve for MDZ→1’-OH MDZ (Plots represents mean data (n=3).), middle: Saturation curve for MDZ→4-OH MDZ (Plots represents mean data (n=3).), and right: Metabolite formation ratio plot (Plots represents mean data ± standard errors (n=3).)) 94

Figure 3.9: Intrinsic clearance plot over a range of physiologically relevant MDZ concentration for both metabolite formation 96

Figure 3.10. MDZ saturation curve for the incubation with RIM (Red:1’-OH MDZ & Green: 4-OH MDZ). Plots represents mean data ± standard errors (n=3). 97

Figure 3.11. Diagnostic plots for the MDZ incubation with RIM (Left: EH plot for MDZ→1’-OH MDZ, middle: EH plot for MDZ→4-OH MDZ, and right: Metabolite formation ratio plot). Plots represents mean data ± standard errors (n=3). 97

Figure 3.12. ESSP1P2 model fitting with the observed data for the MDZ incubation with RIM (Left: Saturation curve for MDZ→1’-OH MDZ, middle: Saturation curve for MDZ→4-OH MDZ, and right: Metabolite formation ratio plot). Plots represents mean data ± standard errors (n=3). 99

Figure 3.13: Intrinsic clearance plot over a range of physiologically relevant MDZ concentration for both metabolite formation 101

Figure 3.14: Time and protein linearity assay of NCD with RIM (n=1) 101

Figure 3.15: Substrate depletion assay of NCD using RLM. Plots represents mean data ± standard errors (n=3). 102

Figure 3.16. NCD saturation curve for the incubation with RLM (Left) and diagnostic Eadie-Hofstee plot (right). Plots represents mean data ± standard errors (n=3). 103

Figure 3.17. Model fitting with the observed data for the NCD incubation with RLM. Plots represents mean observed data ± standard errors (n=3)................................ 104

Figure 3.18: Intrinsic clearance plot over a range of physiologically relevant NCD concentration for DHD NCD formation 106

Figure 3.19: Substrate depletion assay of NCD using RIM. Plots represents mean observed data ± standard errors (n=3). 107

Figure 3.20. NCD saturation curve for the incubation with RIM (Left) and diagnostic Eadie-Hofstee plot (right). Plots represents mean data ± standard errors (n=3)..... 108

Figure 3.21. Model fitting with the observed data for the NCD incubation with RIM. Plots represents mean observed data ± standard errors (n=3)................................ 109

Figure 3.22: Intrinsic clearance plot over a range of physiologically relevant NCD concentration for DHD NCD formation 111

Figure 4.1. The entire process of *in vitro-in vivo* extrapolation (IVIVE) employing human liver microsomes (HLM) or recombinant human cytochrome P450 (CYP). MPPGL is an abbreviation for microsomal protein per gram of liver (adapted from (Choi et al., 2019)). 121

Figure 4.2: Well-stirred hepatic model 122

Figure 4.3. Parallel-tube hepatic model 124

Figure 4.4: Substrate depletion assay of MDZ using HLM. Plots represents mean data ± standard errors (n=3). 138

Figure 4.5. MDZ saturation curve for the incubation with HLM (Left) and diagnostic Eadie-Hofstee plot (right). Plots represents mean data ± standard errors (n=3)..... 139

Figure 4.6. Model fitting with the oberved data for the MDZ metabolic conversion to 1'-OH MDZ by HLM. Plots represents mean data ± standard errors (n=3). Solid lines represent model predicted lines. 140

Figure 4.7: Intrinsic clearance plot over a range of physiologically relevant MDZ concentration for both metabolite formation 142

Figure 4.8. MDZ saturation curve for the incubation with HLM (Left) and diagnostic Eadie-Hofstee plot (right). Plots represents mean data ± standard errors (n=3)..... 143

Figure 4.9. Model fitting with the oberved data for the MDZ metabolic conversion to 4-OH MDZ by HLM. Plots represents mean data ± standard errors (n=3). Solid lines represent model predicted lines. 144

Figure 4.10: Intrinsic clearance plot over a range of physiologically relevant MDZ concentration for both metabolite formation 146

Figure 4.11. Metabolite formation ratio plot for the incubation of MDZ with HLM. Plots represents mean data ± standard errors (n=3). 147

Figure 4.12. ESSP1P2 model fitting with the oberved data for the MDZ incubation with HLM (Left: Saturation curve for MDZ→1’-OH MDZ, middle: Saturation curve for MDZ→4-OH MDZ, and right: Metabolite formation ratio plot). Plots represents mean data ± standard errors (n=3). Solid lines represent model predicted lines. ... 147

Figure 4.13: Intrinsic clearance plot over a range of physiologically relevant MDZ concentration for both metabolite formation by ESSP1P2 model 149

Figure 4.14: Substrate depletion assay of MDZ using HIM. Plots represents mean data ± standard errors (n=3). Solid lines represent model predicted lines........................ 150

Figure 4.15. MDZ saturation curve for the incubation with HIM (Left) and diagnostic Eadie-Hofstee plot (right). Plots represents mean data ± standard errors (n=3)..... 151

Figure 4.16. Model fitting with the oberved data for the MDZ metabolic conversion to 1’-OH MDZ by HIM. Plots represents mean data ± standard errors (n=3). Solid lines represent model predicted lines. 152

Figure 4.17: Intrinsic clearance plot over a range of physiologically relevant MDZ concentration for both metabolite formation 153

Figure 4.18. MDZ saturation curve for the incubation with HIM (Left) and diagnostic Eadie-Hofstee plot (right). Plots represents mean data ± standard errors (n=3)..... 154

Figure 4.19. Model fitting with the oberved data for the MDZ metabolic conversion to 4-OH MDZ by HIM. Plots represents mean data ± standard errors (n=3). Solid lines represent model predicted lines. 155

Figure 4.20: Intrinsic clearance plot over a range of physiologically relevant MDZ concentration for both metabolite formation 157

Figure 4.21 Metabolite formation ratio plot for the incubation of MDZ with HIM. Plots represents mean data ± standard errors (n=3). 158

Figure 4.22. ESSP1P2 model fitting with the observed data for the MDZ incubation with HIM... 158

Figure 4.23: Intrinsic clearance plot over a range of physiologically relevant MDZ concentration for both metabolite formation by ESSP1P2 model 160

Figure 4.24: Substrate depletion assay of NCD using HLM. Plots represents mean data ± standard errors (n=3). Solid lines represent model predicted lines........................ 161

Figure 4.25. NCD saturation curve for the incubation with HLM (Left) and diagnostic Eadie-Hofstee plot (right). Plots represents mean data ± standard errors (n=3)..... 162

Figure 4.26. Model fitting with the oberved data for the NCD incubation with HLM. Plots represents mean data ± standard errors (n=3). Solid lines represent model predicted lines. 163

Figure 4.27: Intrinsic clearance plot over a range of physiologically relevant NCD concentration for DHD NCD formation 165

Figure 4.28: Substrate depletion assay of NCD using HIM. Plots represents mean data ± standard errors (n=3). Solid lines represent model predicted lines........................ 166

Figure 4.29. NCD saturation curve for the incubation with HIM (Left) and diagnostic Eadie-Hofstee plot (right). Plots represents mean data ± standard errors (n=3)..... 167

Figure 4.30. Model fitting with the oberved data for the NCD incubation with HIM. Plots represents mean data ± standard errors (n=3). Solid lines represent model predicted lines. 168

Figure 4.31: Intrinsic clearance plot over a range of physiologically relevant NCD concentration for DHD NCD formation 170

Figure 5.1. Probable fate of a time-dependent inactivator. 1. TDI binds to the CYP, 2. Product formation, 3. Formation of reactive species, 4. MIC formation, 5. Heme destruction/modification, 6. Covalent modification of apoprotein, 7. GSH trapping of the reactive species (Reproduced from (Yadav et al., 2020)) 182

Figure 5.2. Scheme of TDI 183

Figure 5.3. One concentration assay possible outcomes (adapted from (Orr et al., 2012)) 186

Figure 5.4. A simulated example of IC_{50} shift assay. Red and green lines represent the percent remaining enzymatic activity without and with a preincubation step. IC_{50} shifts from 10 units to 1 unit after preincubation.. 188

Figure 5.5. Representative pilot TDI assay plot 196

Figure 5.6. Pilot TDI assay of ABT on MDZ metabolism using RLM (A) and RIM (B) 201

Figure 5.7. Pilot TDI assay of NCD on MDZ metabolism using RLM (left) and RIM (right) 202

Figure 5.8. Pilot TDI assay of ABT on NCD metabolism using RLM 203

Figure 5.9. Experimental PRA plot for CYP3A inhibition by ABT using RLM. Dots represent mean of duplicates. 205

Figure 5.10. Kinetic scheme for ABT TDI with MDZ using RLM (A. MIC-EI model : MIC with single binding without inhibitor depletion, B, MIC-EII model : MIC with double binding without inhibitor depletion, C. MIC-EI-M model : MIC with single binding with inhibitor depletion, D. MIC-EII-M model : MIC with double binding with inhibitor depletion), E. Partial inactivation, and F. Heme destruction plus multiple enzymes involved. (Figure 5.10 A to E adapted from (Korzekwa et al., 2014; Yadav et al., 2020)) 206

Figure 5.11. Determination of K_I and k_{inact} of ABT using MDZ in RLM. Dots represent experimental k_{obs} and the blue line represents the model predicted line. 209

Figure 5.12. Experimental (points) and MIC-EI model fitted (solid lines) PRA plots for CYP3A TDI by ABT. Dots represent mean of duplicates and the solid lines are model predicted lines. 210

Figure 5.13. Sequential metabolism model 211

Figure 5.14. Experimental PRA plot for CYP3A inhibition by NCD using RLM. Dots represent the mean of duplicate. 212

Figure 5.15. Determination of K_I and k_{inact} of NCD using MDZ in RLM. Dots represent the experimental k_{obs} and the blue line represents the model predicted line 214

Figure 5.16. Experimental (points) and MIC-EI model fitted (solid lines) PRA plots for CYP3A TDI by NCD. Dots represent mean of duplicates and the solid lines are model predicted lines. 215

Figure 6.1: Continuous intestinal absorption model (reproduced from (Nagar et al., 2017)) 227

Figure 6.2. Observed (dots) versus 2C predicted (solid line) response of MDZ IV bolus (5 mg) 241

Figure 6.3: 3D plots of different radial compartments after numerical solutions. C1: Intestinal lumen, C2: Enterocytic apical membrane, C3: Enterocytic cytosol, and C4: Intracellular lipids. 242

Figure 6.4. Input function of MDZ 243

Figure 6.5. Predicted vs observed C-t profiles of MDZ in fasted healthy volunteers using tlag of 0.05 hour and fCYP of 0.025 with an EOC of 0.93. 245

Figure 6.6: 3D plots of different radial compartments after numerical solutions. C1: Intestinal lumen, C2: Enterocytic apical membrane, C3: Enterocytic cytosol, and C4: Intracellular lipids. 246

Figure 6.7. Input function of MDZ 247

Figure 6.8. Predicted vs observed C-t profiles of MDZ in fasted healthy volunteers using tlag of 0.05 hour and fCYP of 0.1 with an EOC of 0.93. 249

Figure 6.9. Observed (dots) versus 2C predicted (solid line) response of MDZ IV bolus 250

Figure 6.10 3D plots of different radial compartments after numerical solutions. C1: Intestinal lumen, C2: Enterocytic apical membrane, C3: Enterocytic cytosol, and C4: Intracellular lipids. 252

Figure 6.11. Input function of MDZ in rats 253

Figure 6.12. Predicted vs observed C-t profiles of MDZ in fasted SD rat using tlag of 0.05 hour and fCYP of 0.001 with an EOC of 0.84. 255

Figure 6.13. Observed (dots) versus 2C predicted (solid line) response of NCD IV bolus (0.885 mg) 256

Figure 6.14: 3D plots of different radial compartments after numerical solutions. C1: Intestinal lumen, C2: Enterocytic apical membrane, C3: Enterocytic cytosol, and C4: Intracellular lipids. 258

Figure 6.15. Input function of NCD in human 259

Figure 6.16. Predicted vs observed C-t profiles of NCD in fasted healthy volunteers using tlag of 0.05 hour and fCYP of 0.001 with an EOC of 0.84 when the cytosolic lipid volume is assumed to be 7% of the enterocyte volume (A) and an EOC of 0.88 when the cytosolic lipid volume is assumed to be 3.5% of the enterocyte volume (B). .. 262

Figure 6.17. Observed (dots) versus 2C predicted (solid line) response of MDZ IV bolus (5 mg) 263

Figure 6.18: 3D plots of different radial compartments after numerical solutions. C1: Intestinal lumen, C2: Enterocytic apical membrane, C3: Enterocytic cytosol, and C4: Intracellular lipids. 265

Figure 6.19. Input function of NCD in SD rats 266

Figure 6.20: A. fCYP of 0.001 was used with a lag time 0.05 hour (similar to human NCD model) assuming 3.5% cytosolic lipid volume and B. fCYP of 0.05 with lag time of 0.1 hour assuming 7% cytosolic lipid volume... 268

ABBREVIATIONS

1’-OH MDZ	1’-hydroxymidazolam
4-OH MDZ	4-hydroxymidazolam
ACAT	Advanced compartmental absorption and transit
ACN	Acetonitrile
ADME	Absorption, distribution, metabolism, and excretion
AICc	Corrected Akaike Information Criterion
AUC	Area under the curve
AUCR	Area under the curve ratio
AUMC	Area under the first moment curve
CAT	Compartmental absorption and transit
CE	Collision energy
CL	Clearance
CL_{int}	Intrinsic clearance
C-t	Concentration-time
CXP	Cell exit potential
CYP	Cytochrome P-450 enzyme
D	Dose

DDI	Drug-drug interaction
DHD NCD	Dehydronicardipine
DME	Drug-metabolizing enzyme
DMSO	Dimethyl sulfoxide
DP	Declustering potential
DTZ	Diltiazem
EMA	European medicines agency
EOC	Exposure overlap co-efficiency
EP	Entrance potential
ER	Extraction ratio
ESI	Electro-spray ionization
F	Bioavailability
F_a	Fraction absorbed
F_g	Fraction escaping gut metabolism
F_h	Fraction escaping hepatic metabolism
$f_{u,mic}$	Fraction unbound in microsome
$f_{u,p}$	Fraction unbound in plasma
f_{um}	Fraction unbound in microsome

G6PDH	Glucose-6-phosphate dehydrogenase
GABA	Gamma amino butyric acid
GIT	Gastrointestinal tract
GLUT1/3	Glucose transporter 1/3
HPLC	High-performance liquid chromatography
IS	Internal standard
IVIVC	*In vitro-in vivo* correlation
IVIVE	Iv vitro-*in vivo* extrapolation
ka	First order absorption rate constant
k_{deg}	First order degradation rate constant of the enzyme
K_I	Inactivator concentration at half-maximal inactivation
kinact	Maximal inactivation rate
K_m	Michaelis- Menten constant
k_{obs}	Apparent first order inactivation rate constant
LC	Liquid chromatography
LD_{50}	Median lethal dose
LLOQ	Lower limit quantitation

MAT	Mean absorption time
MBI	Mechanism based inactivator
MDZ	Midazolam
MIC	Metabolite intermediate complex
MM	Michaelis-Menten
MRP3	Multidrug Resistance Protein 3
MRT	Mean residence time
MS	Mass spectrometry
MSE	mean squared error
NADPH	Reduced nicotinamide adenine dinucleotide phosphate
NCD	Nicardipine
NCE	New chemical entity
NMP	1-methyl-2-pyrrolidinone
ODE	Ordinary differential equation
p.o.	Per oral
PBPK	Physiologically based pharmacokinetic
PD	Pharmacodynamic

P-gp	P-glycoprotein
PK	Pharmacokinetics
PK-DDI	Pharmacokinetic drug-drug interaction
PRA	Percent remaining activity
QC	Quality control
Q_{ent}	Enterocytic blood flow rate
R^2	Adjusted R-squared
RIM	Rat intestinal microsome
RLM	Rat liver microsome
SD	Sprague-Dawley
$t_{1/2}$	Half-life
TDI	Time-dependent inactivator
US-FDA	US Food and Drug Administration
V_d	Volume of distribution
V_{max}	Maximal rate of product formation
V_{ss}	Steady-state volume of distribution
WRSS	Weighted sum of residuals

CHAPTER ONE: INTRODUCTION

1.1 Bioavailability and Oral Drug Administration:

The US Food and Drug Administration (US-FDA) defines bioavailability (F) as “the rate and extent to which the active ingredient or active moiety is absorbed from a drug product and becomes available at the site of action” (Chow, 2014; Toutain & Bousquet-Mélou, 2004). However, it is difficult and, in most cases, impractical to determine the drug concentration at the target site of the drug. In general, bioavailability is more conveniently defined as the fraction of administered dose that reaches the systemic circulation unaltered from the site of drug administration. One of the major assumptions behind this definition is that 100% of the active moiety that reaches the systemic circulation will be available to the target successfully (Olivares-Morales et al., 2014). In pharmacokinetics (PK), there are two types of bioavailability calculated: absolute bioavailability and relative bioavailability (Sietsema, 1989; Toutain & Bousquet-Mélou, 2004). Absolute bioavailability is calculated for any dosage form relative to the intravenous dosing, whereas relative bioavailability is calculated for one dosage form relative to another (Sietsema, 1989; Toutain & Bousquet-Mélou, 2004). In both cases, the bioavailability is determined by comparing the area under the curve (AUC) of the plasma concentration-time curves. The plasma drug concentration-time profile, as well as the bioavailability of a drug in a specific dosage form or via a particular dosing route, depend on the principal PK processes such as absorption, distribution, metabolism, and excretion (ADME). These processes are dependent on several factors. The list includes but is not limited to the physical and chemical properties of the drug, drug formulation, and dosing route, presence of food, involvement of the transporters, disease states, individual differences in metabolic genotype and phenotype, age, gender, race, etc. (Lawrence & Amidon, 1999; Nakanishi & Tamai, 2015; Radice, Korzekwa, & Nagar, 2022; Toutain & Bousquet-Mélou, 2004; Vinarov et al., 2021). Moreover, pharmacokinetic drug-drug interactions (PK-DDI) are one of the leading causes of altering plasma concentration profiles and bioavailability of a drug. Drugs can interact with either co-administered food or drugs (Fahmi et al., 2009; Fahmi et al., 2008; Galetin, Gertz, & Houston, 2010; US-FDA, 2020).

Because of its benefits including ease of oral drug administration, patient choice, cost-effectiveness, and simplicity of producing oral dosage forms on a wide scale, oral medicine is the most popular method of drug administration (Alqahtani, Kazi, Alsenaidy, & Ahmad, 2021; Radice et al., 2022). The oral mode of administration is used to administer around 60% of established small-molecule medicinal commercially available medicinal products. According to current estimates, oral formulations account for roughly 90% of the worldwide market share of pharmaceutical products designed for human consumption (Alqahtani et al., 2021). The market value of the top-selling pharmaceutical items, which is now $35 billion with a 10% annual growth rate, is around 84% of those taken orally (Prasad, De Jesús, & Mailankody, 2017; Taxak et al., 2012). Patients are often more compliant with oral formulations than they are with alternative parenteral methods including intravenous, subcutaneous, and intramuscular injections (Ingersoll & Cohen, 2008). Orally administered medications can also be directed to particular areas within the gastrointestinal (GI) tract for the localized treatment of pathological conditions like the stomach and necrotizing enterocolitis, infections, inflammatory disorders, bowel diseases, gastro-duodenal ulcers, and gastroesophageal reflux disorders. Despite these benefits, developing oral formulations is challenging due to the physicochemical characteristics of drugs, such as their low water solubility and membrane permeability (Alqahtani et al., 2021). Drugs' low chemical and biological stability, as well as physiological obstacles, including pH, efflux transporters, and metabolic enzymes, can further impede absorption (Rubbens, Mols, Brouwers, & Augustijns, 2018; Vertzoni et al., 2019). The mechanism of medication absorption and transport, intestinal transit, the microenvironment of the GI tract, and drug stability in GI fluids have all been the subject of countless research over the past 40 years (Alqahtani et al., 2021; Daugherty & Mrsny, 1999; Reix et al., 2012).

The oral bioavailability is expressed by the following equation 1.1 (Alavijeh & Palmer, 2004; Gibaldi & Perrier, 1982; Hedaya, 2012; Sietsema, 1989; Toutain & Bousquet-Mélou, 2004):

$F = Fa.Fg.Fh$ Equation ---1.1

Where the F_a is the fraction absorbed from the lumen, F_g is the fraction escaping gut metabolism, and F_h is the fraction escaping hepatic metabolism. The F_g and F_h are termed as the ‘pre-systemic metabolism’ or ‘first-pass metabolism.’ There are several literature reports that address the impact of pre-systemic metabolism on oral drug bioavailability. Intestinal contribution to the pre-systemic metabolism has been a major issue in absorption model development due to its physiological complexity, food effects, formulation effects, and many other variables to consider (Alqahtani et al., 2021; Lawrence & Amidon, 1999; Sietsema, 1989).

In many instances, due to limited oral bioavailability, medication dosages have to be increased, increasing the risk of toxicity (Alqahtani et al., 2021; Lawrence & Amidon, 1999; Sietsema, 1989). In certain cases, the route of administration has to be changed. Therefore, in order to correctly conceptualize and construct novel orally administered treatments, it is imperative to understand and forecast the complicated biological events occurring from the mouth to the gut.

1.2 Pharmacokinetics of Oral Drug Absorption

Numerous factors affect how well the oral medication is absorbed and made available to the target organ. Inadequate therapy may result from excessive metabolism, drug-drug interactions, and poor absorption from the absorption site (Devadasu, Deb, Maheshwari, Sharma, & Tekade, 2018; Gibaldi & Perrier, 1982; Löbenberg, Amidon, Ferraz, & Bou-Chacra, 2013; Nakanishi & Tamai, 2015; Pal, Deb, Bandopadhyay, Bandyopadhyay, & Tekade, 2018; Palleria et al., 2013; Vertzoni et al., 2019). With the guidance of PK knowledge, safe and effective dosage regimens can be developed. Two preclinical species are often studied before testing in humans (Boxenbaum, 1982; Mahmood & Balian, 1999; Martignoni, 2006; D. Zhang, Luo, Ding, & Lu, 2012). By administering a drug, gathering samples at separate times, evaluating the amounts of the target drug and/or its metabolite(s), and then analyzing the results, *in vivo* PK is examined. Although samples can be taken from many different places, including bile, feces, and urine, venous blood is the most common type and plasma drug concentration versus time (C-t profile) is the most convenient way of representing PK data. Clearance (CL), the volume of distribution (V_d), and bioavailability (F) are the three main PK factors that may be identified from a drug's C-t profile (Gibaldi & Perrier, 1982; Hedaya, 2012; M. Rowland & Tozer, 2011). F is equivalent to 1 for drugs administered arterially or drugs administered intravenously that do not have lung metabolism. Due to insufficient absorption from the site of absorption to the systemic circulation, drugs administered through extravascular administration, including oral, nasal, rectal etc. have decreased bioavailability as shown in equation 1.1 previously (Ferl, Theil, & Wong, 2016).

All the PK process namely absorption, distribution, and elimination occur simultaneously in the body. However, not all the processes predominate all the times. For instance, drugs taken orally can be explained by two main stages (Gibaldi & Perrier, 1982; Hedaya, 2012; Shargel, 2013). The drug is leaving its site of absorption during the first phase, which is the absorption phase. In this phase, absorption predominates than elimination because there are more drugs for absorption than drugs for elimination. The drug is distributed inside the body and removed during the second, post-absorptive phase. In this phase elimination rules over the absorption since usually, absorption occurs more quickly than elimination, which leads to an ultimate elimination-only phase where an elimination half-life ($t_{1/2}$) can be calculated. However, distribution throughout the body is happening all the time and it depends on the drug’s physicochemical properties. In the elimination phase, the time it takes for 50% reduction of a substance by leaving the body is known as the elimination half-life ($t_{1/2}$). Flip-flop kinetics is an uncommon exception to this rule since absorption, which is significantly slower than elimination, is the rate-limiting process. As a result, the $t_{1/2}$ reflects absorption rate constant rather than elimination (Gibaldi & Perrier, 1982; Hedaya, 2012; Shargel, 2013).

The rate and extent of absorption play a pivotal part in establishing a drug's overall bioavailability (Gibaldi & Perrier, 1982; Hedaya, 2012; Shargel, 2013). The extent of absorption (F) measures how much is being absorbed, whereas the rate of absorption (k_a) measures how quickly the drug is being absorbed. Other PK metrics can be determined using C-t profiles. The total exposure to a drug is measured by the area under the concentration-time curve (AUC). On an oral dose, it is also possible to determine the highest concentration (C_{max}) and the time when this reaches the maximum concentration (t_{max}) (figure 1.1). Each measure is important while creating a treatment plan. Since it is challenging to measure concentrations at the therapeutic target, plasma concentrations are frequently used to indicate whether a drug is being used at therapeutic or toxic levels in the body.

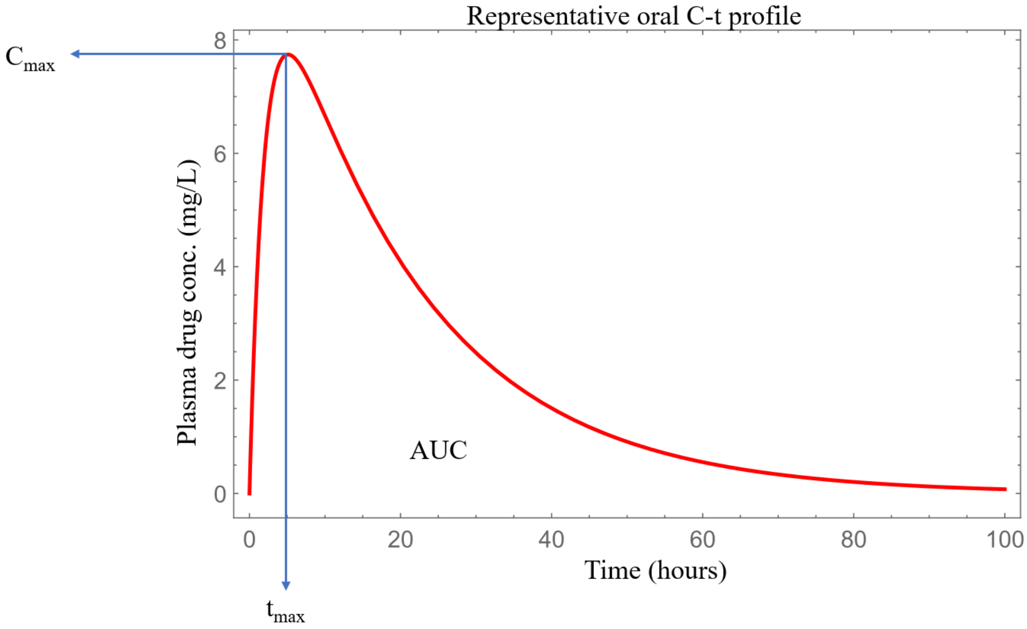

Figure 1.1. A representative C-t profile

The range of plasma concentrations where a drug exerted its target effect with little to no side effects is known as the therapeutic range. For the medicine to be both safe and effective, the C_{max} should fall within this range. The t_{max} of a drug should be consistent with its intended use. A shorter t_{max}, for instance, is better if a drug's impact is required immediately, like with an analgesic, or to get a better reaction by raising the C_{max}. If the therapeutic range is smaller or a prolonged duration of action is required, a longer t_{max} may be required.

Assuming very simple one-compartmental model, following equations can be written which can help to understand the inter-relationship between C_{max}, t_{max}, and k_a with the bioavailability F (Gibaldi & Perrier, 1982; Hedaya, 2012; Shargel, 2013):

$$C = \frac{F.D_{po}.k_a}{V_d(k_a - k)}(e^{-kt} - e^{-k_a t}) \qquad \text{Equation --1.2}$$

In equation 1.2, F is the oral bioavailability, D_{po} is the peroral dose, k_a is the apparent first-order absorption rate constant, V_d is the volume of distribution, and k is the first-order elimination rate constant.

The equation for C_{max} (Gibaldi & Perrier, 1982; Hedaya, 2012; Shargel, 2013):

$$C_{max} = \frac{F.D_{po}.k_a}{V_d(k_a - k)}(e^{-kt_{max}} - e^{-k_a t_{max}}) \qquad \text{Equation ----------------------------------1.3}$$

The equation for t_{max} (Gibaldi & Perrier, 1982; Hedaya, 2012; Shargel, 2013):

$$t_{max} = \frac{Ln(\frac{k_a}{k})}{k_a - k} \qquad \text{Equation ------------------------------------1.4}$$

The equation for AUC (Gibaldi & Perrier, 1982; Hedaya, 2012; Shargel, 2013):

$$AUC = \frac{F.D_{po}}{CL} \qquad \text{Equation} \text{ -- } 1.5$$

In equation 1.5, CL is the systemic clearance of the drug. AUC, C_{max}, and/or t_{max} may change if F and/or k_a change. Equation 1.5 illustrates the proportional relationship between changes in F and the AUC. Similar to the F, the C_{max} and F have a positive correlation, with the C_{max} rising as more drugs enters the circulation. Because the duration to achieve C_{max} is independent of the drug quantity, changes in F have no effect on the t_{max}. The AUC will remain constant if just k_a changes because the same quantity of drug will still be absorbed. However, equations 1.3 and 1.4 demonstrate that the k_a has an impact on the t_{max} and C_{max}. As was previously indicated, both processes happen at the same time, with absorption often happening more quickly than elimination. The t_{max} extends when the rate of drug entry into the systemic circulation is slower because drug accumulation takes more time. Similar to this, a lower C_{max} is the result of less drug accumulation.

1.3 Biopharmaceutic Classification System (BCS)

Drugs are categorized by the FDA into four Biopharmaceutics Classification System (BCS) groups based on their intestinal permeability and water solubility (Dahan, Miller, & Amidon, 2009; Poovi & Damodharan, 2018; Wu & Benet, 2005). This simplifies the relationship between *in vitro* dissolution and *in vivo* bioavailability. Dissolution is the rate at which a solute enters a solution, whereas solubility is a drug's innate capacity to remain in a solution. When the maximum dose of a medication can be dissolved at 37.5°C in less than 250 mL of an aqueous buffer with a pH adjustment between 1.0 and

8.0, the medication is considered to be extremely soluble (Rautio et al., 2008). Looking at figure 1.2, a drug is class I drug if that has high solubility and high permeability. The drug is class II if it has low solubility but high permeability. And, if the drug has high solubility but low permeability, that is class III drug. And finally, class IV drug has low solubility and low permeability. In today's market approximately 35% drugs are class I drugs, 30% are class II, 25 % are class II and about 10% is class IV drugs (Nikolakakis & Partheniadis, 2017).

Class I High solubility High permeability	**Class II** Low solubility High permeability
Class III High solubility Low permeability	**Class IV** Low solubility Low permeability

Figure 1.2 Biopharmaceutics Classification System (BCS) of drugs

There are some reports of predominant routes of drug elimination for drugs categorized into different classes of BCS. For instance, class I and II drugs are mainly eliminated by metabolism, both hepatic and intestinally (Wu & Benet, 2005). Class III and IV usually have significant renal or biliary excretion contribution in their elimination (Wu & Benet, 2005). Based on this observation, an extension of BCS classification system was introduced which is called the Biopharmaceutics Drug Disposition Classification System (BDDCS) (figure 1.3).

Class I High solubility High permeability	**Class II** Low solubility High permeability

Highly metabolized	Highly metabolized
Class III High solubility Low permeability Low metabolism	**Class IV** Low solubility Low permeability Low metabolism

Figure 1.3. Biopharmaceutics Drug Disposition Classification System (BDDCS)

Transporter-wise, class I drugs usually do not have any transport impact. Efflux transporter might impact class II drug's bioavailability (Wu & Benet, 2005). On the other hand, class II drugs are more dependent on intestinal uptake transporters, whereas class IV drugs depend both on efflux and uptake transporters and their interplay (Benet, Broccatelli, & Oprea, 2011; Wacher, Salphati, & Benet, 2001; Wu & Benet, 2005). However, there might be exceptions to this very generalized orders.

1.4 Anatomy and Physiology of Gastrointestinal Tract of Human and Rat

The mammalian alimentary canal is an open-ended tube with epithelial cells lining from the mouth to the anus. Associated organs include the liver, gall bladder, and pancreas. Its diverse functions include digestion of the food, absorption of nutrients and drugs, and propulsion of unwanted or unabsorbed contents. Xenobiotics, including drugs, are metabolized in the gastrointestinal tract, contributing to the first-pass metabolism of orally administered drugs. For the intended thesis, rats will be used as the animal model. However, there are certain differences in the anatomy of the upper alimentary canal of humans and rats, but this region of the alimentary canal does not contribute to drug absorption (J. M. DeSesso & Jacobson, 2001; John M. DeSesso & Williams, 2008).

For both species, the stomach serves the purpose of mixing the food particles with the secreted enzymes, emulsion formation for fatty contents, and propulsion of well-mixed chime into the small intestine for further digestion and absorption of the nutrients. Both species have a single chambered stomach, but rat stomach is divided into two regions: the forestomach with stratified epithelium lining is responsible for bacterial digestion of gastric contents, and the glandular stomach with secretory epithelium serves the acidic secretions and gastric enzymes (Vertzoni et al., 2019). A limiting ridge separates these two regions. On the other hand, the human stomach has three subsections: fundus, corpus, and antrum. The human stomach is lined with the secretory epithelium (J. M. DeSesso & Jacobson, 2001; John M. DeSesso & Williams, 2008). The mucus layer in the stomach is very thick, with a mean thickness of 180 µm, and composed of up to 20 different mucins. This layer protects the stomach from gastric acid and hinders the easy passage of molecules from the stomach to the bloodstream. The gastric environment is highly dependent on the meal that has been ingested. The environment is constantly changing while digesting food and emptying it into the intestine, and this environmental change has a significant impact on drug disintegration and dissolution (Vertzoni et al., 2019).

The major site for the absorption of water, drug, and nutrient is the small intestine which can be divided into three separate anatomic regions: duodenum, jejunum, and ileum. Mucus layer is relatively thinner here (20-50 µm). Majority of the absorption occurs in the duodenum and the upper part of the jejunum. Upon reaching the duodenum, the luminal contents are well mixed with bile, lipase, and protease for further digestion(Vertzoni et al., 2019). The luminal content of human duodenum is watery because of the extensive secretions from enteric glands, pancreas, and bile. Rat duodenal contents are more like a paste (John M. DeSesso & Williams, 2008).

Content propelled from the ileum is further processed in the large intestine or colon. Although water and electrolytes are absorbed from the large intestine, the extent is low due to reduced surface area for absorption. Some compounds face gut microbial metabolisms in the large intestine. Colonic mucus membrane has been identified to be two layered: an inner layer lacking microbiota, and an outer layer containing microbiome flora(Vertzoni et al., 2019). Human large intestine can be divided into several regions like cecum, ascending colon, traverse colon, descending colon, sigmoid colon, rectum, and anal canal. Rats lack the sigmoid colon from the above divisions (J. M. DeSesso & Jacobson, 2001; John M. DeSesso & Williams, 2008).

Based on function, the alimentary canal is divided into two regions: the conduit portion (mouth, pharynx, esophagus, rectum, and anal canal) to push to ingested contents through the canal, and the absorptive portion (stomach, small intestine, and proximal parts of the large intestine) (J. M. DeSesso & Jacobson, 2001; John M. DeSesso & Williams, 2008). The conduit portion is not the efficient part for absorption due to thick epithelial layer, inadequate vascularization of the lamina propria, and low surface area. Conversely, the absorbing portion’s mucosa is composed of a single cell layer of columnar epithelium. The lamina propria beneath it is also highly vascularized. Moreover, a major absorption mechanism is passive diffusion which is directly proportional to the surface area and surface area increase is contributed by various folded region of the small intestine including Kerckring's fold (1-3 times in human, absent in rat), villi (5-10 times), and microvilli (20-25 times). The columnar epithelial cells are termed as enterocytes which are attached to their adjacent cells by tight junctions. In the small intestine, the apical side of enterocytes have approximately 3000-7000 microvilli per cell which impact to the expansion of the absorptive surface area. The lamina propria beneath the absorptive portion is called the muscularis mucosa. It is very well developed in the intestinal region and extends inside the folded area of the villi(J. M. DeSesso & Jacobson, 2001; John M. DeSesso & Williams, 2008).

There are several reports of the dimensions of the alimentary canal for both human and rat. For human, the abundance of data creates a huge diversity of data mainly because of the different methods applied as well as the source e.g., *in vivo* or postmortem. A comparative analysis of both species' alimentary tract is given below:

Table 1.1: Intestinal tract dimensions for human and rat

Region of intestinal tract	Human			Rat		
	Length (cm)[a]	Surface area (m^2)[a]	Surface area relative to total body surface area [c]	Length (cm) [b]	Surface area (m^2)[b]	Surface area relative to total body surface area [c]
Duodenum	25			9.5-10		
Jejunum	260			90-135		
Ileum	395			2.5-3.5		
Total small intestine	**680**	**200**	**111**	**125**	**1**	**25**
Cecum	7			5-7		

Colon	93			9-11		
Rectum	55			8		
Total large intestine	**155**	**0.35**	**0.19**	**25**	**0.034**	**0.85**
Total intestinal tract	**835**			**150**		

[a](Snyder et al., 1975), [b](Hebel & Stromberg, 1986), and [c](J. M. DeSesso & Jacobson, 2001)

The rat and human digestive tracts differ significantly in a number of ways. For example, the human small intestine is almost 81% of the total intestinal tube in length, of which 38% is jejunum and 58% is ileum. In contrast, rat small intestine comprises 83% of the total, of which 90% is jejunum. In case of the cecum, rat's cecum is almost one-fourth of the large intestine whereas human cecum is approximately 5% of the large intestine. Also, rat does not have Kerckring's fold and sigmoid colon (J. M. DeSesso & Jacobson, 2001; John M. DeSesso & Williams, 2008).

With respect to the surface area, small intestine exceeds stomach by a huge margin, almost 3800-fold difference in human. Moreover, the large intestine surface area is 0.17% of that of small intestine. This clearly explains why small intestine the most efficient absorptive region is. Human small intestine possesses 200 times larger surface area than that of rat. Even normalizing with body weights, relative surface area of human small intestine is more than 4 times of the relative surface area of rat small intestine. The main reason behind this difference is the lack of Kerckring's folds in rat intestinal lumen.

Kerckring's folds increase the surface area by a factor 3. Microscopic finger-like extensions called villi increase the surface area by a factor of 10 in human and 5 in rats. Microvilli further extends the surface area by a factor of almost twenty (J. M. DeSesso & Jacobson, 2001). For both species, most of the absorption occurs in the jejunum. The presence of Kerckring's folds in humans and the relative length of the jejunum in rats is the main reason for increased absorption in this region(J. M. DeSesso & Jacobson, 2001; John M. DeSesso & Williams, 2008).

The gastrointestinal tract (GIT) of human and rat is surrounded by a few layers of smooth muscles whose coordinated rhythmic contractions cause the intestinal contents to mix thoroughly and movement of the contents along the axial direction of the intestinal tube. Transit time and velocity of the intestinal contents is another factor that plays a vital role in absorption. Transit time in human pharynx and esophagus is about 6 seconds. In stomach, transit depends on the type of content. The rank order of the emptying rate of content from fast to slow is as follows: water/saline, carbohydrates, protein, and fat. (J. M. DeSesso & Jacobson, 2001; John M. DeSesso & Williams, 2008). This nature of emptying might explain the discrepancies in the oral drug absorption under fasted versus fed condition. During the fasted condition, gastric emptying time for rat is around 10 min, whereas for human it is almost 1 hour (J. H. Lin, 1995). The transit time in human small intestinal ranges between 3 to 4 hours which is also the case for rats. The relative velocity of the luminal content is highest in the upper portion of the small intestine and it gradually decreases down the GIT. However, the transit time depends on numerous external and internal factors, and it should therefore be experimentally determined based on the specific research question(J. M. DeSesso & Jacobson, 2001).

The pH of the intestinal contents plays a significant role in drug absorption, drug degradation and solubilization or precipitation. The majority of the intestinal canal has a slightly basic pH except in the stomach, where pH drops drastically to highly acidic due to the gastric secretion of hydrochloric acid. While human gastric content may experience an extremely low pH of 1-2, rats' gastric content is less acidic (pH 3-5). The pH of upper intestine of human ranges from 6.1 to 7 and in the lower intestine is approximately 8(Vertzoni et al., 2019).

Rats do not have gall bladders, which is another significant distinction that should be recognized. Rats do not have the ability to store and concentrate bile and release it, as necessary. Rather, bile continuously secretes into the duodenum as soon as it is prepared. In contrast, human bile is secreted when intestinal content reaches the duodenum, and it is more concentrated that the rat biliary secretion. Comparing the volume, human gall bladder secretes 2-22 ml/kg/day, rat liver secretes 48 ml/kg/day of bile solution in the duodenum. Enzymes are another major constituent of the gastrointestinal environment. Some enzymes are secreted from digestive tract, some of them are bound to the cell surface membrane, and some are found inside the enterocytes. Their functions range from food digestion to detoxification of endogenous compounds as well as exogenous xenobiotics (J. M. DeSesso & Jacobson, 2001; John M. DeSesso & Williams, 2008).

Water can move back and forth between the intestinal lumen and blood depending on the tonicity of the intestinal content at a specific time. More than 8 liters of fluid enter the upper part of intestinal tract by ingestion of water (approximately 1.5 liters) and secretion of luminal digestive juices. However, around 1 liter of water reaches the large intestine and the water content in human feces is about 100 mL/day. Rat stomach and intestine contain a large number of gut microbiomes, but in human stomach, due to extreme pH, bacteria are not found. Gut microbiota in human is usually found from the distal ileum through the large intestine. There are differences in the microbial flora of rat and human which can significantly impact the drug absorption profile of a compound. These factors largely depend on age, sex, body weight, disease state etc. (J. M. DeSesso & Jacobson, 2001).

The alimentary canal is layered with mucosa which is composed of a thin sheet of epithelium over an extremely thin layer of loose connective tissue called lamina propria. Absorption from the intestinal lumen needs the compound to pass through the epithelium, the lamina propria and the wall of the blood vessels. The alimentary canal is also vascularized with blood and lymphatic capillaries mainly in the lamina propria. The extent of vascularity varies along the intestinal tract. The membrane of the blood capillaries is made of thin endothelium and the distance between the base of the enterocyte membrane and the blood capillaries is in micrometer range. Moreover, these blood capillaries have fenestrations on them which serve to absorb water and hydrophilic compounds (J. M. DeSesso & Jacobson, 2001; John M. DeSesso & Williams, 2008). In contrast, the lymphatic capillaries consist of single sac like structure called lacteals. The distance between the base of the enterocyte and the lacteal is around 50 µm. The lymphatic wall is thinner than the blood capillaries and they lack fenestrations. Hydrophilic compounds like glucose, amino acid etc. preferentially enter more into the blood capillaries whereas fatty compounds enter more in lymphatic capillaries. Most of the drugs enter the blood vasculature from either stomach or intestinal tract. They coalesce into hepatic portal vein which takes the drugs to the liver. Drug comes out of the liver through the hepatic central vein to get drained to the heart via inferior vena cava (J. M. DeSesso & Jacobson, 2001). Then the drug is distributed to the whole body depending on its physicochemical nature. Therefore, for an orally administered drug to reach the systemic circulation, it needs to overcome the absorption barrier, escape the enterocytic metabolism and hepatic metabolism.

Some compounds, while transiting in the liver, may be excreted through the bile duct to the duodenum and again re-absorbed back to the portal vein. This cycle can happen more than once with or without metabolic modification in the liver or in the intestine. This is termed as enterohepatic recycling which may have an important impact on drug disposition (J. M. DeSesso & Jacobson, 2001).

1.5 Mechanisms of Drug Absorption from Gastrointestinal Tract (GIT):

There are several drug-absorption mechanisms by which drugs become available in the bloodstream such as passive diffusion, active transport and facilitated diffusion (J. M. DeSesso & Jacobson, 2001; Devadasu et al., 2018; Dokoumetzidis, Kalantzi, & Fotaki, 2007; Huang, Lee, & Lawrence, 2009). Small molecule therapeutic drugs can often overcome intestinal lipophilic barriers via passive diffusion (Devadasu et al., 2018; Mazhar, Qaiser, Zahra, Fatimad, & Khane). Passive diffusion is determined by several physicochemical properties of the drug. The rate of mass transfer through the intestinal barrier follows Fick’s law of diffusion due to the concentration gradient.

Fick’s law of diffusion (Shargel, 2013) is shown in equation 1.6:

$$\frac{dQ}{dt} = \frac{D.A.K\frac{m}{w}}{h}(C_{GIT} - Cp) \qquad \text{------------------------------Equation 1.6}$$

Where, dQ/dt is the drug diffusion rate through the GIT, D is the diffusion rate constant, A is the surface area, h is the thickness of the intestinal absorption site, $K_{m/w}$ is the partition coefficient between the apical membrane and the gastrointestinal lumen, and (C_{GIT}-C_p) is the concentration gradient in which C_{GIT} is the drug concentration at the GIT and C_p is the plasma drug concentration.

On the luminal side of the membrane, there is high concentration of drug due to the drug dissolution. On the other side, drug concentration is low and continuously transported away through to blood circulation maintaining the concentration gradient (C_{GIT}-C_p). This would ensure almost complete absorption until there is no drug on the luminal side. However, actual complete absorption is rarely seen due to the movement of the drug molecules down the path of the intestine and intestinal metabolism of the drug in the enterocytes. Passive drug diffusion usually follows first-order kinetics unless there is any involvement of transporter molecules. Molecules limited by either molecular size or lipophilicity or both may not be available in the blood through passive diffusion. For them, several other mechanisms are available in our body (Devadasu et al., 2018; Fedi et al., 2021; Löbenberg et al., 2013; Pal et al., 2018; Vinarov et al., 2021).

Intercellular or paracellular transport occurs through the passage of molecules through the tight junctions between two adjacent enterocytes. The integrity of the tight junctions determines the diameter of the allowed molecules including water and some intestinal salts. Calcium is pivotal in maintaining the tightness of the cells. Chelation of calcium causes tight junctions to open for nonelectrolytes (Löbenberg et al., 2013).

Some molecules can be transported via carrier-mediated transport which is a saturable process and its kinetics depend on the concentration of the molecule (Devadasu et al., 2018; Pal et al., 2018; Porat & Dahan, 2018). Carrier-mediated transport can occur along the concentration gradient which is called facilitated diffusion. On the other hand, when it occurs against the concentration gradient, energy consumption is required, and that is called active transport (Löbenberg et al., 2013) .

Both passive diffusion and carrier-mediated transport are transcellular because drugs require to transport across the cell. However, there are some other mechanisms which may contribute to drug absorption including endocytosis, transcytosis, and pinocytosis. Also, there are some efflux transporter on the apical side of the enterocytes including P-glycoprotein (Pgp). Efflux transporters transport the drug back to the lumen from the cell and contribute to reduced intestinal drug availability (Devadasu et al., 2018; L. Lin & Wong, 2017; Pal et al., 2018; Porat & Dahan, 2018; Vinarov et al., 2021).

1.6 Drug-Drug Interaction and Impact on Bioavailability: Focus on Time-Dependent Inactivation (TDI)

Drug-drug interaction (DDI) refers to the impact of one drug on another co-administered drug. There are mainly two types of DDI (Fahmi et al., 2009; Fahmi et al., 2008; Palleria et al., 2013; US-FDA, 2020). When the PK profile of a drug is changed due to the presence of a co-administered drug, this interaction is referred to as a pharmacokinetic drug-drug interaction (PK-DDI). PK-DDIs are one of the leading causes to alter plasma concentration profiles and bioavailability of a drug. Drugs can interact with either co-administered food or drugs. There is another type of DDI which is called the pharmacodynamic (PD) DDI where co-administered drugs influence each other’s PD response. PK-DDI can occur without resulting PD-DDI and vice versa, or they can occur together (Cascorbi, 2012). DDI is more common in geriatric patients because of poly-therapy with a reported prevalence of up to 40% (Palleria et al., 2013).

PK-DDI is related to the ADME of a drug and it can occur due to the effect of one compound on either drug metabolizing enzymes (DME) and/or drug transporters, resulting in treatment inadequacy or toxicity (Fahmi et al., 2009; Fahmi et al., 2008; US-FDA, 2020). The effector drug is termed as the 'perpetrator drug molecule.' The effect might be inhibition or induction. On the other hand, the drug whose PK profile is altered, is called a 'victim drug molecule.' There have been numerous reports of drug withdrawal after marketing due to PK DDI (Qureshi, Seoane-Vazquez, Rodriguez-Monguio, Stevenson, & Szeinbach, 2011). It necessitates the need to identify potential perpetrator drugs and to predict their impact on the PK of other drugs that might be co-administered.

As mentioned previously, PK-DDI can result from the inhibition or induction of DMEs or transporters (Fahmi et al., 2009; Fahmi et al., 2008). In case of DMEs, if a drug inhibits an enzyme which is responsible for the metabolic elimination of another drug, the later drug's clearance will be reduced and its availability will increase. In case of induction, opposite effect will be seen. Responsible enzyme will be more active or more concentrated to metabolize the later drug to reduce its availability by increasing its clearance. The most important impact is found in case of mainly CYP3A4 inhibition or induction since it is the most prevalent enzyme in human intestine and liver (Galetin, Gertz, & Houston, 2008; Galetin et al., 2010; US-FDA, 2020). Clarithromycin, erythromycin, diltiazem, itraconazole, ketoconazole, ritonavir, verapamil, and grapefruit juice are effective CYP3A4 inhibitors. Phenobarbital, phenytoin, rifampicin, St. John's Wort, and glucocorticoids are CYP3A4 inducers (US-FDA, 2020). On the other hand, transporter impact depends on the type of transporter. For example, efflux transporters including Pgp are inhibited by many compounds which can increase the intestinal permeability of a co-administered drug and increase its systemic availability. Amiodarone, clarithromycin, cyclosporine, diltiazem, erythromycin, ketoconazole, itraconazole, propafenone, quinidine, and verapamil are a few examples of Pgp inhibitors (Dou et al., 2020; Melchior et al., 2012; Mouly & Paine, 2003). The opposite impact will be seen in case of the induction of efflux transporters. There are some uptake transporters in the intestine but their impact is most important in liver. If the uptake transporter is inhibited the co-administered drug will be less available to the hepatocytes and its clearance will be decreased to increase its bioavailability. Opposite impact will be seen in case of induction of uptake transporters.

As stated above, drug inhibition can cause PK-DDI. Drug inhibition can be either reversible or irreversible depending on the mechanism of enzyme inhibition. Irreversible enzyme inhibition results from different molecular mechanisms. Irrespective of the mechanism, the outcome is an inactive enzyme(Riley, Grime, & Weaver, 2007; Z.-Y. Zhang & Wong, 2005; Z.-W. Zhou & Zhou, 2009). There are several types of irreversible inhibitors such as mechanism-based inactivator (MBI), slow tight binders, transition state analogs, affinity labeling agents. Among these MBI is the most common(Silverman, 1995; Yadav, Paragas, Korzekwa, & Nagar, 2020). The mechanism of MBI involves the transition of the MBI into a reactive species which ultimately inactivate the enzyme by forming a bond with the enzyme covalently or non-covalently. MBI results in time-dependence, which means that the magnitude of inhibition increases with time. Therefore it is also called time-dependent inactivation (TDI)(K. Korzekwa et al., 2014; Nagar, Jones, & Korzekwa, 2014; Riley et al., 2007; Yadav, Korzekwa, & Nagar, 2019; Yadav et al., 2020). Other than time dependence, TDI possess several properties including saturation of inactivator concentration, substrate protection, irreversibility, inactivator stoichiometry, involvement of a catalytic step. Although not all of the properties are routinely experimented, but, time-dependence, saturation and, involvement of the catalytic step are usually characterized sufficiently in drug discovery (Silverman, 1995; Yadav et al., 2020).

A quite simple scheme of TDI has been provided in figure 1.4. The inactivator binds with the enzyme as a conventional substrate with an initial binding step to form an enzyme-inactivator complex. This complex leads further to the formation of the intermediate (EI*). This intermediate can proceed either to the product formation (E+P) or to the inactive enzyme formation (E**) (Mohutsky & Hall, 2014; Taxak et al., 2012; Yadav et al., 2020; S. Zhou et al., 2005).

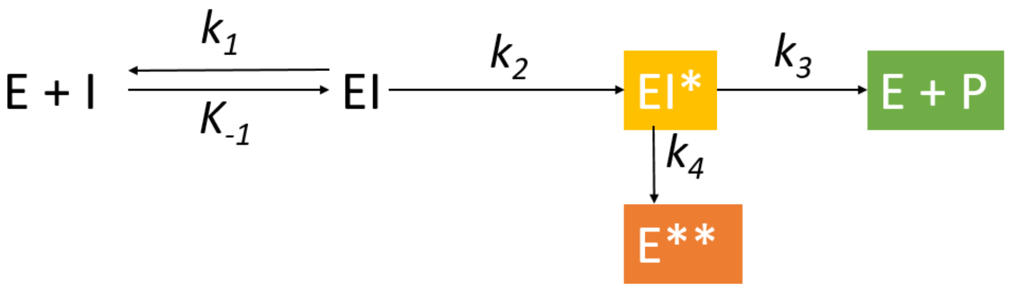

Figure 1.4: Scheme of TDI

At a given concentration of enzyme and inactivator, the intermediate concentration depends on three micro-rate constants: k_2, k_3 and k_4. The rate of E** formation can be described by a Henry-Michaelis-Menten function:

$$\frac{dE^{**}}{dt} = k_{inact}.E.\frac{I}{K_I+I}$$ ------------------------------------Equation 1.7

K_I is the unbound inactivator concentration which can cause 50% inactivation of the enzyme present. The k_{inact} is the maximal rate of inactivation for a given enzyme concentration. The equations expressing K_I and k_{inact} are given below:

$$K_I = \frac{k_{-1}+k_2}{k_1}.\frac{k_3+k_4}{k_2+k_3+k_4}$$ ------------------------------Equation 1.8

$$k_{inact} = \frac{k_2.k_4}{k_2+k_3+k_4}$$ ------------------------------Equation 1.9

K_{inact} is similar to the V_{max} of Michaelis-Menten equation in a sense that when $[I]>>>K_I$, the maximal rate of inactivation occurs. Higher k_{inact} means higher rate of inactivation and lower K_I means higher apparent affinity of the inactivator for the enzyme. Higher the ratio of k_{inact} to K_I, higher is the inactivation potential. This is why incorrect determination of K_I and k_{inact} can lead to misinterpretation of DDI scenario (Riley et al., 2007; Yadav et al., 2020; S. Zhou et al., 2005). Although the mechanism provided here is the simplest mechanism, it is not observed for all inactivators. For complex kinetics, complex TDI schemes are necessary has been shown elsewhere (Barnaba, Yadav, Nagar, Korzekwa, & Jones, 2016; Yadav et al., 2020). In those instances, K_I and k_{inact} will be determined by many additional micro-rate constants.

For the understanding of DDI, a comprehensive idea of DMEs and transporters is important which has been reviewed below briefly.

1.7 Cytochrome P450 Enzymes (CYPs)

Cytochrome P450 enzymes (CYPs) are membrane bound enzymes responsible for the metabolism of endogenous compounds as well as exogenous xenobiotic molecules. CYPs are the most important oxidative DMEs and they have been known to possess broad substrate specificity which makes them versatile to metabolize a wide array of compounds (K. Korzekwa, 2014). This diverse substrate specificity can contribute to the metabolic DDI because more than one drug can bind to the same enzyme or even compete for the same active site in the enzyme. Over the past 60 years, 57 functional genes and numerous CYP proteins have been identified and they have been categorized into different families and subfamilies (Burkina, Rasmussen, Pilipenko, & Zamaratskaia, 2017; S. F. Zhou, Liu, & Chowbay, 2009). Nomenclature of CYP enzymes is done using prefix CYP followed by family, subfamily, and isoform. Within a family there are more than 40% homology, within subfamily there are more than 55% homology in amino acid (Nelson, 2006). For example, for CYP2C8 isoform, it has more than 40% homology with other CYP2 enzymes including CYP2D, and it has more than 55% homology with other CYP2C including CYP2C9. While for human CYPs, only capital letters are used (for example CYP3A4 or CYP1A1), for rodents only first letter capitalized (for instance Cyp1a1 and Cyp3a1) (Nelson, 2006; Nelson et al., 2004).

Only three families of CYPs (CYP1, CYP2, and CYP3) contribute to the metabolic conversion of more than 90% of drugs among which almost 60% of the drugs are metabolized by CYP3A4 (Burkina et al., 2017). Liver is the major metabolizing organ of human body. Among the extrahepatic organs, small intestine, lung, kidney, brain, placenta, and skin also possess some CYPs. Small intestine is the most prominent extrahepatic organ that contributes to a major portion of first pass metabolism (S. F. Zhou et al., 2009).

Oral route of drug administration is the most common route of drug administration due to its better patient compliance and convenience. Because of the anatomical design, small intestine is the first metabolic site in human body that contributes to the first pass metabolism of orally administered drugs. It is also the site which is exposed to the highest concentration of orally administered and dissolved drugs. The lower blood flow compared to the hepatic blood flow also makes it a suitable site for drug biotransformation providing a longer time for the metabolism of a drug by gut enzymes (Galetin et al., 2008, 2010). There are several CYPs expressed in the human small intestine, CYP3A4/5 and CYP2C9 being the two highest contributing enzymes with relative abundance of 80% and 14% respectively. Other CYPs include CYP2C19, 2J2 and 2D6 (<2%) (Galetin et al., 2008; Xie, Ding, & Zhang, 2016). Any impact on CYPs including induction or inhibition may promote DDI. Especially if the site of consideration is small intestine, the effect on CYP3A4 and/or CYP2C9 will likely result in DDI. However, liver is still the major metabolic site which contains almost 35% CYP3A, 12-14% of CYP2C, CYP2E1, and CYP1A2, about 8% CYP2A6, and minor proportions of CYP2B6 and CYP2D6 (Galetin et al., 2008).

Similarly, rat intestine is also the first metabolic site which contributes to the first pass metabolism of the xenobiotics. However, the expression pattern is different from the human intestine. Cyp1a1 is the highest expressed cytochrome P450 enzyme in rat intestine. The other Cyps are Cyp1a2, Cyp2b, Cyp2c, Cyp3a, Cyp4a1, Cyp2j3/4, and Cyp4f12 (Kaminsky & Zhang, 2003; Pałasz et al., 2012). However, the relative abundance of these Cyps is yet to be revealed definitively. It is noteworthy to mention that there are significant differences in the expression levels of Cyps in different strains of rats. However, major hepatic Cyps are Cyp1a1, Cyp1a2, Cyp2b1, Cyp2c11, and Cyp3a2 (Nishiyama et al., 2016). Specifically in the Sprague-Dawley (SD) rats (used in this thesis), four Cyps namely Cyp2b1, Cyp2c6, Cyp2c11, and Cyp2d1 are expressed comparatively similar in both liver and intestine. Similar to most rat strains, Cyp1a1 is the highest expressing enzyme in small intestine of SD rats. However, Cyp2e1 and Cyp3a1 are expressed much higher in liver than in the intestine (Lindell, Lang, & Lennernäs, 2003).

There are significant gender differences observed in SD rat Cyp expressions. For example, Cyp2c11 is a male-specific CYP. This is also the dominant isoform in male rat liver comprising almost 50% of all CYPs (Morgan, MacGeoch, & Gustafsson, 1985). Cyp2c13 is also male-specific, but it is expressed both in hepatic and extra-hepatic tissues including brain (Riedl et al., 2000). On the other hand, Cyp2c12 is female-specific, mostly young female rats (Mugford & Kedderis, 1998). Also, Cyp2c7 isoform is uniquely expressed in female rats (Agrawal & Shapiro, 1997). In addition to the gender dependence, SD rats also show significant age dependence in CYP expression. In male Sprague Dawley rats, Cyp3a2 and Cyp3a18 are only recognized as male-specific isoforms after 8 weeks, whereas Cyp3a9 is a female dominant form (Asaoka et al., 2010). Male rat liver CYP levels are only 20% higher than female rat liver levels, however certain isoforms may differ even more (Nishiyama et al., 2016).

1.8 Fundamentals of Cytochrome P450 Enzyme Kinetics:

Studies on spectral binding and X-ray crystallography confirm that the active site P-450s are big and flexible, allowing them to hold several substrates at once. Atypical kinetics, such as biphasic kinetics, sigmoidal kinetics, and substrate inhibition, can be produced by this multiple substrate binding (K. R. Korzekwa et al., 1998; Tracy, 2006). The wide specificity of the active site, other binding sites, and protein-protein interactions are potential explanations for why these atypical kinetics diverge from the standard single binding Michaelis-Menten kinetics. From a modeling perspective, however, a straightforward single binding ES model or double binding ESS model may effectively represent the majority of the observed saturation curves (Figure 3.1)(Paragas et al., 2021; Wang et al., 2021).

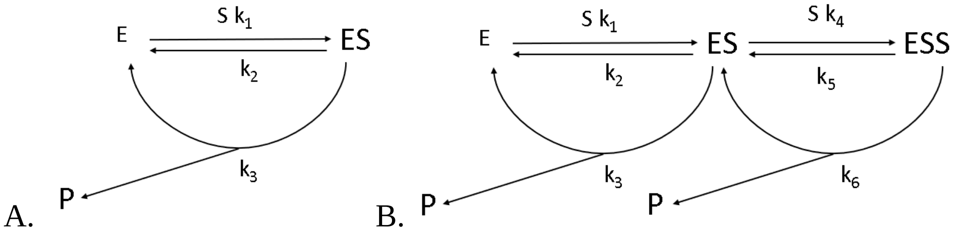

Figure 1.5: (A) A single-substrate binding (ES model) (B) A two-substrate binding (ESS model). (Figure reproduced from (Paragas, Wang, Korzekwa, & Nagar, 2021; Z. Wang, Paragas, Nagar, & Korzekwa, 2021))

The conventional single-substrate binding model is shown in Figure 1.5A. One substrate molecule (S) and one enzyme molecule (E) form the ES intermediate complex by their binding. This ES complex can move on to form an enzyme-product complex (EP) or it can go back to its starting state. According to this scheme, the EP complex is assumed to last less time than the ES complex. Assuming steady-state, the equation derived from this scheme is known as the Michaelis-Menten equation (Michaelis & Menten, 1913; Paragas et al., 2021; Z. Wang et al., 2021)

$$\frac{v}{E_t} = \frac{\frac{v_{max}}{E_t} \cdot [S]}{K_m + [S]} = \frac{k_{cat} \cdot [S]}{K_m + [S]} \qquad \text{Equation -------------------------------1.10}$$

Here, V_{max} is the maximal velocity, k_{cat} is the maximum velocity at unit enzyme concentration (E_t), [S] is the substrate concentration. K_m is the substrate concentration at the half-maximum turnover rate and can be expressed by the following equation (Paragas et al., 2021; Z. Wang et al., 2021):

$$K_m = \frac{k_2 + k_3}{k_1} \qquad \text{Equation --------------------------------------1.11}$$

The K_m and V_{max} values are used to calculate intrinsic clearance (CL_{int}), which is the capacity of an enzyme or organ to metabolize the substrate without blood flow or protein-binding limitations. Intrinsic clearance is expressed as the ratio of the product formation rate to the substrate concentration (Paragas et al., 2021; Z. Wang et al., 2021):

$$CL_{int} = \frac{v}{[S]} = \frac{v_{max}}{K_m + [S]} \qquad \text{Equation --------------------------------------1.12}$$

When $[S] << K_m$, the equation can be rewritten as (Paragas et al., 2021; Z. Wang et al., 2021):

$$CL_{int} = \frac{v_{max}}{K_m} \qquad \text{Equation -------------------------------1.13}$$

A two-substrate model (ESS model) that can lead to non-Michaelis-Menten kinetics is shown in Figure 1.5B. The majority of categories of atypical kinetics may be described by Fig. 1.5B, which does not imply that substrates would bind in a fixed orientation.

According to these models, the first substrate has an apparent K_{m1} and a k_{cat1} turnover rate when it binds to the enzyme active site. The enzyme's second substrate binds to the active site with the K_{m2} affinity and k_{cat2} turnover rate. Assuming steady-state a more complex equation can be derived for ESS mode (Paragas et al., 2021; Z. Wang et al., 2021):

$$\frac{v}{E_t} = \frac{k_{cat1} \cdot [S] + \frac{k_{cat2}}{K_{m2}}[S]^2}{K_{m1} + [S] + \frac{[S]^2}{K_{m2}}}$$ Equation --------------------------------1.14

The K_m values are apparent since both processes occur simultaneously. Sigmoidal kinetics will be observed when $K_{m1} > K_{m2}$ or $k_{cat1} < k_{cat2}$. Biphasic kinetics are observed when $K_{m1} < K_{m2}$ and $k_{cat1} < k_{cat2}$. Substrate inhibition occurs at the condition of $K_{m1} < K_{m2}$ and $k_{cat1} > k_{cat2}$ (Paragas et al., 2021; Z. Wang et al., 2021). The K_m and CL_{int} relationships for the ESS model are as follows:

$$K_{m1} = \frac{k_2 + k_3}{k_1}$$

$$K_{m2} = \frac{k_5 + k_6}{k_4}$$

$$CL_{int1} = \frac{v_{max1}}{K_{m1}}$$

$$CL_{int2} = \frac{v_{max2}}{K_{m2}}$$

Equations --1.15-1.18

The kinetic parameters stated above are often calculated using the information on metabolite production. To extract the micro-rate constants, ordinary differential equations

(ODEs) are developed and fitted to the data using numerical methods. The independence from the assumptions of steady-state and unchanged substrate concentration across the incubation time are the key advantages of employing numerical approaches (K. Korzekwa et al., 2014; Nagar et al., 2014; Yadav, Korzekwa, & Nagar, 2021).

1.9 Hepatic and Intestinal Transporters

In liver, basolateral intake of substances from the blood side (extracellular space) into hepatocytes, basolateral efflux from hepatocytes into the blood, phase I/phase II metabolism, and biliary excretion are some of the intrinsic activities that make up the hepatic elimination process. Because of their wide and overlapping substrate specificities, these stages cooperate in the hepatobiliary clearance of xenobiotics and can contribute to DDI (Fahmi et al., 2008; US-FDA, 2020). The hepatic uptake is controlled by both the passive diffusion and carrier-mediated processes including active transport and facilitated diffusion. In human, the hepatic uptake is mediated by several solute carrier (SLC) transporters including organic anion transporter 2 (OAT2, SLC22A7), and Na-taurocholate co-transporting polypeptide (NTCP, SLC10A1) (Chiba, Hensleigh, & Lin, 1997; Koenen, Kroemer, Grube, & Meyer zu Schwabedissen, 2011; Yoshida, Maeda, & Sugiyama, 2013). Organic cation transporter 1 (OCT1, SLC22A1) mediates the facilitative diffusion (Yoshida et al., 2013). These are called hepatic uptake transporter. Drugs from the liver, undergoing metabolism can also be effluxed out of liver. ATP-binding cassette (ABC) transporters, including P-glycoprotein (Pgp), multidrug resistance-associated protein 2 (MRP2, ABCC2), breast cancer resistance protein (BCRP, ABCG2), and bile salt export pump (BSEP, ABCB11), as well as SLC transporters [multidrug and toxin extrusion 1 (MATE1, SLC47A1)], can excrete the parent substances and/or their metabolites into the bile leading to biliary excretion (Koenen et al., 2011; Lušin et al., 2012; Yoshida et al., 2013). Some drugs can also experience active efflux at the basolateral membrane leading them back to blood mediated by mainly MRP3 (ABCC3) and MRP4 (ABCC4) (Lušin et al., 2012; Yoshida et al., 2013).

Pgp is the most important efflux transporter in the intestine (Lušin et al., 2012; Nakanishi & Tamai, 2015). It often works with similar substrate specificity with CYP3A4 serving as a barrier for the xenobiotics to be available in the blood stream. Digoxin, loperamide, berberine, fexofenadine, nicardipine, and other anticancer including irinotecan, doxorubicin, vinblastine, and paclitaxel are some examples of the substrates of Pgp. BCRP is also an efflux transporter which is found in the intestine (Yoshida et al., 2013). While passive diffusion is the major mechanism for drug permeation from the intestine the involvement of some uptake transporters including OATP2B1 has been reported (Koenen et al., 2011; Yoshida et al., 2013). However, the expression of OATP2B1 depends on age and neonates have the highest expression (Mooij et al., 2014).

1.10 *In Vitro-In Vivo* Extrapolation (IVIVE) for DDI:

There are different modeling strategies to predict DDI. Two strategies are discussed here: static and dynamic modeling. Static modeling predicts DDI using natural turnover rate of the enzymes, TDI parameters obtained from *in vitro* experiments (K_I and k_{inact}), and fraction metabolized by a particular CYP enzyme. For example, Mayhew et al. developed a static model for low ER drugs, but it under predicted intestinal contribution to the DDI(Mayhew, Jones, & Hall, 2000). Wang et al. added gut contribution to modify this model(Y.-H. Wang, Jones, & Hall, 2004). Again, Fahmi et al. modified this model to incorporate more than one mechanism (reversible and irreversible inhibition, induction)(Fahmi et al., 2009; Fahmi et al., 2008). The model by Fahmi et al. is currently used in the US-FDA guidance for *in vitro* DDI studies(Yadav et al., 2020). There are some other static models which are less popular and suffer from under prediction. Major static models are shown below in the table:

Table 1.2: Major static models to predict oral DDI

No.	Equations for static modeling	Reference
1	$AUCr = \dfrac{k_{deg}}{k_{deg} + \dfrac{[I].k_{inact}}{[I] + k_{inact}}}$	(Mayhew et al., 2000)
2	$\dfrac{\mathrm{AUC}'_{\mathrm{po}}}{\mathrm{AUC}_{\mathrm{po}}} = \dfrac{\mathrm{CL}_{\mathrm{int,H}}/F_{\mathrm{G}}}{\mathrm{CL}'_{\mathrm{int,H}}/F'_{\mathrm{G}}} = \dfrac{F'_{\mathrm{G}}}{F_{\mathrm{G}}} \times \dfrac{\mathrm{CL}_{\mathrm{int,H}}}{\mathrm{CL}'_{\mathrm{int,H}}} = \dfrac{F'_{\mathrm{G}}}{F_{\mathrm{G}}} \times \dfrac{1}{\dfrac{f_{\mathrm{m}}}{1 + \sum_{i=1}^{n} \dfrac{k_{\mathrm{inact,i}} \times I_{\mathrm{u,i}}}{k_{\mathrm{deg}} \times (K_{\mathrm{I,u}})_{\mathrm{i}}}} + (1 - f_{\mathrm{m}})}$ $\dfrac{F'_{\mathrm{G}}}{F_{\mathrm{G}}} = \dfrac{A + \mathrm{CL}_{\mathrm{int,G}}}{A + \mathrm{CL}'_{\mathrm{int,G}}} = \dfrac{1}{F_{\mathrm{G}} + (1 - F_{\mathrm{G}}) \times \dfrac{\mathrm{CL}'_{\mathrm{int,G}}}{\mathrm{CL}_{\mathrm{int,G}}}}$ $\dfrac{\mathrm{CL}_{\mathrm{int,G}}}{\mathrm{CL}'_{\mathrm{int,G}}} = 1 + \sum_{i=1}^{n} \dfrac{k_{\mathrm{inact,i}} \times I_{\mathrm{G,i}}}{k_{\mathrm{deg}} \times (K_{\mathrm{I,i}} + I_{\mathrm{G,i}})}$	(Y.-H. Wang et al., 2004)
3	$\dfrac{\mathrm{AUC}'_{\mathrm{p.o.}}}{\mathrm{AUC}_{\mathrm{p.o.}}} = \left(\dfrac{1}{[A \times B \times C] \times f_{\mathrm{m}} + (1 - f_{\mathrm{m}})}\right) \times \left(\dfrac{1}{[X \times Y \times Z] \times (1 - F_{\mathrm{G}}) + F_{\mathrm{G}}}\right)$ $A = \dfrac{k_{\mathrm{deg,H}}}{k_{\mathrm{deg,H}} + \dfrac{[I]_{\mathrm{H}} \times k_{\mathrm{inact}}}{[I]_{\mathrm{H}} + K_{\mathrm{I}}}}$ $B = \mathrm{I} + \dfrac{d \cdot E_{\mathrm{max}} \cdot [I]_{\mathrm{H}}}{[I]_{\mathrm{H}} + \mathrm{EC}_{50,\mathrm{I}}}$ $C = \dfrac{1}{1 + \dfrac{[I]_{\mathrm{H}}}{K_{\mathrm{i}}}}$ $X = \dfrac{k_{\mathrm{deg,G}}}{k_{\mathrm{deg,G}} + \dfrac{[I]_{\mathrm{G}} \times k_{\mathrm{inact}}}{[I]_{\mathrm{G}} + K_{\mathrm{I}}}}$ $Y = \mathrm{I} + \dfrac{d \cdot E_{\mathrm{max}} \cdot [I]_{\mathrm{G}}}{[I]_{\mathrm{G}} + EC_{50,\mathrm{I}}}$ $Z = \dfrac{I}{I + \dfrac{[I]_{\mathrm{G}}}{K_{\mathrm{i}}}}$	(Fahmi et al., 2009; Fahmi et al., 2008)

Static modeling uses a single inhibitor concentration to predict the extent of DDI, which is not the reality *in vivo*. Inhibitor concentration changes over time and using a single concentration may lead to inaccurate DDI prediction. Also, the static model predicts the AUC ratio only. Merely AUC ratio cannot depict the actual scenario because same AUCs can be obtained from vastly different plasma concentration profiles (Figure 1.6). Therefore, exposure overlap coefficients are useful. A representative figure is given below:

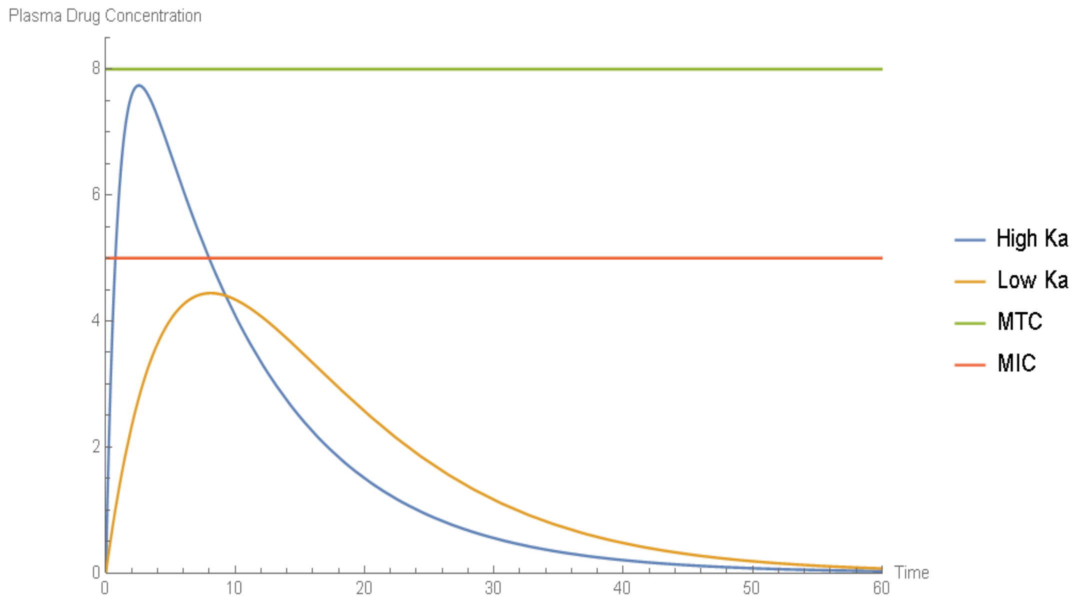

Figure 1.6: Representation of same AUC but different absorption profile.

The green and solid horizontal lines depict maximal therapeutic concentration (MTC) and minimum therapeutic concentration (MIC) respectively. The area under the blue line is the AUC with higher absorption rate constant (k_a). Are under the orange line is the AUC with lower absorption rate constant (k_a).

Static models cannot differentiate between different inhibitor-inhibited drug pairs. Complex kinetics as well as sequential metabolisms cannot be incorporated into the static models easily (Yadav et al., 2020). Static modeling serves enough as a quick tool to predict DDI in some instances, but these limitations necessitate a need for dynamic modeling.

Dynamic models consider the victim and the perpetrator concentration change over time. Dynamic models can be either compartmental models or physiologically-based pharmacokinetic (PBPK) model (Kuepfer et al., 2016; Offman & Edginton, 2015; Wagner et al., 2015; Yadav et al., 2020). Over the past few decades, reports of PBPK modeling have increased significantly (Ferl et al., 2016; Garg & Balthasar, 2007; Kuepfer et al., 2016; Offman & Edginton, 2015; M. Rowland, Lesko, & Rostami-Hodjegan, 2015; Sager, Yu, Ragueneau-Majlessi, & Isoherranen, 2015; Wagner et al., 2015; Wong & Chow, 2017; P. Zhao et al., 2011; Zhuang & Lu, 2016). While the compartmental models do not need a tremendous amount of physiological input, PBPK models require physiological inputs. However, commercial PBPK software has been developed and can incorporate different physiological inputs as well as genetic variability (Kuepfer et al., 2016; Offman & Edginton, 2015).

1.11 *In Vitro* Models for Intestinal Epithelium Permeation

Because of their affordability, great repeatability, and simplicity of use, 2D culture methods are still often used today to assess the bioavailability of an oral medication. 2D culture models are mainly two types: synthetic models and cellular models (Fedi et al., 2021; Gantzsch et al., 2014). Within the synthetic models the Parallel Artificial

Membrane Permeability Assay (PAMPA) and Phospholipid Vesicle-Based Permeation Assay (PVPA) are widely used. PAMPA is an *in vitro* system that produces a phospholipid composition of the desired human intestinal barrier for absorption. It is useful tool for drugs which are mainly absorbed by passive diffusion (Fedi et al., 2021; Gantzsch et al., 2014). But it is unable to characterize drug permeation of hydrophilic compounds which are mainly absorbed by paracellular pathways (L. Lin & Wong, 2017). On the other hand, PVPA is a solvent free synthetic system also used for passively absorbed drugs (Flaten et al., 2015). It is more successful than PAMPA by providing more comparable results to caco-2 monolayer cells. However, it is limited by its inability to morphological and physiological resemblance to intestines including villi and active transport proteins (Flaten, Dhanikula, Luthman, & Brandl, 2006; Flaten et al., 2015; Naderkhani, Isaksson, Ryzhakov, & Flaten, 2014).

Within the cellular models, the caco-2 cell line obtained from a human colon carcinoma is the most widely used model *in vitro* to simulate the biological barrier like gut (Gantzsch et al., 2014; Hu, Ling, Lin, & Chen, 2004; Takenaka et al., 2017). Since they were shown to be particularly useful to understand how substances are absorbed and metabolized across the intestinal epithelium, to predict the amount that will be absorbed by humans, and to study, select, and classify drug candidates under controlled conditions in accordance with the Biopharmaceutics Classification System (BCS), Caco-2 cells represent the gold standard that regulatory authorities accept for ADME-Tox studies (Gantzsch et al., 2014; Hu et al., 2004; Takenaka et al., 2017). In fact, Caco-2 monolayers have the majority of the morphological and functional traits of the small bowel while being derived from the colon(Hidalgo, Raub, & Borchardt, 1989). However, there might be variable results in the literature resulting from the cells' colonic cancerous origins, as they exhibit structural and functional characteristics more in line with large intestinal cells than small bowel ones such as stronger tight junctions, higher transepithelial electrical resistance (TEER) values, altered expression of enzymes and transporters, etc. (Darling, Mobbs, González-Hau, Freer, & Przyborski, 2020; Macedo, Araújo, Martínez, Barrias, & Sarmento, 2018). There are some other cellular models including TC-7 cell line assay, Madin-Darby canine kidney (MDCK) cell line assay etc. Although each has advantages and disadvantages, Caco-2 static monolayer cultures are the industry standard for *in vitro* research of intestinal barrier properties following exposure to pharmaceutical and nutraceutical compounds (Sun, Chow, Liu, Du, & Pang, 2008). Most experts agree that Caco-2 cells are the most useful intestinal epithelial model because they enable for an accurate replication of absorption via the transcellular channel, which is the most typical drug absorption route (Darling et al., 2020; Gantzsch et al., 2014; Hidalgo et al., 1989; Hu et al., 2004; Sun et al., 2008; Takenaka et al., 2017).

Standard Caco-2 cells lack the morphologic and physiological characteristics of fully developed intestinal tissue, even though the use of Caco-2 cell monolayers as an intestinal barrier model is widely established and offers an efficient and affordable screening model (Darling et al., 2020; Vaessen et al., 2017). Standard Caco-2 cultures, for instance, differ from intact intestinal tissue in terms of intestinal metabolism, mucus generation, passive diffusion, paracellular transport via tight junctions, and carrier-mediated uptake and excretion. Also, the intestine has regional variabilities with respect to drug metabolizing enzymes (DMEs) and transporters which caco-2 monolayers will not have. There is significant difference in the expression of DMEs and transporters between human intestine and caco-2 monolayers (Darling et al., 2020; Vaessen et al., 2017). For instance, relevant uptake (GLUT1, OATP2B1 and OATP4A1) and efflux (MRP1 and MRP2) transporters are expressed significantly higher than human jejunum. In case of DMEs, the scenario is opposite to that of transporters (Hayeshi et al., 2008). Most of the intestinal DMEs are at least five-fold lower expressed in caco-2 monolayer with CYP1A1 with the least difference and CYP3A4 with more than 800 fold difference (Darling et al., 2020; Vaessen et al., 2017). Since CYP3A4 is the major DME in human intestine, and because of extremely low expression of all the DMEs in caco-2 cells, its use to characterize intestinal metabolism is not supported by the experts. However, since most of the drugs are passively permeated through the intestine, the use of caco-2 cells are still a very good choice in drug discovery and development (Darling et al., 2020; Gantzsch et al., 2014; Hidalgo et al., 1989; Hu et al., 2004; Sun et al., 2008; Takenaka et al., 2017).. However, in case of transporter involvement additional consideration might be useful because of the difference in transporter expression in caco-2 cells and human intestine (Hayeshi et al., 2008).

1.12 Animal Models in Pharmacokinetics and Use of Rats

Drug discovery and development is expensive and time-consuming, and a massive portion of this work is targeted to ensure that the end-product is safe and efficacious. Due to ethical concerns, it is not possible to use a drug in humans without vigorous testing in preclinical species(Boxenbaum, 1982; Burkina et al., 2017). There are certain instances where the data from preclinical species do not extrapolate successfully to the clinical scenario, but in most cases, the use of preclinical species leveraging pharmacokinetic principles has been beneficial for drug development (J. H. Lin, 1995). Animal models have been developed, modified, and refined over the years to capture the mechanism underlying important PK parameters.

There are reports of successful extrapolation of animal data to human (J. H. Lin, 1995). At the same time, there are reports of significant species differences in absorption profiles across different animal models (Olivares-Morales et al., 2014; Tang & Prueksaritanont, 2010; Toutain & Bousquet-Mélou, 2004). Major factors that impact these variations are GI pH, surface area, variable expression levels of transporters and enterocytic enzymes. There have been reports where fraction absorbed from different species are almost similar, but the oral bioavailability is significantly different due to variable first-pass metabolism among animal models (J. H. Lin, 1995). While dogs are the first choice for pH-independent absorption models, rats are commonly used for pH-dependent models. Rats' average intestinal pH is slightly less than that of human (Boxenbaum, 1982; Burkina et al., 2017; J. H. Lin, 1995). Also, the water content normalized to body weight is higher than human. These factors may have significant impacts on absorption profile (Tang & Prueksaritanont, 2010). In case of intestinal permeability, a correlation between human and rat intestinal permeability has been reported for both energy-dependent and -independent passive transport (Tang & Prueksaritanont, 2010). They both have similar expression patterns of transporters along the length of the intestine except for P-glycoprotein (Pgp), multidrug resistance-associated protein-3 (MRP3), glucose transporter-1 (GLUT1), and glucose transporter-3 (GLUT3) (Burkina et al., 2017; Martignoni, Groothuis, & de Kanter, 2006). However, in case of metabolizing enzyme expression levels, these two species are quite different from each other. These variables may explain the utility of rats in predicting oral drug absorption by transporter-mediated mechanisms but not in determining the intestinal bioavailability for high extraction ratio compounds (Tang & Prueksaritanont, 2010). However, rats, along with mice are the first choice of animal models to determine tissue distribution, but drug distribution is translated to human with caution because of physiological variability (Tang & Prueksaritanont, 2010). There are some other advantages of using rodents as mammalian models. They are inexpensive, they are relatively easier to handle than other mammalian species, they can be accommodated very easily, and importantly, they provide useful pharmacokinetic, metabolic and toxicity data (Boxenbaum, 1982; Dou et al., 2020; Martignoni et al., 2006).

For predicting metabolism, higher animal species more closely resemble the human drug-metabolizing enzymes (DMEs). The reason behind this higher degree of similarity is amino acid sequences and subsequently substrate specificity. There is almost 70% homology in amino acid sequences of human major CYP3A (4/5) and rat major Cyp3a (1/2). It may explain why some of the mechanism-based inhibitors are common for both human CYP3A and rat Cyp3a. However, there is an interesting difference between human and rat CYP3A. The same CYP3A4 is expressed in the intestine and liver for human. But for rat, different Cyp3a isoforms are expressed: Cyp3a62 in the liver and Cyp3a1/2 in the intestine (Burkina et al., 2017; Martignoni, 2006; Martignoni et al., 2006). This species difference can potentially make DDI prediction scaling to human difficult. However, with the ongoing improvement in PK modeling and simulation field, rat has been found to be used by several lab groups to examine the transporter-enzyme interplay especially Cyp3a (Olivares-Morales et al., 2014; Tang & Prueksaritanont, 2010).

1.13 Absorption Models

Drug degradation, stomach emptying, intestinal transit, intestinal permeation and transport, intestinal metabolism, and hepatic metabolism are some of the several processes involved in oral drug absorption. The dosage form, physicochemical and biological characteristics of the active drug component, and physiology of the gastrointestinal (GI) tract are the variables that may affect the rate and amount of drug absorption (Huang et al., 2009; Lawrence & Amidon, 1999). Predictive models for oral drug absorption have been facilitated by knowledge of how these procedures and other variables affect absorption. Currently, drug research, development, and regulation make extensive use of modeling and simulation of oral drug absorption (Huang et al., 2009; Lawrence & Amidon, 1999; L. Lin & Wong, 2017; Vertzoni et al., 2019). The predictive absorption models are employed to build formulation development strategy, facilitate lead drug candidate selection, estimate the rate and extent of orally administered absorption, and support the development of regulatory rules.

Oral drug absorption modeling can be classified into three categories: quasi-equilibrium models, static models, and dynamic models. The quasi-equilibrium models are independent of the regional and temporal variables (Huang et al., 2009; Lawrence & Amidon, 1999). They just include the pH partition hypothesis and absorption potential concepts. Static models assume steady-state conditions. They are also independent of temporal variables but can incorporate regional variables. Static models can predict the extent but not the rate of drug absorption. The dynamic models consider both the temporal variables and the spatial variables. They are capable of characterizing both the rate and extent of oral drug absorption. This is why the dynamic models have exceeded all the previously developed quasi-equilibrium and static models, and they have been incorporated into the regulatory guidelines for the new drug application (NDA) submission.

Dispersion Model:

One of the initial dynamic absorption models was the dispersion model (Huang et al., 2009; Ni, Ho, Fox, Leuenberger, & Higuchi, 1980). This model assumes the GIT as a single tube with spatially varying properties (pH, surface area, etc.) along the length of the intestine. The initial dispersion model did not account for pre-systemic metabolism which contributed to the overestimation of bioavailability (F) for a number of drugs which have significant metabolism before reaching the systemic circulation. Also, this model only considered passive permeability which resulted an overprediction of F for some Pgp substrates. Additional input of enzyme kinetic and transporter kinetics was needed to overcome these issues. However, this model was used as a part of the PK-Sim whole body PBPK model for cimetidine (Willmann et al., 2003).

Compartmental Absorption and Transit (CAT) Model:

This model divides the GIT into several compartments. Passive absorption, instantaneous dissolution, linear transfer kinetics for each segment, and little absorption from the stomach and colon are among the original model's assumptions (Huang et al., 2009; Lawrence & Amidon, 1999). This model was initially created to forecast non-degradable and extremely soluble medication absorption after oral administration. The reliance of the proportion of dosage absorbed on the effective permeability for a variety of medicines with varying absorption properties was nevertheless demonstrated to be captured by this model (Huang et al., 2009; Lawrence & Amidon, 1999; Löbenberg et al., 2013). To forecast plasma concentration-time profiles, the CAT model might potentially be directly connected to pharmacokinetic models.

The CAT model was expanded to predict dose-dependent drug absorption with degradation in the small intestine for cetirizine by integrating Michaelis-Menten kinetics for carrier/transporter-mediated absorption, stomach emptying rate constant, and compartment-dependent degradation rate constant(Huang et al., 2009; Lawrence & Amidon, 1999; Löbenberg et al., 2013). Additionally, a compartment that represents the controlled-release dosage form was added to the CAT model to enable simulation of the dose absorbed in controlled release dosage forms (Huang et al., 2009; Lawrence & Amidon, 1999).

Advanced Compartmental Absorption and Transit (ACAT) Model:

Based on the CAT model, the ACAT model (Agoram, Woltosz, & Bolger, 2001) was created to incorporate first-pass metabolism and intestinal absorption. This model incorporates nine compartments (stomach, seven segments of small intestine, and colon), linear transfer kinetics and nonlinear metabolism/transport kinetics, six drug component states (unreleased, undissolved, dissolved, degraded, and absorbed), and three expelled material states (unreleased, undissolved, and dissolved). Predicting oral medication absorption takes into account physiological aspects (gastric emptying, intestinal transit rate, first-pass metabolism, and luminal transport), physicochemical factors (pKa, solubility, particle size, density, and permeability), and dosage considerations (dosage form and dose) (Agoram et al., 2001; Huang et al., 2009).

Several different drug metabolizing enzymes and transporters are found in the intestinal epithelial cells as discussed earlier. The oral absorption of their substrates may be complicated by the interaction of the metabolizing enzymes and transporters. Utilizing *in vitro* activity data (V_{max} and K_m) of enzymes and transporters, the ACAT model was able to replicate nonlinear saturable Michaelis-Menten kinetics of metabolism and transport in oral drug absorption (Agoram et al., 2001).

Based on the ACAT model, the commercial program GastroPlus^{TM} was created. In comparison to the original ACAT model, this software has experienced a number of advancements in terms of its capacity to forecast the oral absorption of a range of medications. By simulating the *in vivo* absorption profile of pharmaceuticals using *in vitro* dissolution data, the *in vitro-in vivo* correlation has been established utilizing Gastroplus^{TM} (Löbenberg et al., 2013; Löbenberg, Krämer, Shah, Amidon, & Dressman, 2000; Okumu, DiMaso, & Löbenberg, 2008). Gastroplus^{TM} has been utilized to help support biowaivers for certain BCS II drugs by integrating medication physicochemical features and physiological data. GastroPlus^{TM} was also used to estimate the effects of several formulation parameters, including solubility, particle size, and size distribution, on the absorption of oral drugs (Huang et al., 2009; Lawrence & Amidon, 1999). Gastroplus^{TM} also forecasted biorelevant solubility, the strength of food effects, and the oral pharmacokinetics of many medications under fasting and fed settings. Gastroplus^{TM} has been developed for predicting whole-body pharmacokinetic and pharmacodynamic features in humans, in addition to its application for predicting oral drug absorption in the GI tract and combined pharmacokinetic and pharmacodynamic models.

In order to simulate the nonlinear pharmacokinetics (dose-dependent absorption) following administration of a series of doses of talinolol immediate-release tablets, an additional consideration of a heterogeneous expression of P-gp across the intestine was included for drugs that undergo intestinal efflux, such as talinolol (a P-gp substrate) based on the fact that the P-gp expression level increases from duodenum to jejunum (Mouly & Paine, 2003; Tubic, Wagner, Spahn-Langguth, Bolger, & Langguth, 2006).

ADAM Model:

The ADAM model, a compartmental transit model with seven compartments for the small intestine that was recently created based on the CAT model, is comparable to the ACAT model (Dokoumetzidis et al., 2007; Huang et al., 2009). The CAT model and numbers from the literature were used to create the GI physiology, which is considered by the ADAM model. This physiology includes stomach emptying time, small intestinal transit time, and the radius and length of the small intestine.

Continuous Intestinal Absorption Model (CIAM):

Nagar et al. recent developed a continuous intestinal absorption model in which the intestine was assumed to be a continuous cylinder of varying diameter rather than a summation of several separate compartments (Nagar, Korzekwa, & Korzekwa, 2017). Drug concentration change along the length of the intestine (x) and over time (t) was used to model drug absorption from the intestine. Contrary to the ACAT model, there are two independent variables in this model: length of the intestine and time. Hence, partial differential equations (PDEs) were used in place of ODEs. Although, solving PDEs are computationally expensive, recent advances in computation power and speed has made this easier than before.

The continuous intestinal absorption model is based on the basic convection-diffusion equation (Ni et al., 1980; Stoll, Batycky, Leipold, Milstein, & Edwards, 2000):

$$\frac{\partial}{\partial t}C(x,t) = D\frac{\partial^2}{\partial x^2}C(x,t) - \frac{Q}{\prod r^2}.\frac{\partial}{\partial x}C(x,t) - \sum_{i=1}^{n} k_i\,.\,C(x,t) \qquad \text{Equation 1.19}$$

D is the drug's diffusion coefficient, Q is the rate of bulk fluid flow, r is the intestinal lumen radius, and ki is the first-order rate constant for the ith radial transfer process where drug concentration (C) changes as a function of both length of the intestine (x) and time (t).

The first component describes intestinal drug mixing-induced axial diffusion, the second term convection-induced axial bulk movement of the pulse, and the final term radial diffusion. For saturable process like metabolism or transporter involvement k_i will be replaced by a saturable function. This model also includes relevant physiological and physicochemical factors including pKa, LogP, and f_{um} (Nagar et al., 2017; Radice et al., 2022).

1.14 Drugs of Interest:

An absorption model should provide accurate predictions for a variety of compounds including all drugs of BCS. To effectively model intestinal metabolic kinetics, incorporate that kinetics into the absorption model, and finally calculating the fraction escaping gut metabolism was the major goal of this thesis. Additionally, if there is any TDI captured in the intestinal region, this model was expected to include that TDI kinetic parameters into the model. For this purpose, we needed drugs which are significantly metabolized in the intestine.

Midazolam is a BCS class I drug and nicardipine is BCS class II drug (Benet et al., 2011; Dahan et al., 2009; Olivares-Morales et al., 2014; Wu & Benet, 2005). Both of these drugs are metabolized significantly in the intestine as well as in liver. Midazolam is mainly metabolized by single enzyme CYP3A4 with very small contribution from CYP3A5(Klieber et al., 2009; Smith, Eadie, & Brophy, 1981; Wandel et al., 1994). Nicardipine is metabolized by three different CYPs: 3A4, 2D6, and 2C8 (Graham et al., 1985; Nakamura et al., 2005). This served to evaluate the model applicability for single or multi-enzyme involvement in absorption modeling. Nicardipine is also a Pgp substrate (Katoh, Nakajima, Yamazaki, & Yokoi, 2000; Melchior et al., 2012; A. M. Taylor et al., 2001) for which inclusion of Pgp has been conducted in the absorption modeling which served to test model's applicability to include Pgp . Future studies might include the absorption modeling of BCS class III and IV drugs which are also metabolized in the intestine.

Midazolam (MDZ):

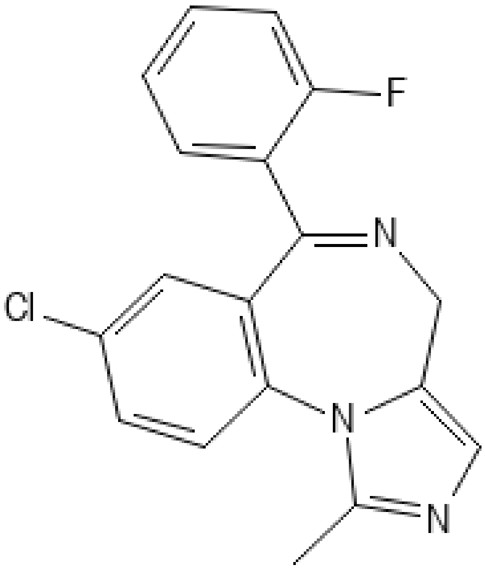

Figure 1.7: Chemical structure of midazolam

MDZ (Figure 1.8) is a member of benzodiazepine drugs. It is a rapid-onset and short-acting sedative-hypnotic drug approved by FDA in 1985. It mediates its anxiolytic activity by potentiating γ-amino butyric acid (GABA) inhibition binding to the GABA-A receptors (Nordt & Clark, 1997). In humans, the oral bioavailability of MDZ is about 40-50% due to extensive first-pass metabolism. Intramuscular MDZ has an availability of 90% (Nordt & Clark, 1997). Its volume of distribution is about 1-3.1 L/kg but it can increase in female, elderly, and obese populations. It is more than 95% protein bound in the plasma, mainly to albumin(Label). Metabolically, it is primarily converted to 1'-OH MDZ (major) and 4-OH MDZ (minor) by CYP3A4 in the gut and liver. They are pharmacologically active and are further metabolized to their respective glucuronides (Nordt & Clark, 1997). The total MDZ clearance is about 0.25-0.54 L/hr/kg. The elimination half-life ranges from 1.8 to 6.4 hours.

In Sprague-Dawley rats, the oral bioavailability was found to be 11%. It was also highly protein bound in rats' plasma (>95%). After an IV MDZ dose of 5mg/kg, the total clearance was 79ml/min/kg. The volume of distribution was 3.1 L/kg. The elimination half-life was 0.49 hours(Kotegawa et al., 2002). However, the major metabolite in rats is 4-OH MDZ primarily produced by Cyp3a1 and Cyp3a2.

Nicardipine (NCD)

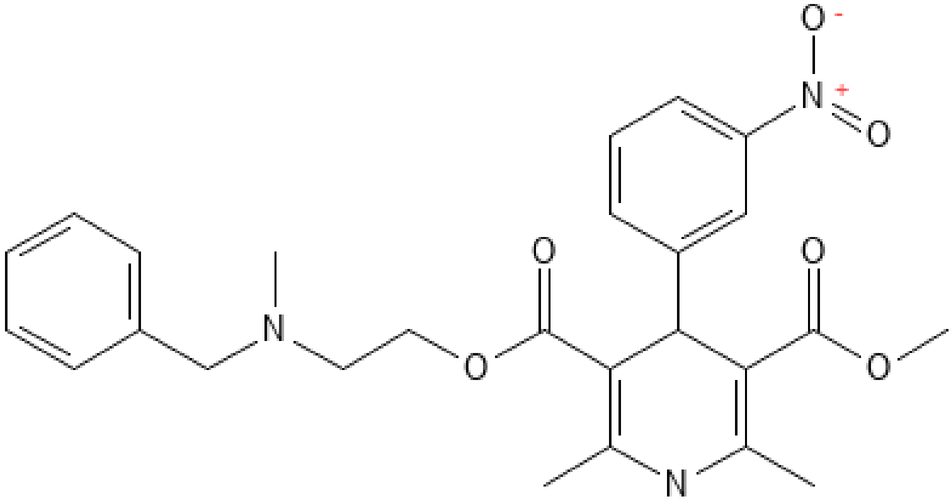

Figure 1.8: Chemical structure of nicardipine

Nicardipine (Figure 1.7) is a potent calcium channel blocker used as an antihypertensive agent. It is a basic compound (Holt, Ye, Nagar, & Korzekwa, 2019). In human, it has an oral bioavailability of 35% after a 30 mg dose. Its volume of distribution, clearance and half-life are 8.3 L/kg, 0.4 L/hr/kg and 8.6 hours respectively (DRUGBANK). It is a highly protein bound drug (DRUGBANK; Graham et al., 1985). It is mainly metabolized by CYP3A4, CYP2C8, and CYP2D6 and its major metabolites are debenzylated nicardipine and dehydronicardipine (J.-S. Choi, Choi, & Kang, 2009; J. S. Choi, Koh, Chung, Choi, & Han, 2008; Graham et al., 1985; Nakamura et al., 2005). Its F_a, F_g and F_h are 1, 0.33 and, .323 to 0.545 respectively (Kato et al., 2003; Takenaka et al., 2017; Yau, Petersson, Dolgos, & Peters, 2017). In SD rats, the total clearance, half-life, and volume of distribution were calculated to be 58.9 mL/min/kg, 7.5 hours, and 38.2 L/kg. The oral bioavailability was 10% (J.-S. Choi et al., 2009).

1.15 Goal of This Thesis

There are different *in vitro* models to predict the fraction escaping gut metabolism (F_g) (Chawla & Bansal, 2003; Fedi et al., 2021; J. H. Lin, Chiba, & Baillie, 1997; Pang, 2003). However, there is no exact consensus or agreement among scientists on how to determine that *in vivo*. There are some methods available using enzyme inhibitors in the intestine, but they are less reliable because there is a chance for hepatic enzyme inhibition too (Paine et al., 1996; Park, Manara, & Dawling, 1989). Another method is using anhepatic phase of liver transplant patients. During liver transplantation, there is a time gap between the removal of diseased liver and the plantation of new liver. Using that time gap, some research group has worked to capture the F_g of midazolam (Paine et al., 1996; Park et al., 1989). However, this method is also very unconventional and depends on the liver-transplant patients. Our main goal is to predict the oral C-t profile of the model drugs (MDZ and NCD) capturing the F_g from the continuous intestinal absorption model. If we can capture the F_g from the model, the F_h can be calculated from the overall F. In addition to that, we had data for regional expression of CYP3A4. We aimed to use that data to include atypical kinetics of MDZ metabolism into the absorption model and predict the C-t profile of MDZ. For NCD, we did not have regional expression of all the enzymes involved (CYP3A4, CYP2D6, and CYP2C8) which is why, NCD oral C-t have been modeled with uniform enzyme distribution assuming NCD is absorbed rapidly through the upper part of the intestine. That upper part of the intestine is assumed have relatively uniform enzyme expression.

Another goal of this thesis was to incorporate the TDI parameters into the model to capture intestinal TDI mediated DDI. Chapter 5 has elaborated all the TDI efforts and discussed all the limitations of intestinal microsomes to capture TDI scenario. Finally, this part of the overall goal has been removed from the absorption modeling. However, since intestinal TDI part was removed from the thesis, simulation of human continuous absorption model incorporating intestinal metabolism was added in this thesis which was not present in the thesis proposal.

1.16 Hypothesis

This thesis evaluated the overall hypothesis that *in vitro* enzyme kinetic parameters of a drug can be incorporated into the continuous intestinal absorption model to predict its oral absorption profile. It was expected the intestinal metabolism of the drug would be captured from the continuous intestinal absorption model. Specifically, the fraction escaping gut metabolism (F_g) was expected to separate from the fraction escaping gut metabolism times fraction escaping hepatic metabolism ($F_g.F_h$) obtained from *in vivo* assays. Finally, it was expected that the incorporation of the *in vitro* enzyme kinetic parameters of the model drugs would be able to characterize both the rate and extent of oral drug absorption.

1.17 Specific Aims

The hypothesis of this thesis proposal was evaluated with the following specific aims. The thesis dissertation document is organized as a specific aim in each chapter.

1. Development and validation of bio-analytical methods for quantitation of study compounds in rat liver microsomes and SD rat plasma
    - *Develop and validate methods for the study compounds (midazolam, 1'-hydroxymidazolam, 4-hydroxymidazolam, nicardipine, dehydronicardipine) using LC-MS/MS.*
2. *In vitro* enzyme kinetics of midazolam and nicardipine using rat intestinal microsomes (RIM) and rat liver microsomes (RLM).
    - *Conduct equilibrium dialysis assay to determine the fraction unbound in microsomes (*f_{um}*) using RLM*
    - *Conduct in vitro enzyme kinetics of midazolam (MDZ) using RIM and RLM*
        - *Run saturation curve assay*
        - *Run substrate depletion assay*
    - *Conduct in vitro enzyme kinetics of nicardipine (NCD) using RIM and RLM*
        - *Run saturation curve assay*
        - *Run substrate depletion assay*

- *Conduct modeling of in vitro enzyme kinetics data*

3. *In vitro* enzyme kinetics of midazolam and nicardipine using human intestinal microsomes (HIM) and human liver microsomes (HLM)
    - *Conduct in vitro enzyme kinetics of midazolam (MDZ) using HIM and HLM*
        - *Run saturation curve assay*
        - *Run substrate depletion assay*
    - *Conduct in vitro enzyme kinetics of nicardipine (NCD) using HIM and HLM*
        - *Run saturation curve assay*
        - *Run substrate depletion assay*
    - *Conduct modeling of in vitro enzyme kinetics data*
4. In-vitro time-dependent inactivation assays using rat intestinal microsome (RIM)/rat liver microsome (RLM) and modeling of TDI data
    - *Run pilot assays to determine time-dependent inactivation (TDI)*
    - *Run full TDI assay to determine* K_I *and* k_{inact}
    - *Conduct modeling of TDI data*
5. Incorporation of intestinal metabolism in the present human and rat continuous intestinal absorption model.

- *Incorporate data collected from specific aims 2 and 3 into the continuous intestinal absorption model to predict the C-t profile of model drugs (MDZ and NCD) in both rat and human*

- *Compare experimentally observed C-t profile of model drugs with the predicted C-t profile and check the goodness of the predictions based on exposure overlap coefficient (EOC).*

CHAPTER TWO: DEVELOPMENT AND VALIDATION OF LC-MS/MS METHOD FOR QUANTIFICATION OF VARIOUS COMPOUNDS

2.1 Rationale

Pharmacokinetic data analysis requires quantifying molecules in various biological matrices, including plasma, urine, microsomal solutions, etc. Using liquid chromatography-tandem mass spectrometry (LC-MS/MS) has provided good sensitivity with less time consumption. However, the LC-MS/MS method used for the analysis of compounds in the biological samples needs to be robust enough to provide accurate bioanalytical results with reliability and reproducibility (Kachingwe, Uang, Huang, Wang, & Lin, 2018; Moein, El Beqqali, & Abdel-Rehim, 2017). Therefore, this chapter aims to develop and validate LC-MS/MS methods for all the compounds mentioned in Table 2.1.

Table 2.1: List of compounds and respective biological matrices for LC-MS/MS method development and validation

Name of the compounds	Biological matrix
1’-hydroxymidazolam and 4-hydroxymidazolam	Rat liver microsome/ Rat intestinal microsome
Nicardipine and dehydro-nicardipine	
Nicardipine	Sprague-Dawley rat plasma

2.2 Materials

Midazolam (MDZ), 1’-hydroxymidazolam (1’-OH MDZ), and 4-hydroxymidazolam (4-OH MDZ) were purchased from Sigma Aldrich (St. Louis, MO). Rat liver microsomes (RLM) and rat intestinal microsomes (RIM) were purchased from Sekisui Xenotech (Kansas City, KS). Nicardipine (NCD) and dehydro-nicardipine (DHD NCD) were bought from Toronto Research Chemical (TRC, ON, Canada). Dimethylsulfoxide (DMSO) and acetonitrile (ACN) were purchased from Fisher Chemical (Fair Lawn, NJ). Formic acid (ACS Reagent) was purchased from Honeywell Fluka (Buches, Switzerland). Sprague Dawley (SD) rat plasma was obtained from Equitech Biotech Inc.

2.3 Assay Development

2.3.1 Preparation of the Stock Solutions, Calibration Standard Samples, and Quality Control (QC) Sample

1’-OH MDZ was available as a 100 µg/mL solution in methanol. It was diluted with 1:1 ACN: water to a concentration of 10 µg/mL. It was further diluted ten times with RLM (0.1 mg/mL)-phosphate buffer solution to 1 µg/mL or 1000 ng/mL. A two-fold serial dilution scheme was applied for the subsequent dilutions to the lowest concentration of 1.95 ng/mL. The stock solutions and QCs (750, 250, 7.81, and 1.95 ng/mL) were freshly prepared on the day of the assays.

Similarly, a 100 µg/mL solution of 4-OH MDZ was accessible in methanol. It was diluted to 10 µg/mL with a 1:1 ACN: water solution. It was then diluted ten times in RIM-phosphate buffer solution (0.1 mg/mL) to 1 µg/mL or 1000 ng/mL. A two-fold serial dilution strategy was used for the successive dilutions to the lowest concentration of 1.95 ng/mL. The stock solutions and QCs (750, 250, 7.81, and 1.95 ng/mL) were freshly produced on the day of the tests.

Based on preliminary experiments, NCD 1 mg/mL solution was made using dimethylsulfoxide (DMSO). Using a hundred-fold dilution with 1:1 ACN: water, it was diluted to 10 µg/mL. For RLM, this solution was further diluted to 1000 ng/mL with RLM (0.1 mg/mL)-phosphate buffer solution. A two-fold serial dilution scheme was applied for the subsequent dilutions to the lowest concentration of 7.81 ng/mL. The stock solutions and QCs (1000, 250, and 7.81 ng/mL) were freshly prepared on the day of the assays. For plasma, 10 µg/mL solution was diluted to 1000 ng/mL with SD rat plasma. A two-fold serial dilution scheme was applied for the subsequent dilutions to the lowest concentration of 7.81 ng/mL. The stock solutions and QCs (1000, 250, and 7.81 ng/mL) were freshly prepared on the day of the assays.

For DHD NCD, 1 mg/mL solution was prepared using DMSO. Using a hundred-fold dilution with 1:1 ACN: water, it was diluted to 10 µg/mL. This solution was further diluted to 500 ng/mL with RIM (0.1 mg/mL)-phosphate buffer solution. A two-fold serial dilution scheme was applied for the subsequent dilutions to the lowest concentration of 15.63 ng/mL. The stock solutions and QCs (500, 125, and 15.63 ng/mL) were freshly prepared on the day of the assays.

Each standard solution (100µL) or QC sample (100µL) was mixed thoroughly with ice-cold internal standard solution (100µL) which contained pure acetonitrile with 0.1% formic acid and phenacetin (PHE) with a concentration of 50 ng/mL for quenching. These mixtures were vortexed and centrifuged at 10000 rpm for 10 minutes. The supernatants were aliquot and 30 µL aliquots were further submitted to the LC-MS/MS for quantitation.

2.3.2 LC-MS/MS

An Agilent 1100 series high-performance liquid chromatography (HPLC) system coupled with ABSciex API 4000 triple quadrupole MS with electrospray ionization (ESI) source was used to analyze compound concentrations in various biological matrices. Positive ionization mode was used for all the compounds analyzed here. MS parameters were obtained by flow injection analysis. LC-MS/MS data were analyzed using Analyst software version 1.6.3.

A Luna 3µm C18(2), 30 x 2 mm HPLC column (Phenomenex) was used for NCD and DHD NCD. On the other hand, a Zorbax Eclipse XDB-C8, 4.6 x 150 mm HPLC column (Agilent), was used for midazolam and its metabolites (1'-OH MDZ and 4-OH MDZ). This more extended column was used to separate two isomeric metabolites of midazolam. The HPLC column was protected by a C18 guard column (4 x 2.0mm). The cartridge of the guard column was replaced when needed (usually every two months). The mobile phases were the same for all the compounds unless needed to change for special situations. The aqueous phase was water with 0.1% formic acid, and the organic phase was pure acetonitrile with 0.1% formic acid. The gradient elution technique was used for all the compounds, and gradients were selected based on the physicochemical properties of the analyte and through trial and error.

The HPLC column was maintained at room temperature during the time of analysis. High purity nitrogen gas was used for collision, curtain, and exhaust gas. Highly purified air was used as the ion source nebulizer gas (GS1) and turbo gas (GS2). The MS parameters for all the compounds were optimized.

2.4 Assay Validation

The calibration curves were prepared using the peak area ratio of the analyte to the IS. The linear least square regression method was used with a weighting factor of $1/X^2$ where X is the analyte concentration. QC samples were used for validation, and the concentration of the QC samples was calculated using y=mx+c. Accuracy and precision were calculated for every compound analyzed in each biological matrix. Intraday and inter-day validation were accomplished according to the latest FDA guidance (FDA, 2018; Kaza, Karaźniewicz-Łada, Kosicka, Siemiątkowska, & Rudzki, 2019; Uvarova, Eremenko, Ramenskaya, Goryachev, & Smirnov, 2019).

Accuracy was calculated using the following formula (FDA, 2018; Kaza et al., 2019; Uvarova et al., 2019),

$$Accuracy = \frac{mean\ observed\ concentration - theoretical\ concentration}{theoretical\ concentration} \times 100$$

Equation-------------------------2.1

Precision was calculated using the following formula (FDA, 2018; Kaza et al., 2019; Uvarova et al., 2019),

$$Precision = \frac{standard\ deviation\ of\ the\ observed\ concentration}{mean\ observed\ concentration} \times 100$$

Equation---------------------------2.2

2.5 Results

MS/MS parameters are summarized in Table 2.2. Entrance potential (EP) was unchanged for the whole operation of LC-MS/MS and was set at 10V for all molecules. Curtain gas (CUR), collision gas (CAD), ion source gas 1 (GS1), ion source gas 2 (GS2), ion-spray voltage (IS), and temperature (TEM) were set at 20 psi, medium psi, 60 psi, 40 psi, 5000.0 V, and 400°C, respectively. The dwell time was 200 msec, and the injection volume was 5-10 µL for all compounds. The concentration ranges for different compounds were selected differently based on the experimental conditions and the sensitivity (LLOQ) of the assays. Table 2.3 shows the HPLC parameters, and tables 2.4 and 2.5 show the validation results.

Table 2.2 MS/MS parameters for compounds evaluated

Compound	Parent ion (Q1)	Product ion (Q3)	DP (V)	CE (V)	CXP (V)
MDZ	326.1	291.1	80	35	12
1’-OH MDZ	342.2	324.1	70	35	15
4-OH MDZ	342.2	234.2	70	35	15
NCD	480.3	314.4	86	33	24
DHD NCD	478.2	312.8	106	35	14
PHE	180.2	110.1	70	35	15

DP→ Declustering potential, CE→ Collision energy, CXP→ Cell exit potential, V→volts

HPLC gradients were determined based on trial and error, and it was selected to ensure efficient separation of the analytes without leaving significant carryover. HPLC gradients are shown in table 2.3 for all the compounds whose LC methods have been generated.

Table 2.3: HPLC gradients for all the compounds

Compound	Time (min)	A%	B%	Flow rate (µl/min)
DHD NCD, NCD	0.0	95	5	400
	0.5	95	5	
	1.8	5	95	
	3.5	5	95	
	3.6	95	5	
	6.5	95	5	
MDZ, 1’-OH MDZ, and 4-OH MDZ	0	70	30	800
	0.5	70	30	
	6	0	100	
	6.5	0	100	
	6.6	70	30	
	9	70	30	

Table 2.4 HPLC parameters for various compounds studied

Compound	Flow Rate (µl/min)	Analyte retention time (min)	IS	IS retention time (min)	Injection volume (µl)	Total run time (min)
DHD NCD	400	2.88	PHE	2.96	5	6.5
NCD	400	2.86	PHE	2.91	5	6.5
MDZ	800	4.33	PHE	4.77	10	9
1’-OH MDZ	800	4.15	PHE	4.77	10	9
4-OH MDZ	800	3.91	PHE	4.77	10	9

The method for 1’-OH MDZ was satisfactory for the quantification over the range of 1.95-1000 ng/mL (Figure 2.1). The retention time of 1’-OH MDZ was 4.15 minutes (Figure 2.2 and Table 2.3). The parent-to-product ion transition used was 342.2→324.1. PHE (50 ng/mL) was used as the IS, for which the retention time was 4.77 minutes and the parent-to-product ion transition was 415.5→178.4 (Figure 2.2 and Table 2.4).

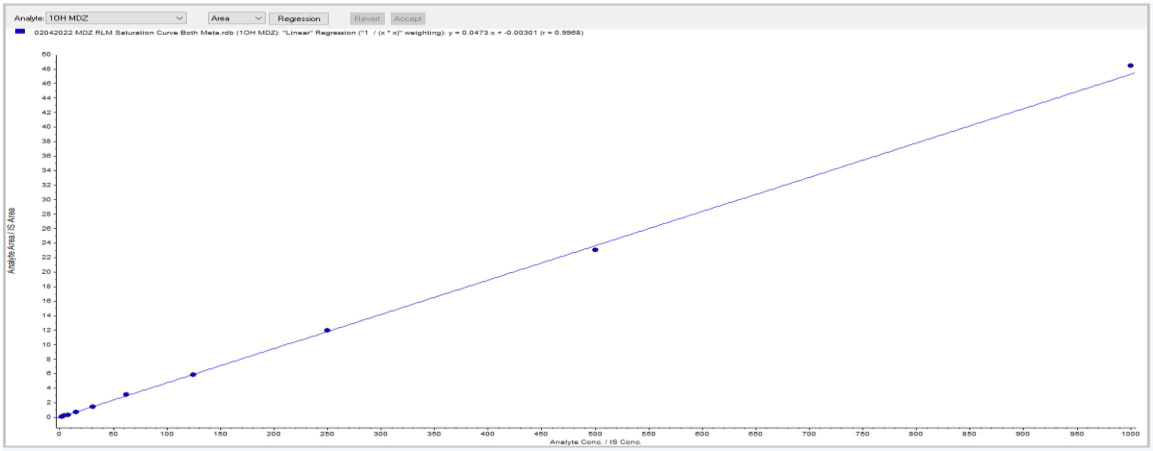
Analyte: 1OH MDZ

Area

02042022 MDZ RLM Saturation Curve Both Meta.rdb (1OH MDZ): "Linear" Regression ("1 / (x * x)" weighting): y = 0.0473 x + -0.00301 (r = 0.9968)

Figure 2.1 Representative calibration curve for 1’-OH MDZ

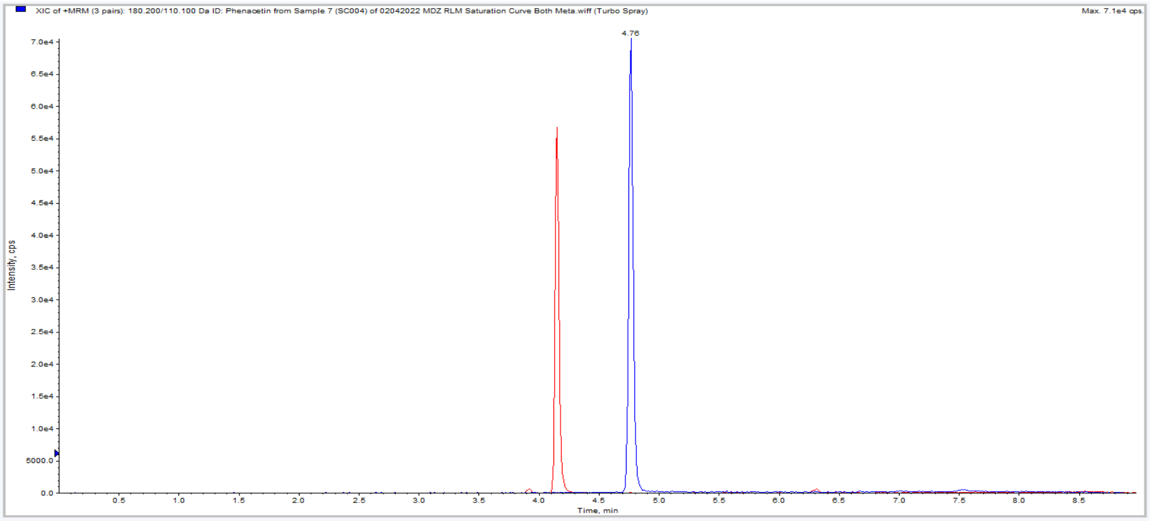
XIC of +MRM (3 pairs): 180.200/110.100 Da ID: Phenacetin from Sample 7 (SC004) of 02042022 MDZ RLM Saturation Curve Both Meta.wiff (Turbo Spray)

Figure 2.2 Representative chromatogram of 1’-OH MDZ (red) with IS phenacetin (blue)

The method for 4-OH MDZ was satisfactory for the quantification over the range of 1.95-1000 ng/mL (Figure 2.3). The retention time of 4-OH MDZ was 3.91 minutes (Figure 2.4 and Table 2.3). The parent-to-product ion transition used was 342.2→234.2. PHE (50 ng/mL) was used as the IS, for which the retention time was 4.77 minutes and the parent-to-product ion transition was 180.2→110. (Figure 2.4 and Table 2.4).

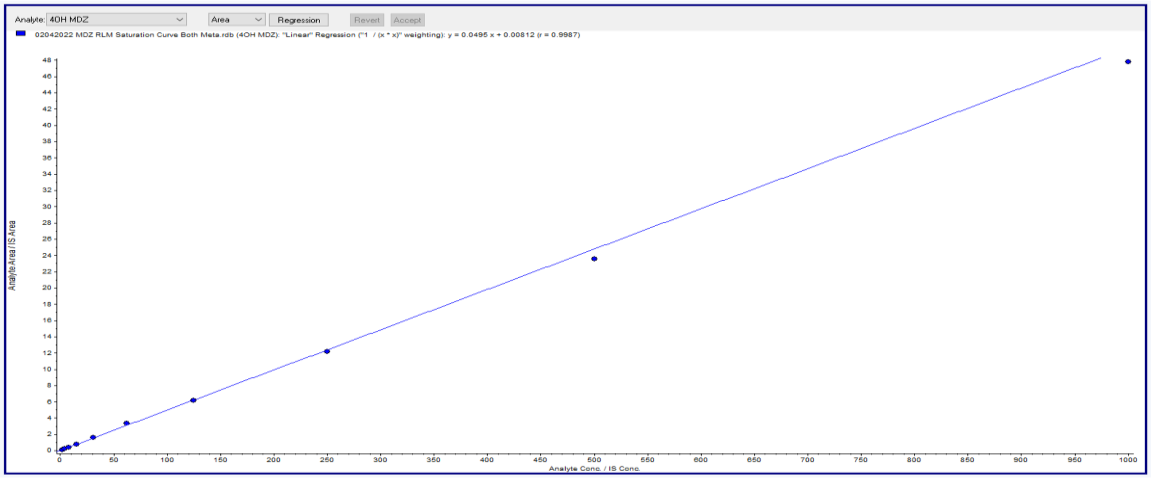

Figure 2.3 Representative calibration curve for 4-OH MDZ

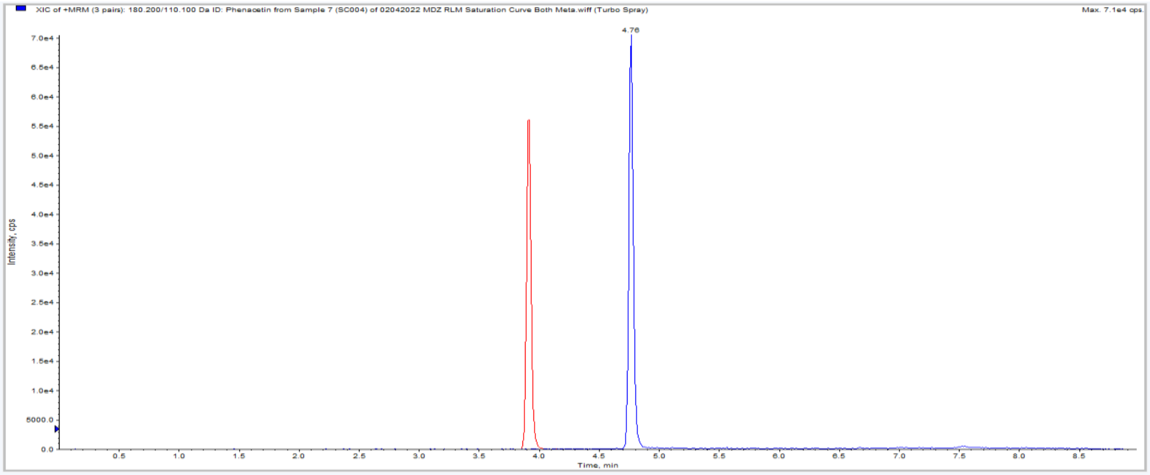

Figure 2.4 Representative chromatogram of 4-OH MDZ (red) with IS phenacetin (blue)

The method for NCD was satisfactory for the quantification over the range of 7.8-2000 ng/mL (Figures 2.5 & 2.6). The retention time of NCD was 2.81 minutes (Figure 2.7 and Table 2.4). The parent-to-product ion transition used was 480.3→314.4. PHE (50 ng/mL) was used as the IS, for which the retention time was 2.96 minutes, and the parent-to-product ion transition was 180.2→110.1 (Figure 2.6 and Table 2.3).

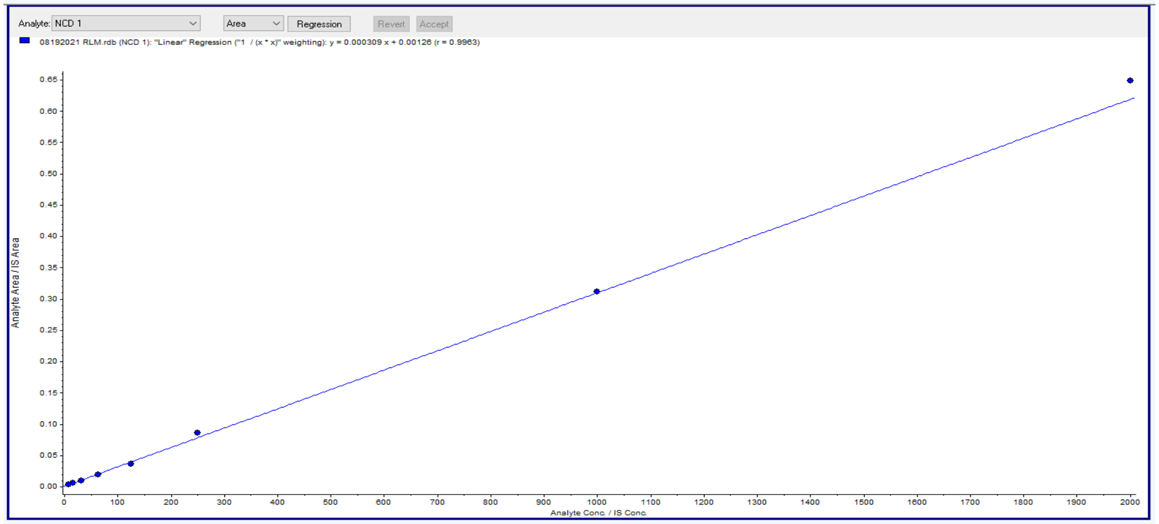

Analyte: NCD 1

Area

08192021 RLM.rdb (NCD 1): "Linear" Regression ("1 / (x * x)" weighting): y = 0.000309 x + 0.00126 (r = 0.9963)

Figure 2.5: Representative calibration curve for NCD in RLM

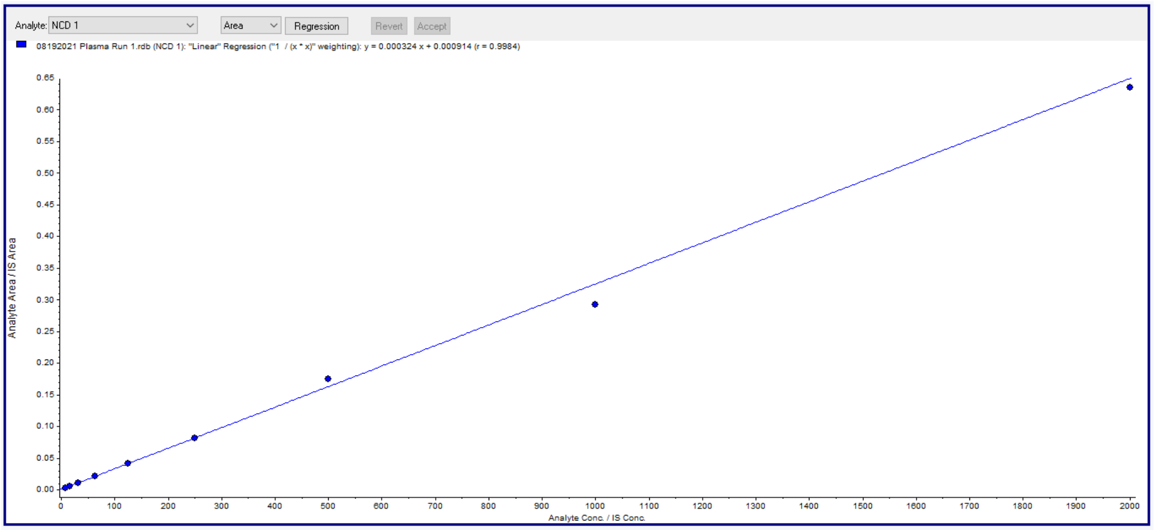

Analyte: NCD 1

Area

08192021 Plasma Run 1.rdb (NCD 1): "Linear" Regression ("1 / (x * x)" weighting): y = 0.000324 x + 0.000914 (r = 0.9984)

Figure 2.6: Representative calibration curve for NCD in SD rat plasma

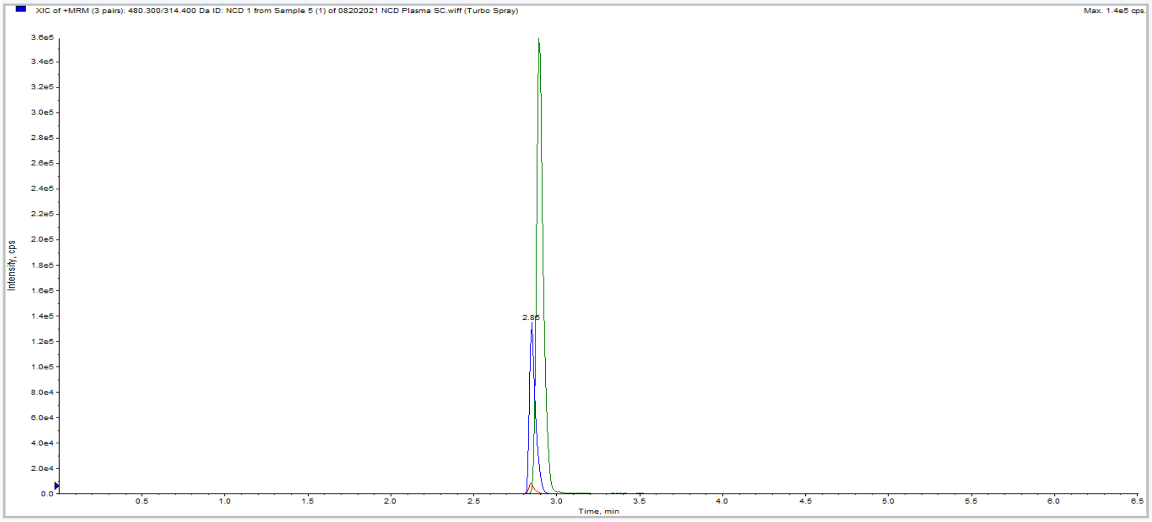

Figure 2.7: Representative chromatogram of NCD (blue) with IS phenacetin (green)

The DHD NCD method was satisfactory for quantifying over the range of 15-500 ng/mL (Figure 2.8). The retention time of DHD NCD was 2.88 minutes (Figure 2.9 and Table 2.3). The parent-to-product ion transition used was 478.2→312.8. PHE (50 ng/mL) was used as the IS, for which the retention time was 2.96 minutes, and the parent-to-product ion transition was 180.2→110.1 (Figure 2.9 and Table 2.3).

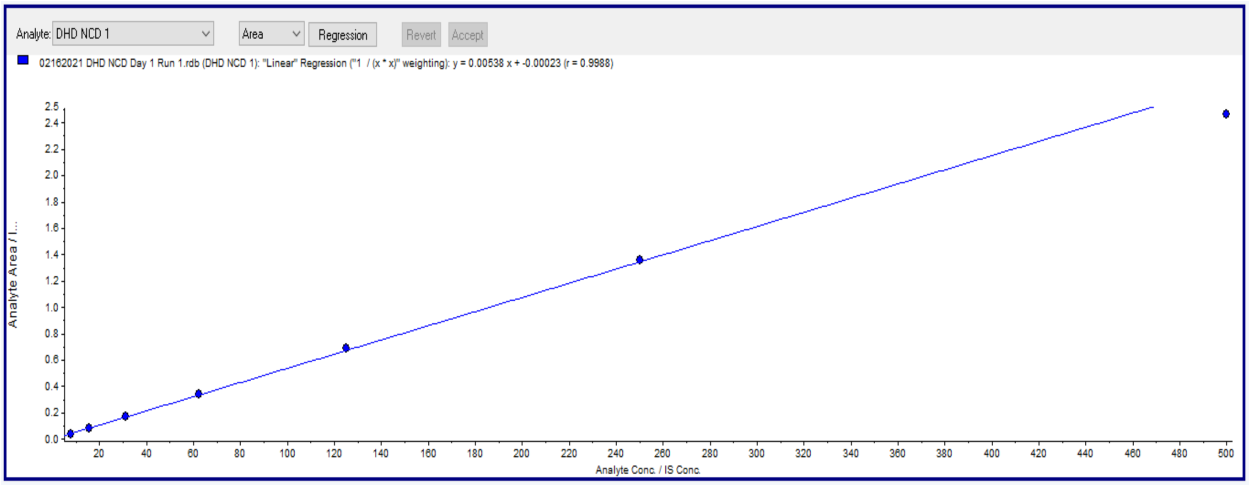
Analyte: DHD NCD 1

Area

02162021 DHD NCD Day 1 Run 1.rdb (DHD NCD 1): "Linear" Regression ("1 / (x * x)" weighting): y = 0.00538 x + -0.00023 (r = 0.9988)
Regression
Revert
Accept
Analyte Area / I...
2.5
2.4
2.2
2.0
1.8
1.6
1.4
1.2
1.0
0.8
0.6
0.4
0.2
0.0
20
40
60
80
100
120
140
160
180
200
220
240
260
280
300
320
340
360
380
400
420
440
460
480
500
Analyte Conc. / IS Conc.

Figure 2.8 Representative calibration curve for DHD NCD

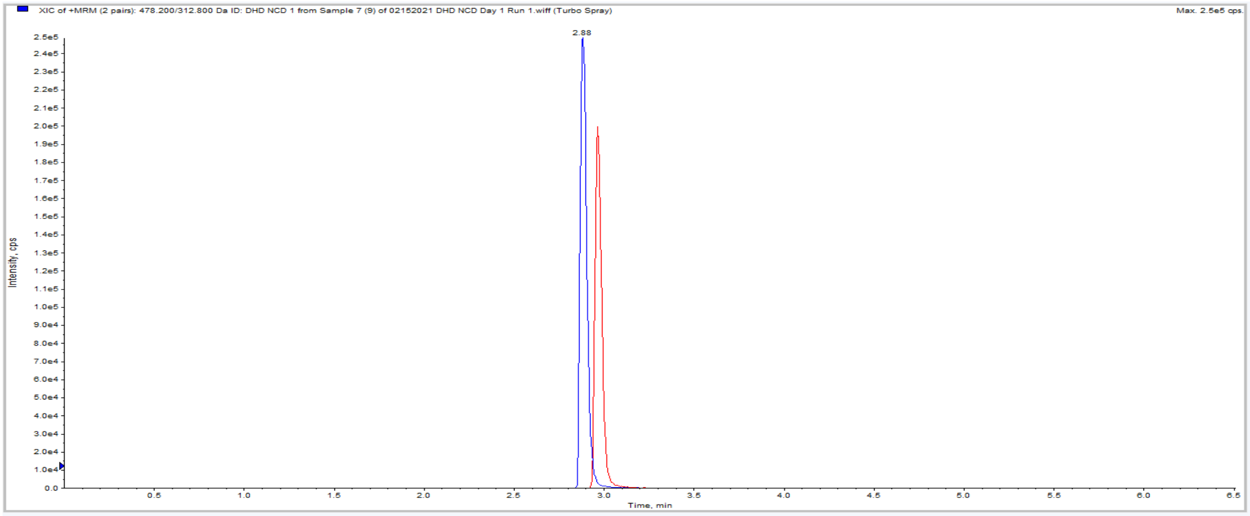

Figure 2.9: Representative chromatogram of DHD NCD (red) with IS phenacetin (blue)

Table 2.5 Validation results of different compounds.

Compound	Matrix	Nominal Conc. (ng/mL)	Intraday validation		Inter-day validation	
			% Accuracy	% Precision	% Accuracy	% Precision
1’-OH MDZ	RLM	750	11.92	4.68	3.92	1.57
		250	8.62	2.19	6.83	2.71
		7.81	-13.45	6.34	-9.43	2.54
		1.95	2.89	1.57	1.10	4.24
4-OH MDZ	RLM	750	12.35	5.65	4.07	2.34
		250	9.01	2.84	8.07	2.92
		7.81	-13.19	5.38	-9.84	2.29
		1.95	3.25	2.50	5.22	5.13

NCD	RLM	1000	-1.77	2.15	-2.42	1.84
		250	1.73	4.08	1.07	4.44
		15.6	-2.88	4.29	-3.53	4.34
		7.8	-7.69	5.95	-8.21	5.53
DHD NCD	RIM	500	12.90	13.27	-0.30	11.97
		125	-4.80	6.40	2.67	0.80
		15.63	5.71	5.28	-4.85	7.63
NCD	SD Plasma	1000	-0.61	4.13	-2.31	3.97
		250	-0.33	4.83	7.07	4.95
		15.6	0.74	8.19	-6.30	6.03
		7.8	-7.32	7.41	-5.66	8.58

2.6 Discussion and Conclusions

Accurate, precise, linear, selective, and sensitive LC-MS/MS methods for determining the concentration of several compounds in biological matrices (RLM/RIM and SD rat plasma) were developed. Four different types of microsomes have been used in this thesis: rat liver microsomes (RLM), rat intestinal microsomes (RIM), human liver microsomes (HLM), and human intestinal microsomes (HIM). Assuming microsomal compositions are similar, only one type of microsome has been used to validate the LC-MS/MS method. However, in each experiment, QC samples were submitted with the calibration curve standards using the matrix of the microsomal experiment to confirm the validity of the validated methods. The validated method ensures the robustness and reproducibility of the *in vitro* enzyme incubation data and *in vitro* TDI data. In terms of sensitivity (LLOQ), several factors have been considered to optimize the S/N ratio, including the selection of the most sensitive MRM of analytes, optimizing compound parameters, optimizing the ion source and gas parameters, optimizing dwell time, choosing optimal mobile phase composition, higher flow rates, higher injection volume. In summary, robust, and reproducible LC-MS/MS methods were established for the subsequent steps of the project.

CHAPTER THREE: *IN VITRO* ENZYME KINETICS OF MIDAZOLAM AND NICARDIPINE USING RAT INTESTINAL MICROSOMES (RIM) AND RAT LIVER MICROSOMES (RLM)

3.1 Rationale

It is crucial to estimate the *in vivo* metabolic clearance as well as transporter-mediated clearance wherever applicable to determine the most appropriate dose and dosing regimen of a drug in any species, including humans (Chiba, Ishii, & Sugiyama, 2009; Hallifax, Foster, & Houston, 2010; Hallifax & Houston, 2012; Kiyomi Ito, Hallifax, Obach, & Houston, 2005). In the drug discovery and development phase, before starting the preclinical experiments, it is also scientifically valid and ethical to determine the dose for the preclinical species in question. Therefore, *in vitro in vivo* extrapolation (IVIVE) has been applied to estimate drug clearance. Different *in vitro* systems have been leveraged, and various modeling techniques have been utilized, including empirical and physiological scaling factors (P. R. Kulkarni, Youssef, & Argikar, 2021).

3.1.1 *In Vitro* Tools for Metabolic Studies:

With the advent of different scientific innovations, multiple *in vitro* options are available to predict *in vivo* metabolic clearance of a drug, including recombinant enzymes, hepatocytes, subcellular fractions, or hepatocyte cocultured systems. Although all of these have their pros and cons, the first three of them are used most widely. Recombinant enzymes are manufactured using baculovirus-transfected insect cell lines (Buters et al., 1994; P. R. Kulkarni et al., 2021). Recombinant enzymes are commercially available for several isoforms of cytochromes P450 (CYPs), UDP-glucuronosyltransferases (UGTs), sulfotransferases (SULT), N-acetyltransferases (NATs), carboxylesterases (CESs), flavin-containing monooxygenases (FMOs), monoamine oxidases (MAOs), and aldehyde oxidases (AOs) (Zöllner et al., 2010). While they can be stored long-termed at -80°C and they can provide helpful information about which particular enzyme is responsible for a drug's metabolism, the major drawback is that the enzyme levels are not usually physiologically relevant (P. R. Kulkarni et al., 2021; Venkatakrishnan, von Moltke, Harmatz, Crespi, & Greenblatt, 2000). Also, if the metabolite produced by one isoform is metabolized by another, this system cannot provide the complete picture. In this case, the hepatocyte is superior to recombinant enzymes as they contain multiple drug-metabolizing systems (e.g., microsomal, and cytosolic enzymes) and drug transporters. Hepatocytes can be fresh or cryopreserved cells in suspended or plated form. Cryopreserved hepatocytes are suitable for longer incubations than microsomes. However hepatocytes also have some limitations, such as drug accumulation, variable expression of enzymes and transporters across different days of plating, donor-to-donor variability, and availability and cost of cells (P. R. Kulkarni et al., 2021; Yadav et al., 2020). Subcellular fractions, including microsomes, cytosol, or S9 fractions, can be obtained from the liver, intestine, kidney, or lung. Subcellular fraction assays require the addition of appropriate cofactors. They do not have a plasma membrane, which is why these assays do not account for transporters' active transport. Microsomes are one of the most widely used subcellular fractions (Yadav et al., 2020). Multiple-step centrifugations of tissue homogenates obtain subcellular fractions. The first centrifugation step at about 9000 g provides S9 fraction. The microsomal fraction needs ultracentrifugation at 100,000 g to separate the cytosolic soluble fraction from the microsomes (Parmentier et al., 2019). The advantages of using microsomes are the ease of use, cost, and availability while providing reasonable IVIVE. They are also stable over almost six months at -80°C (P. R. Kulkarni et al., 2021; Yadav et al., 2020). In this thesis, microsomes have been used as the enzyme source.

3.1.2 Fundamentals of Cytochrome P450 Enzyme Kinetics:

Cytochrome P450s (P450s) are a superfamily of membrane-bound enzymes involved in the metabolism of over 70% of the marketed drugs. P450-mediated clearance and related drug interactions can be a significant issue during drug development (Paragas, Wang, Korzekwa, & Nagar, 2021; Wang, Paragas, Nagar, & Korzekwa, 2021). Spectral binding and X-ray crystallography studies support that the active site P-450s are large and flexible, which can accommodate multiple substrates simultaneously. This multiple substrate binding can result in atypical kinetics, including biphasic kinetics, sigmoidal kinetics, and substrate inhibition (K. R. Korzekwa et al., 1998; Tracy, 2006). These atypical kinetics are different from the conventional single binding Michaelis-Menten kinetics, and possible reasons might be the active site's broad specificity, other binding sites, and protein-protein interaction. From the modeling perspective, however, most of the experimental saturation curves can be adequately modeled by a simple single binding ES model or double binding ESS model (Figure 3.1)(Paragas et al., 2021; Wang et al., 2021).

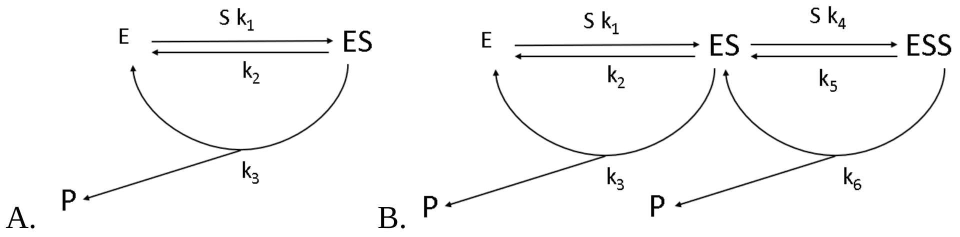

Figure 3.1: (A) A single-substrate binding (ES model) (B) A two-substrate binding (ESS model). (Figure reproduced from (Paragas et al., 2021; Z. Wang et al., 2021))

Figure 3.1 A depicts the traditional single-substrate binding model. One molecule of enzyme (E) binds with one substrate molecule (S) to produce ES intermediate complex. This ES complex can proceed to enzyme-product complex (EP) or reverse to the initial condition. In this scheme, the EP complex is assumed to be short-lived compared with the ES complex. Assuming steady-state, the equation derived from this scheme is known as the Michaelis-Menten equation (Michaelis & Menten, 1913; Paragas et al., 2021; Z. Wang et al., 2021)

$$\frac{v}{E_t} = \frac{\frac{v_{max}}{E_t}.[S]}{K_m+[S]} = \frac{k_{cat}.[S]}{K_m+[S]}$$ Equation -------------------------------3.1

Here, V_{max} is the maximal velocity, k_{cat} is the maximum velocity at unit enzyme concentration (E_t), [S] is the substrate concentration. K_m is the substrate concentration at the half-maximum turnover rate and can be expressed by the following equation (Paragas et al., 2021; Z. Wang et al., 2021):

$$K_m = \frac{k_2+k_3}{k_1}$$ Equation --------------------------------------3.2

The K_m and V_{max} values are used to calculate intrinsic clearance (CL_{int}), which is the capacity of an enzyme or organ to metabolize the substrate without blood flow or protein-binding limitations. Intrinsic clearance is expressed as the ratio of the product formation rate to the substrate concentration (Paragas et al., 2021; Z. Wang et al., 2021):

$$CL_{int} = \frac{v}{[S]} = \frac{v_{max}}{K_m + [S]}$$ Equation --------------------------------3.3

When $[S] \ll K_m$, the equation can be rewritten as (Paragas et al., 2021; Z. Wang et al., 2021):

$$CL_{int} = \frac{v_{max}}{K_m}$$ Equation --------------------------------3.4

Figure 3.1B presents a two-substrate model (ESS model), which can result in non–Michaelis-Menten kinetics. Almost all of the atypical kinetics can be kinetically presented by Fig. 3.1B. This model does not assume specific binding orientation of the substrates. The first substrate is assumed to bind to the enzyme active site with an apparent K_{m1} and turnover rate k_{cat1} and the second substrate is assumed to bind with an affinity K_{m2} and turnover rate k_{cat2}.

If steady-state is assumed, a more complex equation can be derived for ESS mode (Paragas et al., 2021; Z. Wang et al., 2021):

$$\frac{v}{E_t} = \frac{k_{cat1} \cdot [S] + \frac{k_{cat2}}{K_{m2}}[S]^2}{K_{m1} + [S] + \frac{[S]^2}{K_{m2}}}$$ Equation --------------------------------3.5

The K_m values are apparent rather than exact since both processes occur at the same time. Sigmoidal kinetics are observed when K_{m1} is greater than K_{m2} or k_{cat1} is lower than k_{cat2}. Biphasic kinetics are observed when K_{m1} and k_{cat1} are lower than K_{m2} and k_{cat2}, respectively. Substrate inhibition occurs when K_{m1} is smaller than K_{m2} but k_{cat1} is higher than k_{cat2} (Paragas et al., 2021; Z. Wang et al., 2021). The Km and CL_{int} relationships for the ESS model are as follows:

$$K_{m1} = \frac{k_2 + k_3}{k_1}$$

$$K_{m2} = \frac{k_5 + k_6}{k_4}$$

$$CL_{int1} = \frac{v_{max1}}{K_{m1}}$$

$$CL_{int2} = \frac{v_{max2}}{K_{m2}}$$

Equation -------------------------------3.6-3.9

Usually, the metabolite formation data are used to determine the kinetic parameters mentioned above. However, numerical methods are recently being used where ordinary differential equations (ODEs) are created and fitted to the data to extract the micro-rate constants. The significant advantages of using numerical methods are independence from the assumptions of steady-state and unchanged substrate concentration over the incubation period (K. Korzekwa et al., 2014; Nagar et al., 2014; Yadav et al., 2021).

There is another approach to determining metabolic clearance, named substrate depletion, in which the depletion of the substrate at a low concentration is measured over time. This method is advantageous when all the compound metabolites are not available especially during drug discovery. However, this approach provides an overall or apparent metabolic intrinsic clearance. The term 'apparent' is used because exact K_m and V_{max}, and therefore exact CL_{int} for a particular metabolic pathway cannot be determined by this approach (P. R. Kulkarni et al., 2021).

To determine metabolic CL_{int} following equation can be used (P. R. Kulkarni et al., 2021; Naritomi et al., 2001):

$$CL_{int}^{`} = \frac{0.693}{t_{1/2}} \times \frac{1}{microsomal\ conc.(\frac{mg}{mL})} \qquad \text{Equation ---------------------3.10}$$

The $t_{1/2}$ is the *in vitro* half-life of the compound to deplete by 50% from the initial concentration.

Regardless of approaches to determine metabolic intrinsic clearance whether by using metabolites standard or substrate depletion approach, any microsomal intrinsic clearance needs to be corrected with the unbound fraction in microsomes (f_{um}) assuming only unbound drugs are available for metabolism. To determine unbound CL_{int} , following equation can be used (Einolf et al., 2014; Obach & Reed-Hagen, 2002; Scott Obach, 2011):

$$CL_{int,unbound} = \frac{CL_{int}}{f_{um}} \qquad \text{Equation ---------------------------------3.11}$$

3.1.3 Midazolam (MDZ) CYP-Mediated Metabolic Pathway:

In human, MDZ is mainly metabolized into two metabolites - 1’-hydroxymidazolam is the major and 4-hydroxymidazolam is the minor metabolite. Each of them can proceed to 1`,4-dihydroxymidazolam which further proceeds to glucuronidation (Figure 3.2) (Wandel et al., 1994). However, parent MDZ can also be glucuronidated directly by UGT1A4. CYP3A4 has been known to be the major enzyme in CYP-mediated MDZ metabolism. Using heterologous expressed CYPs, it has been determined that CYP3A3 and CYP3A5 are also contributing to the hydroxylation of the MDZ. (Wandel et al., 1994). However, CYP3A4 is much more abundant than any other CYP3A in human liver and intestine (Galetin et al., 2008, 2010; Galetin, Hinton, Burt, Obach, & Houston, 2007).

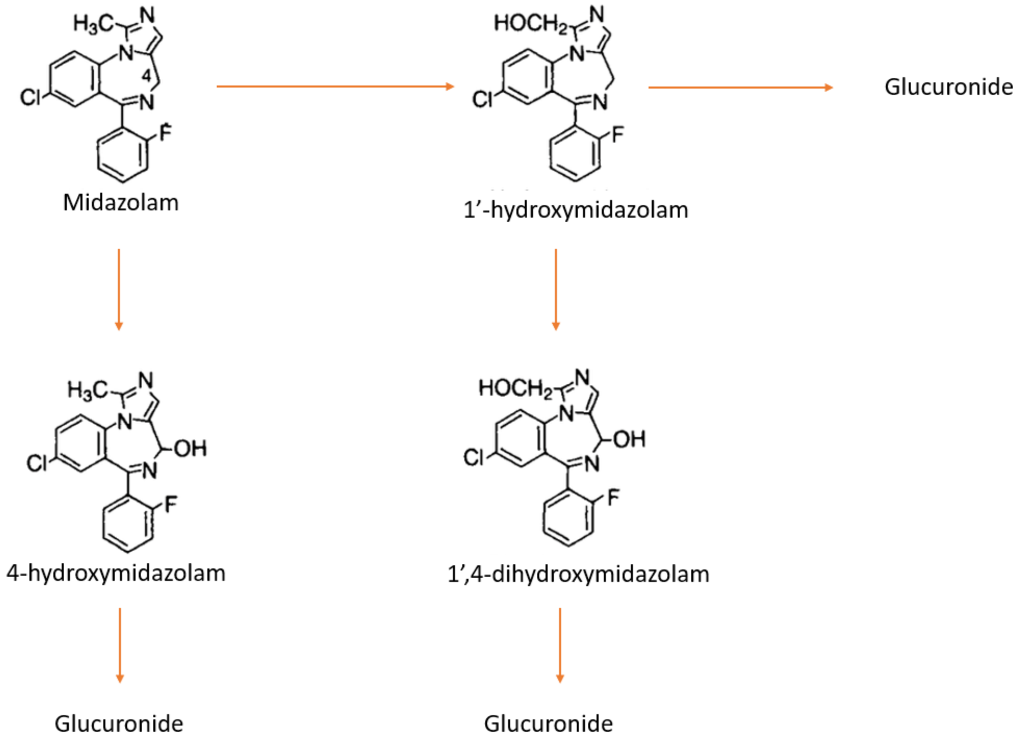
H3C
N
4
Cl
F
Midazolam
HOCH2
1′-hydroxymidazolam
Glucuronide
OH
4-hydroxymidazolam
1′,4-dihydroxymidazolam
Glucuronide
Glucuronide

Figure 3.2: Midazolam metabolic pathway in human (Reproduced from (Christensen, Mathiesen, Postvoll, Winther, & Molden, 2009)

3.1.4 Nicardipine (NCD) CYP-Mediated Metabolic Pathway:

NCD metabolomic studies have been conducted extensively to elucidate the metabolic pathway in human. NCD has been shown to be metabolized extensively pre-systemically: both in the human intestine and liver. Examination of the urine samples in human there was practically no parent NCD present which means that NCD excretes solely as metabolites. In depth investigation revealed a number of metabolites which was fallen into two groups: one where the dihydropyridine ring was intact and one where this was oxidized to pyridine analogues (Graham et al., 1985). The relative quantity of all the metabolites and all of their structures were not determined fully.

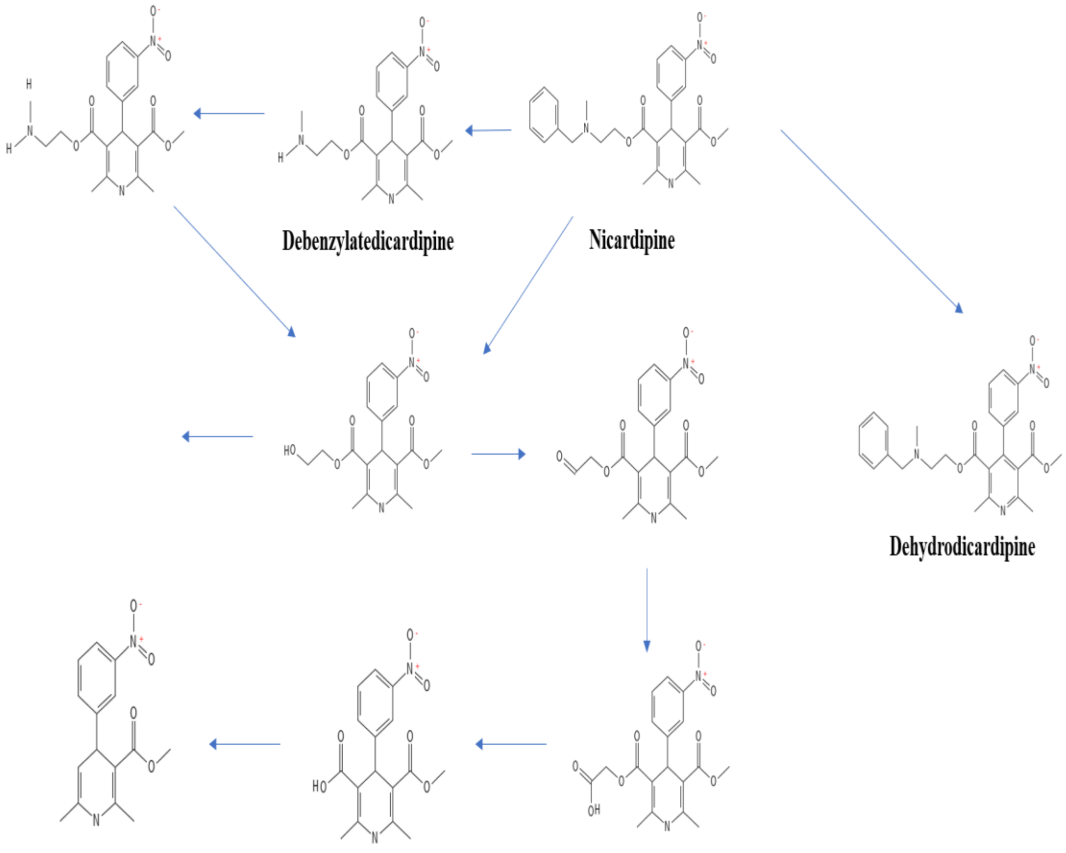

Figure 3.3: Nicardipine metabolic pathway in human (Reproduced from (Graham et al., 1985))

Another study concluded that the NCD is mainly metabolized into two metabolites in human (Labeled in figure 3.3): dehydronicardipine (DHD NCD) and debenzylated nicardipine. It was found that almost all CYPs produce the debenzylated nicardipine whereas the oxidation was catalyzed by only CYP2C8, 2D6, and 3A4 (Nakamura et al., 2005).

This chapter aimed to calculate the metabolic kinetic parameters of MDZ and NCD in SD rats using both RLM and RIM. Metabolic parameters were estimated using the explicit equation (assuming steady state) and the numerical method (using ODEs). In addition, equilibrium dialysis was also performed to determine the unbound fraction in different matrices which will be required for the absorption modeling and DDI prediction in later chapters.

3.2 Materials

Midazolam (MDZ), 1’-hydroxymidazolam (1’-OH MDZ), and 4-hydroxymidazolam (4-OH MDZ) was purchased from Sigma Aldrich (St. Louis, MO). Rat liver microsome (RLM) and rat intestinal microsome (RIM) were purchased from Sekisui Xenotech (Kansas City, KS). NADPH regenerating system (Solution A and Solution B) was purchased from Promega (Madison, WI). Nicardipine (NCD) and dehydro-nicardipine (DHD NCD) were bought from Toronto Research Chemical (TRC, ON, Canada). Dimethylsulfoxide (DMSO) and acetonitrile (ACN) were purchased from Fisher Chemical (Fair Lawn, NJ). Formic acid (ACS Reagent) was purchased from Honeywell Fluka (Buches, Switzerland). Potassium phosphate dibasic anhydrous was purchased from VWR Life Science (Bridgeport, NJ). Potassium phosphate monobasic anhydrous was purchased from Fisher Scientific (Norristown, PA).

3.3 Methods

Buffer preparation:

To prepare 100 mM 1000 mL phosphate buffer pH 7.4, 800 mL deionized (DI) water was taken in a suitable sterile container. Using AAT Bioquest online calculator (Bioquest) the required amount of potassium phosphate dibasic and potassium phosphate monobasic was calculated. In the DI water 12.119 g of potassium phosphate dibasic and 4.14 g potassium phosphate monobasic were dissolved. The final volume was adjusted to 1000 mL by adding DI water. Finally, the pH was adjusted to pH 7.4 by adding HCL or NaOH solution drops.

Drug Stock Preparation:

MDZ and NCD stocks were prepared using methanol. MDZ was available 1 mg/mL solution in methanol. It was dried under liquid nitrogen and reconstituted using methanol to a final concentration of 40 mM. On the other hand, NCD was available as NCD hydrochloride power. It was dissolved in methanol to attain a concentration of 30 mM.

3.3.1 Equilibrium Dialysis Assay to Determine the Fraction Unbound in Microsomes (f_{um}) using RLM and HIM

For the equilibrium dialysis an HTD 96B Teflon-based assembly block was used. The Teflon base minimizes the non-specific binding between the drug and the chamber walls (Cory Kalvass & Maurer, 2002; Plise, Tran, & Salphati, 2010; Riccardi et al., 2015; Vanstraelen et al., 2014; J. Zhang et al., 2010). The membrane is replaceable, and therefore more cost-effective. Furthermore, it is feasible to sample from the donor side and the receiver side simultaneously.

The matrix was RLM with a concentration of 0.25 mg/mL for MDZ and ABT and HIM 0.1 mg/mL for NCD. RLM stock (20 mg/mL) was removed from the -80°C freezer and thawed in ice. The final concentration of 0.25 mg/mL was achieved by adding phosphate buffer to the stock and mixed thoroughly. HIM stock (10 mg/mL) was removed from the -80°C freezer and thawed in ice. The final concentration of 0.1 mg/mL was achieved by adding phosphate buffer to the stock and mixed thoroughly.

The dialysis membranes were hydrated by soaking in distilled H_2O or buffer overnight, followed by adding 20% ethanol (by volume) for a further 1 hour to remove glycerin. Membranes were rinsed twice in distilled water immediately before use. Finally, the membrane was installed between 2 Teflon blocks to complete the dialysis apparatus setup.

After the installation of the membrane, 150 µL of the buffer is added to the receiver side of the dialysis well. Next, the matrix (RLM 0.25 mg/mL), adjusted to pH 7.4, 150 µL and spiked with the test compound (MDZ and NCD final concentration =1 µM with less than 1% v/v organic) was added into the donor site of the dialysis well. An adhesive sealing film was used to prevent evaporation and maintain a constant pH. Samples were dialyzed for at least 8 hours for MDZ and ABT, and 12 hours for NCD in a 37°C incubation chamber with at least 5% CO_2. The rpm was set at 100 in a reciprocating platform shaker.

Sample preparation

For the sample preparation, 90 µL was removed from the receiver side and 10 µL of the matrix was added. For the donor side, 10 µL is removed from the donor side and added to 90 µL buffer. Ice-cold ACN with IS (200 µL) was added to eliminate matrix binding.

This mixture was vortexed and centrifuged at 10000 rpm for 15 minutes at 4 °C. The supernatant was transferred to the LC vials immediately after centrifuging for LC-MS/MS analysis.

Standard curve preparation

Calibration standard samples were prepared with 0.1M potassium phosphate buffer. The serial standard solution in the buffer (20 µL) was mixed with blank matrix (20 µL) and ice-cold ACN (80 µL) with IS was added to eliminate matrix binding. This mixture was vortexed and centrifuged at 10000 rpm for 10 minutes at 4 °C. The supernatant was transferred to the LC vials immediately after centrifuging for LC-MS/MS analysis.

Data analysis:

The unbound fraction in the diluted matrix (RLM 0.25 mg/mL) was calculated using the following equation:

$$f_{um,diluted} = \frac{C_b}{C_m}$$ Equation ------------------------------------3.11

Where $f_{um,diluted}$ is the diluted unbound fraction in microsomes (RLM 0.25 mg/mL), C_b is the concentration in the buffer and C_m is the concentration in the matrix. The undiluted f_{um} was calculated to scale and report at RLM 1 mg/mL using the following equation (Cory Kalvass & Maurer, 2002):

$$f_{um} = \frac{\frac{1}{D}}{\left(\frac{1}{f_{um,diluted}} - 1\right) + \frac{1}{D}}$$ Equation ----------------------------------3.12

D is the dilution factor between the matrix concentration in mg/mL and the standard reporting concentration 1 mg/mL.

3.3.2 *In Vitro* Enzyme Kinetics of Midazolam (MDZ)

Time and protein linearity experiment was performed with protein concentrations ranging from 0.025 mg/ml to 0.2 mg/ml and time points ranging from 0 to 60 minutes using RLM for MDZ metabolism. MDZ concentration was 100 µM. Each incubation was performed in singlet in a shaking water bath at 37.5°C. The incubations were conducted in 100 mM phosphate buffer with a final volume of 500 µL. After a prewarm step of 5 minutes, the reaction was started with the NADPH regenerating system in buffer which achieved a final concentration of 1.3mM NADP+, 3.3mM glucose 6-phosphate (G6P), 3.3mM MgCl2 and 0.4 units/mL glucose 6-phosphate dehydrogenase (G6PDH). The organic solvent (methanol) concentration was below 1% (v/v). At specific time points, 100 µL mixture was aliquot from the incubation and added to the ice-cold quench solution (100 µL) which was ACN containing 0.1% formic acid and internal standard (IS) phenacetin (PHE). After quenching the incubations, the mixture was vortexed and centrifuged to precipitate out the protein. Aliquot was taken to LC-MS/MS for 4-OH MDZ concentration determination.

3.3.2.1 *In Vitro* Metabolic Conversion of Midazolam (MDZ) to 1'-hydroxymidazolam (1'-OH MDZ) and 4-hydroxymidazolam (4-OH MDZ) Using RLM

Time and protein linearity assay provided useful information to decide the protein concentration and the incubation time for the saturation curve assay to determine the kinetic parameters. For MDZ, an RLM concentration of 0.1 mg/ml was used. Incubation time was 10 minutes. The MDZ concentration ranged from 0-400 µM. Each incubation was performed in triplicate in a shaking water bath at 37°C. The organic solvent methanol concentration was kept below 1%. After 5 minutes of prewarm step, reactions were initiated as previously described by the addition of NADPH solution. Incubations were terminated using pure ACN containing the IS. After quenching, the reaction mixture was vortexed and centrifuged. Supernatants were analyzed by LC-MS/MS. Both 1’-OH and 4-OH MDZ were quantified.

3.3.2.2 *In Vitro* Metabolic Conversion of Midazolam (MDZ) to 1’-hydroxymidazolam (1’-OH MDZ) and 4-hydroxymidazolam (4-OH MDZ) Using RIM

For MDZ, an RIM concentration of 0.5 mg/ml were used based on preliminary studies and literature data (Kotegawa et al., 2002). Incubation time was 15 minutes for the RIM assay. The MDZ concentration ranged from 0-400 µM. Each incubation was performed in triplicate in a shaking water bath at 37°C. The organic solvent methanol concentration was kept below 1%. Following the prewarm step for 5 minutes, reactions were started as previously described by the addition of NADPH solution. Incubations were terminated using pure ACN containing the IS. After quenching, the reaction mixture was vortexed and centrifuged. Supernatants were analyzed by LC-MS/MS. Both 1’-OH and 4-OH MDZ were quantified.

Data Analysis:

For the data analysis, diagnostic Eadie-Hofstee plots were created and both the Michaelis-Menten model (ES model) and multiple binding site model (ESS model) were fitted to the data. Kinetic parameters were generated using the numerical method.

Modelling:

Mathematica 12.2.2 student version (Wolfram Research, Champaign, IL) was used for model fitting and plot generation. The ODEs were numerically solved with NDSolve to provide interpolated functions of each enzyme species. NonlinearModelFit function was used to parameterize the rate constants with 1/Y weighting. Specific properties, including MaxSteps → 100,000 and PrecisionGoal → infinity for NDSolve, were used. The corrected Akaike information criteria (AICc) was used to differentiate among models when comparing several models for the same dataset (Sakamoto, Ishiguro, & Kitagawa, 1986; Yamaoka, Nakagawa, & Uno, 1978). Based on saturation curves, the ability for a model to simultaneously model multiple metabolites, and product ratio curves, additional models were constructed and explored (Paragas et al., 2021; Z. Wang et al., 2021). Based on the best-fit model, kinetic parameters were reported. The model-fitted lines were also plotted with the observed data. Finally, intrinsic clearance (CL_{int}) plots were created by plotting product formation rate normalized to substrate concentration over the range of substrate concentration to determine if there is any concentration dependence.

3.3.3 *In Vitro* Enzyme Kinetics of Nicardipine (NCD)

Time and protein linearity experiment was performed with protein concentrations ranging from 0.25 mg/ml to 1 mg/ml and time points ranging from 0 to 60 minutes using RLM for NCD metabolism. NCD concentration was 300 µM. Each incubation was performed in singlet in a shaking water bath at 37.5°C. The incubations were conducted in 100 mM phosphate buffer with a final volume of 500 µL. After a prewarm step of 5 minutes, the reaction was started with the NADPH regenerating system in buffer which contained 1.3mM NADP+, 3.3mM glucose 6-phosphate (G6P), 3.3mM MgCl2 and 0.4 units/mL glucose 6-phosphate dehydrogenase (G6PDH). The organic solvent (methanol) concentration was below 1% (v/v). At specific time points, 100 µL mixture was aliquot from the incubation and added to the ice-cold quench solution (100 µL) which was ACN containing 0.1% formic acid and internal standard (IS) phenacetin (PHE). After quenching the incubations, the mixture was vortexed and centrifuged to precipitate out the protein. Aliquot was taken to LC-MS/MS for DHD NCD concentration determination.

3.3.3.1 *In Vitro* Metabolism of Nicardipine (NCD) Using RLM

3.3.3.1.1 Substrate Depletion Assay to Determine Apparent Intrinsic Clearance

For substrate depletion assay, an RLM concentration of 0.10 mg/ml was selected based on a previously published paper (Naritomi et al., 2001). NCD concentration was 1 µM. Each incubation was performed in triplicate in a shaking water bath at 37°C. The organic solvent methanol concentration was kept below 1%. After 5 minutes of prewarming, reactions were initiated as previously described by the addition of NADPH solution. The reaction volume was 500µL in total. At each time point, 100 µL was aliquot and the reaction was terminated using pure ACN containing the IS up to 5 minutes. After quenching, the reaction mixture was vortexed and centrifuged. Supernatants were analyzed by LC-MS/MS and NCD was quantified.

To determine apparent metabolic CL_{int} equation 3.10 was used (P. R. Kulkarni et al., 2021; Naritomi et al., 2001).

3.3.3.1.2 Saturation Curve Assay for the Conversion of Nicardipine (NCD) to Dehydronicardipine (DHD NCD)

Time and protein linearity assay provided useful information to decide the protein concentration and the incubation time for the saturation curve assay to determine the kinetic parameters. For NCD metabolism, an RLM concentration of 0.10 mg/ml and incubation time of 10 minutes were selected. NCD concentration ranged from 0-50 µM. Each incubation was performed in triplicate in a shaking water bath at 37°C. The organic solvent methanol concentration was kept below 1%. After 5 minutes of prewarm, reactions were initiated as previously described by the addition of NADPH solution. Incubations were terminated using pure ACN containing the IS. After quenching, the reaction mixture was vortexed and centrifuged. Supernatants were analyzed by LC-MS/MS and DHD NCD was quantified.

3.3.3.2 *In Vitro* Metabolism of Nicardipine (NCD) Using RIM

3.3.3.2.1 Substrate Depletion Assay to Determine Apparent Intrinsic Clearance

For substrate depletion assay, an RIM concentration of 1 mg/ml was selected. NCD concentration was 1 µM. Each incubation was performed in triplicate in a shaking water bath at 37°C. The organic solvent methanol concentration was kept below 1%. After 5 minutes of prewarming, reactions were initiated as previously described by the addition of NADPH solution. The reaction volume was 500 µL in total. At each time po$_{\text{int}}$, 100 µL was aliquot and the reaction was terminated using pure ACN containing the IS up to 50 minutes. After quenching, the reaction mixture was vortexed and centrifuged. Supernatants were analyzed by LC-MS/MS and NCD was quantified.

To determine apparent metabolic CL$_{\text{int}}$ equation 3.10 was used (P. R. Kulkarni et al., 2021; Naritomi et al., 2001).

3.3.3.2.2 Saturation Curve Assay for the Conversion of Nicardipine (NCD) to Dehydronicardipine (DHD NCD)

For NCD metabolism, an RIM concentration of 0.25mg/ml and incubation time of 20 minutes were selected. NCD concentration ranged from 0-300 µM. Each incubation was performed in triplicate in a shaking water bath at 37.5°C. The organic solvent (methanol) concentration was kept below 1%. Reactions were initiated as previously described by the addition of NADPH solution. Incubations were terminated using pure ACN containing the IS. After quenching, the reaction mixture was vortexed and centrifuged. Supernatants were analyzed by LC-MS/MS and DHD NCD was quantified.

Data Analysis:

For the data analysis, diagnostic Eadie-Hofstee plots were created and both the Michaelis-Menten model (ES model) and multiple binding site model (ESS model) were fitted to the data. Kinetic parameters were generated using the numerical method.

Modelling:

Mathematica 12.2.2 student version (Wolfram Research, Champaign, IL) was used for model fitting and plot generation. The ODEs were numerically solved with NDSolve to provide interpolated functions of each enzyme species. NonlinearModelFit function was used to parameterize the rate constants with 1/Y weighting. Specific properties, including MaxSteps → 100,000 and PrecisionGoal → infinity for NDSolve, were used. The corrected Akaike information criteria (AICc) was used to differentiate among models when comparing several models for the same dataset (Sakamoto et al., 1986; Yamaoka et al., 1978). Based on the best-fit model, kinetic parameters were reported. The model-fitted lines were also plotted with the observed data. Finally, intrinsic clearance plots were created by plotting product formation rate normalized to substrate concentration over the range of substrate concentration using equation 3.3 and 3.8.

3.4 Results

3.4.1 Equilibrium Dialysis Assay to Determine the Fraction Unbound in Microsomes (f_{um}) using RLM and HIM

Table 3.1 shows the results of equilibrium dialysis for different compounds to determine f_{um}:

Table 3.1: Unbound fraction in microsomes (f_{um}) of different compounds (scaled to 1 mg/mL). Data presented as parameter estimate ± S.E.

Compound	**Fraction unbound in microsome (Mean ± SD) n=3**
MDZ	0.68±0.080
NCD	0.12±0.023
ABT	1.00±0.11

3.4.2 *In Vitro* Enzyme Kinetics of Midazolam (MDZ)

From the time and protein linearity assay, it was found that the incubations were linear up to 30 minutes for all protein concentrations except for 0.2 mg/ml (Figure 3.4 left). On the other hand, the incubations were linear with respect to protein for all incubation time ranges (Figure 3.4 right). Based on this, 0.1 mg/ml RLM with an incubation time of 5 minutes was selected for saturation curve analysis.

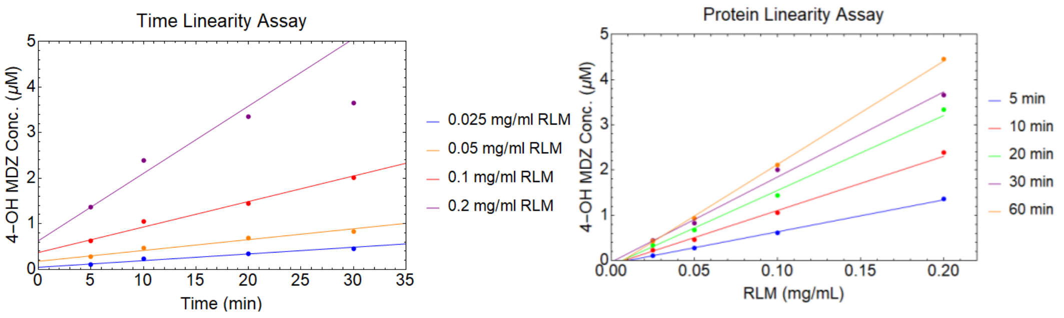

Figure 3.4: Time and protein linearity assay of MDZ with RLM (n=1).

3.4.2.1 *In Vitro* Metabolic Conversion of Midazolam (MDZ) to 1’-hydroxymidazolam (1’-OH MDZ) and 4-hydroxymidazolam (4-OH MDZ) Using RLM

For the saturation curve with RLM, the MDZ concentration range was 0-200 µM (Figure 3.5). Preliminary studies showed that both 1`-OH and 4-OH MDZ were produced comparably in RLM incubation. Therefore, both the metabolites were quantified, and different models were fitted to the data. Figure 3.5 shows the raw plot of the MDZ saturation curve with RLM for individual metabolites.

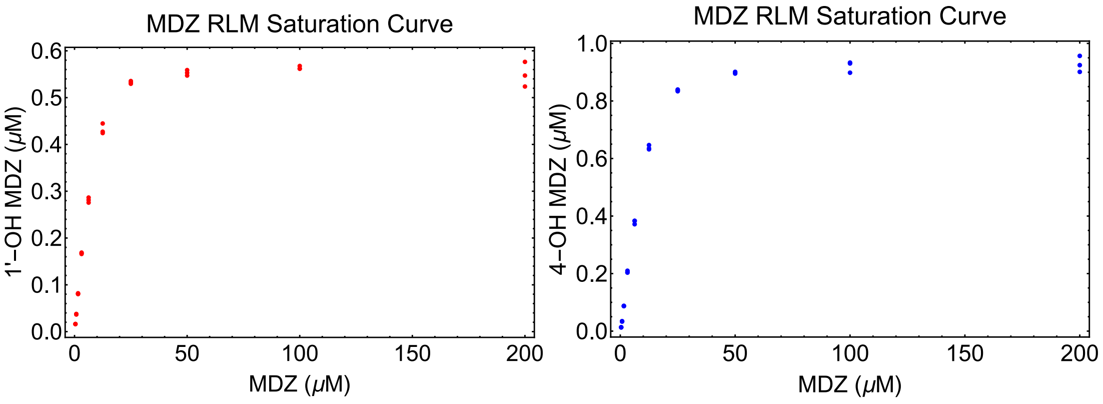

Figure 3.5. MDZ saturation curve for the incubation with RLM (Red:1’-OH MDZ & Blue: 4-OH MDZ). Plots represent mean data (n=3).

Diagnostic Eadie-Hofstee plots and the metabolite formation ratio plot were generated (Figure 3.6), which indicated possible existence of multiple binding kinetics.

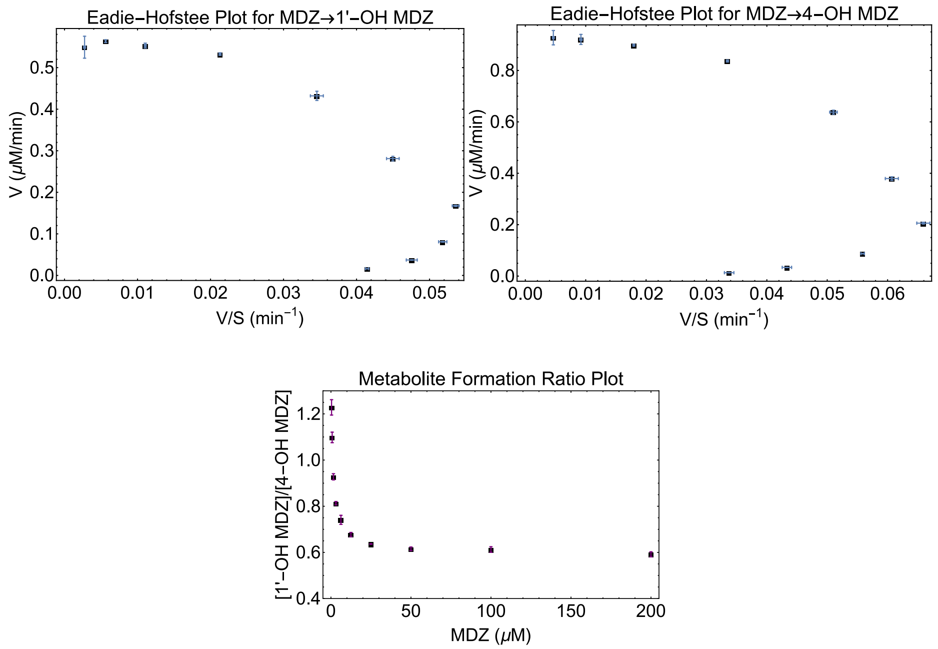

Figure 3.6. Diagnostic plots for the MDZ incubation with RLM (Left: EH plot for MDZ→1'-OH MDZ, middle: EH plot for MDZ→4-OH MDZ, and right: Metabolite formation ratio plot). Plots represents mean data ± standard errors (n=3).

Both the single binding ESP1P2 model and double binding ESSP1P2 model were fitted to the data to choose the best model which explains the observed data (Figure 3.7).

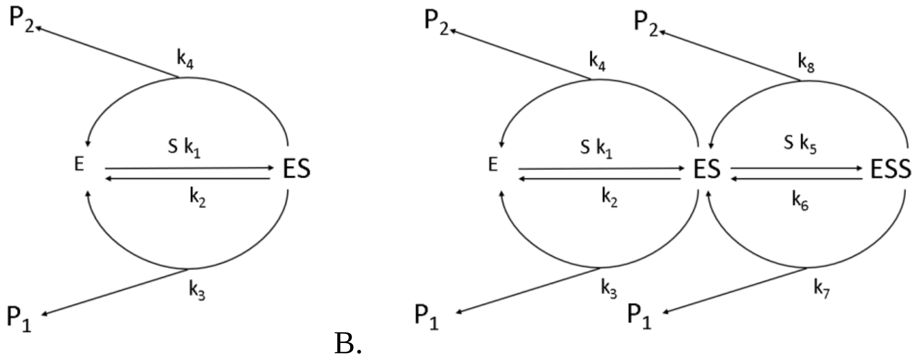

A. B.

Figure 3.7. Schemes for multiple product formation. (A) A one-substrate binding, two-metabolite formation (ESP1P2) scheme. (B) A two-substrate binding, two-metabolite formation (ESSP1P2) scheme (Reproduced from (Paragas et al., 2021; Z. Wang et al., 2021))

Figure 3.7 A depicts the traditional single-substrate binding model but heading to two different metabolites. One molecule of enzyme (E) binds with one substrate molecule (S) to produce ES intermediate complex. This ES complex can proceed to enzyme-product complex (EP1 or EP2) or reverse to the initial condition. In this scheme, the EP complex is assumed to be short-lived compared with the ES complex. Assuming steady-state, the equation derived from this scheme is known as the Michaelis-Menten equation (Michaelis & Menten, 1913; Paragas et al., 2021; Z. Wang et al., 2021)

Figure 3.7B presents a two-substrate model (ESSP1P2 model) heading to two different metabolite formation, which can result in non–Michaelis-Menten kinetics. This model does not assume specific binding orientation.

For the model comparison, different statistical functions were used which are summarized in Table 3.2. Notably, from the AICc values, it was found that the ESSP1P2 model was the better fit to explain the dataset obtained from the saturation curve assay. More specifically, from the K_{m1} and K_{m2} values it was concluded that this metabolic conversion followed sigmoidal atypical kinetics (Paragas et al., 2021; Z. Wang et al., 2021). The curve fitting with the observed data is shown in figure 3.8.

Table 3.2. Statistical functions for model comparison

	ESP1P2 model	ESSP1P2 model
AdjustedRSquared	0.98	0.99
AICc	-197.38	-370.17
MSE (1’-OH MDZ)	0.0024	0.00013
MSE (4-OH MDZ)	0.0033	0.00021

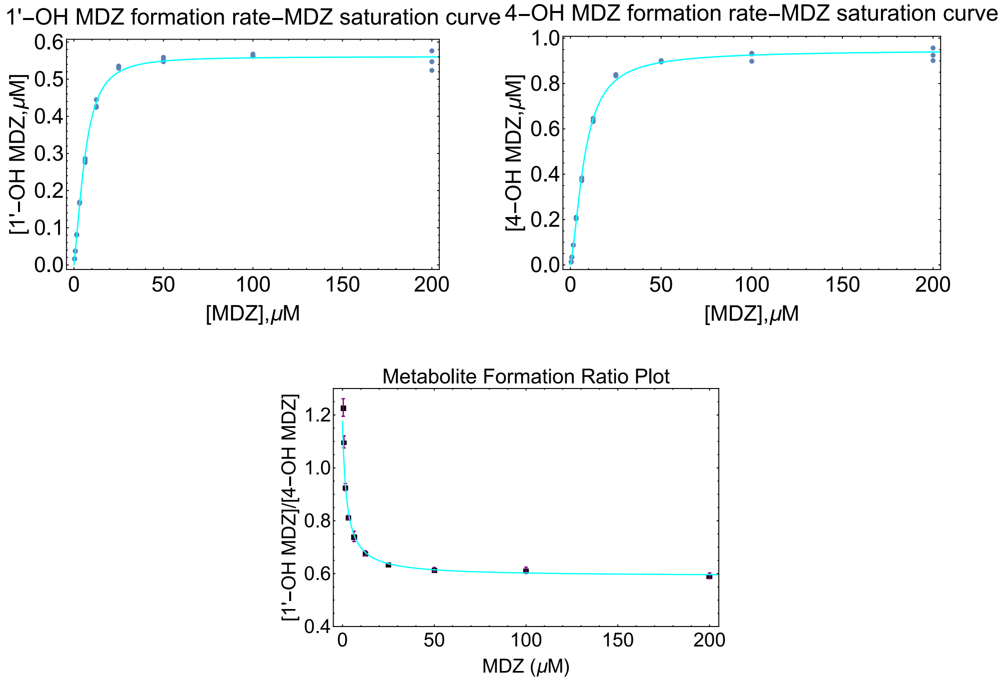

Figure 3.8. ESSP1P2 model fitting with the observed data for the MDZ incubation with RLM (Left: Saturation curve for MDZ→1’-OH MDZ (Plots represents mean data (n=3).), middle: Saturation curve for MDZ→4-OH MDZ (Plots represents mean data (n=3).), and right: Metabolite formation ratio plot (Plots represents mean data ± standard errors (n=3).))

The kinetic parameters obtained from the model fittings are summarized in table 3.3. These parameters will be used in later chapters for absorption modeling. The CL_{int} for the formation of two metabolites over the physiologically relevant concentration are shown in figure 3.9 which shows a moderate concentration dependence. This might necessitate the use of an ODE rather than a single CL_{int} value for IVIVC.

Table 3.3. Comparison of estimates of kinetic parameters from ESP1P2 model and ESSP1P2 model. Data presented as parameter estimate ± S.E.

	ESP1P2 model		ESSP1P2 model	
	1'-OH MDZ	4-OH MDZ	1'-OH MDZ	4-OH MDZ
k_1 ($\mu M^{-1}.min^{-1}$)	270 (fixed)		270 (fixed)	
k_2 (min^{-1})	2954.29±221.17		3248.31±451.64	
K_{m1} (μM)	11.01±0.78		12.08±1.72	
k_{cat1} (min^{-1})	5.44±0.20	8.32±0.27	4.38±0.64	3.73±0.69
$CL_{int1,unbound}$ ($ml.min^{-1}.mg^{-1}$ of RLM protein)	0.13±0.011	0.20±0.016	0.095±0.019	0.081±0.019
k_5 ($\mu M^{-1}.min^{-1}$)	Not applicable		270 (fixed)	
k_6 (min^{-1})			1179.26±86.52	
K_{m2} (μM)			4.41±0.32	
k_{cat2} (min^{-1})			4.49±0.06	7.61±0.07
$CL_{int2,unbound}$ ($ml.min^{-1}.mg^{-1}$ of RLM protein)			0.27±0.020	0.45±0.034

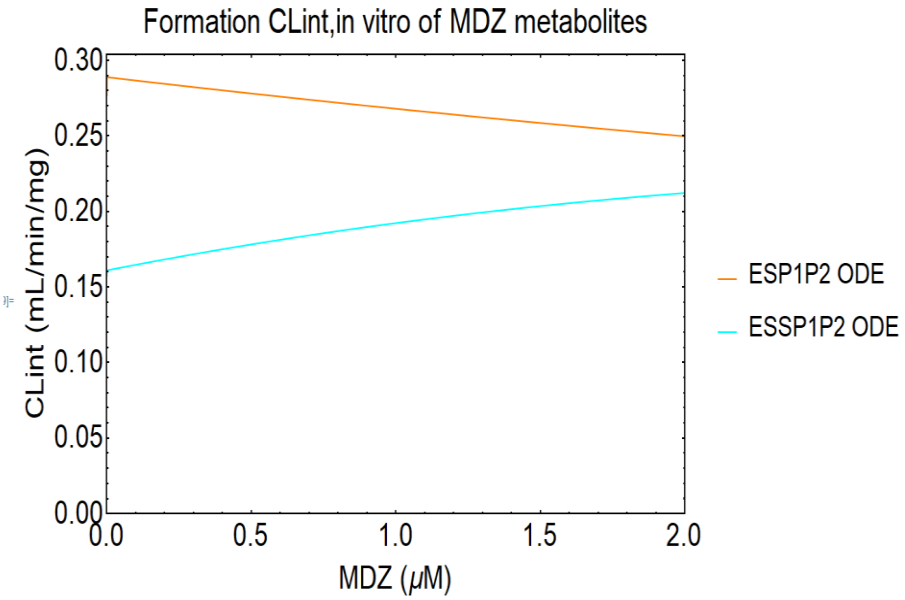

Figure 3.9: Intrinsic clearance plot over a range of physiologically relevant MDZ concentration for both metabolite formation

3.4.2.2 *In Vitro* metabolic Conversion of Midazolam (MDZ) to 1’-hydroxymidazolam (1’-OH MDZ) and 4-hydroxymidazolam (4-OH MDZ) Using RIM

For the saturation curve with RIM, the MDZ concentration range was 0-400 µM (Figure 3.10). Preliminary studies showed that both 1`-OH and 4-OH MDZ were produced comparably in RIM incubation. Therefore, both the metabolites were quantified, and different models were fitted to the data. Figure 3.10 shows the mean raw plot of the MDZ saturation curve with RLM for individual metabolites.

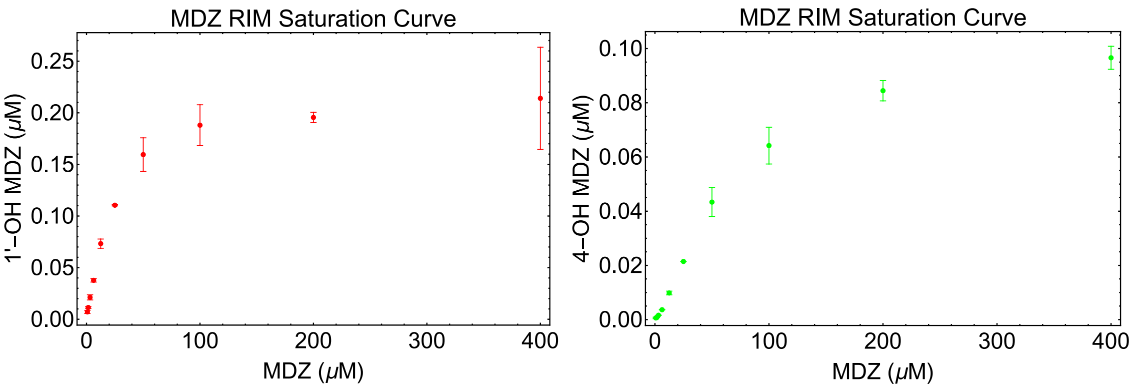

Figure 3.10. MDZ saturation curve for the incubation with RIM (Red:1'-OH MDZ & Green: 4-OH MDZ). Plots represents mean data ± standard errors (n=3).

Diagnostic Eadie-Hofstee plots and the metabolite formation ratio plot were generated (Figure 3.11), which indicated possible existence of multiple binding kinetics.

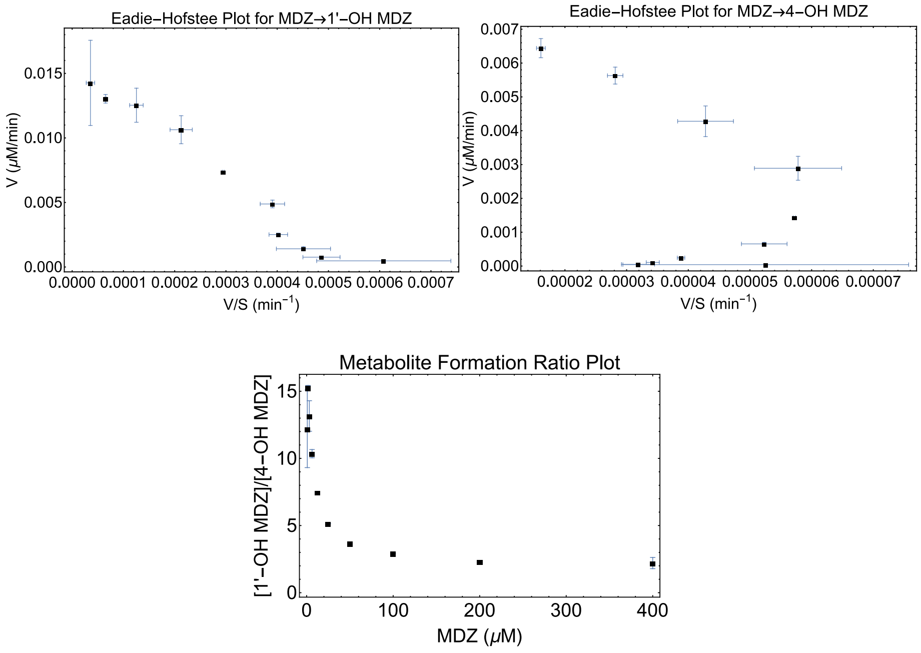

Figure 3.11. Diagnostic plots for the MDZ incubation with RIM (Left: EH plot for MDZ→1'-OH MDZ, middle: EH plot for MDZ→4-OH MDZ, and right: Metabolite formation ratio plot). Plots represents mean data ± standard errors (n=3).

Both the single binding ESP1P2 model and double binding ESSP1P2 model were fitted to the data to choose the best model which explains the observed data (Figure 3.7).

For the model comparison, different statistical matrices were used which are summarized in Table 3.4. Notably, from the AICc values, it was found that the ESSP1P2 model was the better fit to explain the dataset obtained from the saturation curve assay. The 1’-OH MDZ formation showed hyperbolic kinetics but the 4-OH MDZ formation showed a slight sigmoidicity. The curve fitting with the observed data is shown in figure 3.12.

Table 3.4. Statistical matrices for model comparison

	ESP1P2 model	ESSP1P2 model
AdjustedRSquared	0.94	0.99
AICc	-251.39	-320.15
MSE (1’-OH MDZ)	0.00038	0.00017
MSE (4-OH MDZ)	0.00016	0.0000057

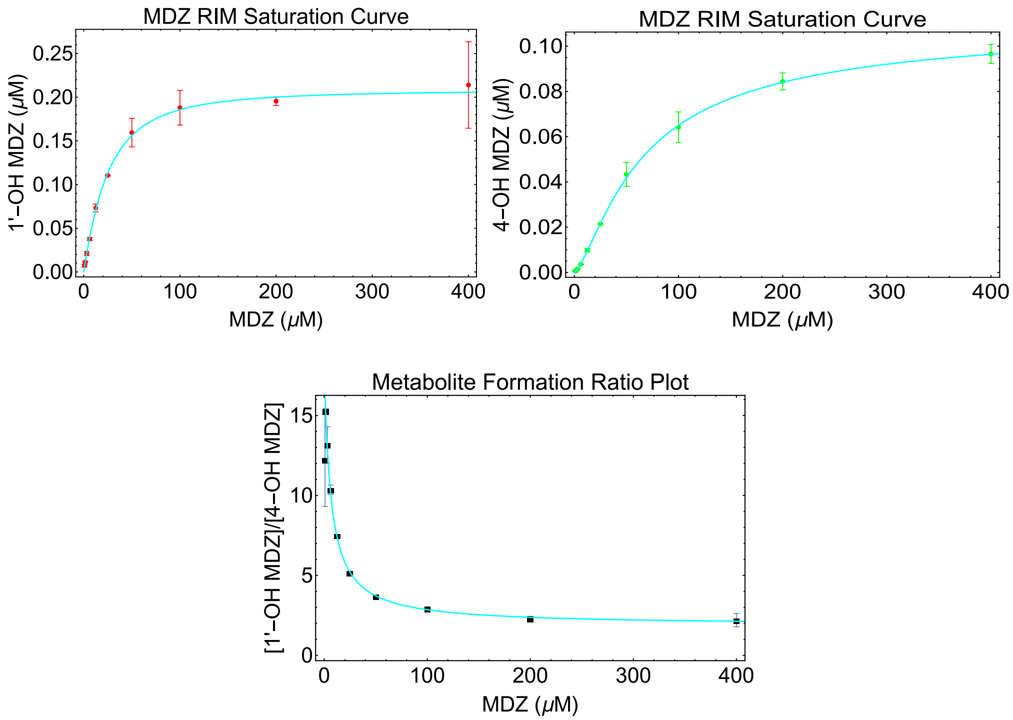

Figure 3.12. ESSP1P2 model fitting with the observed data for the MDZ incubation with RIM (Left: Saturation curve for MDZ→1'-OH MDZ, middle: Saturation curve for MDZ→4-OH MDZ, and right: Metabolite formation ratio plot). Plots represents mean data ± standard errors (n=3).

The kinetic parameters obtained from the model fittings are summarized in table 3.5. These parameters will be used in later chapters for absorption modeling. The CL_{int} for the formation of two metabolites over the intestinally relevant concentration are shown in figure 3.13 which shows a moderate concentration dependence. This might necessitate the use of an ODE rather than a single CL_{int} value for IVIVC.

Table 3.5. Comparison of estimates of kinetic parameters from ESP1P2 model and ESSP1P2 model. Data presented as parameter estimate ± S.E.

	ESP1P2 model		ESSP1P2 model	
	1’-OH MDZ	4-OH MDZ	1’-OH MDZ	4-OH MDZ
k_1 (µM^{-1}.min^{-1})	270 (fixed)		270 (fixed)	
k_2 (min^{-1})	12499.72±1911.75		7460.29±1564.27	
K_{m1} (µM)	46.33±7.24		27.89±6.35	
k_{cat1} (min^{-1})	7.14±0.47	2.04±0.22	5.37±0.90	0.29±0.15
$CL_{int1,unbound}$ (µl.min^{-1}.mg^{-1} of RIM protein)	0.95±0.17	0.27±0.048	1.20±0.33	0.069±0.038
k_5 (µM^{-1}.min^{-1})	Not applicable		270 (fixed)	
k_6 (min^{-1})			17261.69±3540.02	
K_{m2} (µM)			64.52±13.24	
k_{cat2} (min^{-1})			5.56±0.30	2.96±0.18
$CL_{int2,unbound}$ (µl.min^{-1}.mg^{-1} of RIM protein)			0.54±0.12	0.29±0.056

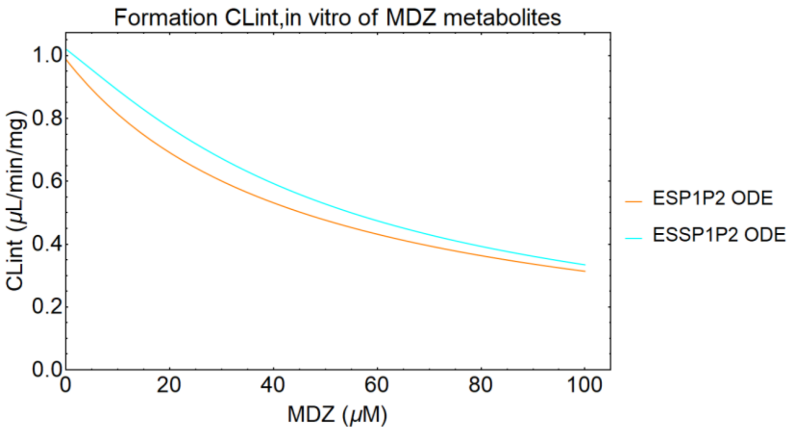

Figure 3.13: Intrinsic clearance plot over a range of physiologically relevant MDZ concentration for both metabolite formation

3.4.3 *In Vitro* Enzyme Kinetics of Nicardipine (NCD)

It was found that the incubations were linear up to 30 minutes for all protein concentrations except for 1 mg/ml (Figure 3.14 left). On the other hand, the incubations were apparently linear with respect to protein concentration for all incubation time ranges (Figure 3.14 right). Based on this, 0.25 mg/ml RIM with an incubation time of 20 minutes was selected for further analysis.

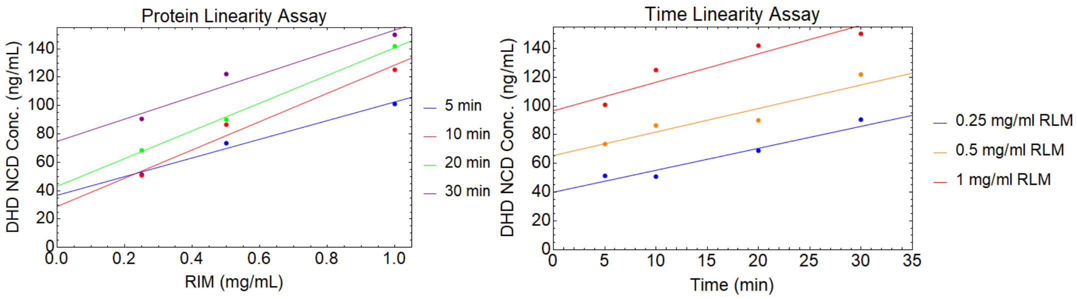

Figure 3.14: Time and protein linearity assay of NCD with RIM (n=1)

3.4.3.1 *In Vitro* Metabolism of Nicardipine (NCD) using RLM

3.4.3.1.1 Substrate Depletion Assay to Determine Apparent Intrinsic Clearance

Figure 3.15 depicts the time course of the unchanged NCD in RLM (0.1 mg/mL). The unchanged drug profile starting at 1000 nM showed the apparently log concentration depletion. Assuming first order depletion at this concentration an apparent *in vitro* intrinsic clearance ($CL_{int\,,\,in\ vitro,\ unbound}$) was calculated to be 9.85 ±0.83 mL/mg/min.

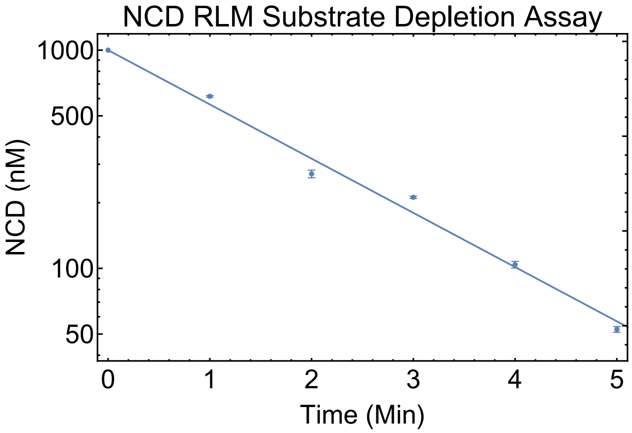

Figure 3.15: Substrate depletion assay of NCD using RLM. Plots represents mean data ± standard errors (n=3).

3.4.3.1.2 Saturation Curve Assay for the Conversion of Nicardipine (NCD) to Dehydronicardipine (DHD NCD)

For the saturation curve with RLM, the NCD concentration range was 0-50 µM (Figure 3.16). Commercially only DHD NCD was available. Therefore, only this metabolite was quantified, and different models were fitted to the data. Figure 3.16 shows the mean raw plot of the NCD saturation curve with RLM. Diagnostic Eadie-Hofstee plots was generated which indicated possible existence of multiple binding kinetics.

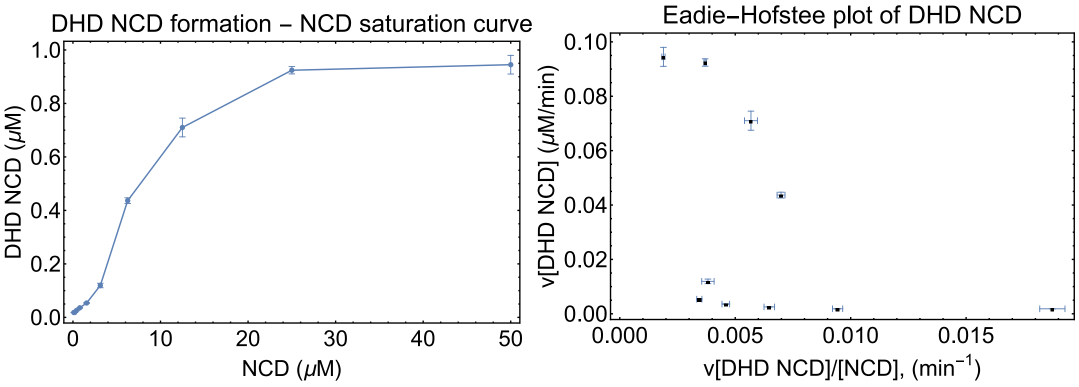

Figure 3.16. NCD saturation curve for the incubation with RLM (Left) and diagnostic Eadie-Hofstee plot (right). Plots represents mean data ± standard errors (n=3).

Both the single binding ESP model and double binding ESSP model were fitted to the data to choose the best model which explains the observed data (figure 3.1).

For the model comparison, different statistical matrices were used which are summarized in Table 3.6. Notably, from the AICc values, it was found that the ESSP model was the better fit to explain the dataset obtained from the saturation curve assay. The curve fitting with the observed data is shown in figure 3.17.

Table 3.6. Statistical matrices for model comparison

	ESP model	ESSP model
AdjustedRSquared	0.94	0.98
AICc	-92.13	-119.28
MSE	0.0078	0.0010

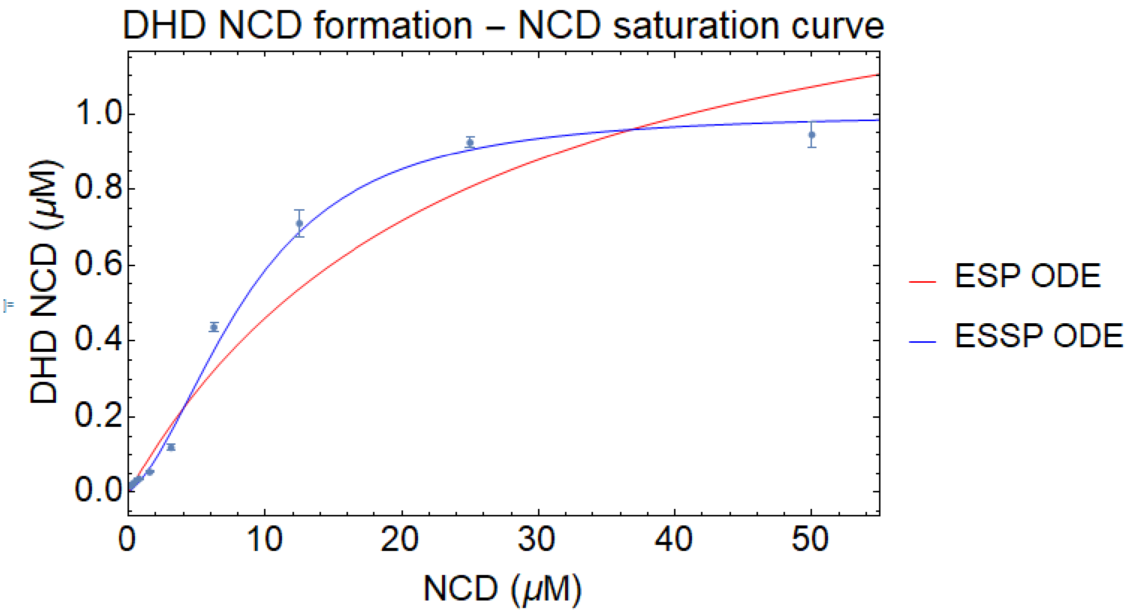

Figure 3.17. Model fitting with the observed data for the NCD incubation with RLM. Plots represents mean observed data ± standard errors (n=3).

The kinetic parameters obtained from the model fittings are summarized in table 3.7. These parameters will be used in later chapters for absorption modeling. The CL_{int} for the formation of DHD NCD over the physiologically relevant concentration are shown in figure 3.18 which shows a moderate concentration dependence. This might necessitate the use of an ODE rather than a single CL_{int} value for IVIVC.

Table 3.7. Comparison of estimates of kinetic parameters from ESP model and ESSP model. Data presented as parameter estimate ± S.E.

	ESP model	ESSP model
k_1 (μM^{-1}.min^{-1})	270 (fixed)	270 (fixed)
k_2 (min^{-1})	6418.67±1327.69	16413.11±1120.23
K_{m1} (μM)	24.09±5.12	61.11±4.09
k_{cat1} (min^{-1})	6.35±0.81	7.05±2.18
$CL_{int1,unbound}$ (ml.min^{-1}.mg^{-1} of RLM protein)	0.067±0.016	0.029±0.0088
k_4 (μM^{-1}.min^{-1})	Not applicable	270 (fixed)
k_5 (min^{-1})		415.67±133.67
K_{m2} (μM)		1.61±0.52
k_{cat2} (min^{-1})		3.97±0.20
$CL_{int2,unbound}$ (ml.min^{-1}.mg^{-1} of RLM protein)		0.64±0.21

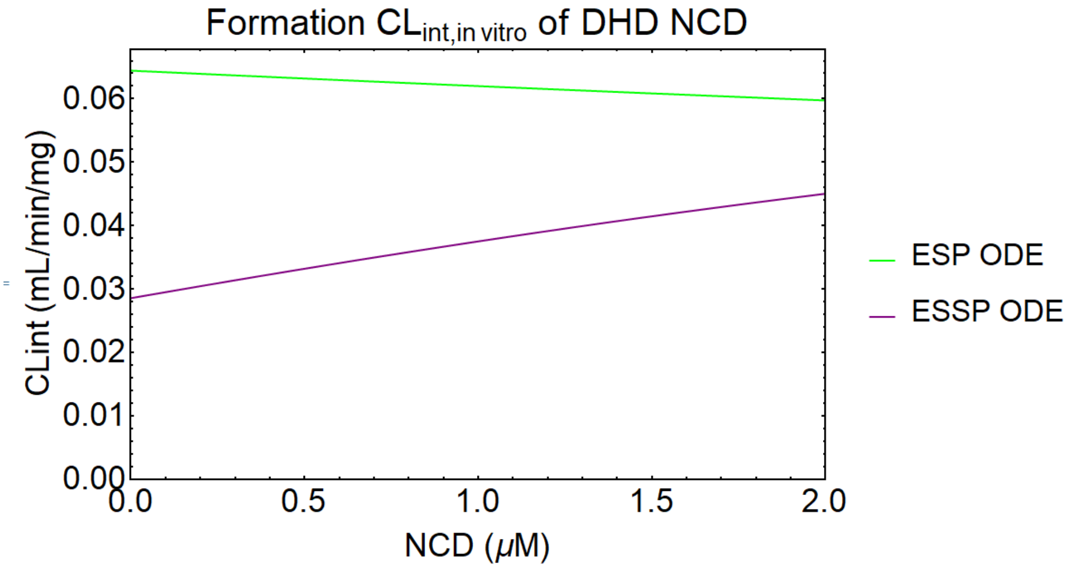

Figure 3.18: Intrinsic clearance plot over a range of physiologically relevant NCD concentration for DHD NCD formation

3.4.3.2 *In Vitro* Metabolism of Nicardipine (NCD) using RIM

3.4.3.2.1 Substrate Depletion Assay to Determine Apparent Intrinsic Clearance

Figure 3.19 depicts the time course of the unchanged NCD in RIM (1 mg/mL). The unchanged drug profile starting at 1000 nM showed the apparently log concentration depletion. Assuming first order depletion at this concentration an apparent *in vitro* intrinsic clearance (CL_{int}, *in vitro*) was calculated to be 0.15 ±0.026 mL/mg/min.

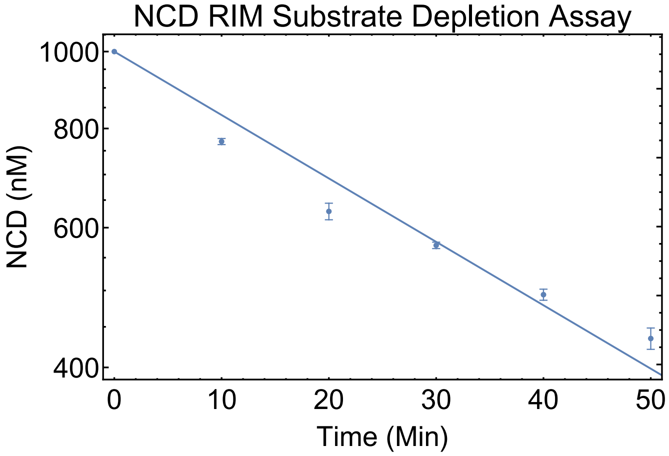

Figure 3.19: Substrate depletion assay of NCD using RIM. Plots represents mean observed data ± standard errors (n=3).

3.4.3.2.2 Saturation Curve Assay for the Conversion of Nicardipine (NCD) to Dehydronicardipine (DHD NCD)

For the saturation curve with RIM, the NCD concentration range was 0-250 µM (Figure 3.20). Commercially only DHD NCD was available. Therefore, only this metabolite was quantified, and different models were fitted to the data. Figure 3.20 shows the raw plot of the NCD saturation curve with RLM. Diagnostic Eadie-Hofstee plots was generated which indicated possible existence of multiple binding kinetics.

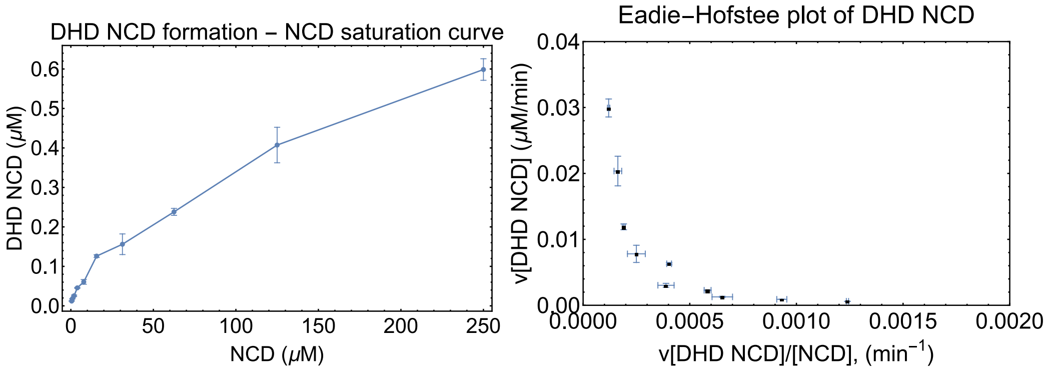

Figure 3.20. NCD saturation curve for the incubation with RIM (Left) and diagnostic Eadie-Hofstee plot (right). Plots represents mean data ± standard errors (n=3).

Both the single binding ESP model and double binding ESSP model were fitted to the data to choose the best model which explains the observed data (Figure 3.1).

For the model comparison, different statistical matrices were used which are summarized in Table 3.8. Notably, from the AICc values, it was found that the ESSP model was the better fit to explain the dataset obtained from the saturation curve assay. The curve fitting with the observed data is shown in figure 3.21.

Table 3.8. Statistical matrices for model comparison

	ESP model	ESSP model
AdjustedRSquared	0.96	0.99
AICc	-136.56	-164.49
MSE	0.00094	0.00046

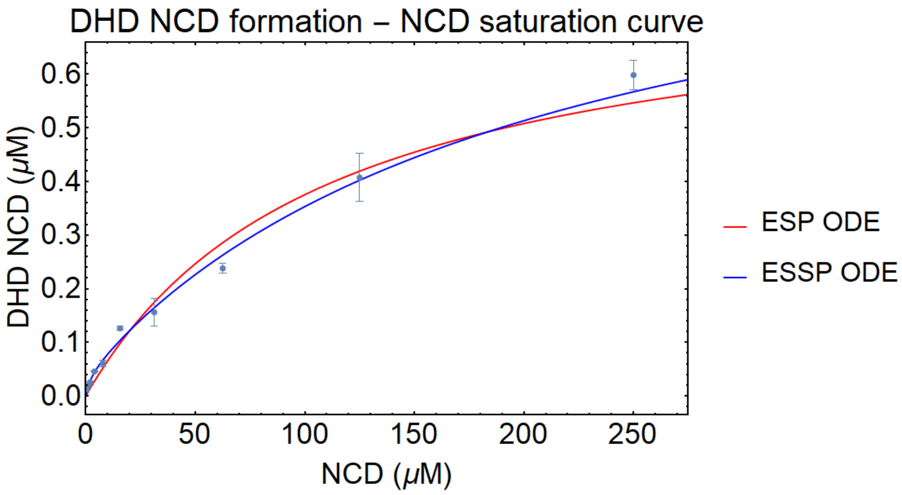

Figure 3.21. Model fitting with the observed data for the NCD incubation with RIM. Plots represents mean observed data ± standard errors (n=3).

The kinetic parameters obtained from the model fittings are summarized in table 3.9. These parameters will be used in later chapters for absorption modeling. The CL_{int} for the formation of DHD NCD over the intestinally relevant concentration are shown in figure 3.22 which shows a moderate concentration dependence. This might necessitate the use of an ODE rather than a single CL_{int} value for IVIVC.

Table 3.9. Comparison of estimates of kinetic parameters from ESP model and ESSP model. Data presented as parameter estimate ± S.E.

	ESP model	ESSP model
k_1 ($\mu M^{-1}.min^{-1}$)	270 (fixed)	270 (fixed)
k_2 (min^{-1})	29364.12±3813.73	661.20±15.79
K_{m1} (μM)	109.49±14.12	2.45±0.06
k_{cat1} (min^{-1})	1.57±0.11	0.11±0.012
$CL_{int1,unbound}$ ($ml.min^{-1}.mg^{-1}$ of RIM protein)	0.00114±0.0049	0.0044±0.00050
k_4 ($\mu M^{-1}.min^{-1}$)	Not applicable	270 (fixed)
k_5 (min^{-1})		57232.91±1192.06
K_{m2} (μM)		212±4
k_{cat2} (min^{-1})		2.02±0.06
$CL_{int2,unbound}$ ($ml.min^{-1}.mg^{-1}$ of RIM protein)		0.0095±0.000033

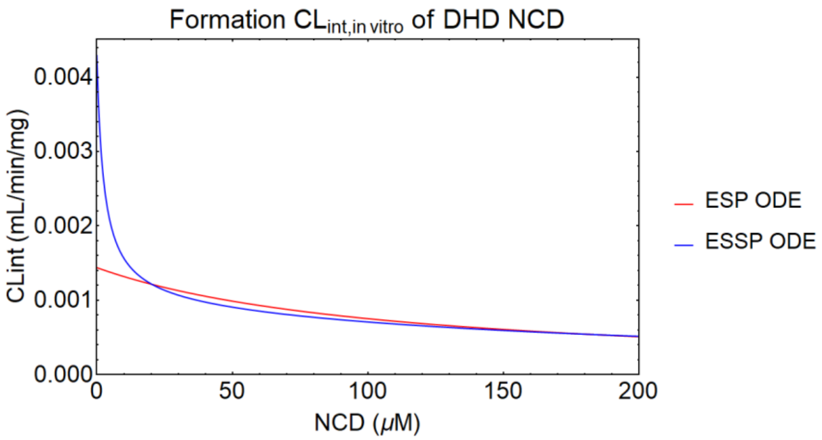

Figure 3.22: Intrinsic clearance plot over a range of physiologically relevant NCD concentration for DHD NCD formation

3.5 Discussion and Conclusions

Equilibrium dialysis is a common strategy to measure the fraction unbound in microsomes and in plasma. A good experimental apparatus should show low non-specific binding and high reproducibility. In the current study, the HTD 96b Teflon block unit was used to determine the fraction unbound. The Teflon base assembly is known to minimize the non-specific binding between the drug and the chamber walls (Cory Kalvass & Maurer, 2002; Plise et al., 2010; Riccardi et al., 2015; Vanstraelen et al., 2014; J. Zhang et al., 2010). The measured unbound fraction (table 3.1) is similar to that reported in the literature (MDZ f_{um} 0.71 and NCD f_{um} 0.039) (Holt et al., 2019).

Due to the differences in expression of CYP enzymes in rat liver versus rat intestine (Kaminsky & Zhang, 2003; Nishiyama et al., 2016; Pałasz et al., 2012), the kinetic parameters obtained from the metabolic assays using liver and intestinal microsomes might be different. The aim of this chapter was to determine the kinetics of metabolic conversion of MDZ and NCD using RLM and RIM. If the drug of interest is known to be metabolized by the membrane bound enzymes including CYPs and UGTs (Barr & Iwuchukwu, 2021), the use of microsomes is always a better choice than rCYPs and hepatocytes due to its ease of availability, cost and lower variability due to pooled sources (P. R. Kulkarni et al., 2021; Yadav et al., 2020). In human, MDZ is primarily metabolized by CYP3A4 enzymes (Wandel et al., 1994) and NCD is metabolized by multiple CYPs (3A4, 2D6, and 2C8) (Graham et al., 1985; Nakamura et al., 2005). While NCD is metabolized to two different metabolites: dehydronicardipine (DHD NCD) and debenzylatednicardipine (Graham et al., 1985; Nakamura et al., 2005), only DHD NCD was commercially available. That is why substrate depletion assay was added (section 3.4.3.1.1 & 3.4.3.2.1) along with the saturation curve (section 3.4.3.1.2 & 3.4.3.2.2) assays to capture the overall metabolic depletion of NCD using liver and intestinal microsomes.

One of the major assumptions of the Michaelis-Menten kinetics is the steady-state assumption. This means, for initial-rate conditions, the metabolic turnover rate must be constant with respect to the protein concentration in the enzyme source and time (Barr, Flora, & Iwuchukwu, 2014; Barr & Iwuchukwu, 2021). Although the use of ODEs can bypass the steady-state assumption, it is always a better idea to start the *in vitro* enzyme kinetics experiments with a set of time linearity and protein linearity assays. This gives the experimenter an idea of optimum incubation time with lowest enzyme concentration. Within the linear range, lowest microsomal protein concentration is the best choice to avoid significant non-specific lipid partitioning to the microsomes. However, within linearity the incubation time and the protein concentration should be sufficient enough to detect and measure metabolite concentration at low substrate concentration(Barr et al., 2014; Barr & Iwuchukwu, 2021). Keeping in mind all these considerations, preliminary time and protein linearity assays were done and lowest possible incubation time and microsomal concentrations were used without reaching the LLOQ of the metabolites. However, for the IVIVC the metabolic intrinsic clearance needs to be corrected with the fraction unbound in microsomes obtained from the equilibrium dialysis experiment. Especially, for highly bound compound NCD, the unbound CL_{int} is dramatically increased when corrected with the f_{um} (Table 3.7 & 3.9).

Rat intestine is the first metabolic site which contributes to the first pass metabolism of the xenobiotics in rats. Cyp1a1 is the highest expressed cytochrome P450 enzyme in rat intestine. The other Cyps are Cyp1a2, Cyp2b, Cyp2c, Cyp3a, Cyp4a1, Cyp2j3/4, and Cyp4f12 (Kaminsky & Zhang, 2003; Pałasz et al., 2012). However, the relative abundance of these Cyps is yet to be revealed definitively. It is noteworthy that there are significant differences in the expression levels of Cyps in different strains of rats (Nishiyama et al., 2016). However, major hepatic Cyps are Cyp1a1, Cyp1a2, Cyp2b1, Cyp2c11, and Cyp3a2 (Nishiyama et al., 2016).

For the saturation curve analysis of MDZ with RLM the highest concentration of MDZ was 200 µM (figure 3.5). Preliminary solubility tests showed that using 1% methanol the MDZ solubility can go up to 400 µM. It is always a good idea to take the concentration range as high as possible for proper characterization of enzyme kinetics. It helps to differentiate atypical kinetics from the apparent Michaelis-Menten kinetics. From the saturation curve assay using both metabolites (1’-OH MDZ & 4-OH MDZ), it was found that the MDZ interaction with RLM follows sigmoidal kinetics (Fig. 3.6). This was not surprising because of the involvement of CYP3A in MDZ metabolism (Turpeinen, Jouko, Jorma, & Olavi, 2005), and CYP3A is fairly known for atypical kinetics including sigmoidal kinetics (K. R. Korzekwa et al., 1998; Tracy, 2006; Witherow & Houston, 1999). However, the *in vivo* unbound concentration will never reach 200 µM with the usual dose of MDZ in rats. Published literature of MDZ rat PK shows that highest possible total plasma concentration can range from 2-5 µM (Kotegawa et al., 2002; Winter et al., 2013). Keeping this concentration range in mind, CL_{int} was plotted against MDZ concentration. It showed a moderate concentration dependence (Figure 3.9) which might rationalize using a variable CL_{int} of MDZ during IVIVC. However, if the use of a variable CL_{int} value does not show a significant improvement in IVIVC, the use of single CL_{int} is obviously better choice from the modelling and simulation point of view due to simplicity.

While 4-OH MDZ was the major metabolite in MDZ incubation with RLM, 1'-OH MDZ was the major metabolite while MDZ incubated with RIM (figure 3.10). This may be due to the variable enzyme expression in liver versus intestine. Due to lower activity reported in RIM interactions with MDZ (Kotegawa et al., 2002), a higher microsomal concentration and a longer incubation time were taken. Individual metabolites' Eadie-Hofstee plots and metabolite formation ratio plots suggested possible involvement of multiple binding kinetics (figure 3.11), and hyperbolic and sigmoidal atypical kinetics were found for 1'-OH MDZ and 4-OH MDZ formation (Figure 3.12 & Table 3.4). Although the $K_{m1}<K_{m2}$ and $k_{cat1}<k_{cat2}$ were found for 4-OH MDZ which initially seemed to be biphasic kinetics, CL_{int1} was significantly lower than the CL_{int2} which indicated sigmoidicity. Similarly, for 1'-OH MDZ it was seemingly hyperbolic (figure 3.12), but

the CL_{int2} indicated sigmoidicity (Paragas et al., 2021; Z. Wang et al., 2021). Enterocytic metabolism occurs inside the enterocyte and there is no published literature that has determined the MDZ enterocyte concentration after an oral dose of MDZ in rats. However, the continuous intestinal absorption model (Nagar et al., 2017) can simulate enterocyte concentration of MDZ after an oral dose. The newly published rat model (Radice et al., 2022) will be used in a later chapter where enterocyte concentration of MDZ can be simulated. It is understandable that the enterocyte MDZ concentration, at least theoretically will be higher than the plasma concentration. That is why the intrinsic clearance plot was created with a higher concentration range of up to 100 µM (Figure 3.13). A significant concentration dependence was found for MDZ metabolic conversion to its metabolites. This might emphasize the use of a variable CL_{int} while incorporating the intestinal metabolism into the continuous intestinal absorption model.

However, The CL_{int} plots of MDZ metabolism using RLM vs RIM are different from each other. In case of MDZ metabolism with RLM, ESP1P2 model depicts a descending pattern but ESSP1P2 model depicts an ascending pattern (figure 3.9) over the physiologically relevant concentration range. This might happen due to the sigmoidal ESSP1P2 model where the $K_{m1}>K_{m2}$. On the other hand, in case of MDZ metabolism with RIM, both ESP1P2 and ESSP1P2 model depicts similar CL_{int} plots (figure 3.13). Although, ESSP1P2 model is showing sigmoidal kinetics but here $K_{m1}<K_{m2}$ which might explain a similar descending CL_{int} pattern for both the models. One might wonder about the underlying mechanism of this difference between RLM versus RIM incubation with MDZ. Again, the relative enzyme expression level (discussed in chapter 1 and here above) and enzyme-substrate interactions might explain these dissimilarities.

Microsomal substrate depletion with specific enzyme cofactors is a common approach to estimate substrate CL_{int} specially in the initial phases of drug discovery when all the metabolite information are not available (Di & Obach, 2015; Obach & Reed-Hagen, 2002; Paragas et al., 2021; Scott Obach, 2011; Z. Wang et al., 2021). One of the metabolites of NCD was not commercially available. Therefore, the substrate depletion assay was done to capture an overall intrinsic clearance mediated by CYPs. Assuming mono-exponential substrate depletion at a relatively low concentration, the *in vitro* elimination rate constant and *in vitro* half-life can be calculated from the slope. However, for CYP reactions with atypical kinetics, the slope can be different when different substrate concentrations are used (Paragas et al., 2021; Z. Wang et al., 2021). Therefore, the depletion profile needs to be validated with different substrate concentrations.

In this study, NCD (1 µM) was incubated with RLM (0.1 mg/mL) for 5 minutes (figure 3.15). The substrate concentration was selected based on a previously published paper (Naritomi et al., 2001). However, the CL_{int} obtained from this substrate depletion assay was much higher than that obtained from the saturation curve (Table 3.7). This implies that the formation of commercially unavailable metabolite cannot be ignored kinetically.

In case of RIM, the microsomal concentration was 1 mg/mL and incubation run for 50 minutes (figure 3.19). The later time points were showing noticeably clear curvature. It might be due to distinct reasons. First, atypical kinetics can cause curvature at later time points. Also, initial studies with RIM shows that it is less stable than the RLM which might cause decreased depletion of NCD at later time points. However, assuming mono-exponential substrate depletion at a relatively low concentration, an apparent CL_{int} was calculated and again, it was much higher than the CL_{int} obtained from the saturation curve of NCD with RIM (Table 3.9). This emphasized that the formation of debenzylatednicardipine cannot be neglected.

NCD metabolic conversion to DHD NCD was known to be catalyzed by three CYP isoforms in human: 2C8, 2D6, and 3A4 (Nakamura et al., 2005). Rat Cyp2d1 is the rat orthologue of human CYP2D6 (Martignoni, 2006; Martignoni et al., 2004; Martignoni et al., 2006). However, rat Cyp2d1 is not highly expressed in liver. On the other hand, Cyp3a1 and 3a2 is expressed in rat liver but the extent is low. Also, many substrates of human CYP3A4 enzymes as dihydropyridine calcium channel blockers including nifedipine are not metabolized by rat Cyp3a1 (Martignoni, 2006; Martignoni et al., 2006). However, Cyp2c11, which is the rat ortholog of human CYP2C8 is the most abundant Cyp2c isoform in rat liver and it participates in the metabolic oxidation of dihydropyridines like nicardipine. Cyp2c11 is also the predominant isoform in male rat liver (more than 50%) (Martignoni, 2006; Martignoni et al., 2006). From all these considerations, it might be safe to assume that mainly Cyp2c11, and partly Cyp3a2 might be responsible for NCD metabolism to DHD NCD in RLM.

The highest concentration for the NCD saturation curve assay with RLM was 50 µM (figure 3.16) due to its solubility limit. It was found to be following atypical kinetics. Specifically, the DHD NCD formation was following sigmoidal kinetics (figure 3.17 & table 3.6, 3.7) producing K_{m1}>K_{m2} and k_{cat1}>k_{cat2} (Paragas et al., 2021; Z. Wang et al., 2021). From the published literatures highest possible NCD concentration was found 1-2 µM (J.-S. Choi et al., 2009; Jun-Shik, Sung-Il, & Dong-Hyun, 2010). Within that concentration range, the formation intrinsic clearance of DHD NCD produced moderate concentration dependence (figure 3.18).

In the rat intestine, the expression of Cyp2c11 and Cyp3a are comparable. The highest concentration for the NCD saturation curve assay with RIM was 250 µM (figure 3.20). Although NCD is not soluble at this concentration, due to its higher partitioning and due to the use of a higher RIM concentration, this concentration use was justified. The DHD NCD formation from this assay was found to be clearly biphasic. This might be due to the comparable involvement of multiple enzymes including Cyp2c11 and Cyp3a1/2, or it might be due to the multiple binding of the NCD with the enzyme. Experiments with recombinant Cyps can help to clear this concern. There is no published literature that has determined the NCD enterocyte concentration after an oral dose of NCD in rats. However, the continuous intestinal absorption model (Nagar et al., 2017) will be able to simulate enterocyte concentration of NCD after an oral dose. The newly published rat model (Radice et al., 2022) will be used in later chapter where enterocyte concentration of NCD will be simulated. The enterocytic NCD concentration, at least theoretically is expected to be higher than the plasma concentration. That is why the intrinsic clearance plot was created with a higher concentration range of up to 200 µM (Figure 3.22). A significant concentration dependence was found for NCD metabolic conversion to DHD NCD. This might emphasize the use of a variable CL_{int} while incorporating the intestinal metabolism into the continuous intestinal absorption model.

In summary, it was found that enzyme kinetic modeling of MDZ and NCD interactions with RLM or RIM are explained by atypical kinetics. Further there was significant differences in intrinsic clearance of NCD using substrate depletion versus saturation curve suggesting incorporating other metabolite consideration in the saturation curve may help to characterize those interaction more in depth.

CHAPTER FOUR: *IN VITRO* ENZYME KINETICS OF MIDAZOLAM AND NICARDIPINE USING HUMAN INTESTINAL MICROSOMES (HIM) AND HUMAN LIVER MICROSOMES (HLM)

4.1 Rationale

In humans, unfavorable pharmacokinetics (PK) is one of the leading causes of drug development termination (Prentis, Lis, & Walker, 1988). The ability of a compound to be translated into a drug is considerably determined by the drug's metabolic and pharmacokinetic (DMPK) characteristics, which are the major roadblocks in pharmaceutical research and development. DMPK problems are responsible for around 40% of medication failures (Alavijeh & Palmer, 2004). Poor efficacy is the leading reason of clinical trial failure (Harrison, 2016). Despite improvements in PK and bioavailability since the 2000s, approximately half of all treatment candidates in development are lost due to inadequate absorption, distribution, metabolism, excretion, and toxicity (ADMET) (Kola & Landis, 2004; J. Wang & Urban, 2004). As a result, one of the major targets of non-clinical research in the drug discovery–development process is to anticipate PK features in people prior to first-in-human (FIH) clinical trials. *In vitro-in vivo* extrapolation (IVIVE) and allometric scaling (AS) are two techniques for predicting PK in humans (G.-W. Choi, Lee, & Cho, 2019).

IVIVE models are based on physiological, biochemical, and biopharmaceutical characteristics such as organ size, blood flow rate, enzyme kinetics, drug permeability, partitioning factor into the organ, and other *in vitro* clearance data. These data are included into IVIVE models to give significant insight into drug characteristics as well as evidence to help decision-making throughout the drug discovery and development.

Despite its benefits, building the IVIVE model involves knowledge of PKs as well as a comprehension of sophisticated mathematical formulae. Additionally, this method is costly and time-consuming (Mahmood & Balian, 1999). Although it is difficult to project *in vitro* to *in vivo* data due to the complexity of interdependent biological systems and their dynamic nature (J. H. Lin, 1998), IVIVE is more physiologically relevant than AS because it incorporates physiological mechanisms and includes the potential to expand with the mechanistic model (Li et al., 2017; Riede, Poller, Umehara, Huwyler, & Camenisch, 2016).

4.1.1 IVIVE for Predicting Human F_h

The goal of IVIVE is to predict human parameters using quantitative extrapolation of *in vitro* data. *In vitro* kinetic data and mathematical formulae are used in a valid extrapolation technique to estimate hepatic metabolic clearance (Lave, Coassolo, & Reigner, 1999). Since IVIVE's introduction by Rane et al. (Rane, Wilkinson, & Shand, 1977), its approach has been updated. *In vitro* data is scaled up to *in vivo* by assessing the association between *in vitro* and *in vivo* data or by adding physiological correction factors. Figure 4.1 depicts the main strategy of IVIVE employing human liver microsomes (HLM) or the recombinant human cytochrome P450 (CYP) system (rhCYP).

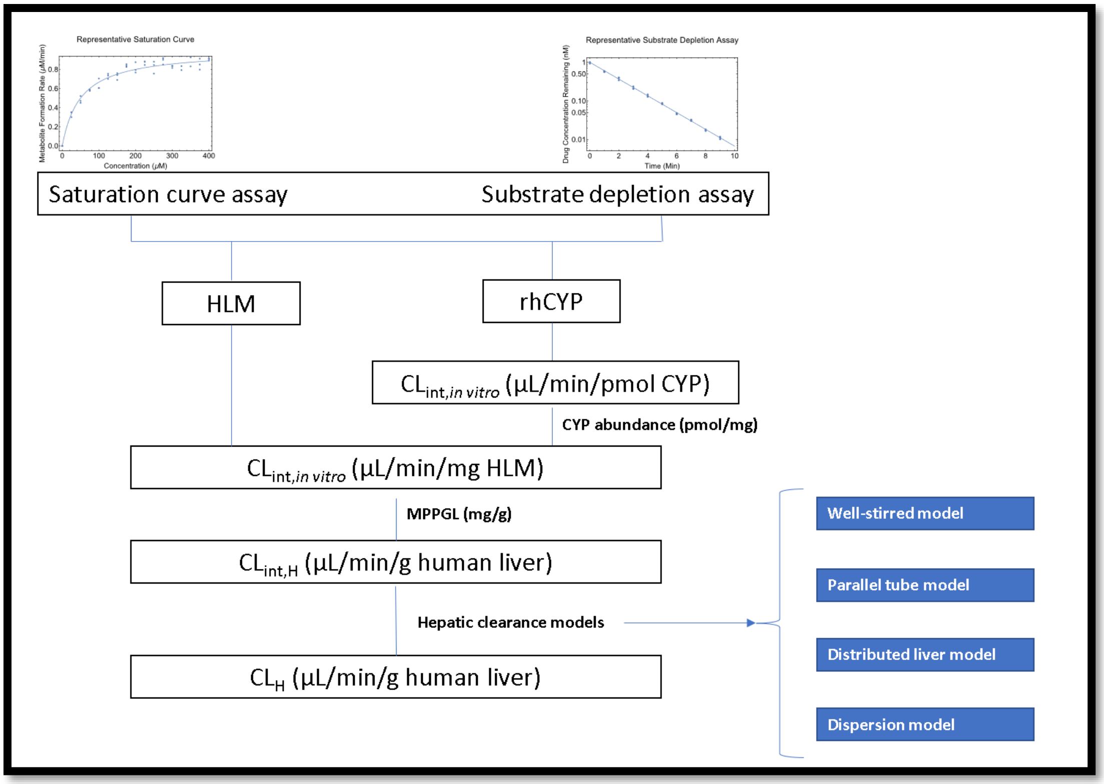
Representative Saturation Curve
Metabolite Formation Rate (μM/min)
0.0
0.2
0.4
0.6
0.8
0
100
200
300
400
Concentration (μM)
Representative Substrate Depletion Assay
Drug Concentration Remaining (nM)
1
0.50
0.10
0.05
0.01
0
2
4
6
8
10
Time (Min)
Saturation curve assay
Substrate depletion assay
HLM
rhCYP
CL$_{int,\textit{in vitro}}$ (μL/min/pmol CYP)
CYP abundance (pmol/mg)
CL$_{int,\textit{in vitro}}$ (μL/min/mg HLM)
MPPGL (mg/g)
CL$_{int,H}$ (μL/min/g human liver)
Hepatic clearance models
CL$_H$ (μL/min/g human liver)
Well-stirred model
Parallel tube model
Distributed liver model
Dispersion model

Figure 4.1. The entire process of *in vitro-in vivo* extrapolation (IVIVE) employing human liver microsomes (HLM) or recombinant human cytochrome P450 (CYP). MPPGL is an abbreviation for microsomal protein per gram of liver (adapted from (G.-W. Choi et al., 2019)).

The *in vitro* metabolic kinetic parameters are calculated using these systems based on metabolite synthesis or substrate depletion (i.e., K_m, V_{max}, and $CL_{int,\textit{in vitro}}$) which has been described in detail in previous chapter of rat *in vitro* studies. Usually, the intrinsic clearance is expressed in µL/min/mg of HLM protein when the incubation protein source is HLM. However, the intrinsic clearance is expressed in µL/min/pmol of CYP enzyme when the enzyme source is recombinant human CYP isoform. This can be converted to µL/min/mg of HLM by correcting with the CYP abundance data which is often provided by the vendor of enzyme sources. Further this intrinsic clearance is converted to intrinsic clearance normalized to liver weight in grams. Different hepatic clearance models can be used from this step to convert this *in vitro* intrinsic hepatic clearance to the *in vivo* projected hepatic clearance.

The liver is important for drug clearance by metabolism and/or excretion via bile acid. Hepatic metabolism participates in the elimination process of most drugs in market. There are mainly four typical hepatic clearance models in the field of pharmacokinetics (Kim, Shin, & Shin, 2018).

1. Well-stirred model
2. Parallel tube model
3. Distributed model
4. Dispersion model

The well-stirred model, in which the liver is considered as a single well-mixed compartment with a constant drug concentration (figure 4.2), is a commonly used model. Simple equations are used to describe this concept.

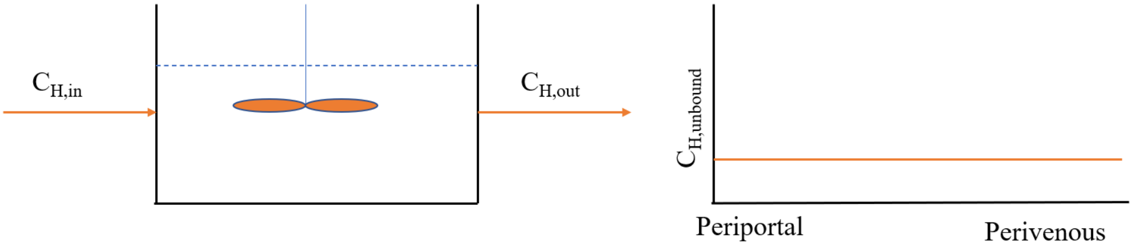

Figure 4.2: Well-stirred hepatic model

Hepatic clearance CL_H is expressed by the following equation:

$$CL_H = Q_H . ER_H \qquad \text{Equation ------------------------------------4.1}$$

ER_H is the hepatic extraction ratio, while Q_H is the hepatic blood flow (20.7 mL/min/kg in humans). CL_H is not directly proportional to Q_H since ER_H is reliant on Q_H. ER often reduces when Q_H rises (Keiding & Andreasen, 1979).

In addition, using ER_H, the following equation is used to compute hepatic availability (F_h):

$$F_H = 1 - ER_H = \frac{Q_H}{Q_H + f_P . CL_{int,H}} \qquad \text{Equation ------------------------------------4.2}$$

Where, f_p is the unbound fraction in plasma and $CL_{int,H}$ can be calculated from *in vitro* data using the following equation (Obach, 1999):

$$CL_{int,H} = \frac{0.693}{in\ vitro\ t_{1/2}} . \frac{mL\ incubation}{mg\ microsomes} . \frac{45\ mg\ microsomes}{1\ g\ liver} . \frac{20\ g\ liver}{1\ kg\ body\ weight}$$

$$\text{Equation ------------------------------------4.3}$$

On the other hand, the parallel-tube model depicts the liver as a series of tubes that form a sinusoid, with hepatocytes doing the elimination (figure 4.3) (Malcolm Rowland, 1985; Ping Zhao, Rowland, & Huang, 2012). In the direction of the hepatic vein, drug concentration in the liver (i.e., sinusoids and hepatocytes) decreases exponentially.

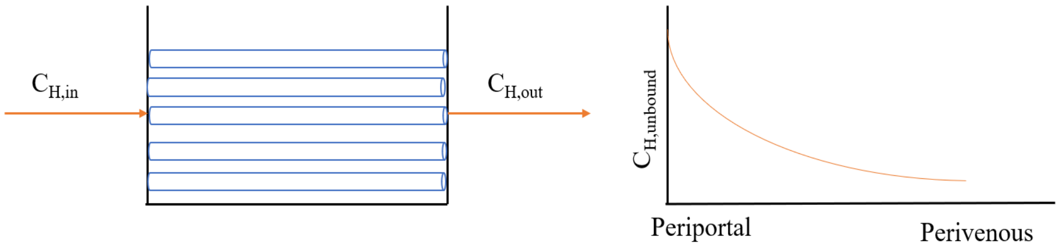

Figure 4.3. Parallel-tube hepatic model

In both the limiting cases the hepatic clearance estimation is similar for these two models. The investigator can choose the model that best explains organ clearance by comparing observed values to anticipated values using these two models. However, prior to an inquiry, it is difficult to select the model with a good match in a realistic experimental context. Most scientists employ the well-stirred model unless there is clear evidence, based on the concept that models should be as simple as feasible but not simpler (E. Lee Forker & Luxon, 1985; Mehvar, 2018).

Drug permeability is not a rate-limiting step in drug removal, according to both well-stirred and parallel-tube models (Mehvar, 2018). However, an extended clearance model has recently been established in which permeability is one of the key parameters impacting the CL_H (Camenisch et al., 2015; Camenisch & Umehara, 2012; Riede et al., 2016).

The liver is clearly neither a well-stirred compartment nor a collection of similar tubes (E. L. Forker & Luxon, 1983). The use of a dispersion model (Roberts & Rowland, 1986a, 1986b) or a dispersed model (Bass, Robinson, & Bracken, 1978; Sawada, Sugiyama, Miyamoto, Iga, & Hanano, 1985) to describe hepatic clearance as more physiologically realistic has been attempted. The liver is described as a series of parallel tubes with varying geometrical features in the distributed model.

Non-specific binding factors can impact intrinsic clearance measurements (G.-W. Choi et al., 2019). Obach et. al. described a technique for predicting human intrinsic hepatic clearance ($CL_{int, H}$) by using non-specific binding factors to microsomes ($f_{u,mic}$) and the f_p (Obach, 1999). The chemical properties of 29 medicines were used to classify them (i.e., basic, neutral, and acidic compounds). The results indicated that human CL of neutral and basic substances could be predicted accurately with or without binding factors. Human CL values were predicted with a considerable degree of inaccuracy in the case of acid substances, omitting binding variables.

According to Howgate et al., the majority of the $f_{u,mic}$ values are high enough to be disregarded in the forecast of clearance (Howgate, Rowland Yeo, Proctor, Tucker, & Rostami-Hodjegan, 2006). However, there are a few drugs which are highly partitioned to microsomes. For these drugs $f_{u,mic}$ values need to be considered to accurately predict *in vivo* clearance. In the preliminary stages of drug research and development, when fundamental knowledge on the compound of interest is limited, including $f_{u,mic}$ is a superior technique to forecast *in vivo* circumstances.

4.1.2 IVIVE for Predicting Human F_g

The small intestine is the site of drug absorption for majority of drugs. Lipophilicity, molecular size, and charge are all principal elements in influencing a drug's permeability. Permeation clearance (CL_{perm}) is the product of intestinal permeability (effective permeability, P_{eff} or *in vitro* apparent permeability, Papp) and surface area accessible for drug absorption (A) with a unit of flow rate (mL/min) (Equation 4.4-4.5).

$$CL_{perm} = P_{eff}.A$$

$$CL_{perm} = P_{app}.A$$

Equation ------------------------------------4.4-4.5

In human, when P_{eff} is utilized, A is considered to be 0.66 m^2, which is the small intestine's cylindrical surface area. Because P_{eff} accounts for the surface area magnifications of Kerckring folds, villi, and microvilli, the gut is regarded as a tube in this case. A is considered to be 200 m^2 when P_{app} is employed, which is the real surface area of the small intestine (Galetin et al., 2008, 2010; Gertz, Harrison, Houston, & Galetin, 2010).

Human intestinal epithelial cells, including enterocytes in the small intestine and colonocytes in the large intestine, contain a range of drug metabolizing enzymes involved in phase I and II processes that result in drug removal via intestinal first pass metabolism (Doherty & Charman, 2002; Kaminsky & Zhang, 2003; Wacher et al., 2001). The most common CYP isozyme in the human gut is CYP3A4, which contributes greatly to drug elimination via first pass metabolism. It has also been revealed that UDP glucuronosyltransferase participates in the first-pass clearance of some pharmaceuticals in the intestine. Although the expression levels of drug-metabolizing enzymes in the intestine are much lower than those in the liver (for example, the total amount of intestinal CYP3A4 represents only 1% of hepatic CYP3A4), first-pass extraction ratios of some drugs in the intestine are frequently comparable to or even higher than those in the liver (Fagerholm, 2007; Paine et al., 1997).

Because orally given drugs are supplied to drug-metabolizing enzymes in enterocytes via a relatively slow intestinal absorption process, first-pass exposure to the enzymes may be larger in enterocytes. However, rapid blood flow (1.5 L/min) and binding to blood components may counteract rapid metabolism in first-pass through the liver for certain drugs. A drug's intestinal first-pass elimination (F_g) involves a complicated interaction of intestinal permeation (passive and active transport), binding to intestinal lumen and enterocyte components, relevant blood flows, and the intrinsic metabolic activity of the enzyme system (Benet & Cummins, 2001). As a result, those F_g factors should be included when modeling events during the first transit of a molecule through the gut.

Several earlier investigations employed a variant of the traditional well-stirred model for hepatic clearance to estimate the F_g, as demonstrated in the following equation:

$$F_G = \frac{Q_G}{Q_G + f_{uG} . CL_{int,G}} \quad \text{Equation ------------------------------------4.6}$$

where Q_G, f_{uG}, and $CL_{int,G}$ are the GI tract blood flow rate, the percentage of drug unbound in the enterocyte, and the net intrinsic metabolic clearance in the GI wall based on unbound drug concentration, respectively (Chiba et al., 1997; J. H. Lin et al., 1997; Zimmerman, Wen, & Remmel, 2000). This model, however, has little physiological significance since orally given drugs transfer drug-metabolizing enzymes to enterocytes via the intestinal permeation process upon first-pass, not the blood flow perfusing the GI tract. The pathway of orally taken medications via the GI tract (pre-systemic or first-pass pathway) differs from the systemic pathway of intravenously administered pharmaceuticals. The orally absorbed drugs face intestinal and hepatic metabolism before being available in the systemic circulation. After being available in the circulation, the pathway of orally administered drugs through the liver is the same (Mizuma, Tsuji, & Hayashi, 2004).

The simplistic Q_{Gut} model, as indicated in the equation 4.7, has recently been presented to allow prediction of the F_g with minimum *in vitro* metabolism and permeation data.

$$F_G = \frac{Q_{Gut}}{Q_{Gut} + f_{uG}.CL_{int,G}} \qquad \text{Equation ------------------------------------4.7}$$

The fuG is fraction unbound in the enterocytes and CL_{int},G is the *in vitro* intrinsic clearance of the drug in the gut. Q_{Gut}, as indicated in Equation 4.8, is a mix of intestinal blood flow and permeability.

$$Q_{Gut} = \frac{Q_{villi.}CL_{perm}}{Q_{villi} + CL_{perm}} \qquad \text{Equation ------------------------------------4.8}$$

where Q_{villi} represents the villous blood flow rate and CL_{perm} represents the intestinal permeation clearance. Estimates of Q_{villi}, CL_{perm}, f_{uG}, and $CL_{int,G}$ are required for Q_{Gut} model implementation. Q_{Gut} in Equation 4.8 indicates mesenteric or mucosal blood flow in the well-stirred model (Chiba et al., 1997; J. H. Lin et al., 1997; Zimmerman et al., 2000). In human, total blood flow to the small intestine (mesenteric blood flow) is around 620 mL/min. Approximately 80% of mesenteric blood flow perfuses the mucosal side of the small intestine (mucosal blood flow, 496 mL/min), and approximately 60% of mucosal blood flow perfuses the villous epithelial cells (villous blood flow [Q_{villi}], 298 mL/min) (Galetin et al., 2008, 2010). In Equation 4.8, CL_{perm} is specified, and f_{uG} is assumed to be one. $CL_{int,G}$ may be evaluated *in vitro* using human intestinal microsomes

(2977 mg microsomal protein/whole small intestine) or estimated using recombinant enzymes (Lown, Ghosh, & Watkins, 1998; Paine et al., 1997; Watkins, 1997). Gertz et. al., used the Q_{Gut} model to estimate F_g using *in vitro* metabolism and permeation data of 25 medications that are CYP3A substrates (Gertz et al., 2010). Drugs with low intestine extraction were typically well predicted, however drugs with high intestinal extraction were predicted less accurately.

Another approach of IVIVE is the empirical scaling factor (G.-W. Choi et al., 2019). *In vitro* data has been utilized to predict *in vivo* clearance using scaling factors. This strategy relies heavily on correction factors. In this technique, many physiological or empirical values have been proposed. To increase the predictability of the IVIVE model, appropriate scaling factors have been established.

There have been several PK simulation models to characterize the oral PK profile and F_g from the *in vitro* drug metabolism and permeability data including the well-known advanced compartmental absorption and transit (ACAT) model (Gobeau, Stringer, De Buck, Tuntland, & Faller, 2016; Huang et al., 2009) and segmented segregated flow model (Pang, 2003). Nagar et. al. (Nagar et al., 2017) developed a continuous intestinal absorption model to capture the orally administered drugs in human. The aim of this chapter was to kinetically model human liver and intestinal metabolic conversion of MDZ and NCD. MDZ and NCD metabolic pathways in human have been illustrated previously. Further, the kinetic parameter estimation strategies have been described in details in chapter 3 using numerical methods (Paragas et al., 2021; Z. Wang et al., 2021). These kinetic parameters will be used for the IVIVE and absorption modeling in later chapters.

4.2 Materials

Midazolam (MDZ), 1’-hydroxymidazolam (1’-OH MDZ), and 4-hydroxymidazolam (4-OH MDZ) was purchased from Sigma Aldrich (St. Louis, MO). Human liver microsome (HLM) and human intestinal microsome (HIM) were purchased from Sekisui Xenotech (Kansas City, KS). NADPH regenerating system (Solution A and Solution B) was purchased from Promega (Madison, WI). Nicardipine (NCD) and dehydro-nicardipine (DHD NCD) were bought from Toronto Research Chemical (TRC, ON, Canada). Dimethylsulfoxide (DMSO) and acetonitrile (ACN) were purchased from Fisher Chemical (Fair Lawn, NJ). Formic acid (ACS Reagent) was purchased from Honeywell Fluka (Buches, Switzerland). Potassium phosphate dibasic anhydrous was purchased from VWR Life Science (Bridgeport, NJ). Potassium phosphate monobasic anhydrous was purchased from Fisher Scientific (Norristown, PA).

4.3 Methods

4.3.1 *In Vitro* Enzyme Kinetics of Midazolam (MDZ)

Buffer Preparation:

To prepare 100 mM 1000 mL phosphate buffer pH 7.4, 800 mL deionized (DI) water was taken in a suitable sterile container. Using AAT Bioquest online calculator (Bioquest) the required amount of potassium phosphate dibasic and potassium phosphate monobasic was calculated. In the DI water 12.119 g of potassium phosphate dibasic and 4.14 g potassium phosphate monobasic were dissolved. The final volume was adjusted to 1000 mL by adding DI water. Finally, the pH was adjusted to pH 7.4 by adding HCL or NaOH solution drops.

Drug Stock Preparation:

MDZ and NCD stocks were prepared using methanol. MDZ was available 1 mg/mL solution in methanol. It was dried under liquid nitrogen and reconstituted using methanol to a final concentration of 40 mM. On the other hand, NCD was available as NCD hydrochloride power. It was dissolved in methanol to attain a concentration of 30 mM.

4.3.1.1 *In Vitro* Metabolism of Midazolam (MDZ) Using HLM

4.3.1.1.1 Substrate Depletion Assay to Determine Apparent Intrinsic Clearance

An HLM concentration of 1 mg/ml was selected and MDZ concentration was 1 µM for substrate depletion assay based a previously published literature (Stringer, Strain-Damerell, Nicklin, & Houston, 2009). Each incubation was performed in triplicate in a shaking water bath at 37.5°C. The organic solvent concentration methanol was kept below 1%. Following the prewarm step for 5 minutes, reactions were initiated by the addition of NADPH solution in buffer which achieved a final concentration of 1.3mM NADP+, 3.3mM glucose 6-phosphate (G6P), 3.3mM $MgCl_2$ and 0.4 units/mL glucose 6-phosphate dehydrogenase (G6PDH). The reaction volume was 500 µL in total. At each time point, 100 µL was aliquot and the reaction was terminated using 100 µL pure ACN containing the IS up to 10 minutes. After quenching, the reaction mixture was vortexed and centrifuged. Supernatants were analyzed by LC-MS/MS, and MDZ was quantified.

To determine apparent metabolic CL_{int} following equation was used (P. R. Kulkarni et al., 2021; Naritomi et al., 2001).

$$CL_{int}^{`} = \frac{0.693}{t_{1/2}} \times \frac{1}{microsomal\ conc.(\frac{mg}{mL})} \qquad \text{Equation ---------------------4.9}$$

The $t_{1/2}$ is the *in vitro* half-life of the compound to deplete by 50% from the initial concentration.

4.3.1.1.2 Saturation Curve Assay for the Conversion of Midazolam (MDZ) to 1'-hydroxymidazolam (1'-OH MDZ) and 4-hydroxymidazolam (4-OH MDZ)

Published literature from several sources (Busse, Leandersson, Amberntsson, Darnell, & Hilgendorf, 2020; Christensen et al., 2009; Galetin & Houston, 2006; Granvil et al., 2003; Horspool, Wang, Scaringella, Taub, & Chan, 2020; Kotegawa et al., 2002; Nguyen, Kimoto, Callegari, & Obach, 2016) provided useful information to decide the protein concentration and the incubation time for the saturation curve assay to determine the kinetic parameters. For MDZ, an HLM concentration of 0.2 mg/ml was used. Incubation time was 5 minutes. The MDZ concentration ranged from 0-400 µM. Each incubation was performed in triplicate in a shaking water bath at 37°C. The organic solvent concentration was kept below 1%. After 5 minutes of prewarming, reactions were initiated as previously described by the addition of NADPH solution. Incubations were terminated using pure ACN containing the IS. After quenching, the reaction mixture was vortexed and centrifuged. Supernatants were analyzed by LC-MS/MS. Both 1'-OH and 4-OH MDZ were quantified.

4.3.1.2 *In Vitro* Metabolism of Midazolam (MDZ) Using HIM

4.3.1.2.1 Substrate Depletion Assay to Determine Apparent Intrinsic Clearance

For substrate depletion assay, an HIM concentration of 1 mg/ml was selected. MDZ concentration was 1 µM. Each incubation was performed in triplicate in a shaking water bath at 37°C. The organic solvent concentration was kept below 1%. Reactions were initiated as previously described by the addition of NADPH solution. The reaction volume was 500 µL in total. At each time point, 100 µL was aliquot and the reaction was terminated using pure ACN containing the IS up to 10 minutes. After quenching, the reaction mixture was vortexed and centrifuged. Supernatants were analyzed by LC-MS/MS and MDZ was quantified.

To determine apparent metabolic CL_{int} equation 4.9 was used (P. R. Kulkarni et al., 2021; Naritomi et al., 2001).

4.3.1.2.2 Saturation Curve Assay for the Conversion of Midazolam (MDZ) to 1’-hydroxymidazolam (1’-OH MDZ) and 4-hydroxymidazolam (4-OH MDZ)

Published literature from several sources (Busse et al., 2020; Christensen et al., 2009; Galetin & Houston, 2006; Granvil et al., 2003; Horspool et al., 2020; Kotegawa et al., 2002; Nguyen et al., 2016) provided useful information to decide the protein concentration and the incubation time for the saturation curve assay to determine the kinetic parameters. For MDZ, an HIM concentration of 0.5 mg/ml was used. Incubation time was 10 minutes. The MDZ concentration ranged from 0-100 µM. Each incubation was performed in triplicate in a shaking water bath at 37°C. The organic solvent methanol concentration was kept below 1%. Following the prewarm step for 5 minutes, reactions were started as previously described by the addition of NADPH solution.

Incubations were terminated using pure ACN containing the IS. After quenching, the reaction mixture was vortexed and centrifuged. Supernatants were analyzed by LC-MS/MS. Both 1’-OH and 4-OH MDZ were quantified.

4.3.2 *In Vitro* Enzyme Kinetics of Nicardipine (NCD)

4.3.2.1 *In Vitro* Metabolism of Nicardipine (NCD) Using HLM

4.3.2.1.1 Substrate Depletion Assay to Determine Apparent Intrinsic Clearance

For substrate depletion assay, an HLM concentration of 0.1 mg/ml was selected based on a previously published paper (Naritomi et al., 2001). NCD concentration was 1 µM. Each incubation was performed in triplicate in a shaking water bath at 37°C. The organic solvent methanol concentration was kept below 1%. After 5 minutes of prewarm, reactions were initiated as previously described by the addition of NADPH solution. The reaction volume was 500 µL in total. At each time point, 100 µL was aliquot and the reaction was terminated using pure ACN containing the IS up to 10 minutes. After quenching, the reaction mixture was vortexed and centrifuged. Supernatants were analyzed by LC-MS/MS and NCD was quantified.

To determine apparent metabolic CL_{int} equation 4.9 was used (P. R. Kulkarni et al., 2021; Naritomi et al., 2001).

4.3.2.1.2 Saturation Curve Assay for the Conversion of Nicardipine (NCD) to Dehydronicardipine (DHD NCD)

For NCD, an HLM concentration of 0.1 mg/ml was used based on preliminary experiments. Incubation time was 15 minutes. The concentration ranged from 0-50 µM. Each incubation was performed in triplicate in a shaking water bath at 37°C. The organic solvent methanol concentration was kept below 1%. After 5 minutes of prewarm, reactions were initiated as previously described by the addition of NADPH solution. Incubations were terminated using pure ACN containing the IS. After quenching, the reaction mixture was vortexed and centrifuged. Supernatants were analyzed by LC-MS/MS and DHD NCD was quantified.

4.3.2.2 *In Vitro* Metabolism of Nicardipine (NCD) Using HIM

4.3.2.2.1 Substrate Depletion Assay to Determine Apparent Intrinsic Clearance

For substrate depletion assay, an HIM concentration of 1 mg/ml was selected. NCD concentration was 1 µM. Each incubation was performed in triplicate in a shaking water bath at 37°C. The organic solvent methanol concentration was kept below 1%. Reactions were initiated as previously described by the addition of NADPH solution. The reaction volume was 500 µL in total. At each time point, 100 µL was aliquot and the reaction was terminated using pure ACN containing the IS up to 20 minutes. After quenching, the reaction mixture was vortexed and centrifuged. Supernatants were analyzed by LC-MS/MS and NCD was quantified.

To determine apparent metabolic CL_{int} equation 4.9 was used (P. R. Kulkarni et al., 2021; Naritomi et al., 2001):

4.3.2.2.2 Saturation Curve Assay for the Conversion of Nicardipine (NCD) to Dehydronicardipine (DHD NCD)

For NCD, an HIM concentration of 0.2 mg/ml was used based on preliminary experiments. Incubation time was 20 minutes. The NCD concentration ranged from 0-50 µM. Each incubation was performed in triplicate in a shaking water bath at 37°C. The organic solvent methanol concentration was kept below 1%. After 5 minutes of prewarm, reactions were initiated as previously described by the addition of NADPH solution. Incubations were terminated using pure ACN containing the IS. After quenching, the reaction mixture was vortexed and centrifuged. Supernatants were analyzed by LC-MS/MS for DHD NCD quantification.

Data Analysis:

For the data analysis, diagnostic Eadie-Hofstee plots were created and both the Michaelis-Menten model (ES model) and multiple binding site model (ESS model) were fitted to the data. Kinetic parameters were generated using the numerical method.

Modelling:

Mathematica 12.2.2 student version (Wolfram Research, Champaign, IL) was used for model fitting and plot generation. The ODEs were numerically solved with NDSolve to provide interpolated functions of each enzyme species. NonlinearModelFit function was used to parameterize the rate constants with 1/Y weighting. Specific properties, including MaxSteps → 100,000 and PrecisionGoal → infinity for NDSolve, were used. The corrected Akaike information criteria (AICc) was used to differentiate among models when comparing several models for the same dataset (Sakamoto et al., 1986; Yamaoka et al., 1978). Based on the best-fit model, kinetic parameters were reported. The model-fitted lines were also plotted with the observed data. Finally, intrinsic clearance plots were created by plotting product formation rate normalized to substrate concentration over the range of substrate concentration using equation 3.3 and 3.8 explained in the chapter three.

4.3.3 *In Vitro-In Vivo* Extrapolation of Midazolam (MDZ) and Nicardipine (NCD)

Using *in vitro* unbound intrinsic clearances ($CL_{int,unbound}$) of MDZ and NCD for both HLM and HIM, fraction escaping hepatic metabolism (F_h) and fraction escaping gut metabolism (F_g) were calculated. For F_h, both well stirred model (equation 4.1) and parallel tube model equations (G.-W. Choi et al., 2019; Sawada et al., 1985) were used. For F_g, Q_{Gut} model equation (equation 4.8) was used.

4.4 Results

4.4.1 *In Vitro* Enzyme Kinetics of Midazolam (MDZ)

4.4.1.1 *In Vitro* Metabolism of Midazolam (MDZ) Using HLM

4.4.1.1.1 Substrate Depletion Assay to Determine Apparent Intrinsic Clearance

Figure 4.4 depicts the time course of the unchanged MDZ in HLM (1 mg/mL). The unchanged drug profile starting at 1 µM showed the apparently log concentration depletion. Assuming first order depletion at this concentration an apparent *in vitro* unbound intrinsic clearance ($CL_{int,\, in\ vitro}$) was calculated to be 0.59 ±0.019 mL/mg/min.

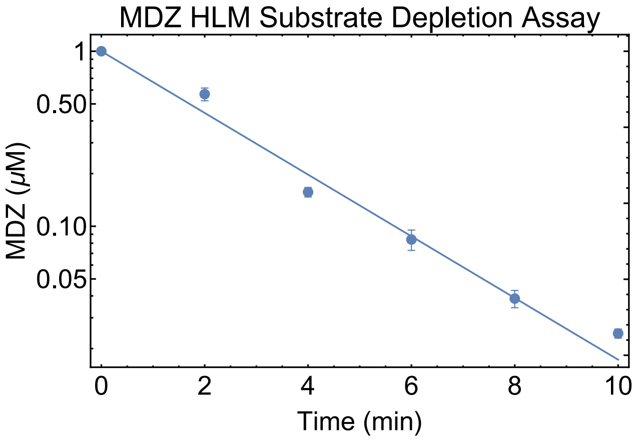

Figure 4.4: Substrate depletion assay of MDZ using HLM. Plots represents mean data ± standard errors (n=3).

4.4.1.1.2 Saturation Curve Assay for the Conversion of Midazolam (MDZ) to 1'-hydroxymidazolam (1'-OH MDZ) and 4-hydroxymidazolam (4-OH MDZ)

CYP3A4 is the prime enzyme to metabolize MDZ to 1'-OH and 4-OH MDZ (Christensen et al., 2009; Klieber et al., 2008; Paragas et al., 2021; Z. Wang et al., 2021). Also, CYP3A4 comprises more than 40% of all hepatic CYPs in HLM (Galetin et al., 2008, 2010; Galetin et al., 2007; Galetin & Houston, 2006). In this thesis both of the metabolites were quantified for the saturation curve. They were fitted individually to the ES and ESS models (Paragas et al., 2021; Z. Wang et al., 2021), and also fitted simultaneously to the ESSP1P2 model. All of the modelling efforts are described below. However, for the utilization of CL_{int}, both modelling efforts have produced similar CL_{int} since intrinsic clearance values are expressed by normalizing to the total enzyme concentration used in the incubation.

4.4.1.1.2.1 Individual Fitting: MDZ Metabolic Conversion to 1'-OH MDZ

Figure 4.5 shows the initial raw plot of 1'-OH MDZ formation vs MDZ concentration indicating substrate inhibition. Diagnostic Eadie-Hofstee plots was generated which indicated possible existence of multiple binding kinetics.

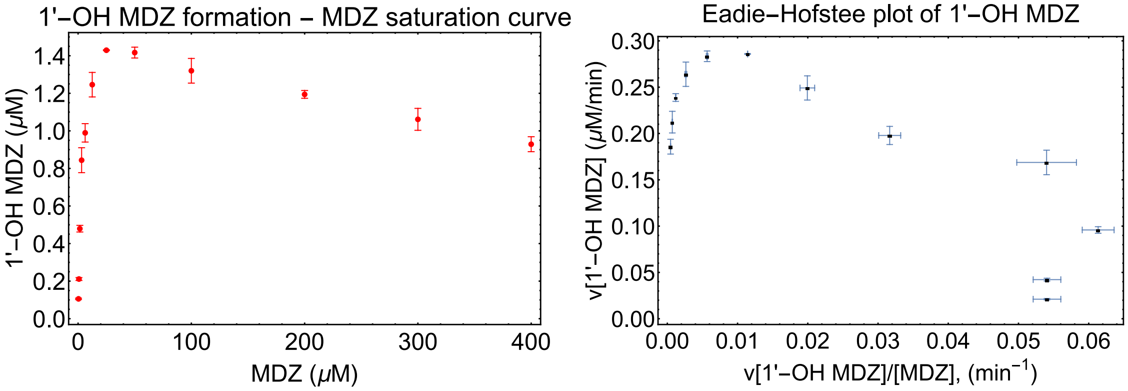

Figure 4.5. MDZ saturation curve for the incubation with HLM (Left) and diagnostic Eadie-Hofstee plot (right). Plots represents mean data ± standard errors (n=3).

Both the single binding ESP model and double binding ESSP model were fitted to the data to choose the best model which explains the observed data (figure 3.1).

For the model comparison, different statistical functions were used which are summarized in Table 4.1. Notably, from the AICc values, it was found that the ESSP model was the better fit to explain the dataset obtained from the saturation curve assay. The curve fitting with the observed data is shown in figure 4.6.

Table 4.1. Statistical functions for model comparison

	ESP model	ESSP model
AdjustedRSquared	0.97	0.99
AICc	-28.37	-88.22
MSE	0.029	0.0036

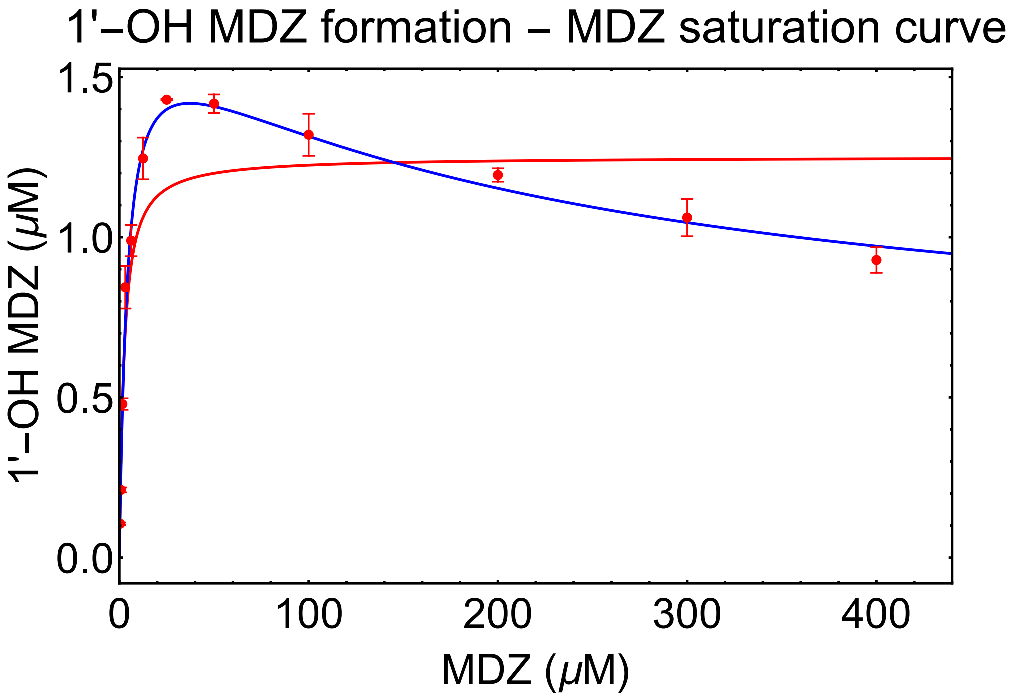

Figure 4.6. Model fitting with the oberved data for the MDZ metabolic conversion to 1’-OH MDZ by HLM. Plots represents mean data ± standard errors (n=3). Solid lines represent model predicted lines.

The kinetic parameters obtained from the model fittings are summarized in table 4.2. The CL_{int} for the formation of 1'-OH MDZ over the physiologically relevant concentration is shown in figure 4.7 which shows a slight concentration dependence.

Table 4.2. Comparison of estimates of kinetic parameters from ESP model and ESSP model. Data presented as parameter estimate ± S.E.

	ESP model	ESSP model
k_1 ($\mu M^{-1}.min^{-1}$)	270 (fixed)	270 (fixed)
k_2 (min^{-1})	575.13±89.31	985.49±21.65
K_{m1} (µM)	2.13±0.33	3.65±0.08
k_{cat1} (min^{-1})	10.02±0.41	13.61±0.26
$CL_{int1,unbound}$ ($ml.min^{-1}.mg^{-1}$ of HLM protein)	0.64±0.11	0.47±0.014
k_4 ($\mu M^{-1}.min^{-1}$)	Not applicable	270 (fixed)
k_5 (min^{-1})		57782.74±2095.24
K_{m2} (µM)		214.01±7.76
k_{cat2} (min^{-1})		4.69±0.42
$CL_{int2,unbound}$ ($ml.min^{-1}.mg^{-1}$ of HLM protein)		0.0029±0.00030

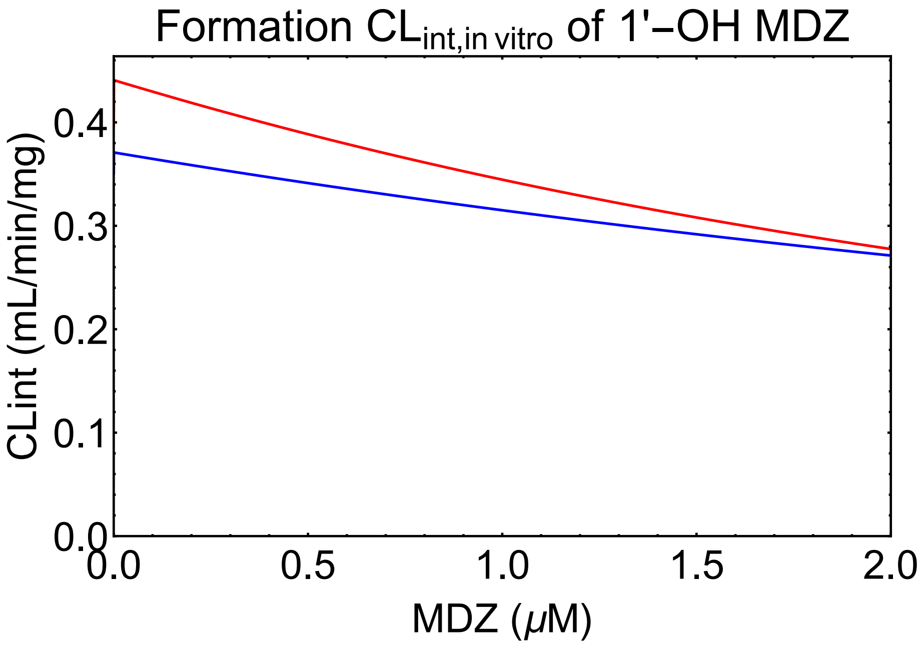

Figure 4.7: Intrinsic clearance plot over a range of physiologically relevant MDZ concentration for both metabolite formation

4.4.1.1.2.2 Individual Fitting: MDZ Metabolic Conversion to 4-OH MDZ

Figure 4.8 shows the initial raw plot of 4-OH MDZ formation vs MDZ concentration indicating substrate inhibition. Diagnostic Eadie-Hofstee plots was generated which indicated possible existence of multiple binding kinetics.

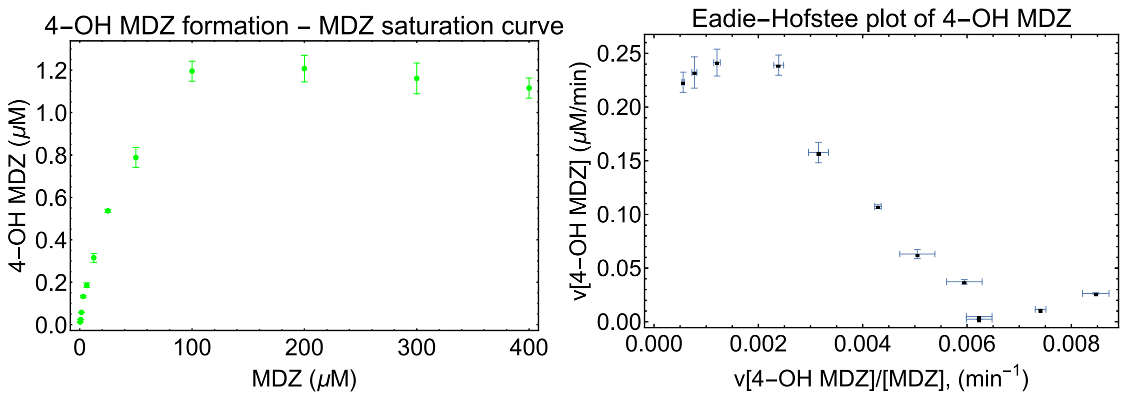

Figure 4.8. MDZ saturation curve for the incubation with HLM (Left) and diagnostic Eadie-Hofstee plot (right). Plots represents mean data ± standard errors (n=3).

Both the single binding ESP model and double binding ESSP model were fitted to the data to choose the best model which explains the observed data (figure 3.1). Different statistical functions were employed to compare the models, as shown in Table 4.3. Notably, the ESSP model was shown to be the best fit to describe the dataset collected from the saturation curve test based on the AICc values. Figure 4.9 depicts the curve fitting with the observed data.

Table 4.3. Statistical functions for model comparison

	ESP model	ESSP model
AdjustedRSquared	0.99	0.99
AICc	-122.27	-141.49
MSE	0.0062	0.0021

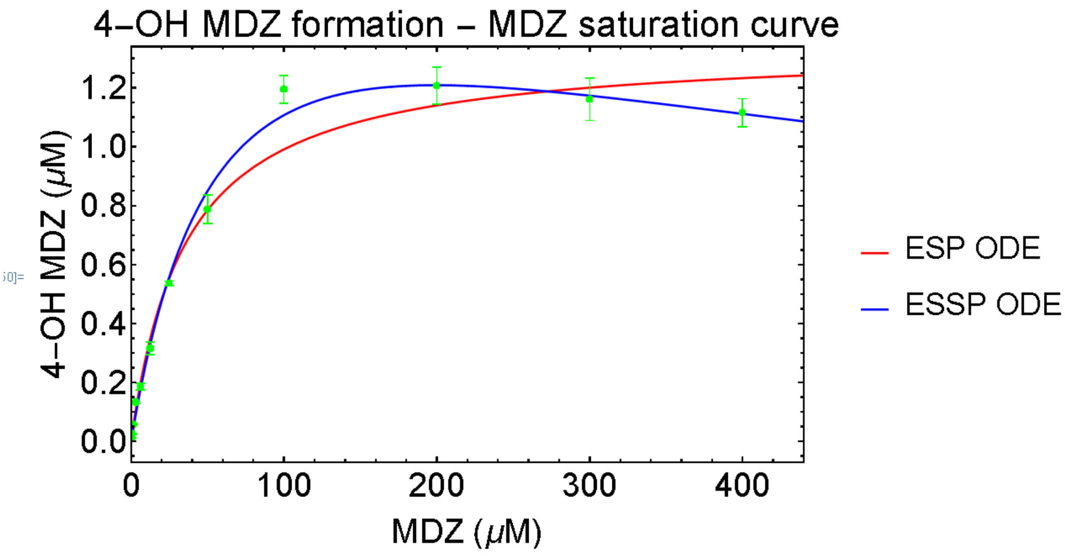

Figure 4.9. Model fitting with the oberved data for the MDZ metabolic conversion to 4-OH MDZ by HLM. Plots represents mean data ± standard errors (n=3). Solid lines represent model predicted lines.

Table 4.4 summarizes the kinetic parameters determined from model fits. Figure 4.10 depicts the CL_{int} for the production of 4-OH MDZ over physiologically relevant concentrations, revealing a modest concentration dependency.

Table 4.4. Comparison of estimates of kinetic parameters from ESP model and ESSP model. Data presented as parameter estimate ± S.E.

	ESP model	ESSP model
k_1 ($\mu M^{-1}.min^{-1}$)	270 (fixed)	270 (fixed)
k_2 (min^{-1})		
K_{m1} (μM)	35.09±2.61	61.23±3.99
k_{cat1} (min^{-1})	10.73±0.30	15.62±1.09
$CL_{int1,unbound}$ ($ml.min^{-1}.mg^{-1}$ of HLM protein)	0.042±0.0034	0.035±0.0038
k_4 ($\mu M^{-1}.min^{-1}$)	Not applicable	270 (fixed)
k_5 (min^{-1})		
K_{m2} (μM)		497.13±49.01
k_{cat2} (min^{-1})		2.21±1.09
$CL_{int2,unbound}$ ($ml.min^{-1}.mg^{-1}$ of HLM protein)		0.00061±0.00029

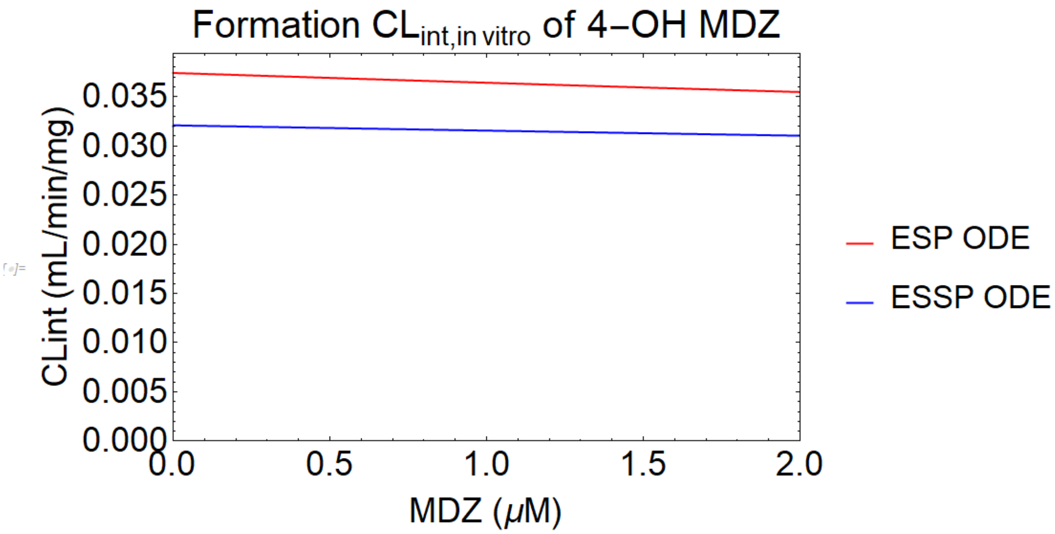

Figure 4.10: Intrinsic clearance plot over a range of physiologically relevant MDZ concentration for both metabolite formation

4.4.1.1.2.3 Simultaneous Fitting: MDZ Metabolic Conversion to 1’-OH and 4-OH MDZ

Since both 1’-OH and 4-OH MDZ are producing from the same incubation mixture, kinetically it was more logical to model both the metabolites to the same model. Previous it has been shown that Eadie-Hofstee plots (figure 4.5 and figure 4.8) indicated existence of multiple binding. Metabolite formation ratio was also created which showed a concentration dependence which is also indicating multiple binding (figure 4.11).

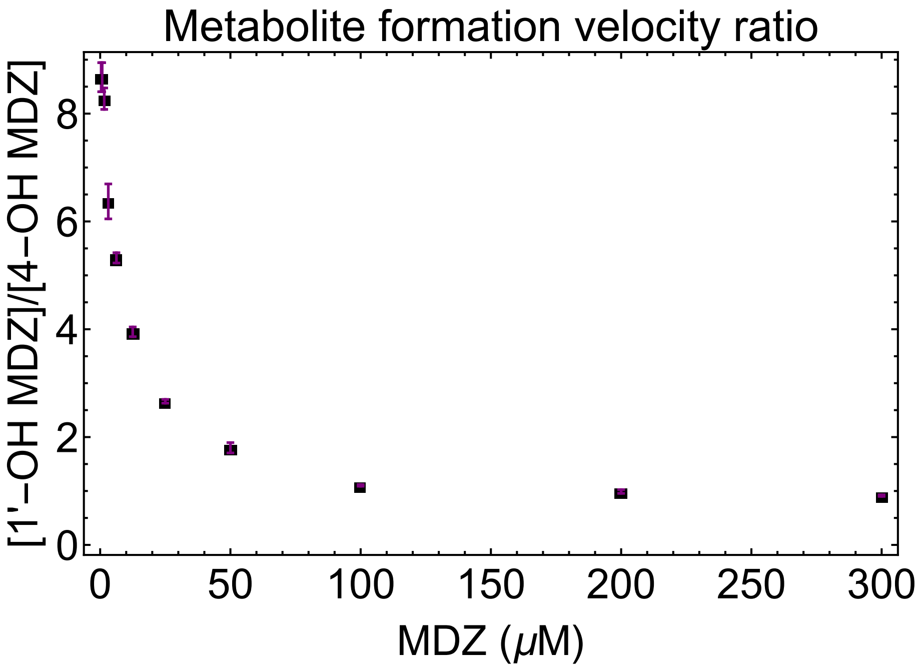

Figure 4.11. Metabolite formation ratio plot for the incubation of MDZ with HLM. Plots represents mean data ± standard errors (n=3).

Double binding ESSP1P2 model (Figure 3.7B) was fitted to the data and fitted model was plotted with the observed data.

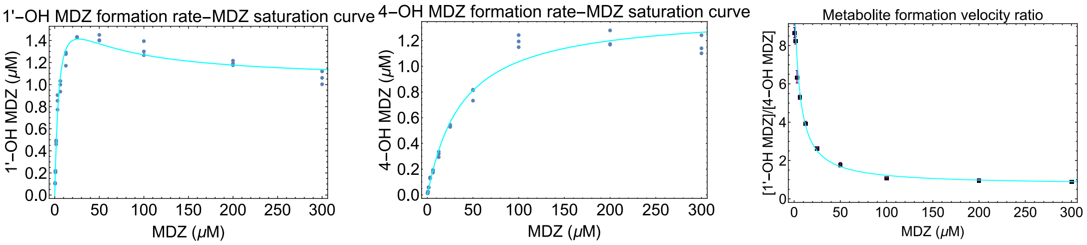

Figure 4.12. ESSP1P2 model fitting with the oberved data for the MDZ incubation with HLM (Left: Saturation curve for MDZ→1'-OH MDZ, middle: Saturation curve for MDZ→4-OH MDZ, and right: Metabolite formation ratio plot). Plots represents mean data ± standard errors (n=3). Solid lines represent model predicted lines.

Table 4.5 summarizes the kinetic parameters determined from model fits. These parameters will be used to predict absorption in later chapters. Figure 4.13 depicts the CL_{int} for the production of two metabolites throughout a physiologically relevant concentration range, revealing a modest concentration dependency. This may imply using an ODE for IVIVC rather than a single CL_{int} value.

Table 4.5. Kinetic parameters from ESSP1P2 model. Data presented as parameter estimate ± S.E.

	ESSP1P2 model	
	1'-OH MDZ	4-OH MDZ
k_1 ($\mu M^{-1}.min^{-1}$)	270 (fixed)	
k_2 (min^{-1})	1131.36±133.28	
K_{m1} (μM)	4.32±0.54	
k_{cat1} (min^{-1})	15.02±0.71	1.39±0.49
$CL_{int1,unbound}$ ($ml.min^{-1}.mg^{-1}$ of HLM protein)	0.48±0.059	0.045±0.017
k_5 ($\mu M^{-1}.min^{-1}$)	270 (fixed)	
k_6 (min^{-1})	11283.81±2256.52	
K_{m2} (μM)	42.05±8.06	
k_{cat2} (min^{-1})	8.27±0.35	11.36±0.43
$CL_{int2,unbound}$ ($ml.min^{-1}.mg^{-1}$ of HLM protein)	0.027±0.0059	0.037±0.0077

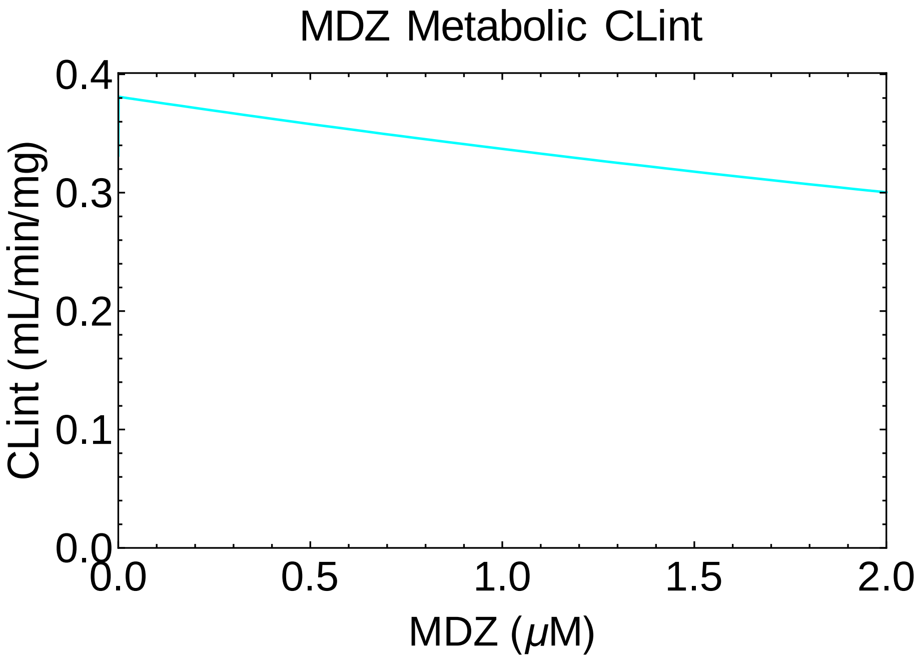

Figure 4.13: Intrinsic clearance plot over a range of physiologically relevant MDZ concentration for both metabolite formation by ESSP1P2 model

4.4.1.2 *In Vitro* Metabolism of Midazolam (MDZ) Using HIM

4.4.1.2.1 Substrate Depletion Assay to Determine Apparent Intrinsic Clearance

Figure 4.14 depicts the time course of the unchanged MDZ in HIM (1 mg/mL). The unchanged drug profile starting at 1 µM showed the apparently log concentration depletion. Assuming first order depletion at this concentration an apparent *in vitro* unbound intrinsic clearance ($CL_{int,\ in\ vitro}$) was calculated to be 0.52±0.011 mL/mg/min.

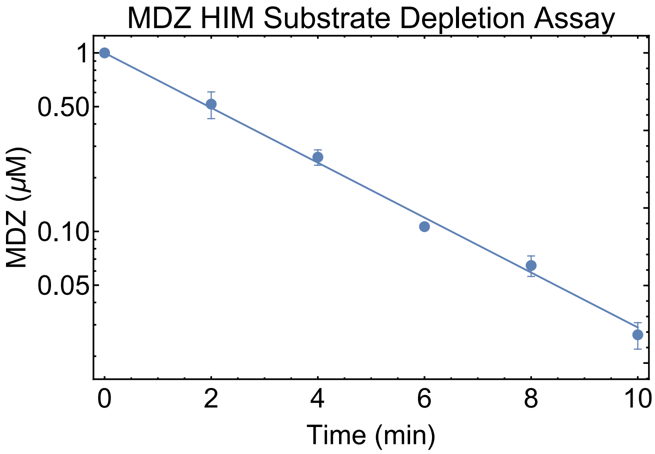

Figure 4.14: Substrate depletion assay of MDZ using HIM. Plots represents mean data ± standard errors (n=3). Solid lines represent model predicted lines.

4.4.1.2.2 Saturation Curve Assay for the Conversion of Midazolam (MDZ) to 1'-hydroxymidazolam (1'-OH MDZ) and 4-hydroxymidazolam (4-OH MDZ)

CYP3A4 comprises almost 80% of all intestinal CYPs in HIM (Galetin et al., 2008, 2010; Galetin et al., 2007; Galetin & Houston, 2006). Both metabolites were measured for the saturation curve in this thesis. They were also fitted to the ES and ESS models separately (Paragas et al., 2021; Z. Wang et al., 2021), as well as the ESSP1P2 model concurrently. The following sections detail all of the modeling attempts.

4.4.1.2.2.1 Individual Fitting: MDZ Metabolic Conversion to 1'-OH MDZ

Figure 4.15 shows the initial raw plot of 1'-OH MDZ formation vs MDZ concentration indicating substrate inhibition. Diagnostic Eadie-Hofstee plots was generated which indicated possible existence of multiple binding kinetics.

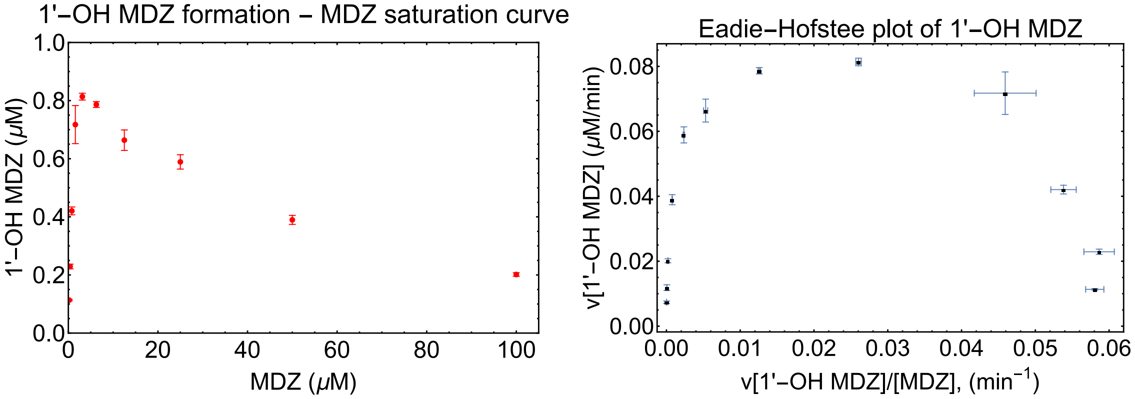

Figure 4.15. MDZ saturation curve for the incubation with HIM (Left) and diagnostic Eadie-Hofstee plot (right). Plots represents mean data ± standard errors (n=3).

Both the single binding ESP model and double binding ESSP model were fitted to the data to choose the best model which explains the observed data (figure 3.1). Several statistical functions were employed to compare the models, which are listed in Table 4.6. The ESSP model was judged to be the best fit to explain the dataset received from the saturation curve test based on the AICc values. Figure 4.16 depicts a curve fitting with observed data.

Table 4.6. Statistical functions for model comparison

	ESP model	ESSP model
AdjustedRSquared	0.53	0.99
AICc	8.40	-140.96
MSE	0.10	0.0015

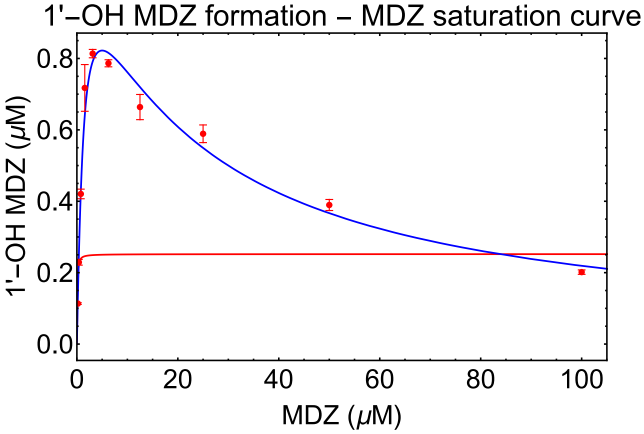

Figure 4.16. Model fitting with the oberved data for the MDZ metabolic conversion to 1'-OH MDZ by HIM. Plots represents mean data ± standard errors (n=3). Solid lines represent model predicted lines.

The kinetic parameters obtained from the model fittings are summarized in table 4.7. The CL_{int} for the formation of 1'-OH MDZ over the physiologically relevant concentration is shown in figure 4.17 which shows a slight concentration dependence.

Table 4.7. Comparison of estimates of kinetic parameters from ESP model and ESSP model. Data presented as parameter estimate ± S.E.

	ESP model	ESSP model
k_1 ($\mu M^{-1}.min^{-1}$)	270 (fixed)	270 (fixed)
k_2 (min^{-1})	8.11±24.29	234.89±16.19
K_{m1} (μM)	0.03±0.09	0.87±0.06
k_{cat1} (min^{-1})	1.011±0.17	4.54±0.08
$CL_{int1,unbound}$ ($ml.min^{-1}.mg^{-1}$ of HIM protein)	2.011±5.12	0.324±0.030

k_4 (µM^{-1}.min^{-1})	Not applicable	270 (fixed)
k_5 (min^{-1})		6447.65±105.36
K_{m2} (µM)		23.88±0.39
k_{cat2} (min^{-1})		0 (fixed)
$CL_{int2,unbound}$ (ml.min^{-1}.mg^{-1} of HIM protein)		0 (fixed)

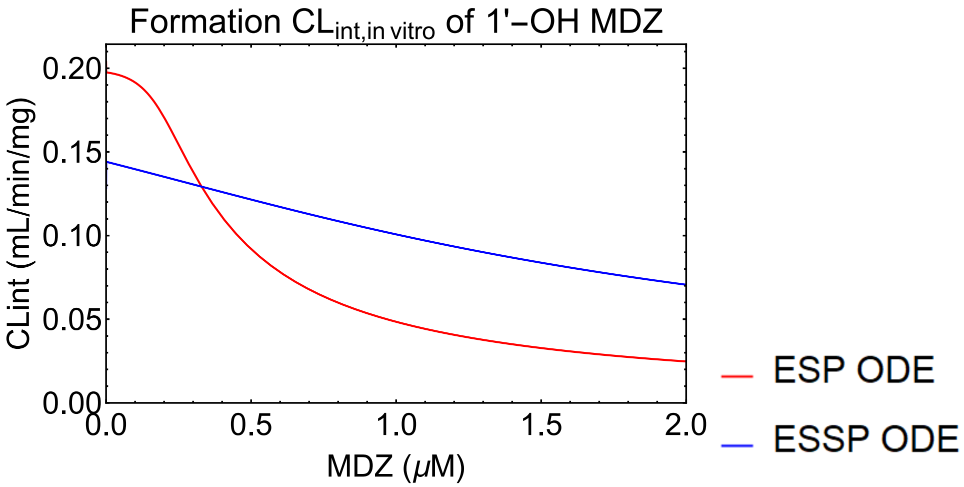

Figure 4.17: Intrinsic clearance plot over a range of physiologically relevant MDZ concentration for both metabolite formation

4.4.1.1.2.2 Individual Fitting: MDZ Metabolic Conversion to 4-OH MDZ

Figure 4.18 shows the initial raw plot of 4-OH MDZ formation vs MDZ concentration indicating substrate inhibition. Diagnostic Eadie-Hofstee plots was generated which indicated possible existence of multiple binding kinetics.

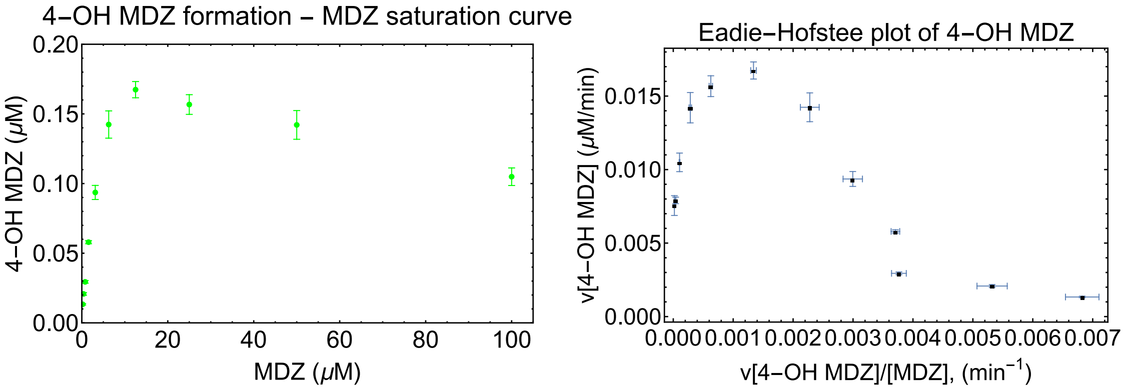

Figure 4.18. MDZ saturation curve for the incubation with HIM (Left) and diagnostic Eadie-Hofstee plot (right). Plots represents mean data ± standard errors (n=3).

Both the single binding ESP model and double binding ESSP model were fitted to the data to choose the best model which explains the observed data (figure 3.1). For the model comparison, different statistical functions were used which are summarized in Table 4.8. Notably, from the AICc values, it was found that the ESSP model was the better fit to explain the dataset obtained from the saturation curve assay. The curve fitting with the observed data is shown in figure 4.19.

Table 4.8. Statistical functions for model comparison

	ESP model	ESSP model
AdjustedRSquared	0.89	0.99
AICc	-156.31	-255.25
MSE	0.0011	0.000038

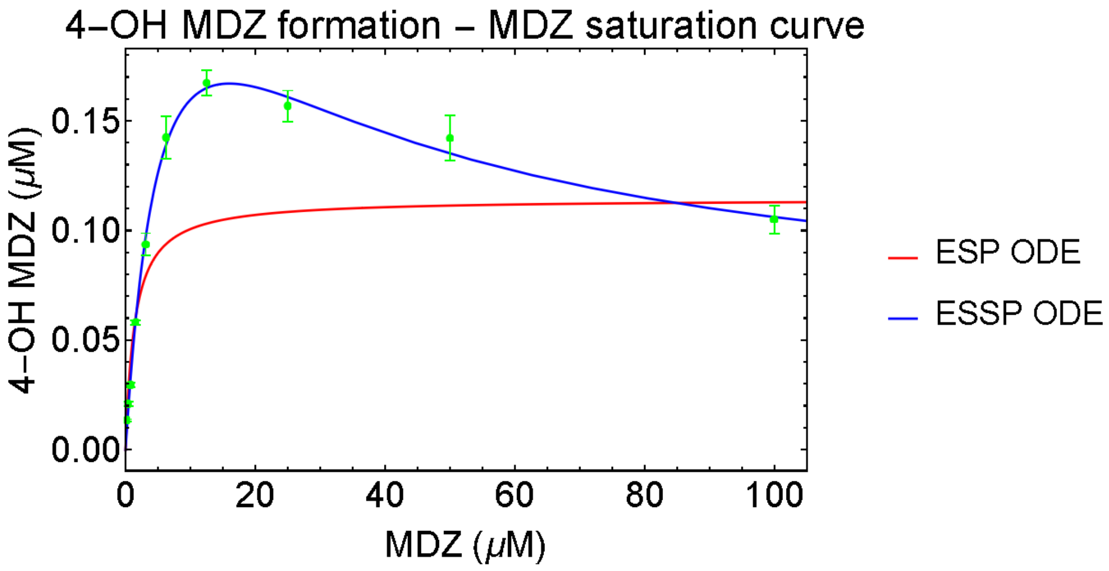

Figure 4.19. Model fitting with the oberved data for the MDZ metabolic conversion to 4-OH MDZ by HIM. Plots represents mean data ± standard errors (n=3). Solid lines represent model predicted lines.

The kinetic parameters obtained from the model fittings are summarized in table 4.9. The CL_{int} for the formation of 4-OH MDZ over the physiologically relevant concentration is shown in figure 4.20 which shows a slight concentration dependence.

Table 4.9. Comparison of estimates of kinetic parameters from ESP model and ESSP model. Data presented as parameter estimate ± S.E.

	ESP model	ESSP model
k_1 ($\mu M^{-1}.min^{-1}$)	270 (fixed)	270 (fixed)
k_2 (min^{-1})	367.22±97.26	1633.49±18.79
K_{m1} (μM)	1.36±0.34	6.05±0.077
k_{cat1} (min^{-1})	0.46±0.031	1.18±0.10
$CL_{int1,unbound}$ ($ml.min^{-1}.mg^{-1}$ of HIM protein)	0.021±0.006	0.012±0.0020
k_4 ($\mu M^{-1}.min^{-1}$)	Not applicable	270 (fixed)
k_5 (min^{-1})		7573.43±1938.67
K_{m2} (μM)		28.05±7.18
k_{cat2} (min^{-1})		0.22±0.020
$CL_{int2,unbound}$ ($ml.min^{-1}.mg^{-1}$ of HIM protein)		0.000050±0.000013

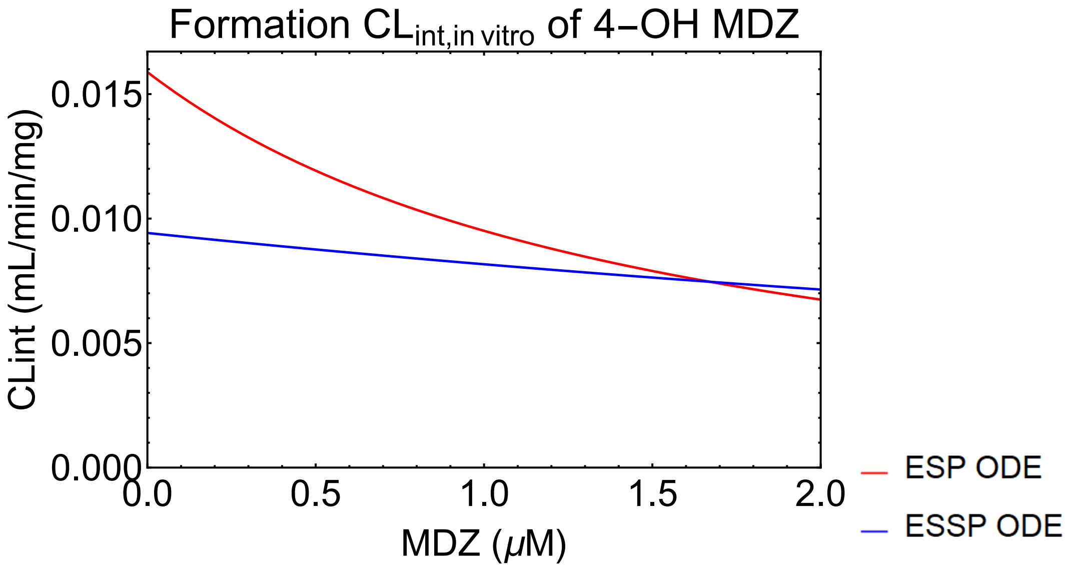

Figure 4.20: Intrinsic clearance plot over a range of physiologically relevant MDZ concentration for both metabolite formation

4.4.1.1.2.3 Simultaneous Fitting: MDZ Metabolic Conversion to 1’-OH and 4-OH MDZ

Because both 1'-OH and 4-OH MDZ are produced from the same incubation mixture, it was more logical to use the same kinetic model for both metabolites. Eadie-Hofstee plots (figure 4.15 and figure 4.18) had previously been shown to reveal the presence of multiple binding. A metabolite formation ratio was also calculated, which revealed a concentration dependence, implying multiple binding (figure 4.21).

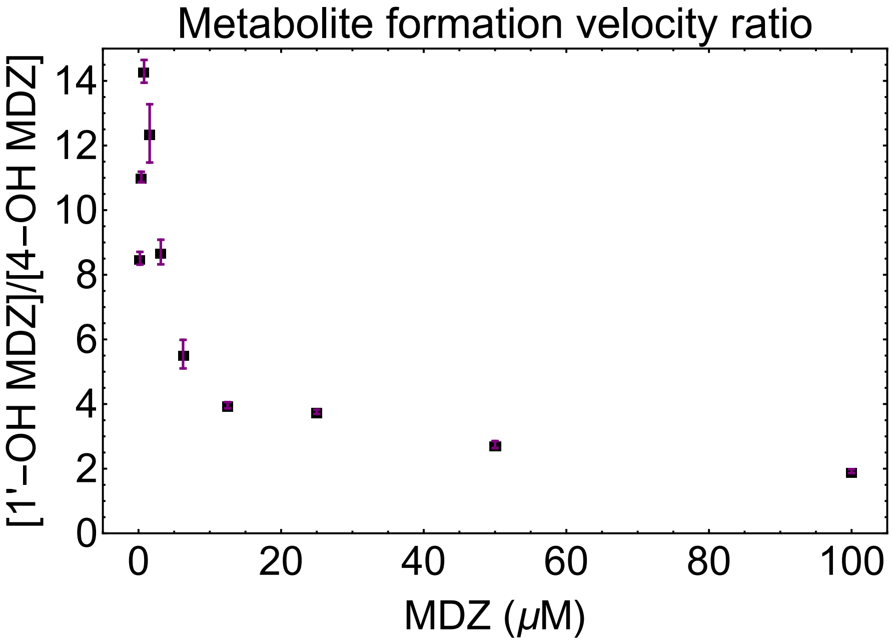

Figure 4.21 Metabolite formation ratio plot for the incubation of MDZ with HIM. Plots represents mean data ± standard errors (n=3).

The data was fitted with a double binding ESSP1P2 model (Figure 3.7B), and the fitted model was shown alongside the observed data.

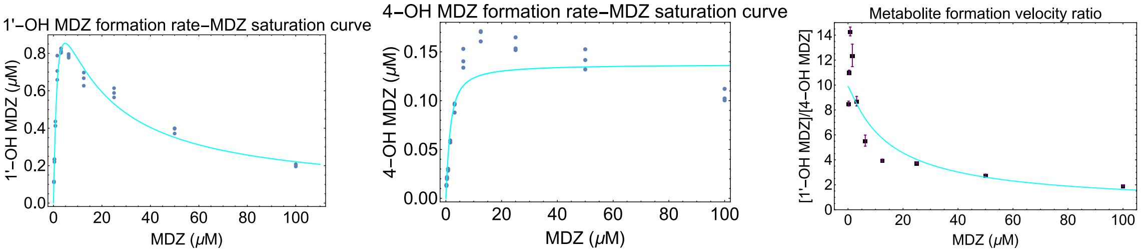

Figure 4.22. ESSP1P2 model fitting with the observed data for the MDZ incubation with HIM

(Left: Saturation curve for MDZ→1’-OH MDZ, middle: Saturation curve for MDZ→4-OH MDZ, and right: Metabolite formation ratio plot). Plots represents mean data ± standard errors (n=3). Solid lines represent model predicted lines.

Table 4.10 summarizes the kinetic parameters acquired from model fittings. These parameters will be used to model drug absorption in later chapters. Figure 4.23 depicts the CL_{int} for the production of two metabolites at physiologically relevant concentrations, revealing a modest concentration dependence. This may imply using an ODE for IVIVC rather than a single CL_{int} value.

Table 4.10. Kinetic parameters from ESSP1P2 model. Data presented as parameter estimate ± S.E.

	ESSP1P2 model	
	1’-OH MDZ	4-OH MDZ
k_1 ($\mu M^{-1}.min^{-1}$)	270 (fixed)	
k_2 (min^{-1})	280.81±10.62	
K_{m1} (µM)	1.06±0.037	
k_{cat1} (min^{-1})	5.10±0.79	0.52±0.04
$CL_{int1,unbound}$ ($ml.min^{-1}.mg^{-1}$ of HLM protein)	0.30±0.021	0.030±0.0029
k_5 ($\mu M^{-1}.min^{-1}$)	270 (fixed)	
k_6 (min^{-1})	4449.09±476.10	
K_{m2} (µM)	16.48±1.76	
k_{cat2} (min^{-1})	0.19±0.13	0.55±0.043
$CL_{int2,unbound}$ ($ml.min^{-1}.mg^{-1}$ of HLM protein)	0.00069±0.00052	0.00206±0.00029

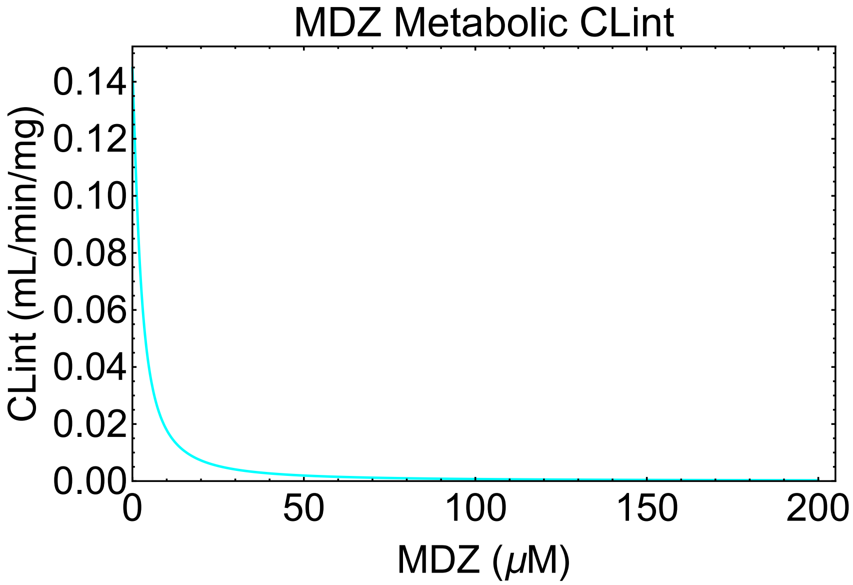

Figure 4.23: Intrinsic clearance plot over a range of physiologically relevant MDZ concentration for both metabolite formation by ESSP1P2 model

4.4.2 *In Vitro* Enzyme Kinetics of Nicardipine (NCD)

4.4.2.1 *In Vitro* Metabolism of Nicardipine (NCD) Using HLM

4.4.2.1.1 Substrate Depletion Assay to Determine Apparent Intrinsic Clearance

Figure 4.24 depicts the time course of the unchanged NCD in HLM (0.1 mg/mL). The unchanged drug profile starting at 1000 nM showed the apparently log concentration depletion. Assuming first order depletion at this concentration an apparent *in vitro* intrinsic clearance ($CL_{int,\ in\ vitro,unbound}$) was calculated to be 6.20 ±0.46 mL/mg/min.

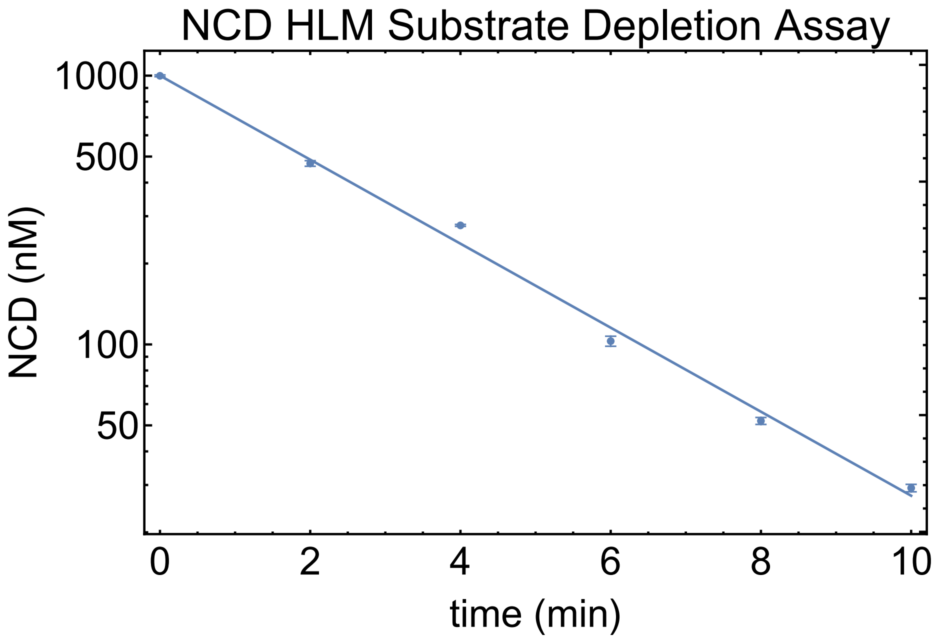

Figure 4.24: Substrate depletion assay of NCD using HLM. Plots represents mean data ± standard errors (n=3). Solid lines represent model predicted lines.

4.4.2.1.2 Saturation Curve Assay for the Conversion of Nicardipine (NCD) to Dehydronicardipine (DHD NCD)

For the saturation curve with HLM, the NCD concentration range was 0-50 µM (Figure 4.25). Only DHD NCD was quantified, and different models were fitted to the data. Figure 4.25 shows the mean raw plot of the NCD saturation curve with RLM. Diagnostic Eadie-Hofstee plots was generated which indicated possible existence of multiple binding kinetics.

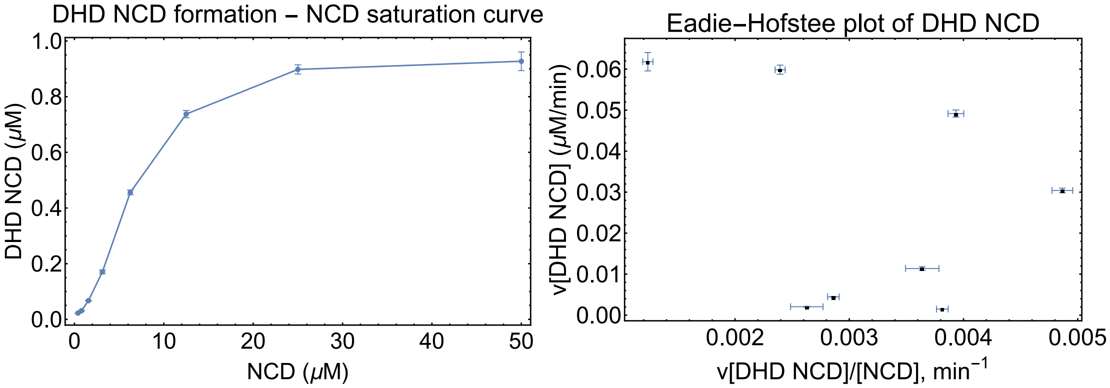

Figure 4.25. NCD saturation curve for the incubation with HLM (Left) and diagnostic Eadie-Hofstee plot (right). Plots represents mean data ± standard errors (n=3).

Both the single binding ESP model and double binding ESSP model were fitted to the data to choose the best model which explains the observed data (figure 3.19). For the model comparison, different statistical functions were used which are summarized in Table 4.11. Notably, from the AICc values, it was found that the ESSP model was the better fit to explain the dataset obtained from the saturation curve assay. The curve fitting with the observed data is shown in figure 4.26.

Table 4.11. Statistical functions for model comparison

	ESP model	ESSP model
AdjustedRSquared	0.95	0.99
AICc	-61.28	-116.36
MSE	0.0082	0.00033

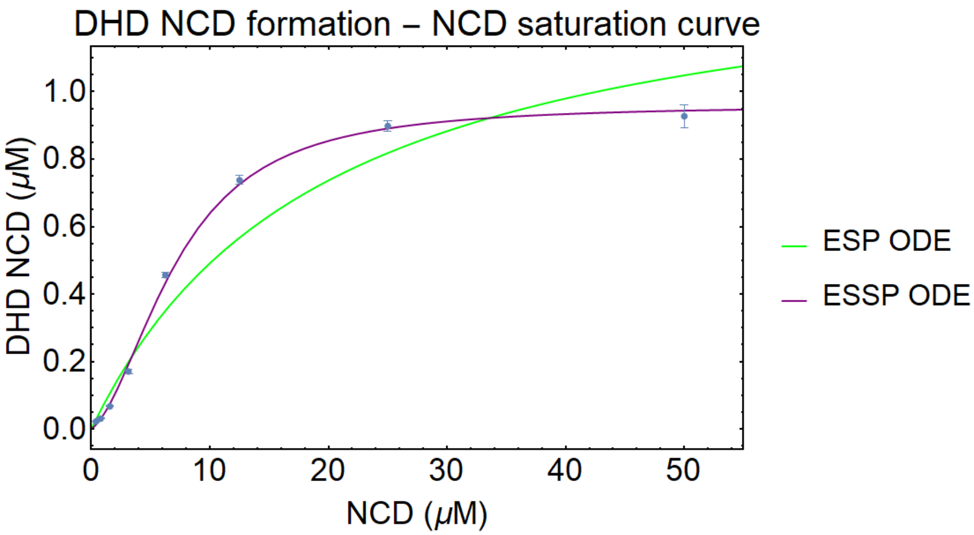

Figure 4.26. Model fitting with the oberved data for the NCD incubation with HLM. Plots represents mean data ± standard errors (n=3). Solid lines represent model predicted lines.

The kinetic parameters obtained from the model fittings are summarized in table 4.12. These parameters will be used in later chapters for absorption modeling. The CL_{int} for the formation of DHD NCD over the physiologically relevant concentration are shown in figure 4.27 which shows a moderate concentration dependence. This might necessitate the use of an ODE rather than a single CL_{int} value for IVIVC.

Table 4.12. Comparison of estimates of kinetic parameters from ESP model and ESSP model. Data presented as parameter estimate ± S.E.

	ESP model	ESSP model
k_1 ($\mu M^{-1}.min^{-1}$)	270 (fixed)	270 (fixed)
k_2 (min^{-1})	5134.61±989.42	12318.15±1895.66
K_{m1} (μM)	19.05±4.16	46.51±7.18
k_{cat1} (min^{-1})	3.91±0.42	3.32±0.28
$CL_{int1,unbound}$ ($ml.min^{-1}.mg^{-1}$ of HLM protein)	0.087±0.021	0.031±0.0059
k_4 ($\mu M^{-1}.min^{-1}$)	Not applicable	270 (fixed)
k_5 (min^{-1})		339.69±89.63
K_{m2} (μM)		1.27±0.33
k_{cat2} (min^{-1})		2.56±0.049
$CL_{int2,unbound}$ ($ml.min^{-1}.mg^{-1}$ of HLM protein)		0.87±0.24

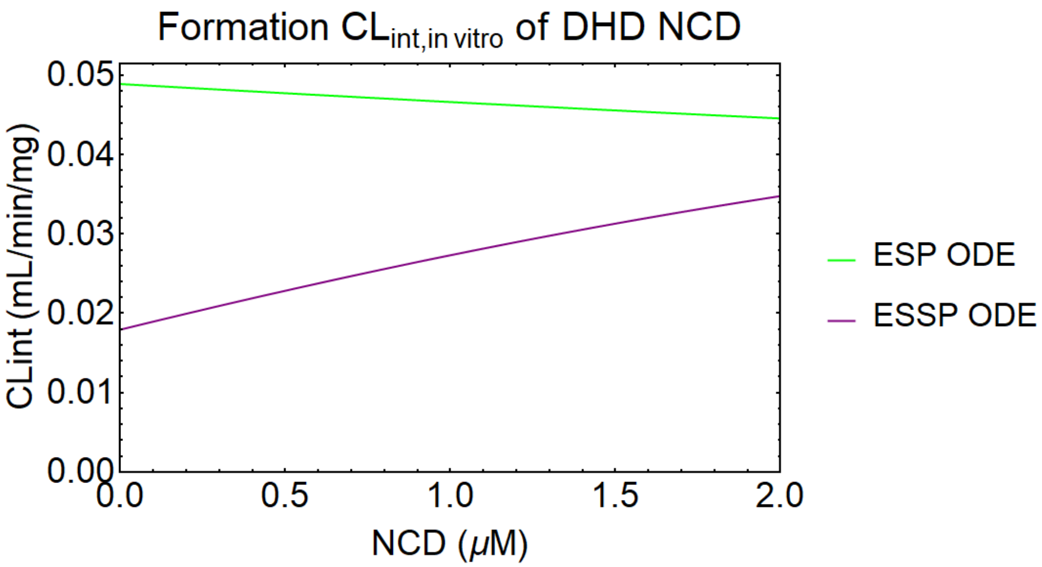

Figure 4.27: Intrinsic clearance plot over a range of physiologically relevant NCD concentration for DHD NCD formation

4.4.2.2 *In vitro* metabolism of nicardipine (NCD) using HIM

4.4.2.2.1 Substrate depletion assay to determine apparent intrinsic clearance

Figure 4.28 depicts the time course of the unchanged NCD in HIM (1 mg/mL). The unchanged drug profile starting at 1000 nM showed the apparently log concentration depletion. Assuming first order depletion at this concentration an apparent *in vitro* intrinsic clearance (CL_{int}, *in vitro*) was calculated to be 1.016 ±0.18 mL/mg/min.

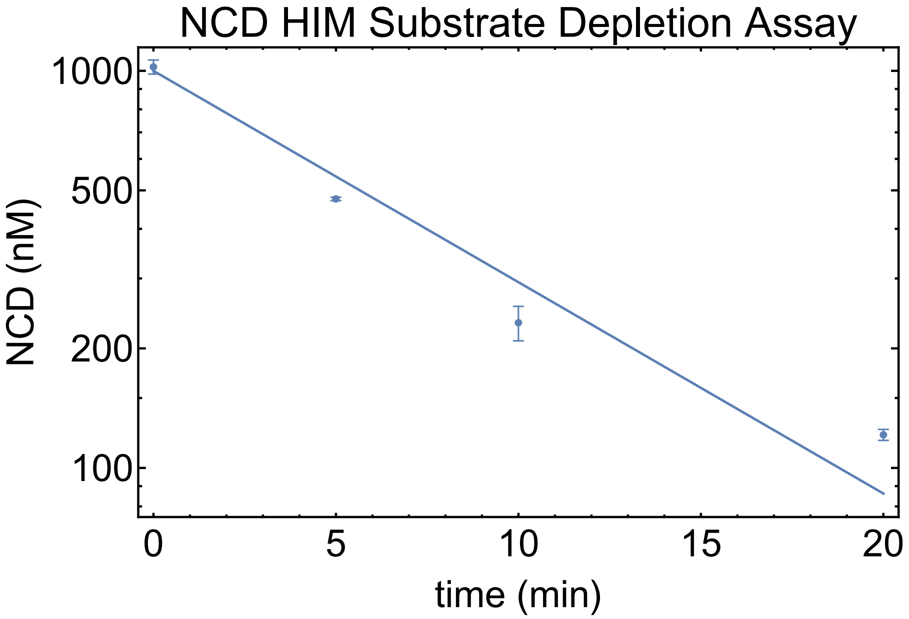

Figure 4.28: Substrate depletion assay of NCD using HIM. Plots represents mean data ± standard errors (n=3). Solid lines represent model predicted lines.

4.4.2.2.2 Saturation Curve Assay for the Conversion of Nicardipine (NCD) to Dehydronicardipine (DHD NCD)

For the saturation curve with HIM, the NCD concentration range was 0-50 µM (Figure 4.29). Commercially only DHD NCD was available. Therefore, only this metabolite was quantified, and different models were fitted to the data. Figure 4.29 shows the mean raw plot of the NCD saturation curve with RLM. Diagnostic Eadie-Hofstee plots was generated which indicated possible existence of multiple binding kinetics.

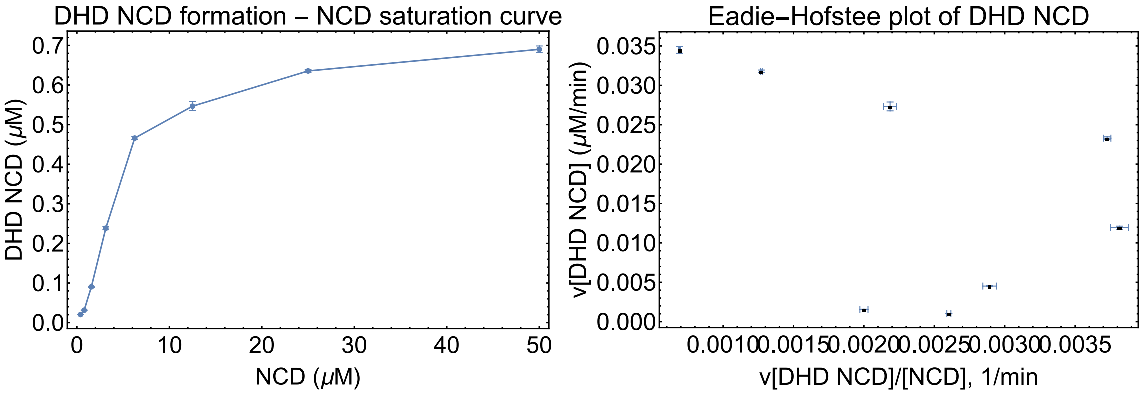

Figure 4.29. NCD saturation curve for the incubation with HIM (Left) and diagnostic Eadie-Hofstee plot (right). Plots represents mean data ± standard errors (n=3).

Both the single binding ESP model and double binding ESSP model were fitted to the data to choose the best model which explains the observed data (Figure 3.1). Different statistical functions were employed to compare the models, which are presented in Table 4.13. Notably, the ESSP model was shown to be the best fit to describe the dataset collected from the saturation curve test based on the AICc values. Figure 4.30 depicts the curve fitting with the observed data.

Table 4.13. Statistical functions for model comparison

	ESP model	ESSP model
AdjustedRSquared	0.96	0.99
AICc	-71.43	-118.20
MSE	0.0034	0.00056

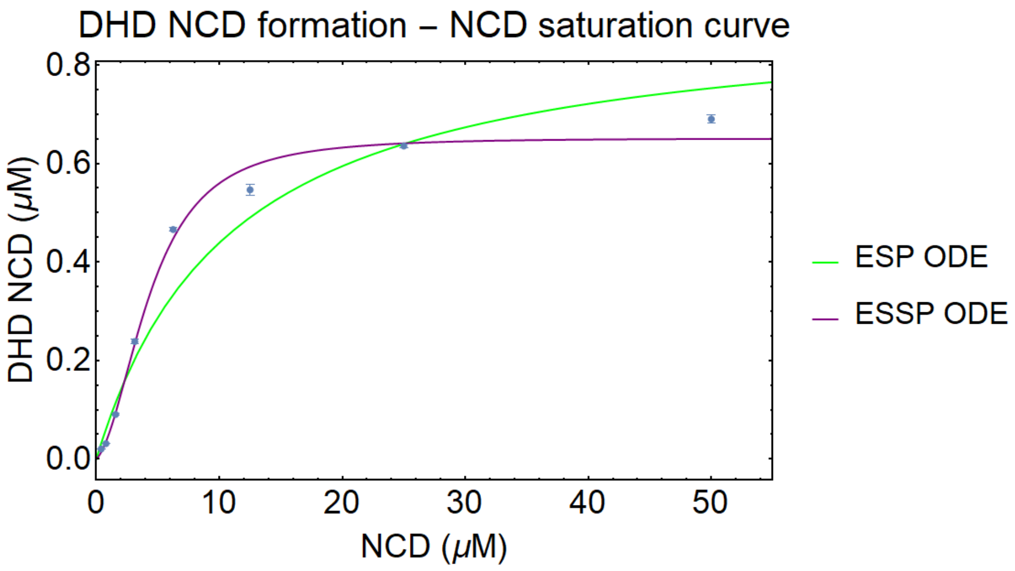

Figure 4.30. Model fitting with the oberved data for the NCD incubation with HIM. Plots represents mean data ± standard errors (n=3). Solid lines represent model predicted lines.

The kinetic parameters obtained from the model fittings are summarized in table 4.14. These parameters will be used in later chapters for absorption modeling. The CL_{int} for the formation of DHD NCD over the relevant concentration are shown in figure 4.31 which shows a moderate concentration dependence. This might necessitate the use of an ODE rather than a single CL_{int} value for IVIVC.

Table 4.14. Comparison of estimates of kinetic parameters from ESP model and ESSP model. Data presented as parameter estimate ± S.E.

	ESP model	ESSP model
k_1 ($\mu M^{-1}.min^{-1}$)	270 (fixed)	270 (fixed)
k_2 (min^{-1})	2884.46±465.41	29628.52±3973.55
K_{m1} (μM)	10.51±1.71	110.08±15.02
k_{cat1} (min^{-1})	1.83±0.14	5.51±0.72
$CL_{int1,unbound}$ ($ml.min^{-1}.mg^{-1}$ of HIM protein)	0.053±0.011	0.015±0.0034
k_4 ($\mu M^{-1}.min^{-1}$)	Not applicable	270 (fixed)
k_5 (min^{-1})		53.31±15.57
K_{m2} (μM)		0.20±0.059
k_{cat2} (min^{-1})		1.29±0.029
$CL_{int2,unbound}$ ($ml.min^{-1}.mg^{-1}$ of HIM protein)		2.011±0.59

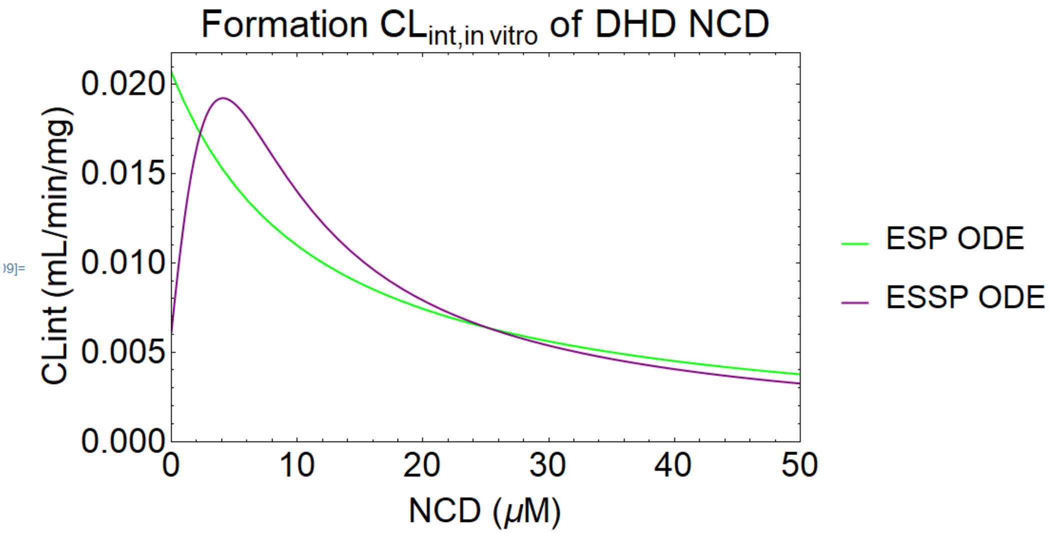

Figure 4.31: Intrinsic clearance plot over a range of physiologically relevant NCD concentration for DHD NCD formation

4.4.3 *In Vitro-In Vivo* Extrapolation of Midazolam (MDZ) and Nicardipine (NCD)

Table 4.15 represents the predicted F_h and F_g calculated from the IVIVE.

Table 4.15: Predicted F_h and F_g obtained from the IVIVE

	MDZ		NCD	
F_h	WS Model	PT Model	WS Model	PT Model
	0.55±0.0082	0.44±0.012	0.33±0.010	0.13±0.012
F_g	Q_{Gut} Model		Q_{Gut} Model	
	0.47±0.016		0.11±0.0058	

WS→Well stirred, PT→Parallel tube.

4.5 Discussion and Conclusions

Because CYP enzyme expression differs between the human liver and the human gut (Galetin et al., 2010; Galetin & Houston, 2006; Gertz et al., 2010; Vieira et al., 2014), the kinetic parameters derived from metabolic experiments utilizing liver and intestinal microsomes may differ. The goal of this chapter was to evaluate the kinetics of MDZ and NCD metabolic conversion utilizing HLM and HIM.

Monitoring product formation rates at varied substrate concentrations has traditionally been used to describe an enzyme's kinetic behavior (Nath & Atkins, 2006; Obach & Reed-Hagen, 2002). However, when practical concerns make product production impossible or unfeasible (initial phases of drug discovery when all the metabolites are not identified), the kinetic parameters of an enzyme process can be determined by measuring substrate depletion as a function of time. This is why the use of substrate depletion to study cytochrome P450 kinetics has become more common at early phases. Nath et. al., (Nath & Atkins, 2006) demonstrated that this connection can be deduced from the Michaelis-Menten equation, and that the kinetic parameters acquired using the substrate depletion method are equal and comparable to those obtained using the classic product formation method. The kinetic parameters of a simulated data set were similar regardless of whether technique was utilized, validating the theoretical outcome. However, their simulated dataset was developed assuming Michaelis-Menten kinetics and simple one product formation was assumed. The kinetic situation might be very different if there is multiple product formation from either one or more enzymes. Moreover, if the enzyme substrate interaction follows atypical kinetics, the substrate depletion might follow a different pattern from the usual first-order depletion assumption, especially in sigmoidal kinetics ($K_{m1}>K_{m2}$). Further, if the substrate concentration used in the substrate depletion assay is not low enough compared to the binding constant K_m, the logarithmic depletion of the substrate might not be linear enough to calculate the apparent intrinsic clearance.

The primary enzyme responsible for converting MDZ to 1'-OH and 4-OH MDZ is CYP3A4. Furthermore, CYP3A4 accounts for more than 40% of all hepatic CYPs in HLM and almost 80% of all intestinal CYPs (Galetin et al., 2008, 2010; Galetin, Hinton, Burt, Obach, & Houston, 2007; Galetin & Houston, 2006). Both metabolites (1'-OH and 4-OH MDZ) were measured for the saturation curve in this thesis. They were fitted to the ES and ESS models separately (Paragas et al., 2021; Z. Wang et al., 2021), as well as the ESSP1P2 model concurrently. Initially, both metabolite data was diagnosed based on the Eadie-Hofstee plots (figures 4.5 and 4.8 for HLM, figures 4.15 and 4.18) and metabolite formation ratio plot (figure 4.11 for HLM, figure 4.21 for HIM). If the substrate enzyme interaction follows single binding kinetics (ESP model or ESP1P2 model), the Eadie-Hofstee plots will be linear, and the metabolite formation ratio plot will be constant over the substrate concentration range. From all of those diagnostic plots, it was clear that the MDZ interaction with HLM or HIM enzymes does not follow single binding kinetics. Therefore, ESSP1P2 model was fitted to the data. Also, since both the metabolites (1'-OH and 4-OH MDZ) are formed presumably via CYP3A4, simultaneous fitting of both metabolites' data was the logical choice. The ESSP1P2 model fitting did a reasonable job to explain the data (figure 4.12 for HLM and figure 4.22 for HIM). However, when the observed data were plotted with the model predicted lines (figure 4.12 for HLM and figure 4.22 for HIM)., fittings of the individual metabolites to ESSP model were needed. Although, mechanistically inappropriate, the fittings of individual metabolites produced better observed versus predicted plots (figures 4.6 and 4.9 for HLM, figures 4.16 and 4.19 for HIM). Recently Paragas et. al., has presented simultaneous model fitting of both metabolites of MDZ to the ESSP1P2 model (Paragas et al., 2021). However, individual model fittings are also found previously in the literature (Nguyen et al., 2016). Further, the intrinsic clearances were reported normalized to the total protein concentration and that is why the overall intrinsic clearances were almost same for both individual fitting versus simultaneous fitting (tables 4.2, 4.4, 4.5, 4.6, 4.8, and 4.10).

The highest concentration of MDZ used in the saturation curve study of MDZ with HLM was 400 µM. (figures 4.5 and 4.8). Preliminary solubility studies revealed that with 1% methanol, MDZ solubility can reach 400 µM. For accurate characterization of enzyme kinetics, the concentration range was taken as high as feasible. It helped in distinguishing atypical kinetics from the classical Michaelis-Menten kinetics. From the saturation curve, it was seen that 1'OH MDZ and 4-OH MDZ were formed comparably but at lower concentrations which are physiologically more relevant, 1'-OH MDZ was the major metabolite (see figure 4.11). The saturation curves obtained were similar to the previously reported literatures (Nguyen et al., 2016; Paragas et al., 2021) From the model fittings, it was obvious that the MDZ enzymatic reaction with HLM follows a multiple binding kinetics (Fig. 4.12). It was found that 1'-OH MDZ formation was following substrate inhibition where $K_{m1}<K_{m2}$ and $k_{cat1}>k_{cat2}$ (table4.5 and figure 4.12). But the 4-OH MDZ formation was following sigmoidal kinetics where $K_{m1}<K_{m2}$ and $k_{cat1}<k_{cat2}$ (table4.5 and figure 4.12). However, from individual fitting 4-OH MDZ formation was also substrate inhibition since $K_{m1}<K_{m2}$ and $k_{cat1}>k_{cat2}$ (figure 4.9 and table 4.4). Because of the involvement of CYP3A4 in MDZ metabolism (Turpeinen et al., 2005), and atypical kinetics has been observed for CYP3A4 (K. R. Korzekwa et al., 1998; Tracy, 2006; Witherow & Houston, 1999) substrate inhibition or sigmoidal kinetics was not surprising. Although pure enzymes are the sole way to examine atypical kinetics with minimal bias, substrate inhibition and sigmoidal kinetics cannot be detected in multi-enzyme kinetics when enzymes exhibit MM kinetics. CL_{int} was plotted versus MDZ concentration while keeping clinical concentration range in mind. It demonstrated a considerable concentration dependency (Figure 4.13), which might justify the use of a variable CL_{int} of MDZ during IVIVC. Although the intrinsic clearance plot (figure 4.13) showed modest concentration dependence within the concentration range of 0-2 µM, for the substrate depletion assay 1 µM MDZ was used as the initial concentration based on previously published literatures (Stringer et al., 2009). However, the intrinsic clearance values obtained from both the saturation curve assay (0.53±0.059 mL/mg/min) and the substrate depletion assay (0.59 ±0.019 mL/mg/min) were similar (table 4.5 and section 4.4.1.1.1).

While 1'-OH MDZ and 4-OH MDZ produced comparably in HLM incubation with MDZ, 1'-OH MDZ was preferably the major metabolite in HIM, with minor formation of 4-OH MDZ (figure 4.22). This difference might be due to the expression differences between liver versus intestinal microsomes. Initial raw plots of both metabolites suggested atypical kinetics, specifically substrate inhibition producing higher metabolite concentration at low MDZ concentration and lower metabolite formation at higher MDZ concentration. When multiple binding ESSP1P2 model was fitted simultaneously to both metabolites' data, the 1'-OH MDZ formation simulated line showed substrate inhibition (where $K_{m1}<K_{m2}$ and $k_{cat1}>k_{cat2}$) which was expected from the initial raw plot, but 4-OH

MDZ simulated line showed multiple binding hyperbolic kinetics (K_{m1}<K_{m2} and $k_{cat1} \approx k_{cat2}$) (Table 4.10). However, from individual fitting 4-OH MDZ formation was also substrate inhibition since K_{m1}<K_{m2} and k_{cat1}>k_{cat2} (figure 4.19 and table 4.9). Inside the enterocyte, enterocytic metabolism occurs, and no published literature has evaluated the MDZ enterocyte concentration following an oral dosage of MDZ in humans. However, the continuous intestinal absorption model (Nagar, Korzekwa, & Korzekwa, 2017) can mimic MDZ concentration in enterocytes after an oral dosage, which will be employed in a subsequent chapter to simulate MDZ concentration in enterocytes. It is logical that the enterocyte MDZ concentration will be higher than the plasma concentration, at least theoretically. As a result, the intrinsic clearance plot was designed with a concentration range of up to 100 µM. (Figure 4.23). The metabolic conversion of MDZ to its metabolites was shown to be concentration dependent due to substrate inhibition. This might highlight the need of using a variable CL_{int} when adding intestinal metabolism into a continuous intestinal absorption model. For the substrate depletion assay using HIM, 1 µM MDZ was used as the initial concentration. The unbound intrinsic clearance obtained from the substrate depletion assay (0.52±0.011 mL/mg/min) was higher than that was calculated from the saturation curve (0.33±0.021). From the saturation curve, the K_{m1} was 1.06±0.037 µM. So, the CL_{int1} obtained from the saturation curve will be comparable to the vmax1/K_{m1} at 10 fold lower concentration of K_{m1}. On the other hand, for substrate depletion a concentration of 1 µM was used. A lower concentration of MDZ might have produced a comparable CL_{int} from the substrate depletion assay.

Overall, both HLM and HIM reactions with MDZ followed atypical kinetics, mainly substrate inhibition kinetics. Since CYP3A4 is the main enzyme involved in MDZ metabolism and CYP3A4 is highly abundant in human liver and intestine, similar saturation curves were not surprising. However, the implication of substrate inhibition for these two sites might be very different. In plasma, the MDZ concentration will not reach high enough to display substrate inhibition, which means the metabolic conversion will be almost concentration independent (figure 4.13). But the enterocytic concentration might be very high in case of oral dose. At higher concentration, the substrate inhibition might be apparent and there might not be practically no metabolism at those initial higher concentrations (figure 4.23).

In case of NCD metabolic studies with human microsomes, one of the metabolites of NCD was not commercially available. This is why the substrate depletion assay was done to capture an overall intrinsic clearance mediated by CYPs. NCD (1 µM) was incubated with HLM (0.1 mg/mL) for 10 minutes (figure 4.24) and with HIM (1 mg/mL) for 20 minutes (figure 4.28) in this investigation. The substrate concentration was selected based on a previously published paper (Naritomi et al., 2001).

The saturation curve assay of NCD conversion to DHD NCD using both HLM and HIM produced sigmoidal atypical kinetics where $K_{m1}<K_{m2}$ and $k_{cat1}>k_{cat2}$ (figure 4.25 and table 4.12 for HLM, figure 4.29 and table 4.14). NCD metabolic conversion to DHD NCD was known to be catalyzed by three CYP isoforms in human: 2C8, 2D6, and 3A4 (Nakamura et al., 2005). There are a number of CYPs expressed in the human small intestine, CYP3A4/5 and CYP2C9 being the two highest contributing enzymes with relative abundance of 80% and 14% respectively. Other CYPs include CYP2C19, 2J2 and 2D6 (<2%) (Galetin et al., 2008; Xie et al., 2016). However, liver contains almost 35% CYP3A, 12-14% of CYP2C, CYP2E1, and CYP1A2, about 8% CYP2A6, and minor proportions of CYP2B6 and CYP2D6 (Galetin et al., 2008). From these regional expressions it can be assumed that the metabolic interaction of NCD with HIM is mainly mediated by CYP3A4 but in liver there might be possible all three CYPs (3A4, 2C8, and 2D6) involvement. The implications of sigmoidal kinetics might be different in these two sites. Figure 4.27 shows the intrinsic clearance of DHD NCD formation in physiological concentration. There is a modest concentration dependence. However, if all the metabolites were possible to quantify, it would have been easier to conclude if there might be any change in NCD intrinsic clearance *in vivo*. The CL_{int} obtained from this substrate depletion experiment in HLM was much greater than the CL_{int} obtained from the saturation curve (9.60 ±0.16 mL/mg/min vs 1.33±0.41 mL/mg/min). This means that the kinetics of the production of a commercially unavailable metabolite cannot be overlooked.

On the other hand, figure 4.31 shows that the intrinsic clearance of DHD NCD can drastically change with enterocytic concentration. It might be necessary to incorporate variable intrinsic clearance while translating *in vitro* enzyme kinetics data to intestinal *in vivo* situation. In HIM, the CL_{int} from substrate depletion produced was lower than that obtained from the saturation curve. However, the underlying reason might be the use of 1 µM NCD concentration which was higher than the k_{m2}. Again, if all the metabolites were possible to quantify, it would have been easier to conclude if there might be any change in NCD intrinsic clearance in the intestine.

Finally, in addition to enzyme kinetics modelling, IVIVE was used to calculate predicted F_g and F_h for MDZ and NCD. For MDZ, the calculated F_h and F_g values were similar to the reported observed value (F_h 0.54 and F_g 0.51 to 0.57) in the literatures (Galetin et al., 2008, 2010; Gertz et al., 2010; Nguyen et al., 2016; Yau et al., 2017). For NCD there is no available report of F_h, but the F_g has been really different from the reported value of 0.78 (Yau et al., 2017). The major reason behind this might be the use of single concentration substrate depletion assay intrinsic clearance. Since the DHD NCD formation follows sigmoidal kinetics, the intrinsic clearance is not constant over the concentration range. Single intrinsic clearance value might be overestimating the metabolic situation in liver and intestine resulting lower than observed F_g.

In summary, it was found that enzyme kinetic modeling of MDZ and NCD reactions with HLM or HIM are explained by atypical kinetics. Further there was significant differences in intrinsic clearance of NCD using substrate depletion versus saturation curve suggesting incorporating other metabolite consideration in the saturation curve may help to characterize those interaction more in depth.

CHAPTER FIVE: *IN VITRO* TIME-DEPENDENT INACTIVATION (TDI) ASSAYS USING RAT INTESTINAL MICROSOMES (RIM) AND RAT LIVER MICROSOMES (RLM) AND MODELING OF TDI DATA

5.1 Background and Significance

Drug inhibition can be either reversible or irreversible, depending on the mechanism of enzyme inhibition. Most drugs' K_m is usually in the micromolar (μM) range. Nevertheless, the unbound concentration of these drugs at their clinical doses generally lies in the sub-micromolar range. It indicates that the probability of competitive, reversible enzyme inhibition is low *in vivo* (Yadav et al., 2020). There has been numerous investigation on time-dependent inactivation (TDI) and it has been established that TDI is the reason behind several clinically significant drug-drug interactions (DDIs). Based on their relative affinity for CYPs, less potent time-dependent inhibitors can contribute significantly to the inhibition of drug metabolism by inactivating the enzyme and rendering long-lasting inhibition outcomes (Mohutsky and Hall, 2014). Predicting DDIs resulting from TDI is becoming increasingly important in drug discovery and development phases (Yadav et al., 2020).

Irreversible enzyme inhibition can result from different molecular mechanisms. Irrespective of the mechanism, the outcome is an inactive enzyme (Zhang and Wong, 2005; Riley et al., 2007; Zhou and Zhou, 2009). Different irreversible inhibitors exist, such as mechanism-based inactivators (MBI), slow tight binders, transition state analogs, and affinity labeling agents. MBI is the most common (Silverman, 1995; Yadav et al., 2020). The mechanism of MBI involves the transition of the MBI into a reactive species, which ultimately inactivates the enzyme by forming a bond with the enzyme covalently or non-covalently. MBI results in time-dependence, meaning that the inhibition magnitude increases with time. Therefore, it is also called time-dependent inactivation (TDI) (Yadav et al., 2020). Other than time-dependence, TDI possesses several properties, including saturation of inactivator concentration, substrate protection, irreversibility, inactivator stoichiometry, and involvement of a catalytic step. Although not all the properties are routinely examined, time dependence, saturation, and involvement of the catalytic step are usually characterized sufficiently in drug discovery (Silverman, 1995; Yadav et al., 2020).

When an MBI is transformed into a reactive intermediate during metabolism, the electrophilic reactive entity can react with the nucleophile present on the CYP enzyme to inactivate it (Silverman, 1995; Zhou et al., 2005; Zhou and Zhou, 2009). Moreover, the reactive species can stay inside the active site of the same enzyme, or it can diffuse out of the active site to inactivate another enzyme nearby. It can be easily identified if the reactive species come out of the active by leveraging a scavenger such as glutathione, superoxide dismutase, or catalase which would decrease the inactivation (Hollenberg et al., 2008). However, there are different molecular mechanisms of CYP inactivation by the reactive entity, which mainly depends on the functional group of the inactivator. Major functional groups frequently involved in TDI are methylenedioxy aromatic groups, acetylenes, olefins, thiophenes, amines, furans, and phenols (Mohutsky and Hall, 2014; Yadav et al., 2020). Depending on the mechanism of inactivation, CYP TDI can be classified into the following three groups:

i. Metabolite intermediate complex (MIC) formation with heme

ii. Apoprotein covalent modification

iii. Heme destruction

Figure 5.1 shows different mechanisms of time-dependent inactivation. When the reactive metabolite forms a quasi-irreversible bond with the heme group of CYP to inactivate the protein, that is called the formation of intermediate metabolite complex (MIC) (Jones et al., 1999; Mayhew et al., 2000; Takedomi et al., 2001; Yadav et al., 2020). Different functional groups leverage different intermediate to form the MIC with the enzyme. For example, the amine functional group (erythromycin (Takedomi et al., 2001), diltiazem (Jones et al., 1999), verapamil (Zhou et al., 2005)) is converted to a nitroso group before forming the MIC (Takakusa et al., 2011; Taxak et al., 2012), whereas methylenedioxyphenyl group (podophyllotoxin, paroxetine, etc.) is converted to carbene group to form the MIC. When the nitroso group binds to the heme, the Fe^{3+} is converted to Fe^{2+}, which is more stable with a λmax of 448-456 nm (Takakusa et al., 2011). On the other hand, MIC formation through carbene intermediate produces a dual λ_{max} of 425-427 and 455 nm. Moreover, there have been reports that the conversion of Fe^{3+}:carbene to Fe^{2+}:carbene can be either irreversible or reversible depending on the enzyme and substrate (Barnaba et al., 2016; Yadav et al., 2020).

When the reactive intermediate covalently binds irreversibly with the structural amino acids of the apoprotein of the CYP enzyme resulting in an inactive enzyme that is referred to as covalent modification of apoprotein (Riley et al., 2007; Mohutsky and Hall, 2014; Yadav et al., 2020). The electrophilic reactive entity targets nucleophilic amino acids such as lysine, serine, cysteine, and threonine. However, the inactivation can be partial or full. Several functional groups have been involved in the covalent modification, including furan (Karjalainen, Neuvonen, & Backman, 2006; Lightning et al., 2000; S.

Zhou et al., 2005), phenol (Henne et al., 2012), thiophene (Ha-Duong et al., 2001; Nishiya et al., 2009; H. Zhang, Amunugama, Ney, Cooper, & Hollenberg, 2011), alkene (Grimm et al., 2009), alkyne (Hollenberg, Kent, & Bumpus, 2008; H.-l. Lin, Kent, & Hollenberg, 2002; H.-l. Lin, Zhang, & Hollenberg, 2018; H. Zhang et al., 2011), and tienilic acid (Dansette et al., 1991; Ha-Duong et al., 2001; Koenigs et al., 1999; Lightning et al., 2000).

A less common mechanism of TDI is the destruction or modification of heme, which can occur by the alkylation of the porphyrin ring of the heme group (Barnaba et al., 2016; Yadav et al., 2020). Compounds that have terminal acetylenes usually fall into this category. For example, gestodene selectively inactivates CYP3A (Guengerich, 1990; Zhou et al., 2005).

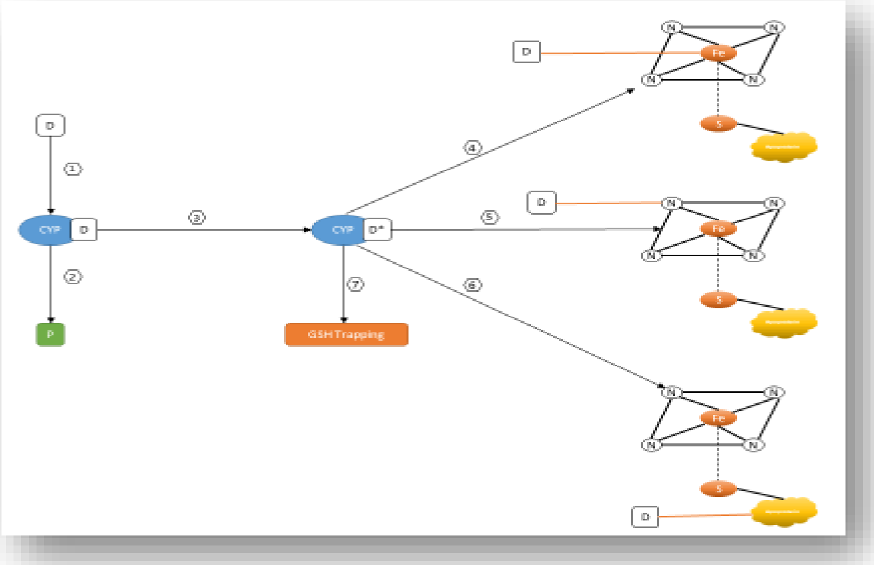

Figure 5.1. Probable fate of a time-dependent inactivator. 1. TDI binds to the CYP, 2. Product formation, 3. Formation of reactive species, 4. MIC formation, 5. Heme

destruction/modification, 6. Covalent modification of apoprotein, 7. GSH trapping of the reactive species (Reproduced from (Yadav et al., 2020))

5.1.1 Kinetics of Time-Dependent Inactivation (TDI):

A very simple scheme of TDI has been provided in fig 5.2. First, the inactivator binds with the enzyme as a conventional substrate with an initial binding step to form an enzyme-inactivator complex. This complex leads further to the formation of the intermediate (EI*). This intermediate can proceed either to the product formation (E+P) or to the inactive enzyme formation (E**) (Mohutsky & Hall, 2014; Taxak et al., 2012; Yadav et al., 2020; S. Zhou et al., 2005).

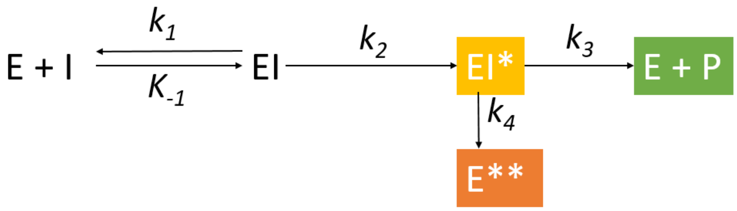

Figure 5.2. Scheme of TDI

At a given concentration of enzyme and inactivator, the intermediate concentration depends on three micro-rate constants: k_2, k_3, and k_4. The rate of E^{**} formation can be described by a Henry-Michaelis-Menten function:

$$\frac{dE^{**}}{dt} = k_{inact}.E.\frac{I}{K_I+I}$$ --------------------------------Equation 5.1

K_I is the unbound inactivator concentration that can cause 50% inactivation of the enzyme. The k_{inact} is the maximal rate of inactivation for a given enzyme concentration. The equations expressing K_I and k_{inact} are given below:

$$K_I = \frac{k_{-1}+k_2}{k_1} . \frac{k_3+k_4}{k_2+k_3+k_4}$$ -----------------------------------Equation 5.2

$$k_{inact} = \frac{k_2.k_4}{k_2+k_3+k_4}$$ ---Equation 5.3

K_{inact} is similar to the V_{max} of the Michaelis-Menten equation in the sense that when $[I]>>>K_I$, the maximal rate of inactivation occurs. Therefore, higher k_{inact} means a higher rate of inactivation, and lower K_I means higher apparent affinity for the enzyme inactivator. Therefore, the higher the ratio of k_{inact} to K_I, the higher the inactivation potential. Incorrect determination of K_I and k_{inact} can lead to misinterpretation of the DDI scenario (Riley et al., 2007; Yadav et al., 2020; S. Zhou et al., 2005). Although the above mechanism is the simplest TDI mechanism, it is not observed for all inactivators. For complex kinetics, complex TDI schemes are necessary, as shown elsewhere (Barnaba et al., 2016; Yadav et al., 2020). In those instances, K_I and k_{inact} will be determined by many additional micro-rate constants.

Several reported methods are available in the literature for evaluating time-dependent inactivators (Barnaba et al., 2016; Hollenberg et al., 2008; Yadav et al., 2020; S. Zhou et al., 2005; Z.-W. Zhou & Zhou, 2009). These published methods can be classified into the following two categories:

i. Screening assays
ii. Determination of TDI kinetic constants (K_I and k_{inact})

5.1.2 Screening Assays

Screening assays are mainly developed to determine if a new chemical entity (NCE) has TDI liability (Mohutsky & Hall, 2014). Screening assays are relatively simpler than the more in-depth kinetic experiments to determine the K_I and k_{inact}. There are several methods available for the TDI screening assays.

5.1.2.1 Two-Time Points Analysis

This is one of the most frequently used screening experiments used in the pharmaceutical industry where the enzyme is incubated with a high concentration of the NCE whose TDI liability is being screened (Grimm et al., 2009; R. W. Wang et al.). Then, the remaining enzyme activity is measured using a saturating concentration of a probe substrate (e.g., midazolam for CYP3A4). The percent activity lost is calculated by comparing the enzymatic activity after a preincubation step (for 30 minutes) with the inactivator to that without the preincubation step. The following equation is used for the determination of percent activity loss.

$$\%\ loss\ of\ activity = 100\ (1 - \frac{A_{inactivator,0}}{A_{inactivator,30}})$$

------------------- Equation 5.4

In eq. 5.4, ‘A’ represents the measured activity without preincubation and after a 30-minute preincubation. If there is a significant loss (more than 20%) of enzyme activity after a 30-minute preincubation, the NCE is a time-dependent inactivator and is further characterized by kinetic constants.

5.1.2.2 One-Concentration Approach

This method relies on a comparison between four different assays (Orr et al., 2012):

i. preincubation of the inactivator with enzyme source plus NADPH for a specific duration of time followed by the addition of probe substrate

ii. incubation of the inactivator, enzyme source, NADPH plus probe substrate but without the preincubation step

iii. preincubation of the enzyme with NADPH for a specific duration of time followed by the addition of probe substrate (no inactivator)

iv. incubation of the enzyme source, NADPH plus probe substrate but without the inactivator and the preincubation step

Activity is measured in each incubation, and enzymatic activity in either i) or ii) or iii) is normalized to that of iv). Incubation ii) is used to differentiate the reversible inhibition, if any, from the inactivation. Incubation iii) is used to differentiate the non-specific enzyme loss over the preincubation time from the enzyme inactivation. There are six possible outcomes which are depicted in the following figure.

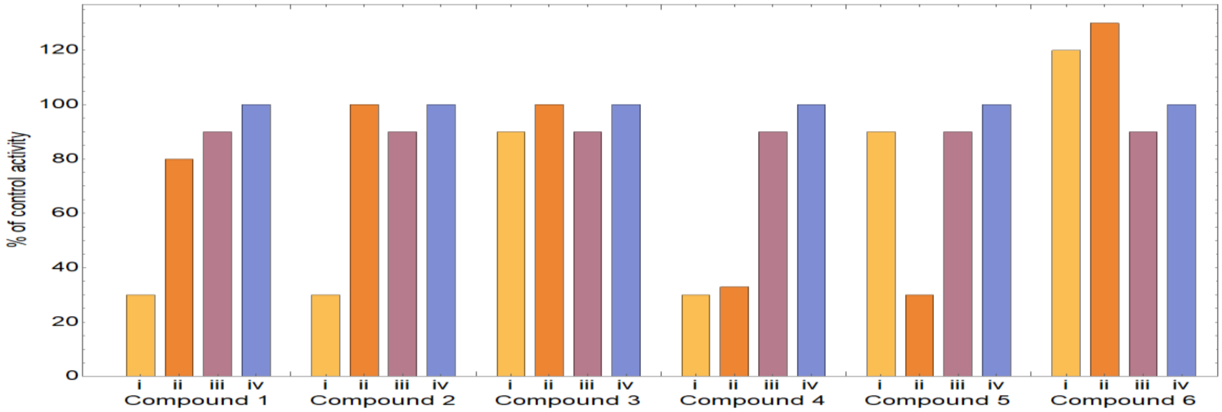

Figure 5.3. One concentration assay possible outcomes (adapted from (Orr et al., 2012))

Compounds 1 and 2 are both TDI, but only 1 has some reversible inhibition property. Compound 3 has neither TDI nor reversible inhibition property. Compound 4 is a strong reversible inhibitor. Compound 5 is a reversible inhibitor but depleted during preincubation. Compound 6 is an inducer.

5.1.2.3 IC_{50} Shift Assay

In this assay, first enzyme activity is measured at a fixed substrate concentration and a fixed enzyme concentration using varying concentrations of an inactivator. It will give an IC_{50} value, the concentration at which 50% inactivation is observed. Next, the same experiment is repeated after a preincubation step with the inactivator for a specified time (e.g., 30 minutes). If the later experiment produces a shift of the IC_{50} to a lower inactivator concentration, the NCE is assumed to have TDI liability (Figure 5.4). This experiment can be done using dilution or without dilution (Mohutsky & Hall, 2014). An IC_{50} shift of more than 1.5x is used as a cutoff value to qualify an NCE as a TDI (Grimm et al., 2009). The major advantage of this assay is that it can differentiate reversible inhibition from the TDI. This assay can also help decide the inactivator concentration range for determining kinetic constants. Major limitations include its inability to determine if the TDI is the parent or the metabolite. Also, if the inactivator is metabolically unstable, the IC_{50} can shift; this assay cannot differentiate this.

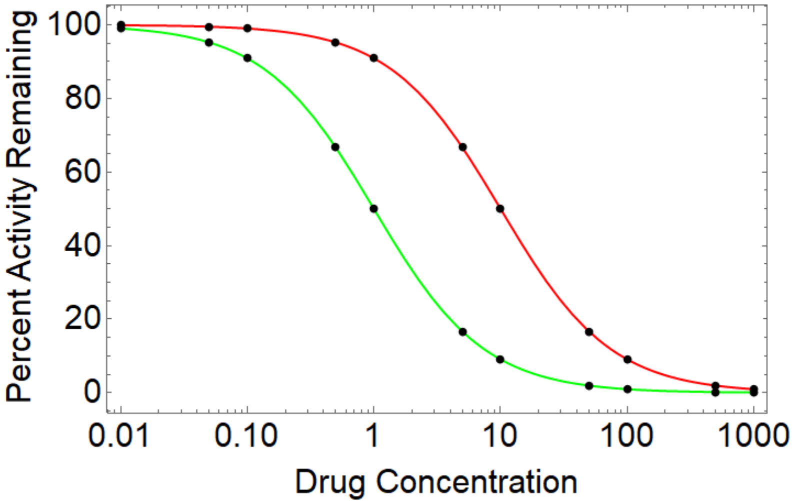

Figure 5.4. A simulated example of IC_{50} shift assay. Red and green lines represent the percent remaining enzymatic activity without and with a preincubation step. IC_{50} shifts from 10 units to 1 unit after preincubation.

5.1.3 Determination of TDI Kinetic Constants (K_I and k_{inact})

Two important parameters of TDI kinetics are K_I (inactivator concentration that causes half-maximal inactivation) and k_{inact} (maximal inactivation rate at a specific enzyme concentration). These two parameters are used to characterize the DDI potential of an inactivator *in vivo* (Grimm et al., 2009; Yadav et al., 2020; S. Zhou et al., 2005). There are different assays to determine these kinetic constants.

5.1.3.1 One-step Incubation for the Progress Curve

As the name implies, this one-step incubation assay is an ‘all at the same time’ approach (Burt et al., 2012; Fairman, Collins, & Chapple, 2007; Salminen, Leppänen, et al., 2011; Salminen, Meyer, Imming, & Raunio, 2011; Yadav et al., 2020). First, probe substrate, enzyme source, and NADPH with varying concentrations of inactivator are incubated together. Then, LC-MS/MS is used to determine the metabolite production and inactivator depletion over time. An assay using the probe substrate is called a paired assay. If the probe substrate is not used, inactivator depletion can be used, which is called an unpaired assay. However, a sensitive analytical assay is required to differentiate between minute differences in concentrations. An advantage of this assay is that it minimizes the experimental error caused by the two-step incubation assay.

5.1.3.2 Two-Step Incubation with Dilution or Non-Dilution

In the two-step incubation assay, the inactivation step is separated from the metabolite formation step (Ghanbari et al., 2006; Yadav et al., 2019; Yadav et al., 2020; Shufeng Zhou et al., 2005). In the inactivation step, the enzyme is incubated with NADPH and the inactivator. Then, the probe substrate is introduced in the second step. The second step can be designed using dilution or non-dilution. The most common method involves dilution (Grimm et al., 2009).

In the standard dilution method, a relatively high enzyme concentration and inactivator concentrations are co-incubated in the presence of NADPH (Yadav et al., 2020). Then, at different preincubation time points, aliquots are taken from the preincubation tube to the secondary incubation tube with a dilution of more than 10x. Dilution is used to ensure minimal competitive inhibition from the inactivator molecule.

5.1.4.3 TDI Data Analysis:

In vitro TDI parameters have been determined by the well-known replot method for a long time (Fairman et al., 2007; Ghanbari et al., 2006; Nishiya et al., 2009; S. Zhou et al., 2005; S.-F. Zhou, Xue, Yu, Li, & Wang, 2007; S. F. Zhou, 2008; Z.-W. Zhou & Zhou, 2009). This method plots the logarithm of percent remaining activity (PRA) against time for different inactivator concentrations. Each inactivator concentration will yield a different slope called the observed first-order rate constant for enzyme inactivation (k_{obs}). These k_{obs} are then graphed against [I]. The following equation is used to determine K_I and k_{inact} by non-linear regression analysis:

$$k_{obs} = k_{inact} \cdot \frac{I}{K_I + I}$$ ---------------------------------Equation 5.5

Conversely, plotting inactivation half-life against 1/[I] will yield a straight line. The parameter k_{inact} can be determined from the y-intercept. From the slope, K_I can be calculated. Inactivation half-life can be obtained from k_{obs} using the following equation:

$$t_{1/2inact} = {}^{0.693}/_{k_{obs}}$$ ----------------------------------Equation 5.6

However, the data analysis described so far has the following common assumptions:

a. Negligible inactivator metabolism in the secondary incubation.
b. Negligible inactivation in the secondary incubation due to dilution.
c. Michalis-Menten kinetics apply, e.g., steady-state assumptions, rapid equilibrium, and negligible change in substrate concentration.
d. Irreversible inactivation.

The major limitations of this data analysis are:

a. The assumptions do not always hold.
b. Replot method propagates error.
c. Atypical kinetics cannot be considered.

The major benefits of this data analysis are:

a. Non-specific enzyme loss can be modeled.

b. The estimated K_I can be corrected for lipid partitioning.

If Michaelis-Menten kinetics apply, the PRA plot will be linear. On the other hand, if the PRA plot is not linear, and the k_{obs} are determined using the linear portion of the PRA plot, it can lead to the overestimation of k_{inact} (Yadav et al., 2020).

Numerical methods have been proposed to overcome the limitations associated with the replot method (K. Korzekwa et al., 2014; Nagar et al., 2014). This method used ordinary differential equations to model the TDI kinetics. It is not limited by the assumptions used by the replot method. That is why models can be generated based on observed data or mechanistic information. However, this method also makes some assumptions:

a. Non-specific enzyme loss can happen from all the active enzyme species
b. Lipid partitioning is non-saturable

Besides all these advantages, this method can also model complex TDI kinetics, including multiple inactivator binding, sequential metabolism, partial metabolism, quasi-irreversible inhibition, inactivator loss, etc., as described elsewhere (Yadav et al., 2020).

5.2 Materials

Midazolam (MDZ), 1’-hydroxymidazolam (1’-OH MDZ), and 4-hydroxymidazolam (4-OH MDZ) were purchased from Sigma Aldrich (St. Louis, MO). Rat liver microsome (RLM), rat intestinal microsome (RIM), human liver microsome (HLM), and human intestinal microsome (HIM) were purchased from Sekisui Xenotech (Kansas City, KS). NADPH regenerating system (Solution A and Solution B) was purchased from Promega (Madison, WI). 1-aminobenzotriazole (ABT), nicardipine (NCD), and dehydro-nicardipine (DHD NCD) were bought from Toronto Research Chemical (TRC, ON, Canada). Dimethylsulfoxide (DMSO) and acetonitrile (ACN) were purchased from Fisher Chemical (Fair Lawn, NJ). Formic acid (ACS Reagent) was purchased from Honeywell Fluka (Buches, Switzerland). Potassium phosphate dibasic anhydrous was purchased from VWR Life Science (Bridgeport, NJ). Potassium phosphate monobasic anhydrous was purchased from Fisher Scientific (Norristown, PA).

5.3 Methods

Buffer Preparation:

To prepare 100 mM 1000 mL phosphate buffer pH 7.4, 800 mL deionized (DI) water was taken in a suitable sterile container. Using AAT Bioquest online calculator (Bioquest), the required amount of potassium phosphate dibasic and potassium phosphate monobasic was calculated. In the DI water, 12.119 g of potassium phosphate dibasic and 4.14 g of potassium phosphate monobasic were dissolved. The final volume was adjusted to 1000 mL by adding DI water. Finally, the pH was adjusted to pH 7.4 by adding HCL or NaOH solution drops.

Drug Stock Preparation:

MDZ and NCD stocks were prepared using methanol. MDZ was available as a 1 mg/mL solution in methanol. It was dried under liquid nitrogen and reconstituted using methanol to a final concentration of 40 mM. On the other hand, NCD was available as NCD hydrochloride power. It was dissolved in methanol to attain a concentration of 30 mM.

5.3.1 Pilot Assays to Determine Time-Dependent Inactivation (TDI)

These assays were done where the enzyme sources were incubated with a high concentration of the inactivator whose TDI liability was being screened (Grimm et al., 2009; R. W. Wang et al.). The remaining enzyme activity was measured using a saturating concentration of a probe substrate (either midazolam or nicardipine). The percent activity lost was calculated by comparing the enzymatic activity after a preincubation step (in this thesis, 60 minutes) with the inactivator to that without the preincubation step (0 minutes) using equation 5.4.

5.3.1.1 Determination of TDI Liability of ABT on MDZ Metabolism Using RLM/RIM

The MDZ (100 µM) was used as the probe substrate in this assay. Briefly, two concentrations (0 and 1000 µM) of inactivator (ABT) were incubated at 37°C with a 1mg/ml suspension of RLM or a 2.5 mg/ml suspension of RIM in 0.1 M potassium phosphate buffer, pH 7.4 as a primary incubation. After 5 minutes of prewarming, the primary incubation reaction was initiated by adding the NADPH regenerating system in buffer (final concentration 1.3mM NADP+, 3.3mM glucose-6 phosphate, 0.4 U/ml glucose 6- phosphate dehydrogenase, and 3.3mM magnesium chloride). At two time points (0 and 60 minutes), an aliquot (15 µl) of the primary incubation was added to the secondary incubation (135 µl) containing probe substrate to create a ten-fold dilution of the inactivated enzyme and the inactivator. The secondary incubation ran for 10 minutes, followed by quenching with ice-cold acidified acetonitrile containing PHE as the internal standard. After centrifugation at 10000 rpm for 10 minutes, the supernatant was removed to measure the amount of 4-OH MDZ in the supernatant. LC-MS/MS was utilized for the analysis of the supernatant.

5.3.1.2 Determination of TDI Liability of NCD on MDZ Metabolism Using RLM/RIM

The MDZ (100 µM) was used as the probe substrate in this assay. Briefly, two concentrations (0 and 100 µM) of inactivator (NCD) were incubated at 37°C with a 1mg/ml suspension of RLM or a 2.5 mg/ml suspension of RIM in 0.1 M potassium phosphate buffer, pH 7.4 as a primary incubation. After 5 minutes of prewarming, the primary incubation reaction was initiated by adding the NADPH regenerating system in buffer (final concentration 1.3mM NADP+, 3.3mM glucose-6 phosphate, 0.4 U/ml glucose 6- phosphate dehydrogenase, and 3.3mM magnesium chloride). At two time points (0 and 60 minutes), an aliquot (15 µl) of the primary incubation was added to the secondary incubation (135 µl) containing probe substrate to create a ten-fold dilution of the inactivated enzyme and the inactivator. The secondary incubation ran for 10 minutes, followed by quenching with ice-cold acidified acetonitrile containing PHE as the internal standard. After centrifugation at 10000 rpm for 10 minutes, the supernatant was removed to measure the amount of 4-OH MDZ in the supernatant. LC-MS/MS was used for the analysis of the supernatant.

5.3.1.3 Determination of TDI Liability of ABT on NCD Metabolism Using RLM

This assay used the NCD (100 µM) as the probe substrate. Two concentrations (0 and 1000 µM) of inactivator (ABT) were incubated at 37°C with a 1mg/ml suspension of RLM in 0.1 M potassium phosphate buffer, pH 7.4 as a primary incubation. After 5 minutes of prewarming, the primary incubation reaction was initiated by adding the NADPH regenerating system in buffer (final concentration 1.3mM NADP+, 3.3mM glucose-6 phosphate, 0.4 U/ml glucose 6- phosphate dehydrogenase, and 3.3mM magnesium chloride). At two time points (0 and 60 minutes), an aliquot (15 µl) of the primary incubation was added to the secondary incubation (135 µl) containing probe substrate to create a ten-fold dilution of the inactivated enzyme and the inactivator. The secondary incubation was 10 minutes and stopped quenching with ice-cold acidified acetonitrile containing PHE as the internal standard. After centrifugation at 10000 rpm for 10 minutes, the supernatant was removed to measure the amount of 4-OH MDZ in the supernatant. LC-MS/MS was used for the analysis of the supernatant.

Data Analysis for the Pilot TDI Assay:

The logarithm of percent remaining activity (PRA) for each pilot assay was calculated based on equation 5.4. Moreover, it plotted against the preincubation time. Figure 5.xx shows a representative pilot TDI assay plot. The 0 µM inactivator PRA plot at 0 and 60 minutes indicated the non-specific enzyme loss. On the other hand, comparing PRA points of 0 µM inactivator and the highest concentration of inactivator points at 0 minutes, the existence of competitive, reversible inhibition was captured. Finally, keeping all these considerations, the presence of TDI was ensured by the PRA of 0 µM inactivator and the highest concentration of inactivator points at 60 minutes.

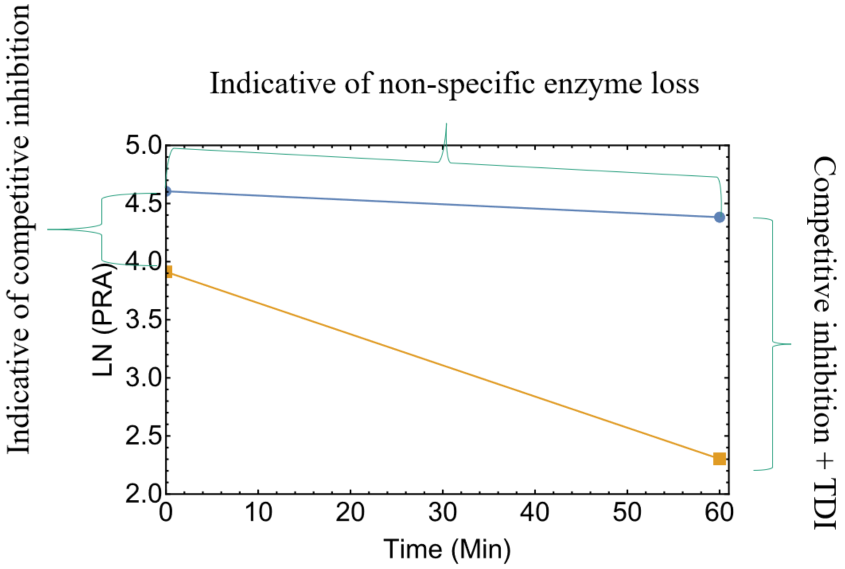

Figure 5.5. Representative pilot TDI assay plot

5.3.2 Full TDI Assay to Determine K_I and k_{inact}

ABT and NCD were assessed using a standard two-step approach for TDI assay using RLM. Briefly, eight concentrations of inactivators (ABT or NCD) prepared using a 2-fold dilution scheme were incubated at 37°C with a 1 mg/ml suspension of RLM in 0.1 M potassium phosphate buffer, pH 7.4 as a primary incubation. After 5 minutes of prewarming, the reaction was initiated by adding the NADPH regenerating system in buffer (final concentration 1.3mM NADP+, 3.3mM glucose-6 phosphate, 0.4 U/ml glucose 6- phosphate dehydrogenase, and 3.3mM magnesium chloride). At specific time points, an aliquot (15 µl) of the primary incubation was added to the secondary incubation (135 µl) containing probe substrate 50 µM MDZ and NADPH. The primary incubation was run for 0-60 minutes, with data collected at eight-time points. Then, the secondary incubation was allowed to run for 5 minutes, followed by quenching with ice-cold acidified acetonitrile containing PHE as the internal standard. After centrifugation at

10000 rpm for 15 minutes, the supernatant was removed to measure the amount of 4-OH MDZ in the supernatant. LC-MS/MS was used for the analysis of the supernatant. Each assay was conducted in duplicate. Stock solutions of inactivators and substrates were prepared in methanol. The final methanol concentration in the primary incubation was less than 1% (v/v). Assays were also performed without inactivators to assess the non-specific loss of enzyme activity.

Model Development:

For the development of TDI models to explain the observed data, the following assumptions were employed:

1. Lipid partitioning is non-saturable
2. Lipid partitioning has 1:1 stoichiometry
3. Rapid equilibrium
4. All active enzyme species deplete in first-order
5. All active enzyme species are considered in non-specific enzyme loss
6. Association is not rate-limiting

The *in vitro* TDI concentrations of 4-OH MDZ were transformed to log percent remaining activity plots (PRA plots) and assessed further for model building. Both ABT and NCD used in the TDI assays are known MBIs (de Montellano, 2018; Shufeng Zhou et al., 2005; S.-F. Zhou et al., 2007; S. F. Zhou, 2008; Z.-W. Zhou & Zhou, 2009). ABT is a mechanism-based inhibitor that converts into benzyne within the enzyme active site reacting with the heme before diffusing away from the active site cavity (de Montellano, 2018). On the other hand, NCD is a calcium channel blocker with an amine functional group that undergoes N-dealkylation, resulting in metabolite intermediate (Shufeng Zhou et al., 2005; S. F. Zhou, 2008). Based on the reported inactivation mechanism for MIC (Barnaba et al., 2016) and the datasets generated, kinetic models for CYP3A TDI were developed.

As previously shown, the concave upward curvature indicates either quasi-irreversible or partial inactivation (K. Korzekwa et al., 2014; Nagar et al., 2014; Yadav et al., 2021; Yadav et al., 2020). Kinetic models were fitted to the data, and kinetic parameters were determined using the numerical technique (K. Korzekwa et al., 2014; Nagar et al., 2014; Yadav et al., 2021; Yadav et al., 2020).

If activity loss over time was seen in the absence of an inactivator (0 M inactivator), non-specific loss of enzyme activity was integrated into the model. Fitting a first-order degradation model to control inactivator data yielded an initial estimate for the rate constant for non-specific enzyme loss (k_{12}). Non-specific enzyme loss from all enzyme species or the enzyme species was used in model construction. In addition, to establish an initial estimate for K_I, a competitive inhibition model was fitted to 0-minute and 60-minute time point data. Multiple binding was indicated by a variation in initial K_I estimations from 0 to 60 minutes. MIC production, as previously demonstrated (Barnaba et al., 2016), is a multi-step process including the formation of Fe^{3+}: carbene and Fe^{2+}: carbene. As a result, three rate constants were used to describe enzyme inactivation: k_6 and k_{11} for Fe^{3+}: carbene formation, k_7 for the re-formation of active enzyme, and k_8 for Fe2+: carbene creation. Association rate constants (k_1, k_4, and k_9) were fixed at 270 $\mu M^{-1} min^{-1}$. Lipid partitioning was also included in the NCD models since its extreme lipid partitioning. The association constant for lipid interaction (k_{on}) was fixed at 2000 μM^{-}

^{1}min$^{-1,}$ and the dissociation rate constant (k_{off}) was calculated using the following equation:

$$k_{off} = \frac{f_{u,mic} \cdot k_{on}}{1 - f_{u,mic}} \qquad \text{---------------------------------------Equation 5.7}$$

Where $f_{u,mic}$ is the unbound fraction in the microsomes.

Ratios of association and dissociation rate constants were used to calculate K_I values (assuming rapid equilibrium). Since lipid partitioning was included in the model, the numerically calculated K_I is the same as unbound $K_{I,u}$ ($K_{I,u} = K_I$). AICc (Sakamoto et al., 1986; Yamaoka et al., 1978) and adjusted R^2 were used to compare different models for each dataset.

Data Analysis:

The numerical and replot methods were used to examine the in-vitro TDI datasets. First, the datasets were evaluated using only the linear section of the PRA plot using the replot approach (Silverman, 1995). Then, estimates of K_I and k_{inact} were obtained using Equations 5.2 and 5.3.

K_I derived from the replot approach was adjusted for microsomal partitioning by multiplying K_I with $f_{u,mic}$ to get $K_{I,u}$ for comparison with the numerical method. Mathematica 12.3.3.0 was used to fit the models (Wolfram Research, Champagne, IL). With PrecisionGoal = 10, finite difference derivatives of order 4, and 1/Y weighting, the NonlinearModelFit function was used to fit the model to the data. The diluting step was incorporated into the model using the WhenEvent function.

5.4 Results

5.4.1 Pilot Assays to Determine Time-Dependent Inactivation (TDI)

5.4.1.1 Determination of TDI Liability of ABT on MDZ Metabolism Using RLM/RIM

Figure 5.6 shows the pilot TDI assay of ABT on MDZ metabolism. In case of control ABT (0 µM), the extent of non-specific enzyme loss was low in RLM. On the other hand, the non-specific enzyme loss was significantly high in RIM since the activity decreased significantly over time. Furthermore, competitive inhibition was apparent in RLM and RIM when comparing the 0-minute data points of control ABT and 1000 µM ABT. Considering all these, at 60-minute time points, there is considerable time dependence comparing the 0-minute data points of control ABT and 1000 µM ABT in RLM. Nevertheless, the time-dependence was not visible in case of RIM, probably due to the less stable RIM.

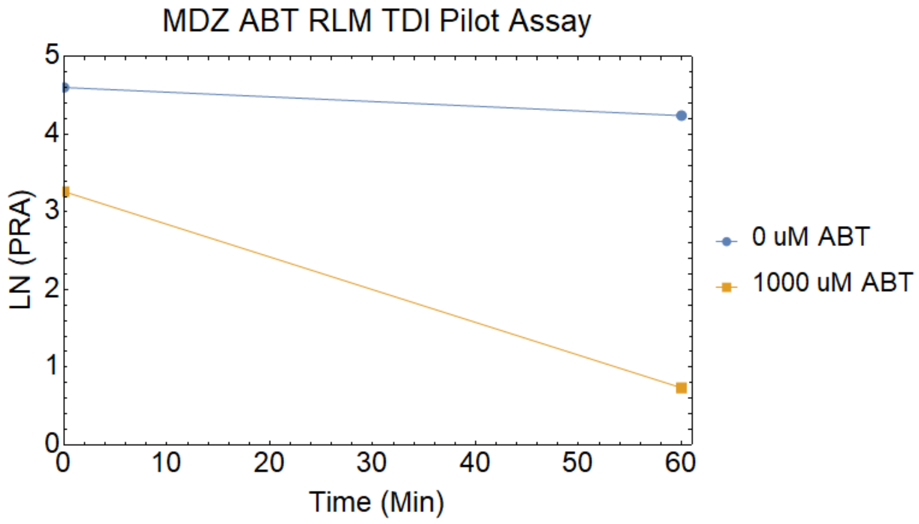

A.

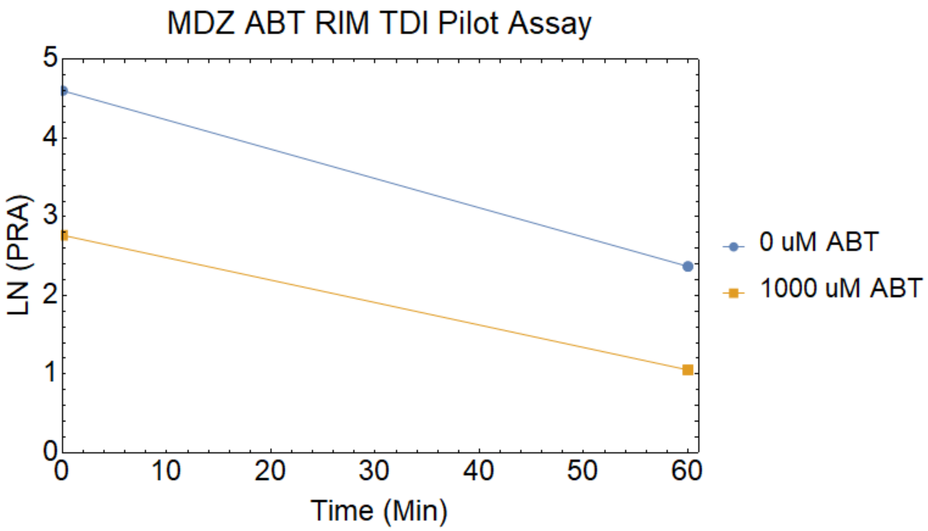

B.

Figure 5.6. Pilot TDI assay of ABT on MDZ metabolism using RLM (A) and RIM (B)

5.4.1.2 Determination of TDI Liability of NCD on MDZ Metabolism Using RLM/RIM

The pilot TDI experiment of NCD on MDZ metabolism is shown in Figure 5.7. The degree of non-specific enzyme loss in RLM and RIM was visible in the case of control NCD (0 M) but higher in RIM. Comparing the 0-minute data points of control NCD and 100 µM NCD in both RLM and RIM revealed that the presence of competitive inhibition was almost insignificant. Considering all of these, there is substantial time dependence at 60-minute intervals when comparing the 0-minute data points of control NCD and 100 µM NCD in RLM. However, again the time dependence was absent in the case of RIM, which is likely related to the fact that RIM is less stable.

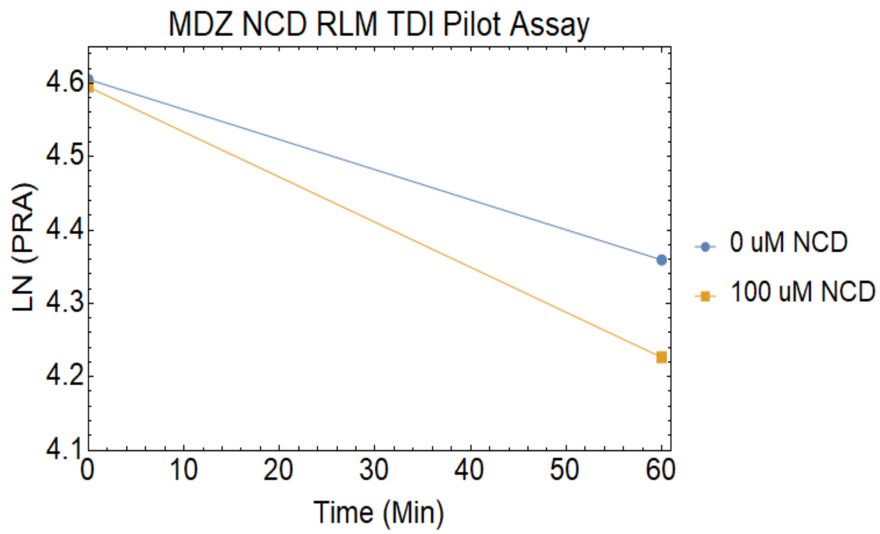

A.

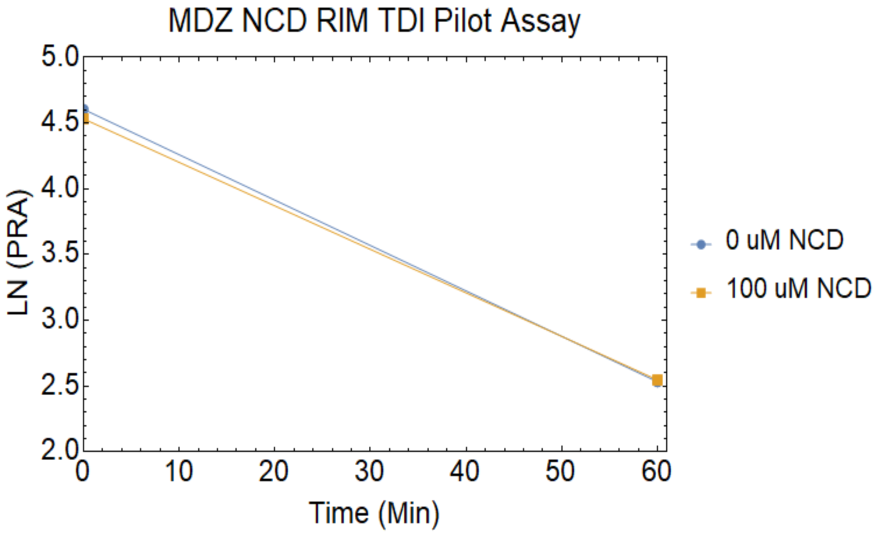

B.

Figure 5.7. Pilot TDI assay of NCD on MDZ metabolism using RLM (left) and RIM (right)

5.4.1.3 Determination of TDI Liability of ABT on NCD Metabolism Using RLM

Figure 5.8 depicts the ABT pilot TDI experiment on NCD metabolism. In the case of control ABT (0 M), non-specific enzyme loss was observed in RLM. The presence of competitive inhibition was significant when comparing the 0-minute data points of control ABT and 1000 µM ABT in RLM. Considering all of this and comparing the 0-minute data points of control ABT and 1000 µM ABT in RLM, there is practically no time-dependence at 60-minute intervals.

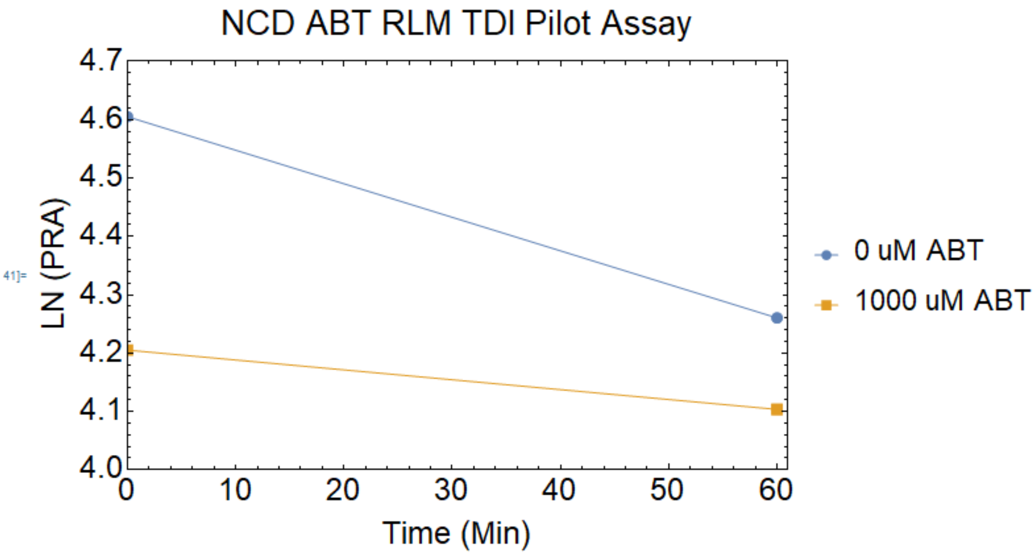

Figure 5.8. Pilot TDI assay of ABT on NCD metabolism using RLM

5.4.2 Full TDI Assay to Determine K_I and k_{inact}

5.4.2.1 Determination of K_I and k_{inact} of ABT Using MDZ as the Probe Substrate in RLM

Preliminary pilot *in vitro* TDI assays with RLM shows that ABT was an inactivator with significant competitive inhibition properties at high concentration (figure 5.9). In the full TDI assay of ABT with MDZ probe in RLM, the observed PRA plot showed concave upward curvature. This indicated the possible existence of either quasi-irreversible inhibition or partial inactivation. ABT is not partitioned in the microsome significantly (f_{um}= 1.00 ±0.11 shown in chapter three), which ruled out the incorporation of lipid partitioning in the model development. However, non-specific enzyme loss was included in the model captured from the 0 µM ABT data over time. Mechanistically, ABT inactivates CYPs by converting to benzyne, which reacts with the heme. Although, the mechanism of inactivation was heme modification, the concave-upward curve indicated presence of either quasi-irreversible mechanism, partial inactivation, or the involvement of multiple enzymes to metabolize the probe drug midazolam. However, the MDZ fraction metabolized by Cyp3a (f_{mCYP3A}) to 4-OH MDZ (which is quantified here) is 0.99 (Chovan, Ring, Yu, & Baldino, 2007) which contradicts the consideration of multiple enzymes. Additionally, there is no report of quasi-irreversible heme-modification so far. Based on all these considerations, several models similar to quasi-irreversible MIC along with inhibitor depletion and double binding and a partial inactivation were generated (Figure 5.10A-E). In addition to all these models, keeping in mind the mechanism of inactivation by ABT, a model assuming 4-OH MDZ formation from multiple enzymes also generated (Figure 5.10F). The partial inactivation model assumes there will still be some enzymatic activity from the inactivated enzyme (Figure 5.10E). And, in the heme destruction plus multiple enzyme involvement model assumes complete inactivation of one enzyme and a constant enzymatic activity (k_{alt}) from an alternative pathway from another enzyme (Figure 5.10F). The constant enzyme activity from the 2nd enzyme is assumed because of the use of a saturated concentration of probe substrate MDZ.

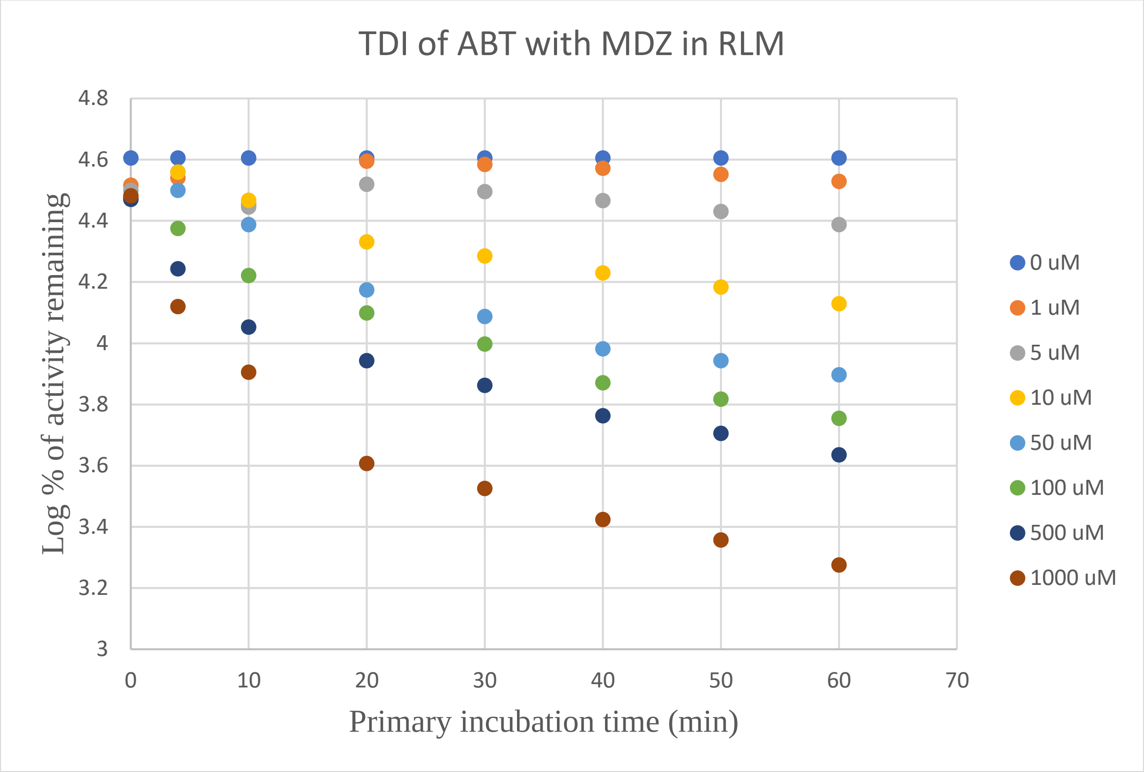

Figure 5.9. Experimental PRA plot for CYP3A inhibition by ABT using RLM. Dots represent mean of duplicates.

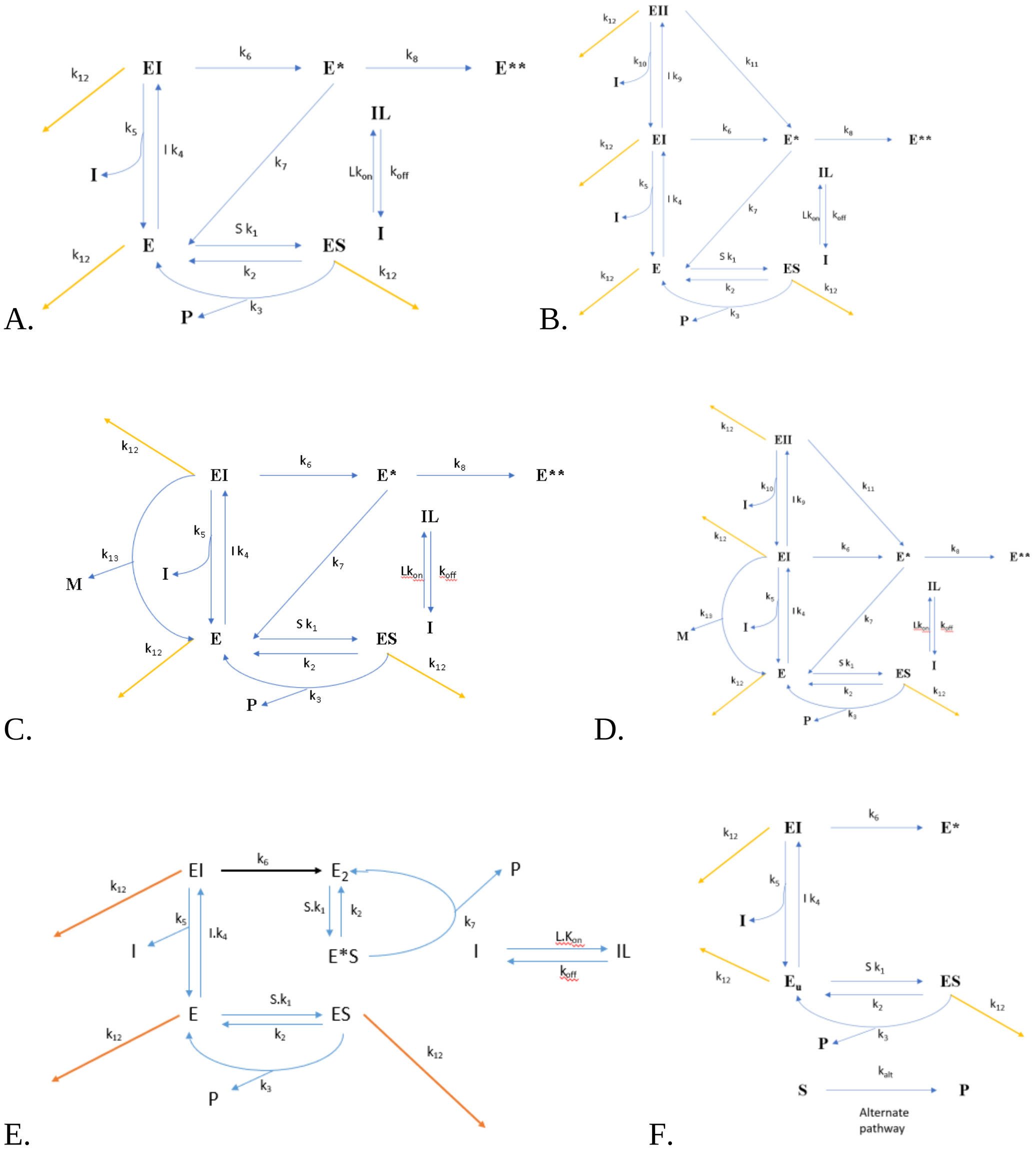
A.
EI
E*
E**
k6
k8
k12
k5
I k4
k7
I
IL
Lkon
koff
E
ES
S k1
k2
k3
P
B.
EII
k10
I k9
k11
C.
M
k13
D.
E.
E2
S.k1
E*S
L.Kon
F.
Eu
kalt
S
Alternate pathway

Figure 5.10. Kinetic scheme for ABT TDI with MDZ using RLM (A. MIC-EI model : MIC with single binding without inhibitor depletion, B, MIC-EII model : MIC with double binding without inhibitor depletion, C. MIC-EI-M model : MIC with single binding with inhibitor depletion, D. MIC-EII-M model : MIC with double binding with inhibitor depletion), E. Partial inactivation, and F. Heme destruction plus multiple enzymes involved. (Figure 5.10 A to E adapted from (K. Korzekwa et al., 2014; Yadav et al., 2020))

Table 5.1. Results of different model fittings

Model	AICc	R^2	Remarks
MIC-EI	**-242.53**	**0.99**	**All open**
MIC-EII	-235.27	0.99	All open
MIC-EI-M	Did not converge		All open
MIC-EI-M	Did not converge		k_{13}=0.1 min^{-1}
MIC-EI-M	-242.51	0.99	k_{13}=0.01 min^{-1}
MIC-EII-M	Did not converge		All open
Heme destruction plus multiple enzymes involved	-222.19	0.99	All open
Partial inactivation	-219.85	0.99	All open

Table 5.2: Micro-rate constants associated with all the models. Data presented as parameter estimates (SD)

	MIC-EI	MIC-EII	MIC-EI-M	Heme destruction	Partial inactivation
k_1 ($\mu M^{-1}.min^{-1}$)	270 (fixed)	270 (fixed)	270 (fixed)	270 (fixed)	270 (fixed)
k_2 (min^{-1}) Obtained from MDZ saturation curve with RLM	270*12 (fixed)	270*12 (fixed)	270*12 (fixed)	270*12 (fixed)	270*12 (fixed)

k_3 (min^{-1})	5.73 (0.098)	5.76(0.11)	5.73(0.098)	4.70(0.13)	5.52(0.097)
k_4 (µM^{-1}.min^{-1})	270 (fixed)	270 (fixed)	270 (fixed)	270 (fixed)	270 (fixed)
k_5 (min^{-1})	15988.81 (5423.82)	15258.11(7401.01)	15991.01(5426.63)	17034.61(5054.87)	135181(70128)
k_6 (min^{-1})	0.17 (0.063)	0.18(0.077)	0.16(0.062)	0.057(0.0091)	0.35(0.15)
k_7 (min^{-1})	0.11 (0.039)	0.13(0.035)	0.13(0.040)	NA	2.40(0.11)
k_8 (min^{-1})	0.017 (0.0043)	0.018(0.00006)	0.010(0.0040)	NA	NA
k_9 (µM^{-1}.min^{-1})	NA	270 (fixed)	NA	NA	NA
k_{10} (min^{-1})	NA	102798(24327.2)	NA	NA	NA
k_{11} (min^{-1})	NA	0.14(0.057)	NA	NA	NA
k_{12} (min^{-1}) (Fixed from the solvent control)	0.0083	0.0083	0.0083	0.0083	0.0083
k_{13} (min^{-1})	NA	NA	0.01 (fixed)	NA	NA
k_{alt}(µM. min^{-1})	NA	NA	NA	0.014(0.0013)	NA
K_{I1} (µM)	59.22±20.088	56.51(27.41)	59.23(20.10)	63.091(18.72)	500.66 (259.74)
k_{inact1} (min^{-1})	0.0097±0.0050	0.010(0.0051)	0.0054(0.0034)	0.057(0.0091)	0.14(0.0637)
K_{I2} (µM)	NA	380.73(901.006)	NA	NA	NA
k_{inact2} (min^{-1})	NA	0.0090(0.0042)	NA	NA	NA

The replot method was applied using the linear portions of the PRA plot (figure 5.11). The MIC-EI-M and MIC-EII-M models did not converge with all the micro-rate constants open. However, when k_{13} was fixed at less than 0.01/min, the MIC-EI-M model converged, indicating minimal inhibitor depletion. However, the MIC-EI model (single binding without inhibitor depletion) produced the best fit, providing the lowest AICc (Table 5.1).

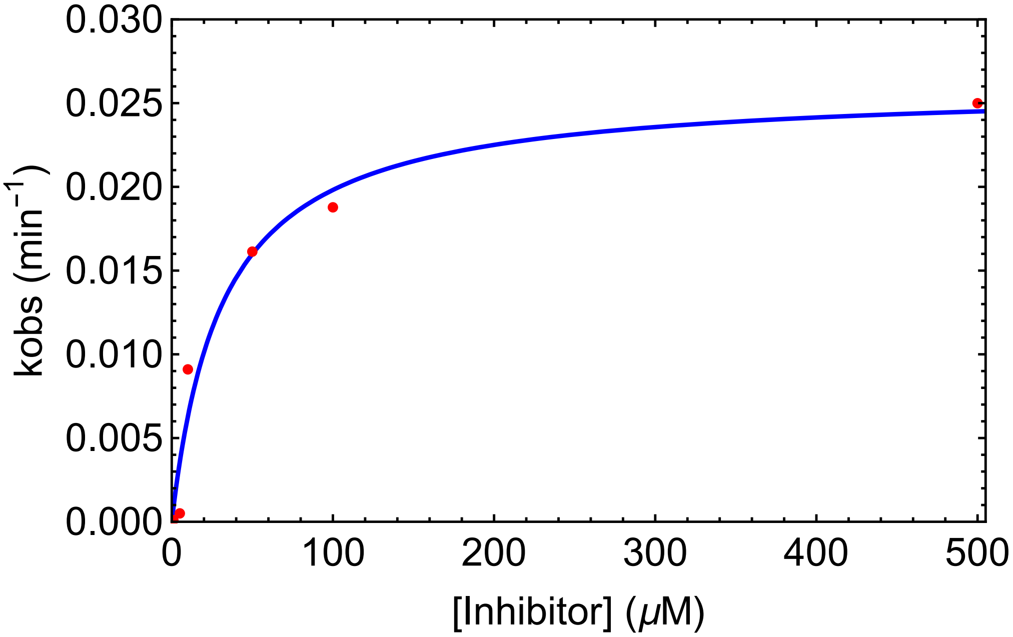

Figure 5.11. Determination of K_I and k_{inact} of ABT using MDZ in RLM. Dots represent experimental k_{obs} and the blue line represents the model predicted line.

Table 5.3. TDI parameters of ABT with MDZ using RLM

Replot method			Numerical method (MIC-EI model)		
$K_{I,unbound}$ (µM)	k_{inact} (min^{-1})	$k_{inact}/K_{I,unbound}$ (µM^{-1}.min^{-1})	$K_{I,unbound}$ (µM)	k_{inact} (min^{-1})	$k_{inact}/K_{I,unbound}$ (µM^{-1}.min^{-1})
31.43±9.79	0.026±0.0022	0.00083±0.00027	59.22±20.088	0.0097±0.0050	0.00016±0.00010

The micro-rate constants associated with all the converged model has been shown in Table 5.2. The K_I and k_{inact} values obtained from the traditional replot method and best-fit model from the numerical analysis are shown in table 5.3. Numerical method produced

5.19 fold lower k_{inact}/K_I. The observed data with the best fit model is shown in figure 5.12.

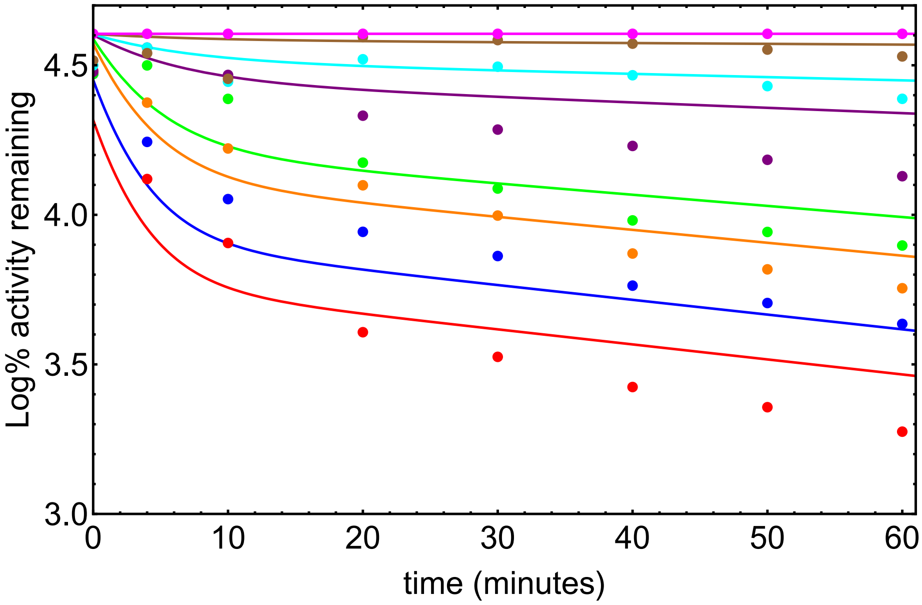

Figure 5.12. Experimental (points) and MIC-EI model fitted (solid lines) PRA plots for CYP3A TDI by ABT. Dots represent mean of duplicates and the solid lines are model predicted lines.

5.4.2.2 Determination of K_I and k_{inact} of NCD Using MDZ as the Probe Substrate in RLM

Preliminary pilot *in vitro* TDI assays with RLM shows that NCD was an inactivator with almost invisible competitive inhibition properties at even high concentration (figure 5.7). In the full TDI assay of NCD with MDZ probe in RLM, the observed PRA plot showed concave upward curvature. This indicated the possible existence of either quasi-irreversible inhibition or partial inactivation. However, the possibility of partial inactivation was ruled out due to the presence of different plateaus at different NCD concentrations. Furthermore, NCD is partitioned significantly in the microsome, which emphasizes the incorporation of lipid partitioning in the model development.

Additionally, non-specific enzyme loss was included in the model, which was captured from the 0 µM NCD data over time. Several models incorporating microsomal partitioning, MIC formation with single or double binding with or without inhibitor depletion (figure 5.10A-D), and sequential metabolism models (figure 5.13) were generated. Our preliminary study showed that NCD is rapidly metabolized in RLM. However, inactivation was still persistent at a later time, indicating the potential role of NCD metabolites in the NCD TDI mechanism. The sequential TDI model was also included in the model fittings. However, which metabolite of NCD was responsible for the inactivation could not be determined due to the commercial unavailability of all the metabolites.

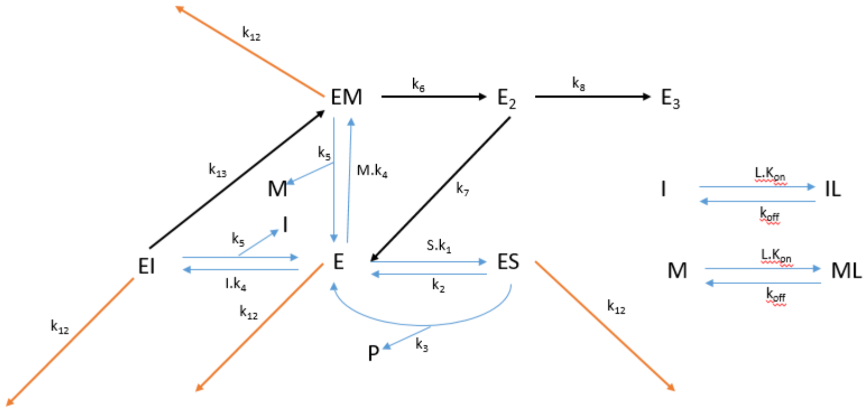

Figure 5.13. Sequential metabolism model

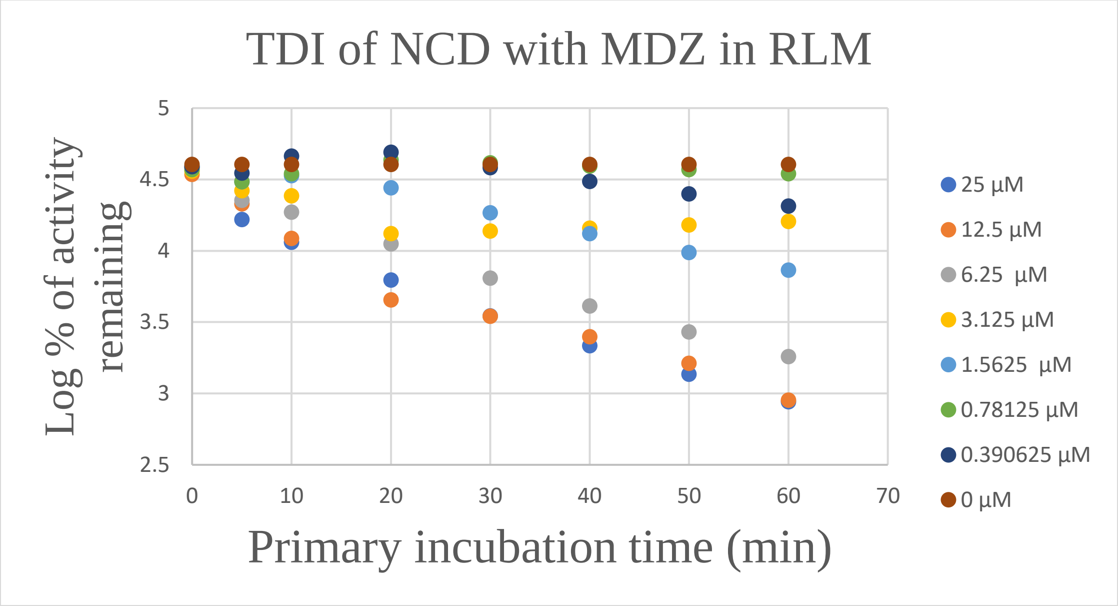

Figure 5.14. Experimental PRA plot for CYP3A inhibition by NCD using RLM. Dots represent the mean of duplicate.

Table 5.4. Statistical functions of different model fittings for model comparison

Model	AICc	R^2	Remarks
MIC-EI	**-259.69**	**0.99**	**All open**
MIC-EII	-243.96	0.98	All open
MIC-EI-M	-246.66	0.98	All open
MIC-EII-M	Did not converge		All open
Sequential Metabolism	-252.81	0.98	All open

Table 5.5: Micro-rate constants associated with all the models. Data presented as parameter estimates (SD)

	MIC-EI	MIC-EII	MIC-EI-M	Seq. Meta.
k_1 ($\mu M^{-1}.min^{-1}$)	270 (fixed)	270 (fixed)	270 (fixed)	270 (fixed)
k_2 (min^{-1}) Obtained from MDZ saturation curve with RLM	270*12 (fixed)	270*12 (fixed)	270*12 (fixed)	270*12 (fixed)
k_3 (min^{-1})	3.97 (0.075)	4.04 (0.073)	3.90 (0.078)	3.94 (0.067)
k_4 ($\mu M^{-1}.min^{-1}$)	270 (fixed)	270 (fixed)	270 (fixed)	270 (fixed)
k_5 (min^{-1})	232.47 (5.50)	115.68 (1.52)	360.86 (78.46)	267.27 (2.78)
k_{5a} (min^{-1})	NA	NA	NA	301.72 (1.89)
k_6 (min^{-1})	0.19 (0.023)	0.12 (0.013))	0.30 (0.036)	0.25 (0.0095)
k_7 (min^{-1})	0.034 (0.0083)	0.072 (0.0099)	0.052 (0.012)	0.036 (0.0049)
k_8 (min^{-1})	0.018 (0.0057)	0.038 (0.0055)	0.030 (0.0064)	0.019 (0.0041)
k_9 ($\mu M^{-1}.min^{-1}$)	NA	270 (fixed)	NA	NA
k_{10} (min^{-1})	NA	5669.31(61.41)	NA	NA
k_{11} (min^{-1})	NA	0.14 (0.0091)	NA	NA
k_{12} (min^{-1}) (Fixed from the solvent control)	0.014	0.014	0.014	0.014
k_{13} (min^{-1})	NA	NA	0.78 (0.22)	48.67 (0.27)
K_{I1} (μM)	0.86(0.020)	0.43(0.0056)	1.33(0.29)	0.99(0.010)
k_{inact1} (min^{-1})	0.014(0.0051)	0.020(0.0038)	0.023(0.0062)	0.015(0.0034)
K_{I2} (μM)	NA	20.99(0.23)	NA	NA
k_{inact2} (min^{-1})	NA	0.022(0.0036)	NA	NA

The replot method was applied using the linear portions of the PRA plot (figure 5.15). The K_I value obtained here was corrected with the unbound fraction in RLM which was obtained previously and shown in chapter 3. In the numerical method, the lipid partitioning is explicitly modeled, and the obtained K_I value is already corrected with the microsomal partitioning in the model fitting. The double binding MIC with inhibitor depletion model (MIC-EII-M) did not converge. However, all the other models converge, and from the AICc value, the single binding MIC model without inhibitor depletion (MIC-EI) model was the best fit (Table 5.4). Table 5.5 presents all the micro-rate constants estimated from the model fittings.

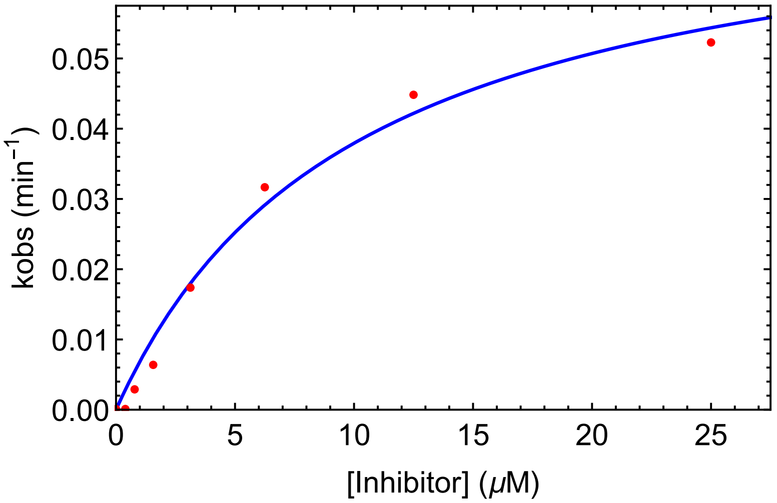

Figure 5.15. Determination of K_I and k_{inact} of NCD using MDZ in RLM. Dots represent the experimental k_{obs} and the blue line represents the model predicted line.

Table 5.6. TDI parameters of NCD with MDZ using RLM

Replot method			Numerical method (MIC-EI model)		
$K_{I,unbound}$ (μM)	k_{inact} (min^{-1})	$k_{inact}/K_{I,unbound}$ (μM^{-1}.min^{-1})	$K_{I,unbound}$ (μM)	k_{inact} (min^{-1})	$k_{inact}/K_{I,unbound}$ (μM^{-1}.min^{-1})
0.57±0.13	0.076±0.0077	0.132±0.032	0.87±0.020	0.014±0.0051	0.016±0.0061

The K_I and k_{inact} values obtained from the traditional replot method and the numerical analysis are shown in table 5.4. Numerical method produced eight folds lower k_{inact}/K_I. The observed data with the best fit model is shown in figure 5.16.

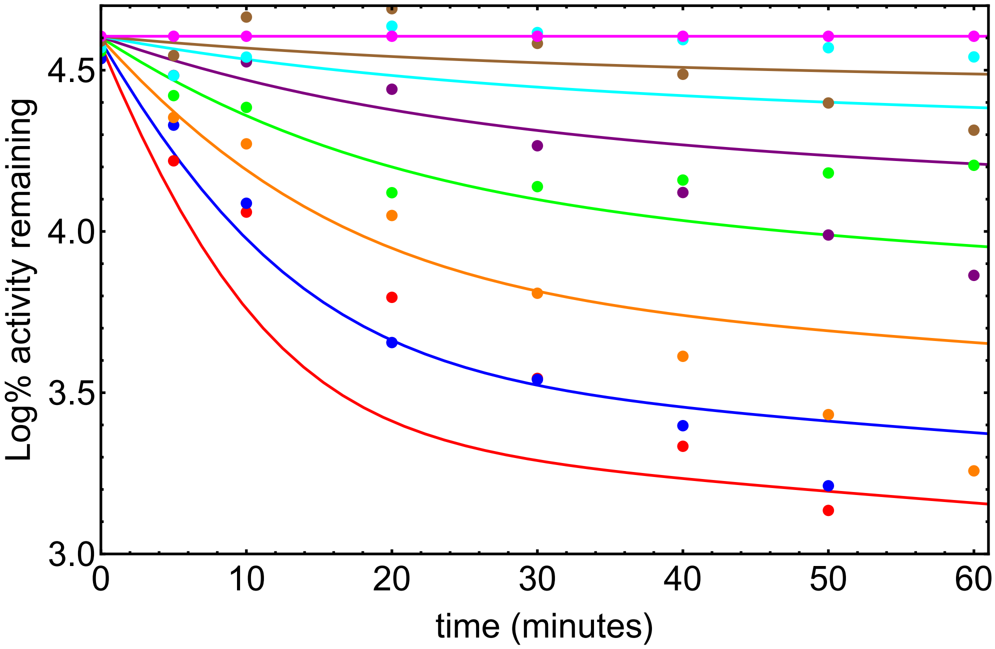

Figure 5.16. Experimental (points) and MIC-EI model fitted (solid lines) PRA plots for CYP3A TDI by NCD. Dots represent mean of duplicates and the solid lines are model predicted lines.

5.5 Discussion and Conclusions

Pilot *in vitro* TDI assays were conducted initially to determine if there is any time-dependence between the inactivator and the enzyme source. Briefly, pilot TDI assays using RIM could not capture the time-dependent inhibition (figure 5.6 right and figure 5.7 right) contributed by the inactivators (ABT or NCD). ABT and NCD are both very well-known MBIs causing TDI. ABT is a pan-specific CYP inactivator (Burkina et al., 2017; de Montellano, 2018; De Montellano & Mathews, 1981; Hollenberg et al., 2008), and NCD has published reports of CYP3A inactivation (Aueviriyavit, Kobayashi, & Chiba, 2010; Ghanbari et al., 2006; Yamazaki, Niwa, Murayama, & Emoto, 2008). Therefore, it was quite surprising because of the absence of any visible TDI using RIM. However, our hypothesis is that the RIM is less stable *in vitro* which is unsuitable to capture inactivation over a long range of time. This non-specific enzyme loss over time can contribute hiding the TDI contributed by the inactivators (ABT or NCD). To our knowledge, there is no published literature using RIM for the TDI studies with these inactivators. Therefore, we suggest that using recombinant CYPs for the intestinal TDI and then translating them to intestinal physiology might help to determine the TDI in the intestinal region of the body. However, a recent publication has used a human intestinal microsome (HIM) for the TDI study (Tanna et al., 2021). However, in that study, the primary incubation ranged only 20 minutes, which might not be sufficient to characterize the TDI behavior of an inactivator fully. According to recent understanding of TDI (K. Korzekwa et al., 2014; Nagar et al., 2014; Yadav et al., 2021; Yadav et al., 2020), without sufficient time points, it will be difficult to properly characterize the TDI mechanisms, especially those that display a PRA plot such as concave upward. Also, using limited-time points might indicate merely MIC formation, whereas the mechanism might be quasi-irreversible inhibition (K. Korzekwa et al., 2014; Nagar et al., 2014; Yadav et al., 2021; Yadav et al., 2020).

However, pilot TDI assays using RLM have demonstrated significant TDI characteristics both for ABT and NCD, necessitating full TDI assays to determine the K_I and k_{inact}. Surprisingly, when ABT was diagnosed as a TDI for NCD metabolism using RLM, there was no visible inactivation contributed from the ABT. The probable reason was initially unclear. However, later full TDI assays with NCD demonstrated that NCD itself is an inactivator of CYP3A with a very low K_I and higher inactivation potential (k_{inact}/K_I). Therefore, we hypothesize that the non-specific enzyme loss at 0 µM ABT visible in figure 5.8 was due to the impact of probe substrate NCD. However, at 1000 µM there should have been some inactivation from ABT which might be invisible due to the stronger inactivation effect from the NCD in the secondary incubation as the probe substrate. From all these observations, two full TDI assays were conducted: ABT with MDZ probe in RLM and NCD with MDZ probe in RLM.

This chapter aimed to develop kinetic models and estimate TDI parameters using the numerical method. *In vitro* TDI experiments were conducted with RLM using ABT and NCD as the inactivators and MDZ as the probe substrate. Both ABT and NCD used in the TDI assays are known MBIs (de Montellano, 2018; Shufeng Zhou et al., 2005; S.-F. Zhou et al., 2007; S. F. Zhou, 2008; Z.-W. Zhou & Zhou, 2009). A pan-specific, mechanism-based inactivator of the cytochrome P450 forms that metabolize xenobiotics in living things such as animals, plants, insects, and microbes is 1-aminobenzotriazole (ABT). The biological functions of cytochrome P450 enzymes, their involvement in the bioconversion of endobiotics as well as xenobiotics, and their impact on the metabolism-dependent toxicity of medications and chemicals have all been studied extensively using this method. Mechanistically, ABT inactivates CYPs by converting to benzyne, which reacts with the heme. This process does not involve the destruction of accompanied cytochrome b5 or the stimulation of lipid peroxidation. The inactivation requires NADPH, and it can be inhibited by CO (de Montellano, 2018; De Montellano & Mathews, 1981). All these features implicate an autocatalytic situation. Further the glutathione does not prevent the inactivation, which indicates that the benzyne does not diffuse away from the active site cavity (de Montellano, 2018). Overall, the mechanism of inactivation is heme destruction. Although, the mechanism of inactivation was heme modification, the concave-upward curve indicated presence of either quasi-irreversible mechanism, or partial inactivation, or the involvement of multiple enzymes to metabolize the probe drug midazolam. However, the MDZ fraction metabolized by Cyp3a (f_{mCYP3A}) to 4-OH MDZ (which is quantified here) is 0.99 (Chovan et al., 2007) which contradicted the consideration of multiple enzymes. Additionally, there is no report of quasi-irreversible heme-modification so far. Based on all these considerations, several models similar to quasi-irreversible MIC along with inhibitor depletion and double binding were generated. In addition to all these models, keeping in mind the mechanism of inactivation by ABT, a model assuming 4-OH MDZ formation from multiple enzymes also generated.

On the other hand, NCD is a calcium channel blocker that contains a tertiary amine group. This amine converts into a nitroso compound, forming a stable metabolic intermediate complex (MIC) with the heme group of CYPs (Aueviriyavit et al., 2010; Ghanbari et al., 2006; Yamazaki et al., 2008). Many of the TDI happening through MIC formation shows quasi-irreversible inhibition. Additionally, there was a possibility that the metabolite of NCD (debenzylated nicardipine and dehydronicardipine) might be contributing to its TDI. Overall, the mechanism of inactivation was MIC formation; the concave-upward curve in PRA plot indicated the presence of quasi-irreversible mechanism. Based on all these considerations, MIC-forming TDI schemes were developed. Further, atypical kinetics of TDI, inhibitor depletion, non-specific partitioning of the inactivators into the microsomes, and non-specific enzyme loss were incorporated into the models.

The association rate constants in all the kinetic models were fixed at 270 $\mu M^{-1} min^{-1}$. This assumed that the association rate constant is not rate limiting, and this value has been used in all the recent publications from this lab (Paragas et al., 2021; Z. Wang et al., 2021; Yadav et al., 2019, 2021; Yadav et al., 2020). Another significant assumption was that the non-specific enzyme loss would happen from all the active enzyme species. This assumption might not hold if there is CYP protection by the substrate (Yadav et al., 2021; Yadav et al., 2020). The non-specific enzyme has been assumed to be a first-order process and constant for all active enzyme species (E, ES, EI, EII, etc.), which might be different due to the different binding of substrate molecules.

Further this non-specific loss can also depend on the assay conditions, buffer preparations, or the quality of the individual microsomal batch. Considering all these, the non-specific enzyme loss has been modeled from all active enzyme species. The lipid-binding has been assumed to be unsaturable with a single binding site. For highly partitioned inactivators, explicit lipid partitioning needs to be included in the model because there is a possibility of equilibrium shift during the dilution step (Yadav et al., 2019, 2021; Yadav et al., 2020).

Atypical kinetics are a characteristic of CYPs, particularly CYP3A. In-vitro in-vivo extrapolation has made tremendous progress in mechanistic knowledge and compensating for atypical kinetics. Because of its underlying assumptions, the usual replot approach does not consider the abnormal kinetics displayed by CYPs. If the plot of k_{obs} versus [I] deviates from the expected hyperbolic curve, atypical behavior can be identified. Atypical behavior is hidden in the plot of k_{obs} vs. [I] in this research because only the linear portion of the PRA plot is utilized to calculate k_{obs}, making it challenging to identify atypical kinetics. For unusual kinetics, PRA plots could serve as useful diagnostic plots. Asymmetric PRA graphs suggest atypical kinetics. Any of the following factors, including inhibitor depletion, multiple binding, simultaneous activation and inactivation, protein heterogeneity, and substantial lipid partitioning, might cause atypical kinetics. By considering all these parameters, the numerical technique provides a useful tool to examine the effects of all these events on TDI kinetics and estimate $K_{I,u}$, and k_{inact} more accurately. The intricacy of the models and the quantity of data needed to construct sophisticated models are drawbacks of the numerical technique. In the initial stages of drug development, generating an 8 by 8 matrix or more could be difficult. However, the models provided could be solved using an 8 × 8 matrix.

The rate of inactivation is significantly influenced by the MIC's aging, as demonstrated by Barnaba et al. (Barnaba et al., 2016). It was discovered that the intermediate Fe^{3+}: carbene may either be reduced to the terminally inactive Fe^{2+}: carbene, or it can be released to unleash the active enzyme, creating a branching route (e.g., k_6, k_7, and k_8 in all kinetic models). The aging of MIC was included in the kinetic models for ABT and NCD when MIC was considered. Additionally, sequential metabolism was included in the NCD models to find a better model to explain NCD TDI dataset. In the sequential metabolism, there might be a lag time. Lack of lag time may occur from the absence of initial time points or very rapid metabolite formation inactivating enzymes.

In case of the TDI of ABT in RLM using MDZ as the probe, the PRA plot was created, which was concave upward, indicating either a quasi-irreversible, partial inactivation, or multiple enzyme mechanism. Due to differences in the plateau of individual inactivator concentrations, only quasi-irreversible and multiple enzyme involvement were considered. Non-specific enzyme loss was observed, and assuming the first-order depletion from all the active enzyme species, the first-order rate constant (k_{12}) was determined and fixed in the model fitting. Additionally, ABT depletion was also considered. There was no lag in the PRA plot, and there is no evidence of a sequential TDI mechanism for ABT interaction with CYPs, this mechanism was not considered.

Additionally, lipid partitioning was not included due to negligible partitioning of ABT in microsomes (f_{um}=1.00±0.11 shown in Chapter three). Six different models were fit to the data naming A. MIC-EI model: MIC with single binding without inhibitor depletion, B, MIC-EII model: MIC with double binding without inhibitor depletion, C. MIC-EI-M model: MIC with single binding with inhibitor depletion, D. MIC-EII-M model: MIC with double binding with inhibitor depletion, E: Multiple enzyme involvement mechanism, and F. Partial inactivation. The single binding MIC-EI model and double binding MIC-EII model converged, providing stable parameter estimation. However, the single binding MIC-EI-M model did not converge with all parameters open. Changing k13 from 0.001/min to 0.01/min, this model converged, but there was no difference in K_I and k_{inact}. Double binding MIC-EII-M did not converge as well. Based on the AICc, the MIC-EI model was the best fit. Replot method was also used to determine the K_I and k_{inact}. The numerical method produced significantly lower TDI potential (k_{inact}/K_I). The published report also supports ABT single binding stoichiometry with the enzyme (de Montellano, 2018; De Montellano & Mathews, 1981).

In case of the TDI of NCD in RLM using MDZ as the probe, based on the PRA plot, only quasi-irreversible was considered. Non-specific enzyme loss was observed and fixed in the model fitting. Additionally, NCD depletion was also considered. There was no lag in the PRA plot, but NCD is rapidly metabolized with a similar tertiary amine group causing MIC. This is why the sequential metabolism model was also considered. However, due to the lack of metabolite standard for NCD, the individual TDI assay with the metabolites could not be done. In that case, some of the micro-rate constants could have been fixed.

Additionally, lipid partitioning was included due to significant partitioning of NCD in microsomes (f_{um} 0.12 from chapter three). Five different models were fit to the data: A. MIC-EI model: MIC with single binding without inhibitor depletion, B, MIC-EII model: MIC with double binding without inhibitor depletion, C. MIC-EI-M model: MIC with single binding with inhibitor depletion, D. MIC-EII-M model: MIC with double binding with inhibitor depletion, E. Sequential metabolism model. Except for the double binding MIC model (MIC-EII-M) with inhibitor depletion which did not converge, the other four models converged to stable parameter estimation. Replot method was also used to determine the K_I and k_{inact}. The numerical method produced significantly lower TDI potential (k_{inact}/K_I). Previously it has been published (Barnaba et al., 2016; Yadav et al., 2019, 2021; Yadav et al., 2020) that the replot method might overestimate TDI potential considering only the linear portion of the PRA plots, which was also evident in this thesis.

In summary, TDI schemes of ABT or NCD inactivating CYP3A in RLM were developed and evaluated. The best fit model was established based on the experimental observations and statistical parameters. These inactivation parameters might be helpful to predict the *in vivo* situation involving these inactivator and victim pairs.

CHAPTER SIX: INCORPORATION OF INTESTINAL METABOLISM IN THE PRESENT HUMAN AND RAT CONTINUOUS INTESTINAL ABSORPTION MODEL

6.1 Rationale

PK modeling aims to predict drug absorption and disposition *in vivo* using different *in vitro* as well as *in vivo* parameters. There are numerous models available which serve different purposes in different scenarios (Fedi et al., 2021; J. H. Lin et al., 1997; Mizuma et al., 2004; Ni et al., 1980; Pang, 2003; van de Kerkhof, de Graaf, & Groothuis, 2007; Yau et al., 2017). Well-known classical compartmental models divide the whole body into discrete, pharmacokinetically equilibrated compartments (Gibaldi & Perrier, 1982; Hedaya, 2012). Although this approach seems simplistic, it can be very useful in many circumstances providing primary PK parameters (volume of distribution and clearance). In contrast, physiologically based pharmacokinetic (PBPK) models are more mechanistic and divide the whole body into organ compartments using real organ volume and blood flow (Kuepfer et al., 2016; Offman & Edginton, 2015; M. Rowland et al., 2015; Sager et al., 2015; Wagner et al., 2015; Wong & Chow, 2017; Zhuang & Lu, 2016). Hybrid models have also been proven useful where some of the most related organs are modeled explicitly (e.g., liver, kidney, etc.) and rest of the body is divided into central and peripheral compartments (Nagar et al., 2017).

One such example of hybrid model is the advanced compartmental absorption and transit (ACAT) model. ACAT model was based on previously developed compartmental absorption and transit (CAT) model (Huang et al., 2009; Lawrence & Amidon, 1999). CAT model divides the intestine into seven compartments. It also assumes passive diffusion, instantaneous dissolution, and minor gastric and colonic absorption (Lawrence & Amidon, 1999). ACAT model extends the CAT model by incorporating stomach and colon into the absorption model (Gobeau et al., 2016; Huang et al., 2009). ACAT model also includes three different states of drug inside the GIT: unreleased, undissolved, and dissolved. It also includes physicochemical factors of the drug (pKa, solubility, particle size and density, permeability etc.) as well as physiological factors (gastric emptying rate, intestinal motility, first-pass metabolism, transporter expression level and luminal transport etc.) This model uses ordinary differential equations (ODEs) to express intercompartmental drug transport (Nagar et al., 2017).

On the other hand, Nagar et al. recently developed a continuous intestinal absorption model in which the intestine was assumed to be a continuous cylinder of varying diameter rather than a summation of several separate compartments (Nagar et al., 2017). Drug concentration change along the length of the intestine (x) and over time (t) was used to model drug absorption from the intestine. Contrary to the ACAT model, there are two independent variables in this model: length of the intestine and time. Hence, partial differential equations (PDEs) were used in place of ODEs. Although, solving PDEs are computationally expensive, recent advances in computation power and speed has made this easier than before.

The continuous intestinal absorption model is based on the basic convection-diffusion equation (Ni et al., 1980; Stoll et al., 2000):

$$\frac{\partial}{\partial t}C(x,t) = D\frac{\partial^2}{\partial x^2}C(x,t) - \frac{Q}{\prod r^2}.\frac{\partial}{\partial x}C(x,t) - \sum_{i=1}^{n} k_i\,.\,C(x,t)$$

------Equation 6.1

Where drug concentration (C) varies as a function of both length of the intestine (x) and time (t), D is the drug molecule diffusion coefficient, Q is the bulk fluid flow rate, r is the radius of the intestinal lumen, and k_i is the first-order rate constant for the ith radial transfer process.

The first term describes axial diffusion, the spread of the drug pulse due to intestinal drug mixing, the second term describes convection, the axial bulk movement of the pulse, and the last term describes radial diffusion (Nagar et al., 2017). For saturable process like metabolism or transporter involvement k_i was replaced by a saturable function. This model also includes relevant physiological and physicochemical factors, which was discussed in detail in the method section.

The basic structure of the human model (Nagar et al., 2017) was a continuous cylinder with a radius of 8 mm for the small intestine and 1.6 cm for colonic region (Figure 6.1). The lengths of duodenum, jejunum, ileum, and colon were used as 0.2 m, 1.3 m, 2.5 m, and 3 m, respectively. The radial compartments were apical membrane, enterocyte cytosol, intracellular lipid, and basolateral blood compartment.

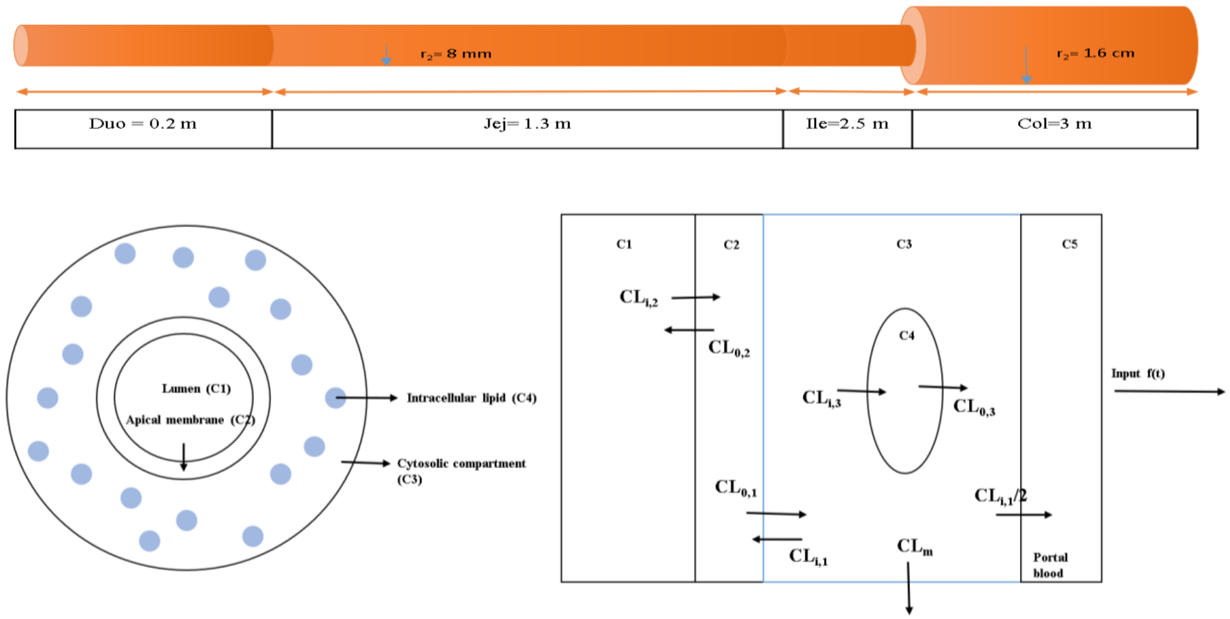
r₂= 8 mm
r₂= 1.6 cm
Duo = 0.2 m
Jej= 1.3 m
Ile=2.5 m
Col=3 m
Lumen (C1)
Apical membrane (C2)
Intracellular lipid (C4)
Cytosolic compartment (C3)
C1
C2
C3
C4
C5
CLi,2
CL0,2
CLi,3
CL0,3
CL0,1
CLi,1
CLm
CLi,1/2
Input f(t)
Portal blood

Figure 6.1: Continuous intestinal absorption model (reproduced from (Nagar et al., 2017))

(adapted from (Nagar et al., 2017)).Continuous intestinal absorption model. (A) Intestine is assumed a continuous cylindrical tube. The length of each region of the intestinal tract used in the model is labeled. Duo: duodenum, Jej: jejunum, and Ile: ileum. (B) Cross-sectional view of the continuous intestine model, with concentric tubes depicting the lumen (drug concentration C1), apical membrane (C2), enterocyte cytosol (C3), and intracellular lipid (C4). (C) Two-dimensional depiction of the concentric tubes, modeled as a six-compartment model with drug concentrations C1–C4 as defined above, and portal blood concentration (C5). Diffusional clearances in and out of each compartment are as defined under Methods.

In the process of absorption, the drug also moves in a radial direction. The drug can move reversibly from the lumen (C1) to the apical enterocyte membrane (C2) and then into the enterocyte cytosolic compartment (C3), where it can enter intracellular lipids (C4) or it can be irreversibly metabolized (CL_m). Finally, the medication penetrates permanently into the basolateral blood (C5) (Figure 6.1). The diffusional clearance parameters Cli and Clo express movement into and out of compartments, respectively.

Rats are a common pre-clinical species used for PK studies. Although the intestinal enzyme expressions are different that the human intestine, a correlation of the intestinal permeability of rats and human can be found (K. Ito & Houston, 2005; Olivares-Morales et al., 2014; Tang & Prueksaritanont, 2010; Xie et al., 2016). Therefore, the development of a continuous intestinal absorption model that accounts for species-specific physiologic differences might be beneficial. The physiological differences between rat intestine and human intestine have already been discussed in chapter one. Recently, a rat continuous absorption model has been developed by Radice et. al. and the impact of food and particle size in suspension dosage form have been evaluated (Radice et al., 2022).

The aim of this chapter is to simulate the oral PK of MDZ and NCD, both in rats and humans to by incorporating intestinal metabolism into the continuous intestinal absorption model. Chapter three has provided *in vitro* metabolic profiles of MDZ and NCD in rats which was incorporated into the rat continuous intestinal absorption model to estimate fraction escaping gut metabolism in rats. Similarly, chapter four has provided the *in vitro* metabolic profiles of MDZ and NCD in humans which was incorporated into the human continuous intestinal absorption model. For the disposition functions, IV data was collected from the literature. Oral PK profiles was also obtained from the literature. Certain parameters were optimized, while additional parameters were collected from the literature too.

6.2 Methods

The human model is a continuous cylinder with four different radius for the four segments of the intestinal tract, which is based on the published paper on human continuous intestinal absorption model (Nagar et al., 2017). The lengths and radii are given in the Table 6.1.

Table 6.1: Length and radii of the intestinal segments of humans

Intestinal Segment	Average length (m)	Average radius (mm)	Reference
Duodenum	0.2	8	(Nagar et al., 2017)
Jejunum	1.3	8	
Ileum	2.5	8	
Colon	3	16	

On the other hand, the rat model is a continuous cylinder with four different radius for the four segments of the intestinal tract, which is based on the published radius of Sprague-Dawley rat intestine (Radice et al., 2022). The lengths and radii are given in the Table 6.2.

Table 6.2: Length and radii of the intestinal segments of SD rats

Intestinal Segment	Average length (cm)	Average radius (cm)	Reference
Duodenum	10	0.79	(Radice et al., 2022)
Jejunum	113	0.92	
Ileum	3	0.89	
Colon	15	1.17	

There are five radial compartments (Figure 6.1): concentric tubes which denote the intestinal lumen, surrounded by apical enterocyte membrane, cytosolic compartment, cytosolic intracellular lipids, and basolateral membrane.

The drug from the stomach introduced into the intestine was expressed as the drug pulse. This drug pulse moves along the length of the intestine with a predefined velocity and axial diffusion profile. At the same time, drugs move radially for absorption. Radial movement from one compartment to another compartment follows reversible nature. However, the intestinal metabolism was contributed from the cytosolic compartment, which is irreversible.

6.2.1 Input Parameters

To derive partial differential equations (PDEs) for the concentration of drug as a function of distance along the intestine (x) and time (t), all the necessary expressions was developed. There are mainly three types of input parameters that was used for the generation of three types of input functions: physiologic functions, drug-specific physicochemical functions, and formulation function for the dosing. Logistic functions were used to develop appropriate expression for these functions. These expressions allowed us to construct a continuous function for the smooth transition between intestinal regions without any discontinuity. The following section discusses the input parameters and their relevant sources.

6.2.1.1 Physiologic Input Parameters

Table 6.3 contains all the physiologic input parameters and their uses for the input functions.

Table 6.3 Physiologic input parameters to develop physiologic expression as a function of intestinal length (x)

Physiologic input parameter	Used for the input function
Length and radii of the intestinal regions	➢ Velocity function ➢ Cross-sectional area ➢ Luminal surface area per unit length ➢ Cross-sectional area for the enterocyte apical membrane ➢ Cross-sectional area for the enterocyte cytosol

	➢ Cross-sectional area for the cytosolic lipid
Villi factor for surface area amplification	➢ Luminal surface area per unit length ➢ Cross-sectional area for the enterocyte apical membrane ➢ Cross-sectional area for the enterocyte cytosol ➢ Cross-sectional area for the cytosolic lipid
Microvilli factor for surface area amplification	➢ Luminal surface area per unit length ➢ Cross-sectional area for the enterocyte apical membrane
pH of the intestinal regions	➢ Luminal pH function
Regional expression of intestinal enzyme	➢ Intestinal enzyme function

Intestinal motility data from literature was used to generate a function for axial velocity as a function of x. In the published models used here, the effective axial diffusion was considered to directly related to the velocity function. Similarly, intestinal pH as a function of x, pH(x) was generated using published reports (Radice et al., 2022) of rat intestinal regional pH.

6.2.1.2 Drug-Specific Input Parameters

First, the drug-specific physicochemical properties were collected. For MDZ and NCD, these physicochemical properties are given below (Table 6.3):

Table 6.4. Physicochemical properties of MDZ and NCD used for the continuous intestinal absorption model

Physicochemical properties	MDZ	Source	NCD	Source
Caco-2 apparent permeability (cm/s)	$32.4\text{x}10^{-6}$	(Gertz et al., 2010)	$20\ \text{x}10^{-6}$	(Castillo-Garit, Marrero-Ponce, Torrens, & García-Domenech, 2008)
Solubility (mg/mL)	0.00987	(Drugbank)	0.00247	(DRUGBANK)
LogP	3.89	(Drugbank)	4.34	(DRUGBANK)
Diffusion coefficient (m^2/hr)	$2.6\text{x}10^{-6}$	(Bittermann & Goss, 2017)	$1.8\text{x}10^{-8}$	(Bittermann & Goss, 2017)
Fraction unbound in microsomes (f_{um})	0.68	Chapter 3	0.12	Chapter 3
pKa	6.01	(Drugbank)	8.6	(DRUGBANK)
Baseflag (1)/Acidflag (0)	1	(Drugbank)	1	(DRUGBANK)

Table 6.5 contains all the drug-specific input parameters and their application in the continuous intestinal absorption model.

Table 6.5: Drug-specific input parameters to generate input expressions as a function of x

Drug-specific input parameter	Used for the input function
Caco-2 apparent permeability	➢ Apparent permeability function ➢ Membrane diffusional clearance
Fraction unbound in microsomes and membrane partition constant (Kp)	➢ Membrane diffusional clearance
pk_a of the drugs	➢ Apparent permeability function ➢ Membrane diffusional clearance

In this model, apparent permeability was used to calculate the membrane diffusional clearances. Caco-2 apparent permeability was scaled with a scaling factor. Since the permeability for non-neutral drugs changes with pH, a function was developed for the apparent permeability using the scaled apparent permeability and pH(x).

6.2.1.3 Formulation Input Parameters

Formulation input parameters are mainly the dose and the volume of solution that was administered to dose the drug. A unit pulse function was used with a lag time to build the solution dosing input functions (Nagar et al., 2017; Radice et al., 2022).

6.2.2 Solution Dosing Partial Differential Equations (PDEs):

Drug absorption from the intestine required the drug transfer from the lumen to the portal blood through the apical membrane and cytosol. In the cytosol, the drug can diffuse into lipid compartments. Also, the intestinal metabolism can happen in the cytosol. Taking all these in consideration, drug disposition from the drug solution in the intestinal lumen was modeled with the following partial differential equations (PDEs) for the drug concentration in the lumen, C1(x,t), enterocyte apical membrane, C2(x,t), enterocyte cytosol, C3(x,t), and a lipid compartment within the cytosol, C4(x,t).

$$\frac{\partial}{\partial x}C1(x,t) = dif(x)\frac{\partial^2}{\partial x^2}C1(x,t) + \left(-vel(x) + \frac{\partial}{\partial x}dif(x) + \frac{dif(x)}{a(x)}\frac{\partial}{\partial x}a(x)\right)\frac{\partial}{\partial x}C1(x,t) + \left(-\frac{\partial}{\partial x}vel(x) - \frac{vel(x)}{a(x)}\frac{\partial}{\partial x}a(x)\right)C1(x,t) - \frac{CL_{i,2}(x)}{a(x)}C1(x,t) + \frac{CL_{o,2}(x)}{a(x)}C2(x,t)$$

------------------------------Equation 6.2

$$\frac{\partial}{\partial x}C2(x,t) = \frac{CL_{i,2}(x)}{a_{mem}(x)}C1(x,t) - \left(\frac{CL_{o,1}(x)+CL_{o,2}(x)}{a_{mem}(x)}\right)C2(x,t) + \frac{CL_{i,1}(x)}{a_{mem}(x)}C3(x,t)$$

-----------------------------Equation 6.3

$$\frac{\partial}{\partial x}C3(x,t) = \frac{CL_{0,1}(x)}{a_{cell}(x)}C2(x,t) - \frac{CL_{i,1}(x)}{a_{cell}(x)}C3(x,t) - \frac{CL_{i,1}(x)}{2a_{cell}(x)}C3(x,t) + \frac{CL_{0,1}(x)}{a_{cell}(x)}C4(x,t) - f_{CYP}.CL_m.C3(x,t)$$

------------------------------Equation 6.4

$$\frac{\partial}{\partial x}C4(x,t) = \frac{CL_{i,1}(x)}{a_{lip}(x)}C3(x,t) - \frac{CL_{o,1}(x)}{a_{lip}(x)}C4(x,t)$$

--------------------------Equation 6.5

In equation 6.32, CL_m is the *in vitro* metabolic clearance of the victim drug in the gut obtained from chapters three and four. There are four different simulations performed in this chapter. Oral PK simulation of MDZ and NCD, in both humans and rats. In all the cases, single intrinsic clearance value obtained from the *in vitro* metabolic assays of NCD and MDZ in human and rat using intestinal microsomes were used as the CLm. However, for MDZ oral PK simulation, we had regional expression of CYP3A4 in humans' gut, and only for this scenario, in addition to the use of single intrinsic clearance approach, another approach was used to include MDZ's atypical kinetics substrate inhibition phenomenon to generate a CLm along the length of the intestine $\mathrm{CL_m}$(t,x).

First, substrate inhibition kinetics observed in HIM was used to generate a velocity equation:

$$\frac{v}{Et} = \left(\frac{\frac{k_{cat1}C3(x,t)}{K_{m1}}+\frac{k_{cat2}C3(x,t)^2}{K_{m1}K_{m2}}}{1+\frac{C3(x,t)}{K_{m1}}+\frac{C3(x,t)^2}{K_{m1}K_{m2}}}\right) \qquad \text{--------------------Equation 6.6}$$

Then the equation 6.34 was normalized to the substrate concentration in the cytosol to generate the intrinsic clearance CLm(t,x):

$$CL_m(x,t) = \frac{v}{C3(x,t).Et} = \left(\frac{\frac{k_{cat1}}{K_{m1}}+\frac{k_{cat2}C3(x,t)}{K_{m1}K_{m2}}}{1+\frac{C3(x,t)}{K_{m1}}+\frac{C3(x,t)^2}{K_{m1}K_{m2}}}\right) \qquad \text{----------------Equation 6.7}$$

The equation 6.32 was modified in this case as follows:

$$\frac{\partial}{\partial x}C3(x,t) = \frac{CL_{0,1}(x)}{a_{cell}(x)}C2(x,t) - \frac{CL_{i,1}(x)}{a_{cell}(x)}C3(x,t) - \frac{CL_{i,1}(x)}{2a_{cell}(x)}C3(x,t) + \frac{CL_{0,1}(x)}{a_{cell}(x)}C4(x,t) -$$

$$f_{CYP}.\,CYP3A(x).\,CL_m(x,t).\,C3(x,t) \qquad \text{----------------Equation 6.8}$$

CYP3A(x) is the regional expression of CYP3A along the length of human intestine. The f_{CYP} was an empirical scaling factor which was optimized based on the observed data.

The Dirichlet boundaries for the above mentioned PDEs in case of rats were:

C1(0,t)=pulse(t), C1(x,0)=$C_{0.0001,0}$=Concentration at the start of pulse=pulse(t) at t=0

C1(1.23,t)=C2(0,t)=C2(1.23,t)=C2(x,0)=C3(0,t)=C3(x,0)=C3(1.23,t)=C4(x,0) = C4(0,t)=C4(1.23,t)= 0, assuming the total length of rat intestine 1.23m.

The Dirichlet boundaries for the above mentioned PDEs in case of humans were:

C1(0,t)=pulse(t), C1(x,0)=$C_{0.0001,0}$=Concentration at the start of pulse=pulse(t) at t=0

C1(8,t)=C2(0,t)=C2(8,t)=C2(x,0)=C3(0,t)=C3(x,0)=C3(8,t)=C4(x,0) = C4(0,t)=C4(8,t)= 0, assuming the total length of rat intestine 8m.

The equations for the input function from the cytosol to the systemic circulation are given below:

$$Input\ f(t) = \int_{x=0}^{x=1.23} \frac{CL_{i,1}(x)}{2} . C_3(x,t)$$

----------------Equation 6.9 for rats

$$Input\ f(t) = \int_{x=0}^{x=8} \frac{CL_{i,1}(x)}{2} . C_3(x,t)$$

----------------Equation 6.10 for human

6.2.3 Disposition Functions from the IV Data

MDZ and NCD IV data were collected from the literature for both humans and rats. Mathematica version 12.3.1 was used for modeling, using 1/y weighting. For each case, the data were fit to the classical compartmental PK models (either 2C or 3C). Based on the AICc and R^2, best model was chosen for every dataset. From the best fit model, intercompartmental rate constants and the volume of the central compartment were recorded which have been used in convolving with the input functions generated from the continuous intestinal absorption model.

6.2.4 Data Analysis

Mathematica 12.3.1 was used to create all of the models. NonLinearModelFit with a PrecisionGoal of Infinity and 1/Y weighting was used to fit intravenous data. The NDSolve function was used to simulate ODEs and PDEs. PDEs were resolved utilizing the SpatialDiscretization TensorProductGrid, DifferenceOrder 2, and Lines with Default Step Sizes methods.

For the calculation of fraction absorbed (F_a) and the fraction escaping gut metabolism (F_g), following equations were used:

$$Amount\ metabolized = \int [f_{cyp}.CL_m.C3[t,x],(\{t,0,24\}),(x,0,8)]$$

----------------Equation 6.10

$$Amount\ out = \int [(Cl_i/2).C3[t,x],(\{t,0,24\}),(\{x,0,8\})]$$

----------------Equation 6.11

$$F_a = \frac{Amount\ out + Amount\ metabolized}{Oral\ Dose}$$

----------------Equation 6.12

$$F_g = 1 - \frac{Amount\ metabolized}{Amount\ out + Amount\ metabolized}$$

----------------Equation 6.13

To compare the simulated C-t profiles to the experimental oral PK profiles, an exposure overlap coefficient (EOC) was determined. The experimental oral C-t data were used to build an interpolation function (Interpolation function in Mathematica with Method Spline and InterpolationOrder 2). The simulated C-t profile was standardized to have the same area under the curve (AUC) as the actual profile since experimental clearances were utilized. The AUC for overlap was calculated by integrating the minimum of the two C-t functions. Finally, the EOC was determined as the overlap AUC minus the experimental AUC. The EOC value ranges from zero (no overlap) to one (full overlap).

Finally, the model applicability was evaluated based on the observed vs predicted values of fraction absorbed (F_a), fraction escaping gut metabolism (F_g), maximal plasma drug concentration after oral administration (C_{max}), and time to reach Cmax (t_{max}).

6.3 Results

6.3.1 Simulation of Oral PK of MDZ in Humans

MDZ IV bolus and oral data were collected and digitized from Smith et. al. (Smith et al., 1981). This literature source was chosen due to fact that exact same healthy volunteers were used for both oral and IV PK studies. Total number of participants were six, among which five were male and one was female. Each of the volunteers were examined to be healthy with normal hematological and blood biochemical parameters. IV bolus dose was given as MDZ maleate solution equivalent to 5 mg MDZ. Parenteral MDZ solution was also administered orally in a dose equivalent to 10 mg MDZ. There was a washout period of three weeks between the IV and oral study.

MDZ IV data (Smith et al., 1981) were fitted to the classical two-compartment and three-compartment models. Based on AICc and adjusted R2 values (table 6.6), it was found that the two-compartmental model was a better fit to explain the observed IV data. The intercompartmental first-order transfer rate constants and the volume of the central compartment was parameterized from the best fit model and recorded as the disposition functions (table 6.7) which was convolved with the input function to simulate the oral PK profile.

Table 6.6. Model comparison functions for IV bolus data

	2C model	**3C model**
Adjusted R^2	0.99	0.99
AICc	64.16	74.54

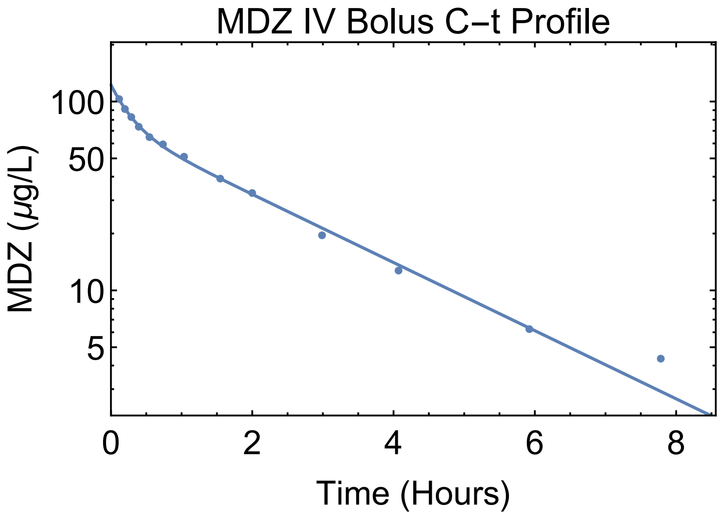

Figure 6.2. Observed (dots) versus 2C predicted (solid line) response of MDZ IV bolus (5 mg)

Table 6.7. Kinetic parameters as disposition function. Data presented as the parameter estimates (S.E.)

Parameters	Estimates (S.E.)
k_{12} (hour^{-1})	1.049 (0.35)
k_{21} (hour^{-1})	2.36 (0.54)
k_{10} (hour^{-1})	0.64 (0.037)
V_c (L)	40.83 (2.32)

6.3.1.1 Simulation of Oral MDZ Without Regional Expression of CYP3A4 and Atypical Kinetics:

The PDEs described in the method section were numerically solved and the numerical solution provided the following plots of C1 through C4. These plots were helpful to visualize and understand the MDZ transport across the radial compartments over time and along the length of the intestine. From these plots, it was found that the MDZ was rapidly absorbed mainly through the upper part of the intestine (Figure 6.3).

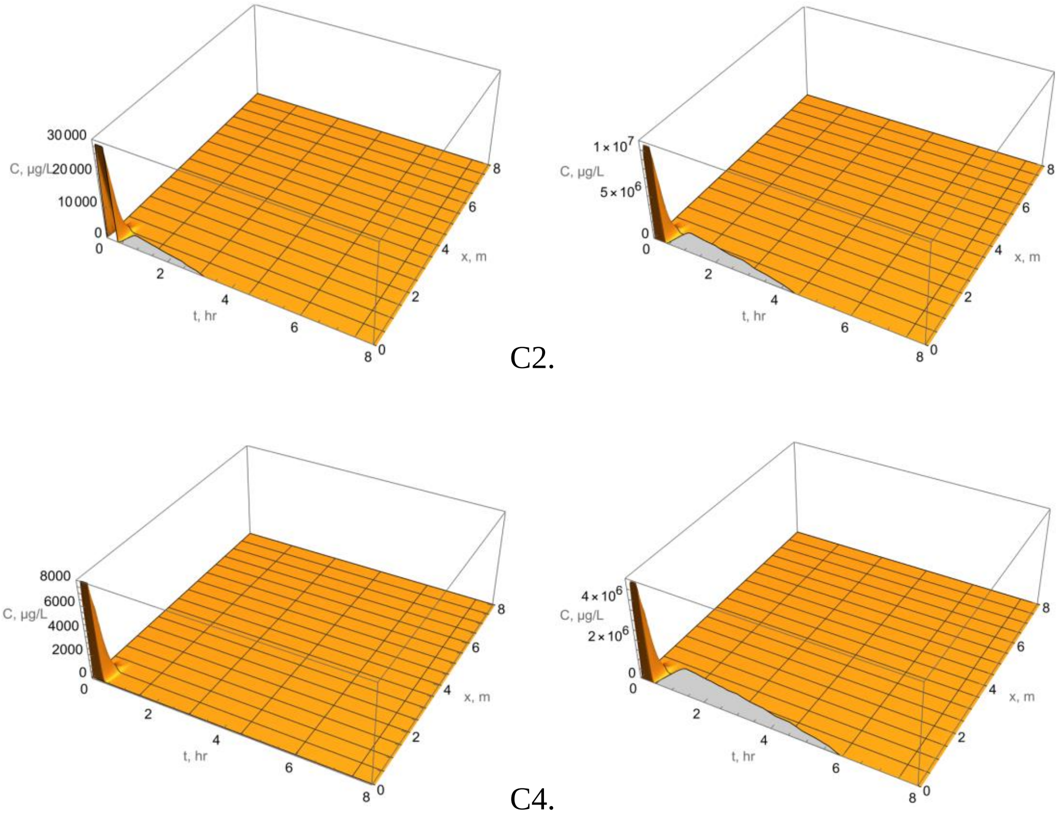

C1. C2.

C3. C4.

Figure 6.3: 3D plots of different radial compartments after numerical solutions. C1: Intestinal lumen, C2: Enterocytic apical membrane, C3: Enterocytic cytosol, and C4: Intracellular lipids.

Following input function was obtained after the numerical solution of the PDEs (Figure 6.4):

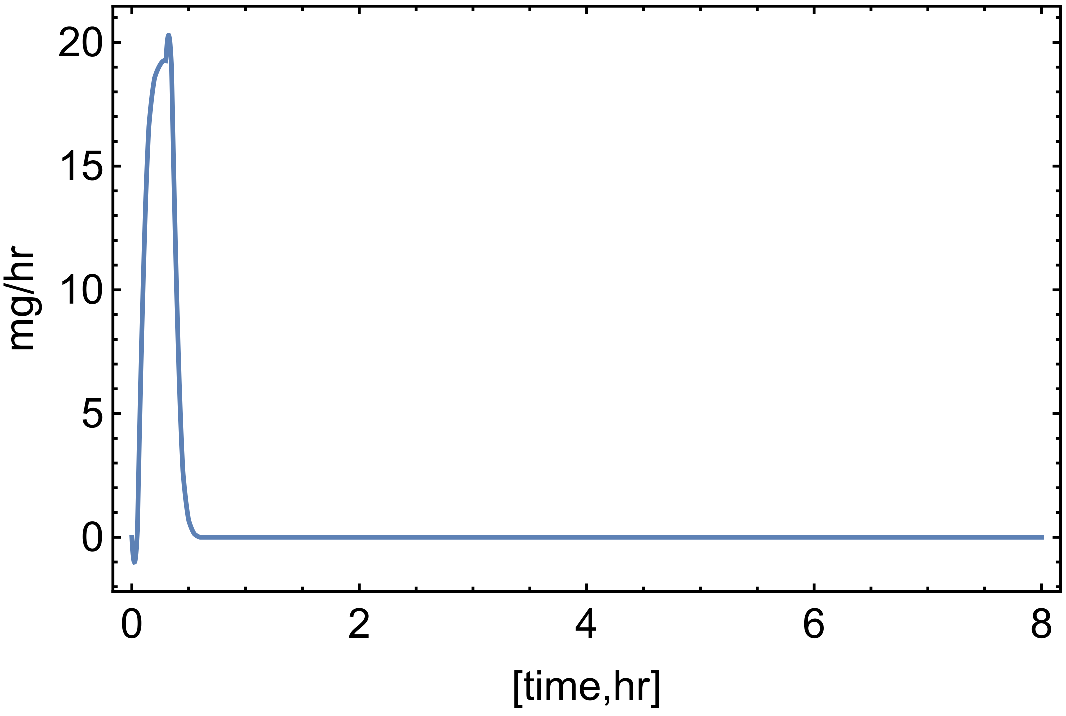

Figure 6.4. Input function of MDZ

Finally, the input function was convolved with the disposition function obtained from the IV bolus data. Before finalizing the simulated oral PK profile, a sensitivity analysis was conducted varying stomach lag time (ranging from 0.01 to 0.2 hours) and the empirical scaling factor (ranging from 0 to 0.1) to find out the best combination and to match the observed F_g.

Table 6.8. Sensitivity analysis changing the stomach lag time (t_{lag}) and empirical scaling factor (f_{CYP}) and their impact on EOC, Fa, F_g, t_{max}, and C_{max}. Bold values are the finalized values for model finalization.

t_{lag} (hr)	f_{CYP}	EOC	F_a	F_g	Actual t_{max}	t_{max} (hr)	Actual C_{max} (µg/L)	C_{max} (µg/L)
0.01	0	0.91	0.91	1	0.4	0.4	62.38	51.20
	0.025	0.92	0.91	0.40		0.4		62.38
	0.05	0.93	0.91	0.27		0.4		62.33
	0.1	0.93	0.91	0.16		0.4		62.86
0.05	0	0.92	0.99	1		0.5		64.76
	0.025	**0.93**	**0.99**	**0.54**		**0.4**		**67.80**
	0.05	0.93	0.99	0.37		0.4		68.93
	0.1	0.93	0.99	0.23		0.4		69.69
0.1	0	0.90	1	1		0.5		66.12
	0.025	0.91	1	0.54		0.5		67.45
	0.05	0.91	1	0.37		0.5		62.38
	0.1	0.91	1	0.22		0.5		67.11
0.2	0	0.86	1	1		0.6		62.38
	0.025	0.87	1	0.54		0.6		67.47
	0.05	0.87	1	0.36		0.6		67.58
	0.1	0.87	1	0.22		0.6		62.38

Based on the sensitivity analysis, it was found that the tlag from 0.01-0.2 hours produced reasonable prediction with tlag 0.2 hour had the lowest EOC and tlag 0.05 hour had the highest EOC (Table 6.8). Also, tlag of 0.2 deviated highest from the experimental tmax. On, the other hand, the empirical scaling factor of 0.025 was found to match the observed F_g. Practically, the tlag and fCYP did not have any impact on Fa. Based on these observations, tlag of 0.05 hour and fCYP of 0.025 was chosen to finalize the model prediction.

Figure 6.5 shows the final model prediction vs the observed data.

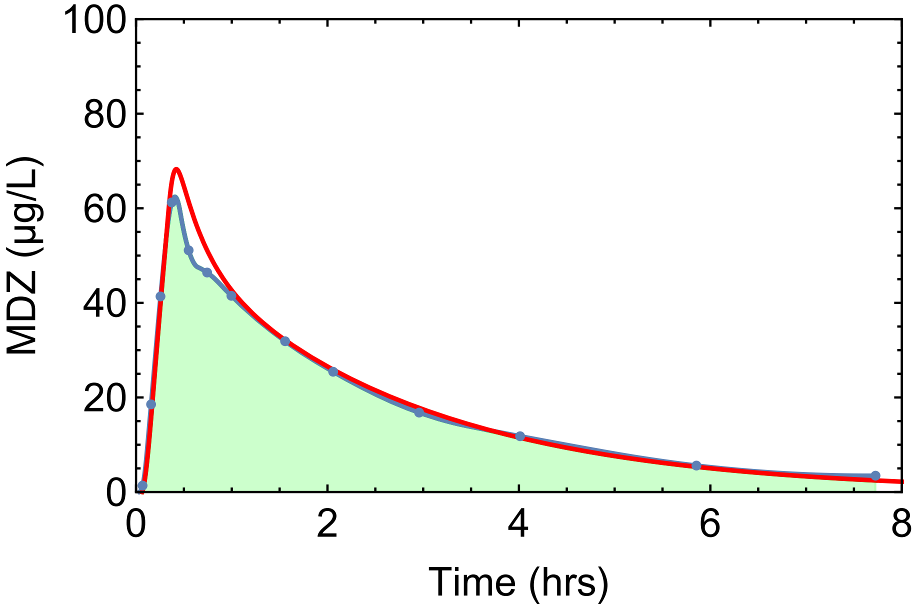

Figure 6.5. Predicted vs observed C-t profiles of MDZ in fasted healthy volunteers using tlag of 0.05 hour and fCYP of 0.025 with an EOC of 0.93.

6.3.1.2 Simulation of Oral MDZ with Regional Expression of CYP3A4 and Atypical kinetics:

The numerical solution of the PDEs presented in the method section produced the following graphs of C1 through C4. These plots helped to clarify and comprehend how MDZ was transported throughout time and the entire length of the gut across the radial compartments. Again, these plots revealed that the upper section of the gut was the principal site via which the MDZ was quickly absorbed (Figure 6.6).

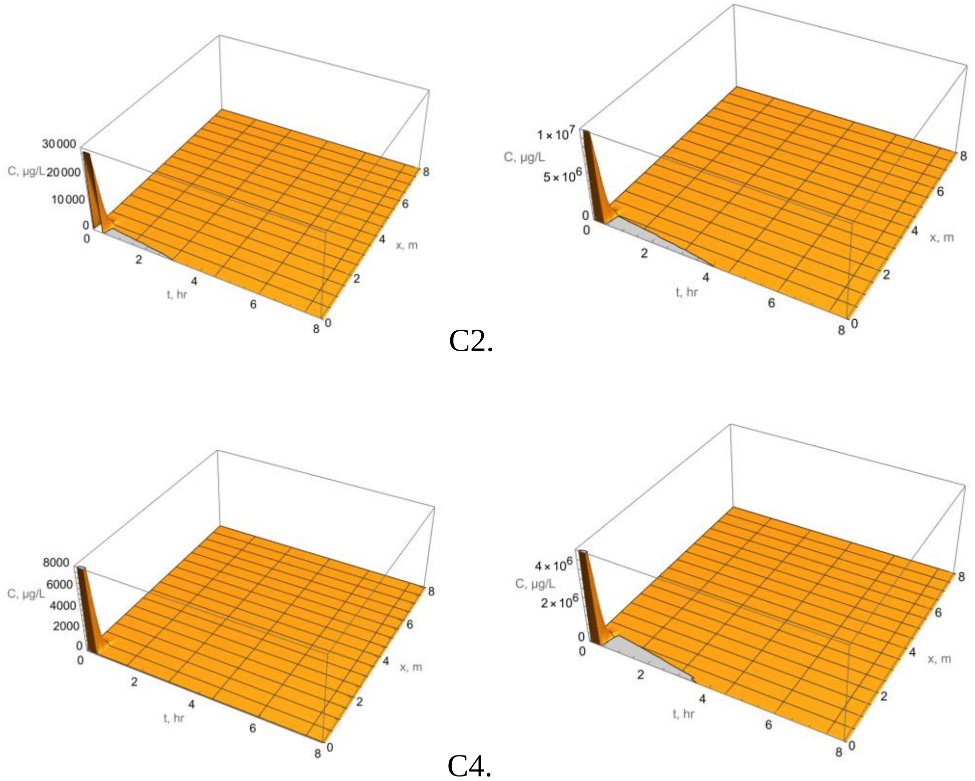

C1. C2.

C3. C4.

Figure 6.6: 3D plots of different radial compartments after numerical solutions. C1: Intestinal lumen, C2: Enterocytic apical membrane, C3: Enterocytic cytosol, and C4: Intracellular lipids.

Using equation 6.22, following input function was obtained after the numerical solution of the PDEs (Figure 6.7):

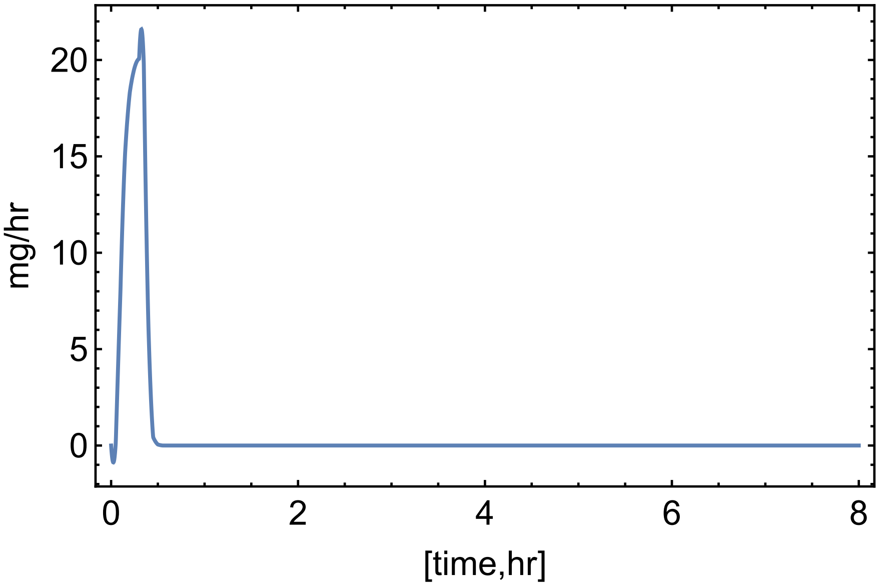

Figure 6.7. Input function of MDZ

Finally, the input function was convolved with the disposition function obtained from the IV bolus data. Before finalizing the simulated oral PK profile, a sensitivity analysis was conducted varying stomach lag time (ranging from 0.01 to 0.2 hours) and the empirical scaling factor (ranging from 0 to 0.2) to find out the best combination and to match the observed F_g.

Table 6.9. Sensitivity analysis changing the stomach lag time (t_{lag}) and empirical scaling factor (f_{CYP}) and their impact on EOC, Fa, F_g, t_{max}, and C_{max}. Bold values are the finalized values for model finalization.

t_{lag} (hr)	f_{CYP}	EOC	F_a	F_g	Actual t_{max}	t_{max} (hr)	Actual C_{max} (µg/L)	C_{max} (µg/L)
0.01	0	0.91	0.89	1	0.4	0.4	62.38	51.20
	0.1	0.89	0.89	0.73		0.4		46.08
	0.2	0.87	0.89	0.57		0.5		38.61
0.05	0	0.92	0.99	1		0.5		64.76
	0.1	**0.93**	**0.99**	**0.52**		**0.4**		**70.68**
	0.2	0.93	0.99	0.21		0.4		71.66
0.1	0	0.90	1	1		0.5		66.12
	0.1	0.91	1	0.51		0.5		68.43
	0.2	0.91	1	0.20		0.4		69.053
0.2	0	0.86	1	1		0.6		66.11
	0.1	0.87	1	0.51		0.6		68.45
	0.2	0.87	1	0.23		0.5		69.077

The tlag between 0.01-0.2 hours generated respectable predictions, with tlag 0.2 hour having the lowest EOC and tlag 0.05 hour having the greatest EOC, according to the sensitivity analysis (Table 6.8). Additionally, the experimental tmax was most greatly deviated by tlag of 0.2. On the other hand, it was discovered that the measured F_g

matched the empirical scaling factor of 0.1. These observations led to the final model prediction being made with a tlag of 0.05 hour and fCYP of 0.1.

Figure 6.9 shows the final model prediction vs the observed data.

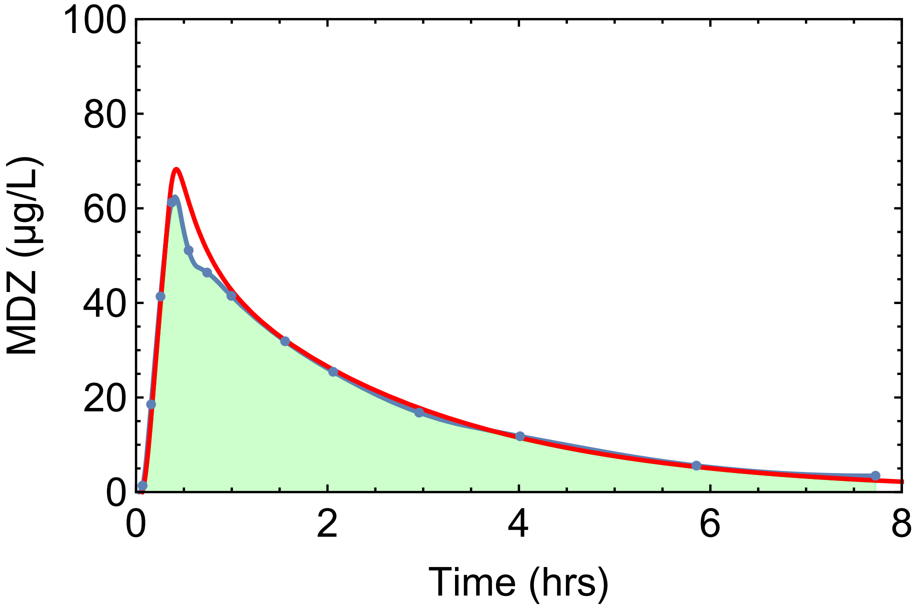

Figure 6.8. Predicted vs observed C-t profiles of MDZ in fasted healthy volunteers using tlag of 0.05 hour and fCYP of 0.1 with an EOC of 0.93.

6.3.2 Simulation of Oral PK of MDZ in SD Rats

MDZ IV bolus and oral data were collected and digitized from a Pfizer group's work (Strelevitz, Foti, & Fisher, 2006). This literature source was chosen due to fact that this had both oral and IV PK studies. Total number of SD rats in each studies were three. Male Sprague-Dawley rats (125-200 g; Charles River, Wilmington, MA) with jugular vein cannulas and free access to water were utilized for oral administration of probe medicines. They were then fed 4 hours after the dosage. The IV bolus dose was 1 mg/kg and the oral dose was 10 mg/kg.

MDZ IV bolus data (Strelevitz et al., 2006) were fitted to the classical two-compartment and three-compartment models. Based on AICc and adjusted R2 values (table 6.10), it was found that the two-compartmental model was a better fit to explain the observed IV data. The intercompartmental first-order transfer rate constants and the volume of the central compartment was parameterized from the best fit model and recorded as the disposition functions (table 6.11) which was convolved with the input function to simulate the oral PK profile of MDZ in rats.

Table 6.10. Model comparison functions for IV bolus data

	2C model	**3C model**
Adjusted R^2	0.99	0.99
AICc	107.89	118.28

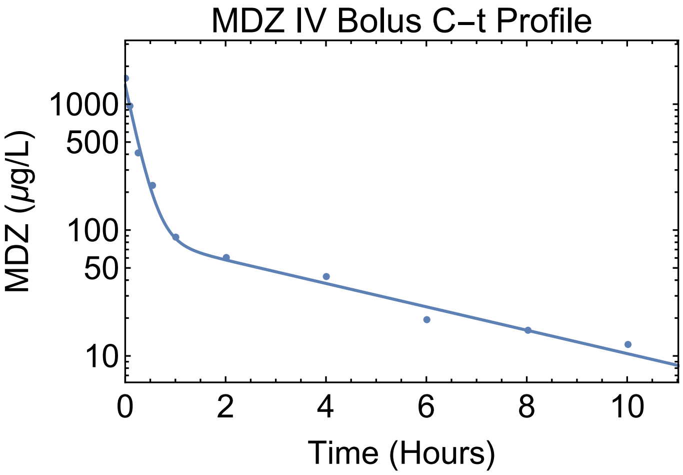

Figure 6.9. Observed (dots) versus 2C predicted (solid line) response of MDZ IV bolus

Table 6.11. Kinetic parameters as disposition function. Data presented as the parameter estimates (S.E.)

Parameters	**Estimates (S.E.)**
k_{12} (hour^{-1})	2.25 (0.43)
k_{21} (hour^{-1})	0.48 (0.089)
k_{10} (hour^{-1})	1.99 (0.25)
V_c (L/kg)	0.71 (0.099)

The PDEs described in the method section were numerically solved and the numerical solution provided the following plots of C1 through C4. These plots were helpful to visualize and understand the MDZ transport across the radial compartments over time and along the length of the intestine. From these plots, it was found that the MDZ was rapidly absorbed mainly through the upper part of the rat intestine (Figure 6.10).

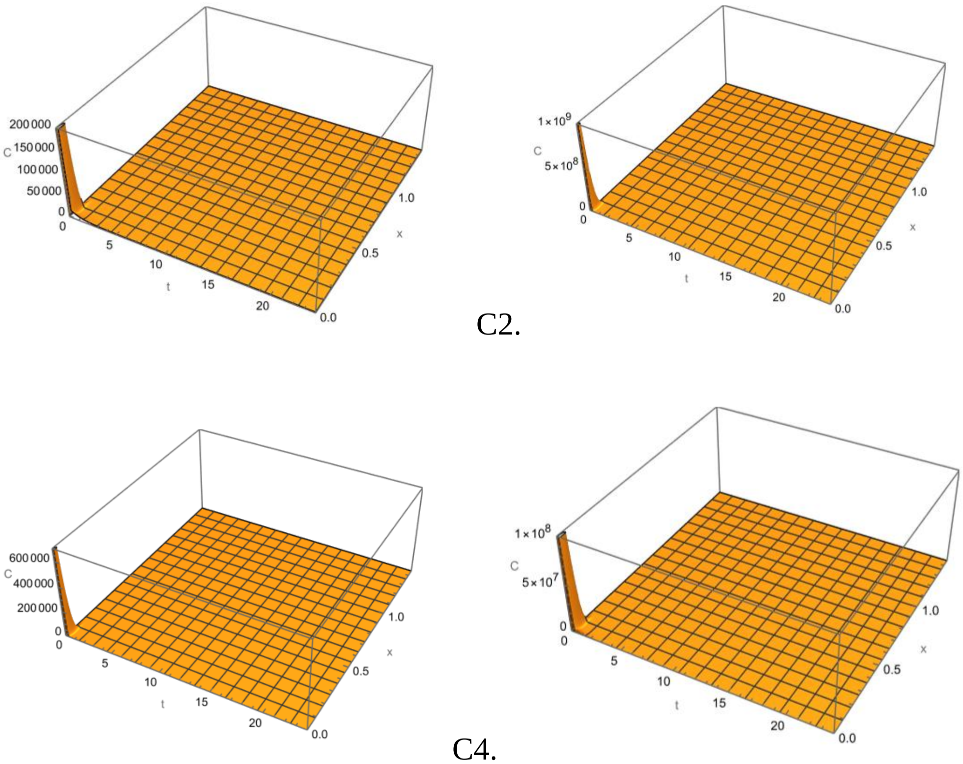

C1.

C2.

C3.

C4.

Figure 6.10 3D plots of different radial compartments after numerical solutions. C1: Intestinal lumen, C2: Enterocytic apical membrane, C3: Enterocytic cytosol, and C4: Intracellular lipids.

Following input function of MDZ in rats was obtained after the numerical solution of the PDEs (Figure 6.11):

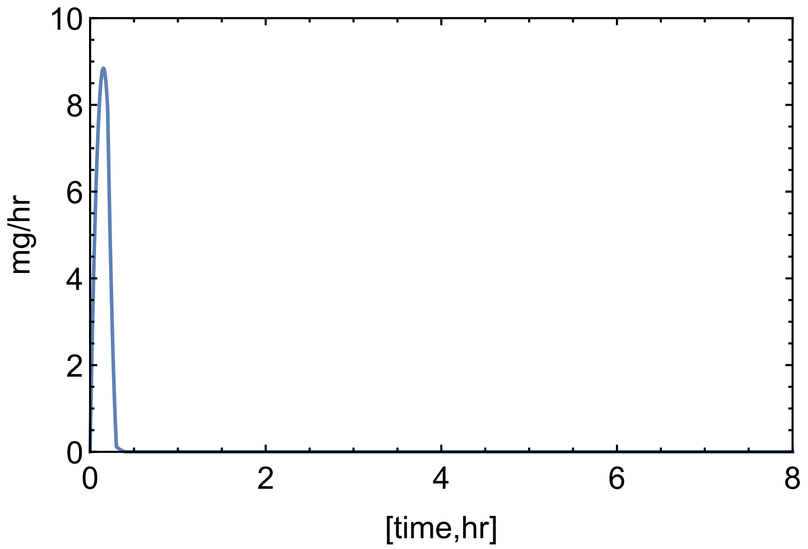

Figure 6.11. Input function of MDZ in rats

Finally, the input function was convolved with the disposition function obtained from the IV bolus data. Before finalizing the simulated oral PK profile, a sensitivity analysis was conducted varying stomach lag time (ranging from 0.01 to 0.1 hours) and the empirical scaling factor (ranging from 0 to 0.01) to find out the best combination and to match the observed F_g.

Table 6.12. Sensitivity analysis changing the stomach lag time (t_{lag}) and empirical scaling factor (f_{CYP}) and their impact on EOC, Fa, F_g, t_{max}, and C_{max}. Bold values are the finalized values for model finalization.

t_{lag} (hr)	f_{CYP}	EOC	F_a	F_g	Actual t_{max}	t_{max} (hr)	Actual C_{max} (µg/L)	C_{max} (µg/L)
0.01	0	0.85	1	1	0.3	0.3	211.066	233.26
	0.001	0.82	1	0.50		0.3		245.9
	0.01	0.80	1	0.093		0.2		266.84
0.05	0	0.83	1	1		0.3		237.31
	0.001	**0.84**	**1**	**0.49**		**0.3**		**248.88**
	0.01	0.84	1	0.10		0.3		247.96
0.1	0	0.79	1	1		0.4		249.25
	0.001	0.79	1	0.50		0.4		252.34
	0.01	0.80	1	0.085		0.3		268.82

Based on the sensitivity analysis, it was found that the tlag from 0.05-0.1 hours had an impact on the tmax but the impact was really very minor. However, the tlag of 0.05 hour was chosen for the final model. The empirical scaling factor was ranged from 0 to 0.01. The scaling factor of 0.001 was used to match the result with rat MDZ F_g. Most of the cases, the EOC ranged from 0.80-0.85 probably due to the variable disposition function in different rats. Because the exact same rats were not used for the IV and oral PK studies. Finally, the tlag 0.05 hour and fCYP of 0.001 were chosen for the final model with an EOC of 0.84.

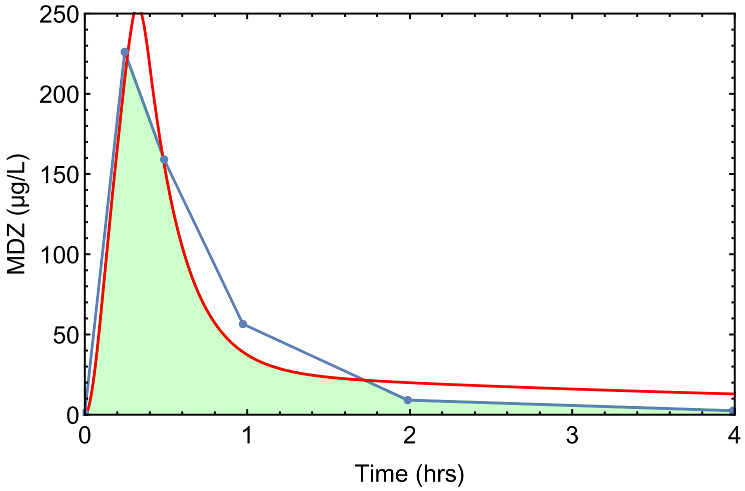

Figure 6.12. Predicted vs observed C-t profiles of MDZ in fasted SD rat using tlag of 0.05 hour and fCYP of 0.001 with an EOC of 0.84.

6.3.3 Simulation of Oral PK of NCD in Humans

NCD IV bolus data (Higuchi & Shiobara, 1980) and oral data (Graham et al., 1985) were collected from the literature. Two different sources were chosen due to the fact that no literature had the NCD PK data in same volunteers for the IV bolus and oral solution. The IV bolus study (Higuchi & Shiobara, 1980) included healthy male individuals (n=3, 52-66 kg, 24-40 years old). The medication was given intravenously as a solution in physiological saline. Using a heparinized syringe, blood samples were taken from the cubital vein. The oral dose was given to four young healthy male volunteers in fasted condition (Graham et al., 1985). The day before the oral dose, they were instructed to fast.

NCD IV bolus data (Higuchi & Shiobara, 1980) were fitted to the classical two-compartment and three-compartment models. Based on AICc and adjusted R2 values (table 6.13), it was found that the two-compartmental model was a better fit to explain the observed IV data. The intercompartmental first-order transfer rate constants and the volume of the central compartment was parameterized from the best fit model and recorded as the disposition functions (table 6.14) which was convolved with the input function to simulate the oral PK profile of NCD.

Table 6.13. Model comparison functions for IV bolus data

	2C model	**3C model**
Adjusted R^2	0.99	0.99
AICc	61.88	Did not converge

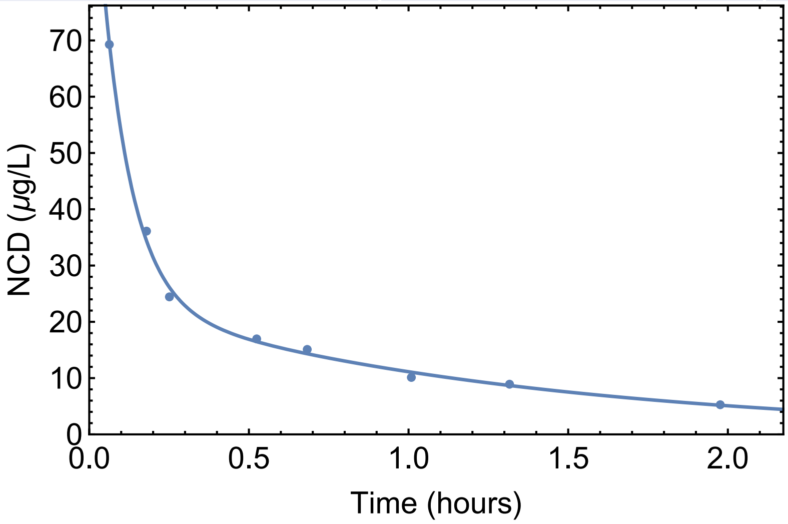

Figure 6.13. Observed (dots) versus 2C predicted (solid line) response of NCD IV bolus (0.885 mg)

Table 6.14. Kinetic parameters as disposition function. Data presented as the parameter estimates (S.E.)

Parameters	**Estimates (S.E.)**
k_{12} (hour^{-1})	5.74 (0.85)
k_{21} (hour^{-1})	2.88 (0.42)
k_{10} (hour^{-1})	2.92 (0.27)
V_c (L)	12.10 (0.98)

The PDEs described in the method section were numerically solved and the numerical solution provided the following plots of C1 through C4. These plots were helpful to visualize and understand the NCD transport across the radial compartments over time and along the length of the intestine. From these plots, it was found that the NCD was rapidly absorbed mainly through the upper part of the intestine. However, due to the lower f_{um} value of NCD, it was found to reside in the lipophilic compartments including apical membrane (C2) and intracellular lipid (C4) significantly higher than the intestinal lumen (C1) and cytosol (C3).

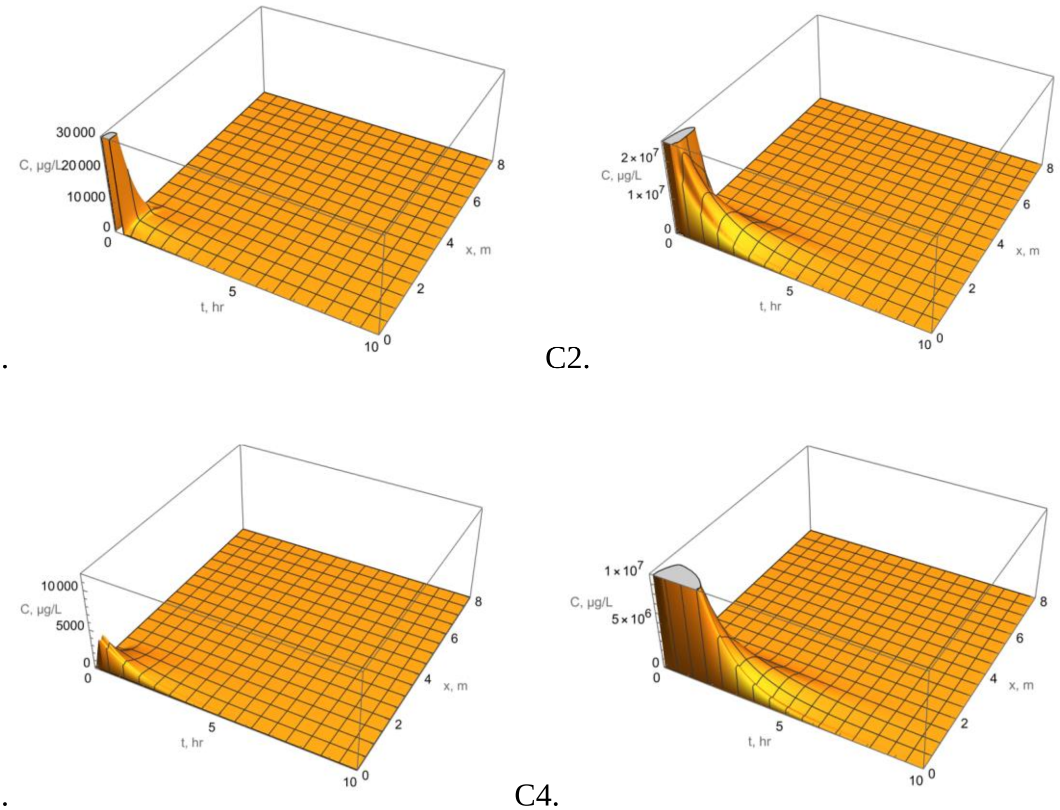

C1. C2.

C3. C4.

Figure 6.14: 3D plots of different radial compartments after numerical solutions. C1: Intestinal lumen, C2: Enterocytic apical membrane, C3: Enterocytic cytosol, and C4: Intracellular lipids.

Following input function of NCD in human was obtained after the numerical solution of the PDEs (Figure 6.15):

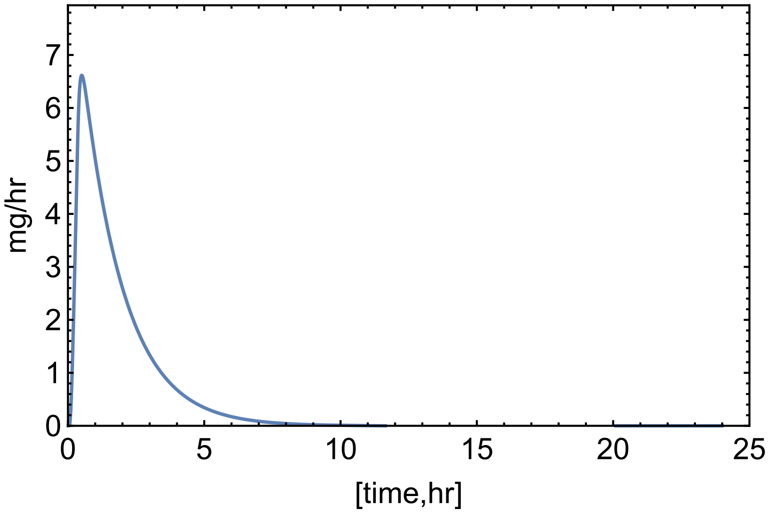

Figure 6.15. Input function of NCD in human

Finally, the input function was convolved with the disposition function obtained from the IV bolus data. Before finalizing the simulated oral PK profile, a sensitivity analysis was conducted varying cytosolic lipid volume (ranging from 7% to 3.5%), stomach lag time (ranging from 0.01 to 0.2 hours) and the empirical scaling factor (ranging from 0 to 0.1) to find out the best combination.

Table 6.15. Sensitivity analysis changing the cytosolic lipid volume, stomach lag time (t_{lag}) and empirical scaling factor (f_{CYP}) and their impact on EOC, Fa, F_g, t_{max}, and C_{max}. Grey values are the finalized values for model finalization.

Lipid volume	t_{lag} (hr)	f_{CYP}	EOC	F_a	F_g	Actual t_{max}	t_{max} (hr)	Actual C_{max} (µg/L)	C_{max} (µg/L)
	0.01	0	0.75	0.85	1		1.8		19.89
		0.001	0.85	0.86	0.62		1.5		25.59

7%		0.002	0.89	0.87	0.47	0.5	1.2	39.60	29.50
		0.2	0.72	0.86	0.011		0.4		91.06
	0.05	0	0.78	0.99	1		1.7		21.96
		0.001	0.84	0.99	0.75		1.5		25.91
		0.002	0.87	0.99	0.60		1.3		29.35
		0.2	0.71	0.99	0.014		0.4		99.20
	0.1	0	0.76	0.99	1		1.8		21.89
		0.001	0.82	0.99	0.75		1.6		25.59
		0.002	0.86	1	0.60		1.4		29.13
		0.2	0.73	1	0.014		0.5		101.21
	0.2	0	0.74	0.99	1		1.9		21.78
		0.001	0.79	0.99	0.75		1.7		25.58
		0.002	0.83	1	0.60		1.5		29.01
		0.2	0.74	1	0.014		0.6		101.83
3.5%	0.01	0	0.88	0.85	1		1.3		27.051
		0.001	0.91	0.86	0.62		1		35.10
		0.002	0.90	0.87	0.47		0.8		40.11
		0.2	0.71	0.87	0.011		0.4		92.23
	0.05	0	0.88	0.99	1		1.2		32.25
		0.001	**0.88**	**0.99**	**0.75**		**1**		**37.50**
		0.002	0.87	0.99	0.60		0.9		42.26
		0.2	0.70	0.99	0.015		0.4		103.93
	0.1	0	0.87	1	1		1.3		31.94

		0.001	0.87	1	0.75		1.1		37.17
		0.002	0.86	1	0.60		1		41.53
		0.2	0.70	1	0.014		0.5		104.041
	0.2	0	0.84	1	1		1.4		32.07
		0.001	0.80	1	0.75		1.7		25.58
		0.002	0.84	1	0.60		1.1		41.55
		0.2	0.70	1	0.014		0.		104.42

Based on the sensitivity analysis, it was found that the tlag from 0.01-0.2 hours produced reasonable prediction with tlag 0.2 hour had the lowest EOC and tlag 0.05 hour had the highest EOC (Table 6.14). The tlag of 0.01 hour was found to produce F_a significantly lower than 1 (observed NCD F_a=1), which is why it was eliminated from further consideration. The empirical scaling factor of 0.001 was found to match closely with the observed and predicted F_g of NCD from the literature. The lipid volume did not have a very significant effect on the EOC when the tlag was 0.05-0.2 hour and the fCYP was 0.0005. However, the 3.5% lipid volume had the lowest deviation from the observed tmax of NCD. Based on these observations, lipid volume both 7% and 3.5%, tlag 0.05 hour, and fCYP of 0.001 were chosen for the finalization of the model prediction.

Figure 6.16 shows the final model prediction vs the observed data.

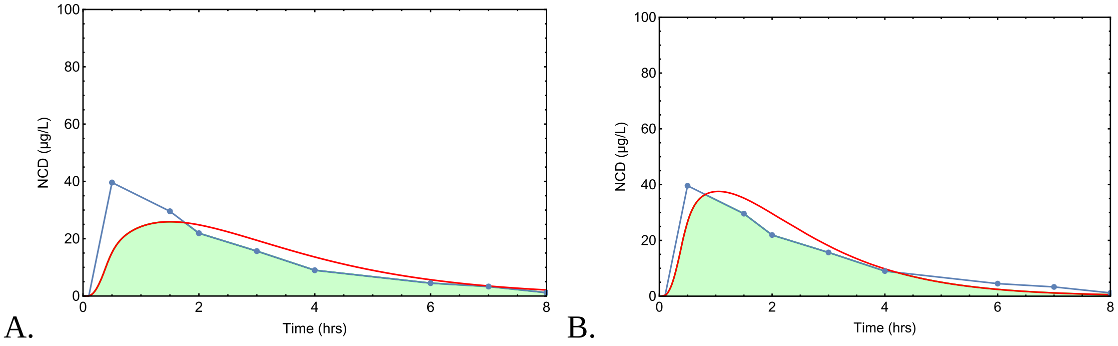

Figure 6.16. Predicted vs observed C-t profiles of NCD in fasted healthy volunteers using tlag of 0.05 hour and fCYP of 0.001 with an EOC of 0.84 when the cytosolic lipid volume is assumed to be 7% of the enterocyte volume (A) and an EOC of 0.88 when the cytosolic lipid volume is assumed to be 3.5% of the enterocyte volume (B).

6.3.4 Simulation of Oral PK of NCD in SD Rats

NCD IV bolus and oral data in SD rats were collected and digitized from the literature (Jung et al., 2022). This literature source was chosen due to fact that this source has both the IV bolus as well as oral solution PK data. Dosing solutions were made in 5 percent dextrose solution or 5 percent dextrose solution-ethanol (85:15, v/v). For intravenous administration, the dosing solutions had a concentration of 1 mg/ml and for oral administration, 2.5 mg/ml. Nicardipine was given in dosages of 1 mg/kg for intravenous administration and 10 mg/kg for oral administration. The least number of animals necessary for a normal pharmacokinetic study was three rats, and this was done in accordance with the 3Rs (replacement, reduction, and refinement).

NCD IV bolus data were fitted to the classical two-compartment and three-compartment models. Based on AICc and adjusted R2 values (table 6.16), it was found that the two-compartmental model was a better fit to explain the observed IV data. The intercompartmental first-order transfer rate constants and the volume of the central compartment was parameterized from the best fit model and recorded as the disposition functions (table 6.17) which was convolved with the input function to simulate the oral PK profile.

Table 6.16. Model comparison functions for IV bolus data

	2C model	**3C model**
Adjusted R^2	0.99	0.99
AICc	102.64	Infinity

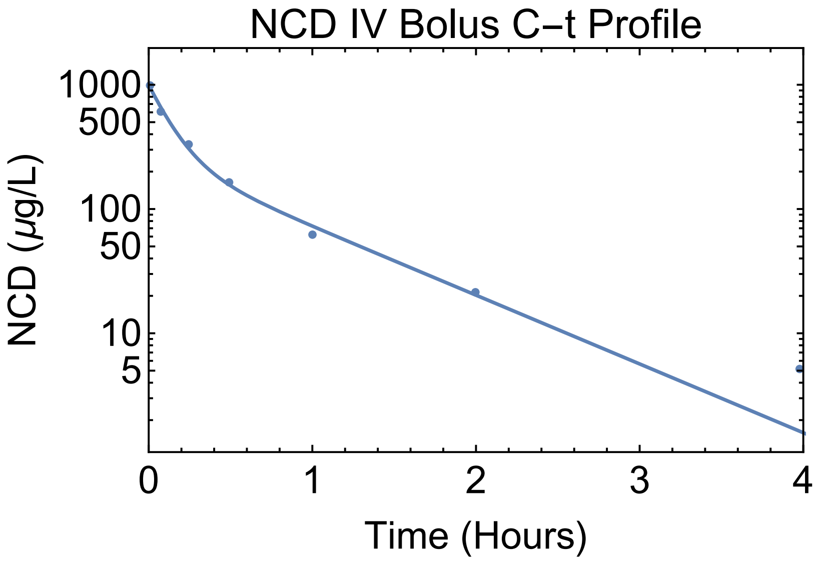

Figure 6.17. Observed (dots) versus 2C predicted (solid line) response of MDZ IV bolus (5 mg)

Table 6.17. Kinetic parameters as disposition function. Data presented as the parameter estimates (S.E.)

Parameters	Estimates (S.E.)
k_{12} (hour $^{-1}$)	2.61 (0.76)
k_{21} (hour $^{-1}$)	2.90 (1.18)
k_{10} (hour $^{-1}$)	3.31 (0.29)
V_c (L/kg)	1.0022 (0.059)

The PDEs described in the method section were numerically solved and the numerical solution provided the following plots of C1 through C4. These plots were helpful to visualize and understand the NCD transport across the radial compartments over time and along the length of the intestine. From these plots, it was found that the NCD was rapidly absorbed mainly through the upper part of the intestine. However, due to the lower f_{um} value of NCD, it was found to reside in the lipophilic compartments including apical membrane (C2) and intracellular lipid (C4) significantly higher than the intestinal lumen (C1) and cytosol (C3).

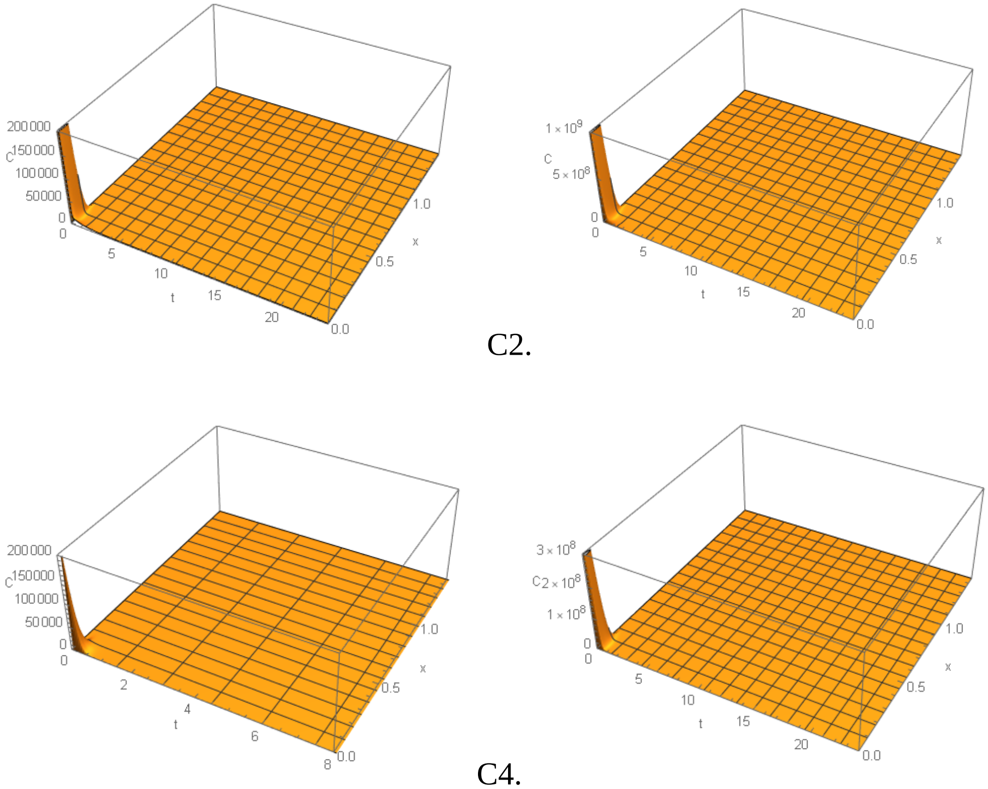

C1. C2.

C3. C4.

Figure 6.18: 3D plots of different radial compartments after numerical solutions. C1: Intestinal lumen, C2: Enterocytic apical membrane, C3: Enterocytic cytosol, and C4: Intracellular lipids.

Following input function was obtained after the numerical solution of the PDEs:

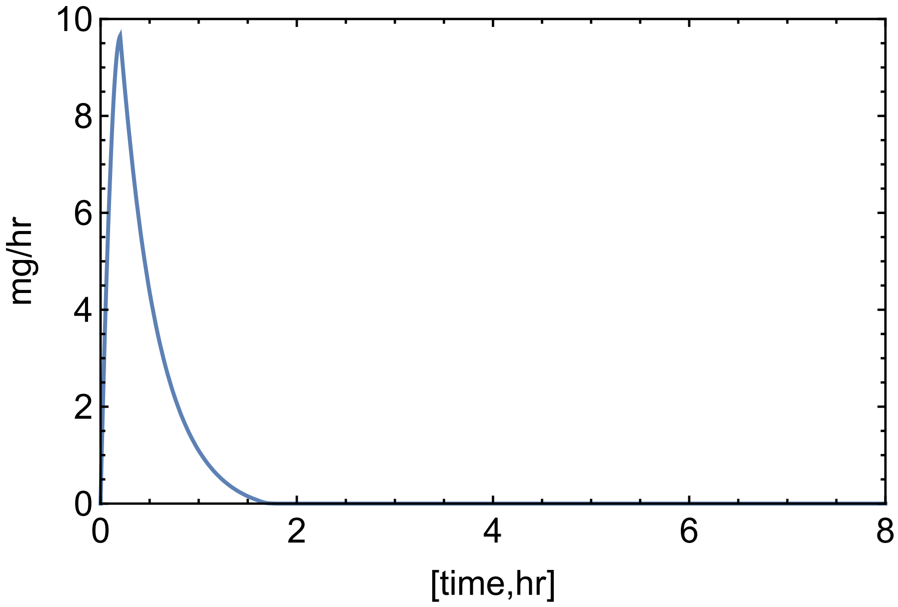

Figure 6.19. Input function of NCD in SD rats

Finally, the input function was convolved with the disposition function obtained from the IV bolus data. Before finalizing the simulated oral PK profile, a sensitivity analysis was conducted varying cytosolic lipid volume (ranging from 7% to 3.5%), stomach lag time (ranging from 0.05 to 0.1 hours) and the empirical scaling factor (ranging from 0 to 0.1) to find out the best combination.

Table 6.18. Sensitivity analysis changing the cytosolic lipid volume, stomach lag time (t_{lag}) and empirical scaling factor (f_{CYP}) and their impact on EOC, Fa, F_g, t_{max}, and C_{max}. Grey values are the finalized values for model finalization.

Lipid volume	t_{lag} (hr)	f_{CYP}	EOC	F_a	F_g	Actual t_{max}	t_{max} (hr)	Actual C_{max} (µg/L)	C_{max} (µg/L)
3.5 %	0.05	0	0.88	1	1		0.4		166.94

		0.001	**0.88**	**1**	**0.80**	0.4	**0.4**	149.81	**149.0047**
		0.005	0.89	1	0.45		0.4		162.19
		0.05	0.77	1	0.072		0.2		283.63
	0.1	0	0.73	1	1		0.6		92.48
		0.001	0.77	1	0.80		0.6		105.57
		0.005	0.84	1	0.44		0.5		145.37
		0.05	0.81	1	0.071		0.3		297.52
7 %	0.05	0	0.84	1	1		0.5		131.57
		0.001	0.81	1	0.80		0.5		107.57
		0.005	0.83	1	0.44		0.5		112.15
		0.05	0.82	1	0.072		0.3		235.99
	0.1	0	0.61	1	1		0.9		60.25
		0.001	0.65	1	0.80		0.8		69.11
		0.005	0.76	1	0.44		0.6		100.19
		0.05	**0.85**	**1**	**0.067**		**0.3**		**245.22**

Based on the sensitivity analysis, it was found that the tlag from 0.05-0.1 hours had an impact on the tmax but the impact was really very subtle. The empirical scaling factor was ranged from 0 to 0.05. The scaling factor of 0.001 was used to compare the result with human NCD data and the how the same scaling factor works for both if this species. However, this 0.001 fCYP was found to significantly overpredict the F_g. The fCYP of 0.05 was found to closely approximate with the literature values. Finally, the cytosolic lipid volume had some impact on the EOC and but when the tlag was fixed at 0.1 hour and the fCYP at 0.05, the EOC was higher for 7%, rather than for 3.5%. However, in this case the Cmax was significantly over predicted. Figure 6.xx shows both case when fCYP of 0.001 was used with a lag time 0.05 hour (similar to human NCD model) assuming 3.5% cytosolic lipid volume and fCYP of 0.05 with lag time of 0.1 hour assuming 7% cytosolic lipid volume.

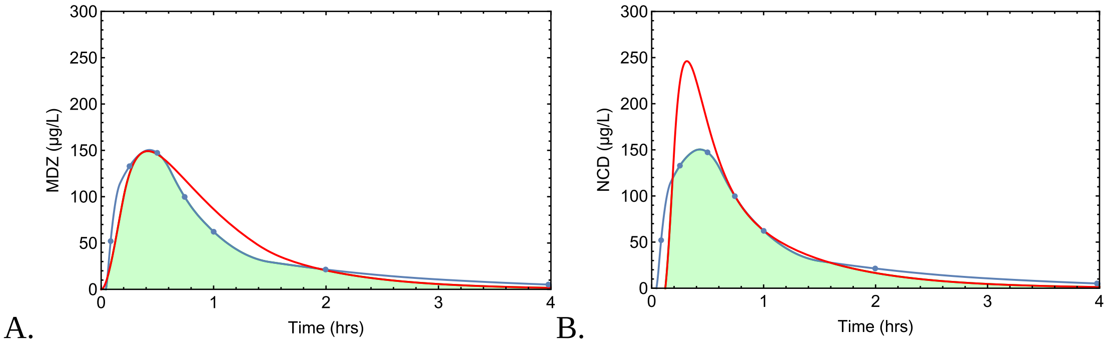

Figure 6.20: A. fCYP of 0.001 was used with a lag time 0.05 hour (similar to human NCD model) assuming 3.5% cytosolic lipid volume and B. fCYP of 0.05 with lag time of 0.1 hour assuming 7% cytosolic lipid volume.

6.4 Discussion and Conclusions

The majority of medications that enter the systemic circulation need a limited amount of time to spread evenly across the available body area. This feature becomes especially clear after a quick intravenous infusion. Drug concentration in the plasma will drop faster during this distributive phase than it will during the post-distributive phase. Depending on how often blood samples are obtained, a distributive phase may or may not be seen. A distributive phase might span few minutes, many hours, or even several days. The levels of the drug in all tissues and fluids connected to the central compartment should decrease more quickly during the distributive phase than during the post-distributive phase after an intravenous administration of a medication that shows multicompartment pharmacokinetics. In contrast, during the distributive phase, drug levels in tissues with poor blood flow initially increase, then reach a top point, and then start to decrease. After some time, a pseudo-distribution equilibrium is reached between the core compartment's tissues and fluids and the less perfused or accessible tissues. After pseudo-distribution equilibrium has been reached, a mono-exponential process exhibiting kinetic homogeneity with regard to drug levels in all bodily fluids and tissues is used to characterize the loss of drug from the plasma. Depending upon the extent of post-distribution equilibrium and number of kinetically similar tissues, multi-compartment PK models are developed.

For the successful prediction of oral PK profile using continuous intestinal absorption model requires a comprehensive and in-depth information about a number of input parameters and disposition function. Without proper characterization of these would result in underprediction or overprediction of the oral AUC leading to poor EOC which means a significant deviation from the observed data. One of the most key factors to collect while working with this absorption model is the disposition function, since this disposition function will determine the overall drug distribution and elimination reflecting in the final predicted oral PK profile. Disposition functions are usually collected from the IV bolus data. For the proper characterization of the disposition function using classical compartmental PK models, it requires the blood collection and sample analysis for a long time, so that the tail end of the IV PK profile is sufficiently determined. Usually, blood collection up to 5 half-lives might ensure sufficient blood collection, given that the sensitivity of LC-MS/MS will be able to capture the post-distributive phase too. If the elimination phase of the IV data is not correctly estimated, it may lead to faulty estimates of intercompartmental rate constants and the elimination rate constants. For instance, if a drug has three compartmental characteristics, but due to shorter blood collection time points, or due to the limitation of the analytical sensitivity, if the IV bolus PK data displays two-compartment characteristics, it can significantly overpredict the elimination rate constant leading to the rapid decline of the oral PK profile. The elimination half-life of MDZ and NCD in humans are 6.8 (Nordt & Clark, 1997) and 8.6 (J.-S. Choi et al., 2009) hours, respectively. The IV data used for the data analysis did not have sufficient blood collection time point. Simulation of oral MDZ and NCD might have been compromised due to the lack of sufficient IV PK profile. It can be expected to improve the EOC of both of the drugs if the disposition functions would be more accurate, meaning extracted from the IV data which had sufficient blood collection time points.

There are a number of models to calculate the fraction escaping gut metabolism (F_g) from *in vitro* data discussed in chapter 4. The determination of *in vivo* F_g has been a challenging job so far for several reasons. For example, if a drug does not have any lung metabolism, and if the drug is 100% absorbed from the gut (F_a=1), the comparison of dose normalized AUC from IV bolus vs oral data can provide an estimation of $F_g.F_h$. Now, if the drug is given into the hepatic portal vein rather than orally, it can provide only the F_h, from which F_g can be separated from $F_g.F_h$. Another method has been used for MDZ (Paine et al., 1996; Park et al., 1989) leveraging anhepatic phases of liver transplantation patients, in which phase practically there is no liver. In this case there can be a direct estimation of F_g. However, given confounding factors associated with the use of anesthetics, surgery, and the sometimes poor health of patients, interpretation of this PK data is hard. Due to ethical, practical, and financial considerations, these investigations are rarely conducted on humans (Lennernas, Nylander, & Ungell, 1997; Lennernäs et al., 1992; Peters, Jones, Ungell, & Hatley, 2016; van de Kerkhof et al., 2007; Yau et al., 2017). However, one of the most popular methods to estimate F_g has been the use of grapefruit juice (GFJ) as the CYP3A inhibitor. The dose-normalized AUC ratios with and without the GFJ can approximate F_g for drugs which are exclusively metabolized by CYP3A including midazolam, felodipine, cyclosporine, alfentanil etc. However, this method is also reliant on the assumptions that the factors limiting oral absorption including low Fa, or efflux transporter involvements minimal, and transporter mediated uptake is absent (Peters et al., 2016; Yau et al., 2017).

In this thesis, intestinal metabolism has been incorporated into the continuous intestinal absorption model. Initially, single intrinsic clearance has been used along with an empirical scaling factor to match the observed F_g. However, the major limitations of this method might be:

1. The intrinsic clearance might be concentration dependent as observed in the atypical kinetics.
2. The regional expression of enzymes involved in the intestinal metabolism varies through the intestine, which was not considered for this method.
3. For drugs metabolized by multiple enzymes, the relative contribution of each enzyme was not included in this model.
4. Different scaling factors for different drugs.

Whereas this approach offers a relatively simple framework to estimate the F_g, in future it will need a lot of drugs to decide upon a global scaling factor. If the global scaling factor does not work, the drugs can be categorized based on their chemical and metabolic similarity to produce a single scaling factor within the subgroups. Also, due to species difference, it was expected to have different scaling factor for the same drug in human's vs rats. This empirical scaling factors can be further modified based on the species involved. The regional expression of the all the intestinal enzymes, and their relative contribution for the drug's metabolism are critical information if one wants to develop mechanistic intestinal model for drugs. However, all these information in different species are yet to be resolved and there is significant inter-laboratory variability for the available information. Given the improvement in analytical ability, it might be possible in future to capture the regional enzyme expression profiles of different species to incorporate into the intestinal models. For the drugs which are transporter substrate, both efflux and uptake transporters (mainly BCS class II and IV drugs), regional expression of intestinal transporters are also very important to consider for the absorption modeling. In case of efflux transporter involvement including Pgp for a particular drug, without considering might lead to significant overprediction of intestinal availability. Opposite scenario might be observed if the drug is uptake transporter substrate including OATP2B1 in the absorption model.

Atypical kinetics is often observed in drug metabolism due to the fact that the CYP enzymes can accommodate multiple molecules at the same time within the binding site (K. R. Korzekwa et al., 1998; Tracy, 2006). There are a number of literatures that address the atypical kinetics and its importance in the characterization of *in vitro* metabolic profile of a drug (K. R. Korzekwa et al., 1998; Paragas et al., 2021; Tracy, 2006; Z. Wang et al., 2021). For the substrate inhibition ($K_{m1}<K_{m2}$ and $k_{cat1}>k_{cat2}$) and biphasic kinetics ($K_{m1}<K_{m2}$ and $k_{cat1}<k_{cat2}$), the atypical kinetics might not be obvious if the drug concentration is not high enough. Notably, the plasma drug concentration usually does not reach high enough to show substrate inhibition or biphasic kinetics. Which is why, for the hepatic clearance estimation, often Michaelis-Menten can be used except for drugs which shows sigmoidal kinetics when $K_{m1}>K_{m2}$ or $k_{cat1}<k_{cat2}$. However, in the intestinal region, drug concentration can be really high in case of oral dosing, specifically solution dose. If the drug is highly permeable, it might produce significantly high enterocytic drug concentration leading to atypical kinetics. Michaelis-Menten kinetics show concentration-independent intrinsic clearance whereas atypical kinetics will have concentration dependence. The summary is the contribution of atypical kinetics might be more apparent in the intestine rather than the liver. Which is why, using *in vitro* intrinsic clearance data to calculate F_g should be done with caution if the drug is showing atypical kinetics. However, to properly use the atypical kinetics in the absorption model, we will definitely need the regional expression of the enzymes responsible for the metabolism of the drug in question.

Another important thing to consider is the cytosolic lipid content in the enterocytes. There are a number of lipids available in the enterocyte cytosols including cholesterol, triglycerides (TG), triacylglycerol (TAG), diacylglycerol (DAG), ceramides, and phospholipids including sphingomyelins, phosphatidylcholine (Beilstein, Carrière, Leturque, & Demignot, 2016; Demignot, Beilstein, & Morel, 2014). The lipid content is also dependent on the fasted versus fed condition and the type of food present in the gut

(Beilstein et al., 2016; Demignot et al., 2014; J. A. Kulkarni et al., 2019; Poovi & Damodharan, 2018; Sedic et al., 2018). However, the phospholipid content remains relatively constant. Usually, drugs partition into the phospholipids based on their lipophilicity. In the absorption model, a 7% cytosolic lipid volume has been used based on previously published paper of continuous intestinal absorption model (Nagar et al., 2017; Radice et al., 2022), given that no literature has been found exactly on the phospholipid percentage in enterocytes. This lipid content is particularly important for those drugs which are highly partitioned into the microsomes including nicardipine, felodipine, mibefradil, etc. However, given the lack of appropriate literature data, a sensitivity analysis is always an alternative method to check if the lipid volume has any impact on these drugs oral PK profile.

One of the most impactful drug parameters that is used in this absorption model in the fraction unbound in microsomes (f_{um}), which is further used to calculate the tissue to plasma partition coefficient (Kp). This is particularly important if the drug is highly partitioned into the microsomes rendering less free drugs in the biological matrix. NCD is a highly partitioned drug. Initially, following the standard protocols of equilibrium dialysis, its f_{um} was found to be 0.12. However, to ascertain that the equilibrium has been reached, another experiment was conducted adding drug to the receiver compartment using the similar incubation protocols mentioned in chapter 3. However, adding the drug in the receiver compartment increased the f_{um} from 0.13 to 0.17 (Appendix A), which is a clear indication that the equilibrium was not reached in the previous experiment. However, it might be safe to assume that the f_{um} of NCD lies between 0.12 to 0.17 plus-minus the standard error associated with this. Further research might be needed to capture the exact f_{um}, probably using a higher incubation time, or reducing the microsomal protein concentration, or both.

For the simulation of MDZ oral PK profile, the tlag of 0.05 hour was found to generate the highest EOC, matching the exact tmax, and with a reasonably close Cmax to the observed value. From chapter 4, intrinsic clearance of 0.33 mL/min/mg of HIM was taken as the CL_m in the absorption model. The empirical scaling factor (fCYP) of 0.025 was finalized based on the observed F_g. The value of fCYP will change if the unit of intrinsic clearance is changed. Since MDZ is a BCS class I drug, any intestinal transporter involvement is highly unlikely. Also, midazolam is known to be highly permeable Pgp substrate (Tolle-Sander, Rautio, Wring, Polli, & Polli, 2003). This means that, MDZ might bind to Pgp but its permeability is not limited by Pgp. This is why, Pgp has not been included in the absorption modeling of MDZ.

Only for the case of MDZ oral PK in humans, regional expression of CYP3A was available (Bruyere et al., 2010). Which is why, concentration dependent intrinsic clearance using atypical kinetics was possible to incorporate into the absorption model for this purpose. However, it did not statistically improve the oral PK profile prediction, but in this case the scaling factor reduced to 0.1. More in depth knowledge about the regional expression and *in vitro* metabolic profile with atypical kinetics might lead to lack of necessity of the scaling factor (f_{CYP}=1) in future given that all knowledge gaps from *in vitro* to *in vivo* translation are fulfilled.

In case of NCD in humans, cytosolic lipid volumes were reduced to 3.5% to see if there is any improvement in prediction. Reduced cytosolic lipid improved the EOC. NCD is a highly partitioned drug with an f_{um} of 0.12. Which is why it was found to reside significantly higher in the lipophilic radial compartments than the hydrophilic compartments. The fCYP of 0.001 was chosen to match the observed F_g. NCD is a BCS class II drug, meaning that efflux transporter might play a significant role in its absorption. However, NCD is a Pgp substrate with a relatively higher IC50. Also, the efflux ratio of NCD is significantly lower than 2 (J.-S. Choi et al., 2009; Katoh et al., 2000). It was quite expected that the incorporation of Pgp into the model would not improve the prediction and the expectation proved to be correct with literally no improvement in prediction. Overall, the NCD human oral PK profile was well predicted using the lipid volume of 3.5%, tlag of 0.05 hour and the fCYP of 0.001 with an EOC close to 0.90.

The oral PK profile for MDZ in rats were predicted with an EOC of 0.84 using the tlag of 0.05 hour, and the fCYP of 0.001. The tmax was well predicted but the Cmax was overpredicted in this case. There might be several reasons for relatively poorer prediction of oral MDZ profile in rats. These might include mis-estimation of disposition functions, physiologic variability in rat intestine, etc. On the other hand, the oral PK profile of NCD was much better predicted than that of MDZ with tlag of 0.05 hour, fCYP of 0.001 and 3.5% lipid volume with an EOC of 0.88. The predicted tmax and Cmax were very close to the observed value.

In summary, the continuous intestinal absorption model did an overall well prediction of MDZ and NCD oral PK profiles both in humans and rats. At the same time, this model provided a simple framework to account for the intestinal metabolism. Also, this modeling effort suggests for further model improvement including regional expression of all the enzymes in the intestine, relative contribution of enzymes for the metabolic conversion in the intestine, and inclusion of atypical kinetics in the intestine.

CHAPTER SEVEN: FUTURE DIRECTIONS AND SUMMARY

7.1 Regional Expression of CYPs Along the SD Rat Intestine

For the proper characterization of the fraction escaping gut metabolism (F_g), it might be helpful if the regional expression of all the enzymes' data is available. To our knowledge, not all the enzymes regional expression is available. There are some data available for some part of the intestine, but for the regional characterization of CYPs, more in depth research might be of great interest.

Western blot is one of the widely used method to quantify protein levels. This method relies on the separation based on the molecular weight and this method identifies the protein by labeling them by specific antibodies (Cima-Cabal, Vazquez, los Toyos, & Mar García-Suárez, 2019; Spencer, Kalman, Cotter, & Deak, 2000; S. C. Taylor, Berkelman, Yadav, & Hammond, 2013; S. C. Taylor & Posch, 2014). The discovery of promising diagnostic and prognostic biomarkers in a variety of diseases, including cancer, has been made possible by proteomic research techniques like matrix-assisted laser desorption ionization imaging mass spectrometry (MALDI/IMS) and nano-liquid chromatography tandem mass spectrometry (nano-LC-MS/MS). With the use of low flow chromatographic separation and nano-electrospray ionization, nano-LC-MS/MS can increase detection limits, offer precise peptide masses, and improve protein identification (Chen, Yan, Gao, & Zhang, 2015; Donnarumma & Murray, 2016; Gaspari & Cuda, 2011; Kachingwe et al., 2018; Michel et al., 2006). It is possible to use histopathological techniques and spatial distribution maps of mass spectra to determine how proteins and peptides are distributed within tissues. The most effective technique for creating high mass ions for mass spectrometry analysis is matrix-assisted laser desorption/ionization, or

MALDI (Chang et al., 2007; Chaurand, Luetzenkirchen, & Spengler, 1999; Kaufmann, 1995; Tsuchida, Umemura, & Nakayama, 2020). Because most parent ions produced by MALDI are singly charged, the spectra are more suited for mixture analysis. Without the necessity for liquid chromatography for pre-separation, it has been widely employed for the majority of proteome analyses. MALDI has been used to analyze oligonucleotides, polysaccharides, glycoproteins, glycolipids, and synthetic polymers in addition to proteins and peptides. MALDI has also been widely utilized for oligonucleotide sequencing, illness detection, and single nucleotide polymorphism (SNP) analysis because of the quick analytical time. MALDI is especially helpful for capturing heterogeneity both within primary tumors and within distant tissues with different metastatic burdens. To quantify therapy responses and find possible biomarkers in primary tumors, several studies have used electrospray ionization and MALDI methods.

Using MALDI, proteomic analysis can be done on SD rat intestines. Although larger proteins might be difficult to analyze, but using trypsin digestion, multiple peptides can be separated and identified.

7.2 Inclusion of BCS Class III and IV Drugs for the Absorption Modeling Incorporating Intestinal Metabolism and Transporters

In this thesis, only two drugs have been used where the MDZ was a BCS class I drug and the NCD was a BCS class II drug. Usually, BCS class I drugs do not display any transporter dependence absorption since they are highly soluble and highly permeable. Even if they are transporter substrate, because of their high solubility, the transporters will be saturated easily and most of the drugs will be permeated through passive diffusion mainly. On the other hand, BCS class II drugs are highly permeable with low solubility. Their permeation does not depend on the uptake transporters usually, but if they are efflux transporters including Pgp, it might impact their absorption profile. In this thesis, even though NCD was a Pgp substrate, but its efflux ratio was far below than 2 (Katoh et al., 2000; Lentz, Polli, Wring, Humphreys, & Polli, 2000), which is why it was expected that the Pgp will not play a significant role. It has also been illustrated in Appendix B. However, in future, some other drugs of BCS class II with an efflux ratio more than 2 would be an excellent choice of drug to determine this absorption model's ability to predict their absorption profile.

BCS class III drugs including cimetidine, atenolol, and amoxicillin have high solubility, but their absorption is permeability limited. Which is why, uptake transporters might play a significant role in their absorption. In human intestine, OATP2B1 is one of the major uptake transporters (Koenen et al., 2011; Yoshida et al., 2013) and its expression also depends on the age of human (Mooij et al., 2014). In future, some BCS class III drugs, which are OATP2B1 substrates, might be of greater interest to include in the research of this absorption model. Also, how those drugs absorption profile changes in different age groups might be predicted through this absorption model.

BCS class IV are the drugs (e.g., sulfamethoxazole, ritonavir, paclitaxel, and furosemide) for which both the uptake transporters and efflux transporters contribute to the absorption profile. While researching on these drugs for the prediction of their absorption profile, both the transporters interplay might need to be included in the absorption model.

In addition to the transporters, if the drug is metabolized in the intestine, their metabolic properties will need to be incorporated in the absorption model. Moreover, if those drugs display atypical kinetics, it should also be incorporated in the absorption model.

7.3 Time-Dependent Inactivation Assay Using Recombinant CYP Enzymes and Translating to the Intestinal DDI Scenario

In this thesis, initial target was to capture the TDI of intestinal CYP enzymes. Using intestinal microsomes, it was found that the intestinal microsomes were relatively incompetent to capture the TDI properties of a drug. The underlying reason might be less stability of intestinal microsomes rendering non-specific enzyme loss which clouded the TDI of a perpetrator molecule. Moreover, intestinal microsomes CYP contents are much lower than the liver microsomes resulting in usage of much higher microsomal protein concentrations in the primary incubation. This in turn can impact the higher microsomal partitioning of a highly partitioned perpetrator molecule, for example nicardipine, resulting less nicardipine for determining the TDI of this molecule.

Although, liver microsomes are still the first choice for TDI experiments (Grimm et al., 2009), for intestinal TDI situation, recombinant CYPs (rCYPs) might be an alternative. The TDI parameters can be generated using the rCYPs, and then can be translated to the relative CYP contents in intestinal regions. However, rCYPs usually have higher inactivation efficiency (k_{inact}/K_I) than microsomes (Ernest, Hall, & Jones, 2005; McConn, Lin, Allen, Kunze, & Thummel, 2004). Also, rCYPs will fail to detect cases if the metabolite generated by one CYP inactivates another CYP (Yadav et al., 2021; Yadav et al., 2020). Another alternative might be the use of cultured enterocytes. Usually, the cell based assays might provide more physiologically relevant scenario. The cultured cells might need to induce with dexamethasone to increase the relative CYP contents before using for the TDI experiments. Also, cell based system might be more stable than the microsomes, allowing for longer primary incubation time points.

In this thesis, all the *in vivo* data were collected from the literature for the in silico modeling. However, future work might include the *in vivo* rat works for these two drugs. In addition to the single drugs' oral PK studies, TDI studies should also be conducted where the intestinal enzymes might be inactivated by multiple dosing of the inactivator drug followed by the dosing of the victim drug.

7.4 Summary and Significance of this Thesis

This thesis has worked on two model drugs: midazolam and nicardipine. They are BCS class I and II drugs (Dahan et al., 2009; Wu & Benet, 2005), respectively. Moreover, they are highly metabolized in the intestine and in liver (J.-S. Choi et al., 2009; J. S. Choi et al., 2008; Graham et al., 1985; Jung et al., 2022; Nakamura et al., 2005; Paine et al., 1996; Park et al., 1989; Smith et al., 1981; Wandel et al., 1994). This makes them suitable choices for the intention of this thesis. Midazolam's *in vitro* enzyme kinetics is well established, both in human and SD rat intestinal and liver microsomes. There are plenty of research already done on midazolam. However, most of these studies' data analysis have been done using conventional Michaelis-Menten kinetics. Recently, midazolam's *in vitro* enzyme kinetics using human liver microsomes has been revisited using numerical method where ordinary differential equations have been used to establish the kinetic parameters (Paragas et al., 2021). The authors clearly demonstrated that the use of numerical method had several following advantages over the traditional Michaelis-Menten method (Paragas et al., 2021; Z. Wang et al., 2021):

a. This method does not rely on the steady-state assumption of Michaelis-Menten model.
b. This method can model single as well as multiple binding kinetics of enzyme-substrate reactions.
c. This method can model more than one product formation simultaneously.
d. Simulations and observed data analysis established that this method provides better parameter estimate resulting probable better *in vitro in vivo* correlation (IVIVC).
e. This model clearly demonstrates that the intrinsic clearance can be concentration dependent *in vivo* which can lead to inaccurate IVIVC if traditional Michaelis-Menten assumption does not hold.

Although midazolam's *in vitro* enzyme kinetics using human liver microsome has been published in the literature recently using this numerical method (Paragas et al., 2021), midazolam's *in vitro* enzyme kinetics using human intestinal microsome, rat liver and intestinal microsome are yet to be published which has been accomplished in this thesis. In chapter 3 and 4, it has been clearly demonstrated the differences between the *in vitro* kinetic parameters using single substrate versus multiple substrate binding phenomena of midazolam. Better kinetic parameter estimation using this numerical method is expected to provide better predicted F_g and F_h if used for static modeling.

However, human body is a dynamic system rather than static. One of the most essential information that this thesis demonstrated is the concentration dependent intrinsic clearance of midazolam. Michaelis-Menten equation defines intrinsic clearance as the ratio of k_{cat} over K_m, which is concentration independent. But, the numerical method shows that the intrinsic clearance can be concentration dependent, which is more significant in atypical kinetics (Paragas et al., 2021; Z. Wang et al., 2021). Although, biphasic kinetics ($K_{m1}<K_{m2}$ and $k_{cat1}<k_{cat2}$) and substrate inhibition kinetics ($K_{m1}<K_{m2}$ and $k_{cat1}>k_{cat2}$) is more apparent in high concentration, the sigmoidal kinetics ($K_{m1}>K_{m2}$ or $k_{cat1}<k_{cat2}$) can be easily apparent in even lower concentration especially when $K_{m1}>K_{m2}$. In liver, the available unbound concentration in the might is not very high rendering significant impact of atypical kinetics, but in the intestine its impact cannot be ignored. For example, in human intestinal microsome, the midazolam enterocytic concentration might be high enough to produce substrate inhibition resulting no metabolism at all. All these information is crucial in drug metabolism field for extrapolating *in vitro* data *in vivo* data and this might help better prediction.

Whereas midazolam is a well-researched drug in terms of *in vitro* enzyme kinetics using human and rat microsomes, there is a definitive lack of information on the nicardipine's *in vitro* enzyme kinetics using microsomes. To our knowledge, there is no published paper on nicardipine's *in vitro* enzyme kinetics using human or rat intestinal or liver microsomes. Most of the research was done on nicardipine because of its inhibitory potential, both reversible and TDI (Aueviriyavit et al., 2010; Ghanbari et al., 2006; Nakamura et al., 2005; Niwa, Murayama, & Yamazaki, 2010; Yamazaki et al., 2008). Although, in this thesis only one metabolite of nicardipine was used to capture its *in vitro* kinetics, this added significant knowledge about the nicardipine's reaction with CYP enzymes establishing multiple binding kinetics, both biphasic and sigmoidal. In future, if all the metabolite standards can be found commercially, it might be possible to better characterize its *in vitro* metabolic properties, including multiple substrate binding, multiple product formation and sequential metabolism, if any.

The first paper on continuous absorption model was published in 2017 (Nagar et al., 2017). Recently, the second paper has been published on a rat absorption model where the impact of food and particle size of the drug have been investigated (Radice et al., 2022). Ongoing refinement and improvement led us to think to add the intestinal metabolism into this absorption model. This thesis can be thought as the first step towards incorporating intestinal metabolism into this absorption model. Our first aim was to use one single intrinsic clearance into the model. For midazolam and nicardipine, in humans and rats, use of a single intrinsic clearance has been done to capture the fraction escaping gut metabolism and to separate the fraction escaping hepatic metabolism. Additionally, this model went one step further incorporating atypical kinetics into the absorption model for midazolam in humans. For other cases, it was not possible at present due to lack of literature data. However, these efforts have added significant direction about how to add the intestinal metabolism and atypical kinetics in this model which might be very useful in future.

Lastly, in this thesis, the fraction unbound in microsome for nicardipine was done again adding the drug in the receiver compartment (Appendix A). This showed that the f_{um} increased from 0.13 to 0.17. This might indicate that the equilibrium was yet to be achieved even after 12 hours. This is a very significant knowledge, especially for the highly partitioned drugs. Following recommendations can be made from this thesis for highly partitioned drug's f_{um} determination:

1. Use of lower microsomal protein concentration.
2. Use of longer incubation time ensuring stability.
3. Adding drug both in donor and receiver compartment to ensure that the equilibrium was actually reached.

One of the major unfulfillment of this thesis was the lack of intestinal TDI data. Chapter 5 has illustrated elaborately why intestinal TDI could not be captured. The major reasons included lack of stability of intestinal microsomes and low protein content for metabolism. It also provided some direction how to capture the intestinal TDI if anyone wants to continue this project further down the road. However, the TDI studies using rat liver microsomes produced significant insight about 1-aminobenzotrizole's (ABT) and nicardipine's TDI properties. The numerical method for TDI data analysis has been emphasized in several publications (K. Korzekwa et al., 2014; Nagar et al., 2014; Yadav et al., 2019; Yadav et al., 2020). In chapter 5, it has been shown that the numerical method can model the TDI of the molecules and the TDI kinetic properties generated using this method produced significantly lower inactivation potential than the replot method which is used traditionally. This again can emphasize why many of the TDI found in *in vitro* experiment do not show TDI impact in *in vivo* (Yadav et al., 2021; Yadav et al., 2020).

Another unfulfillment that might need to be mentioned is the lack of *in vivo* data that was originally proposed in the thesis proposal. As mentioned previously, the *in vitro* intestinal TDI was not being captured by using intestinal microsomes. We then decided to exclude the consideration of intestinal TDI for this thesis. However, we included the simulation of human continuous intestinal absorption modeling of MDZ and NCD incorporating intestinal metabolism in the model which was not in the original thesis proposal. Human absorption modeling has been done using clinical *in vivo* data. In case of rats, since there were already plenty of rat *in vivo* data (both IV and oral solution) available in the literature, those data have been used for the rat absorption modeling purpose. In this case, we have applied reduction and refinement of 3R principle (replacement, reduction, and refinement). Although, chapter six has displayed one dataset for each of the simulation cases (MDZ and NCD, humans and rats, total four simulations), multiple datasets, both humans and rats, were used for the absorption modeling to validate the prediction ability of this absorption model.

In summary, this thesis has added significant knowledge to the *in vitro* enzyme kinetics of midazolam and nicardipine. This thesis also went one step further in the continuous intestinal absorption modeling incorporating intestinal metabolism and the atypical kinetics.

BIBLIOGRAPHY

Agoram, B., Woltosz, W. S., & Bolger, M. B. (2001). Predicting the impact of physiological and biochemical processes on oral drug bioavailability. *Advanced drug delivery reviews, 50,* S41-S67.

Agrawal, A. K., & Shapiro, B. H. (1997). Gender, age and dose effects of neonatally administered aspartate on the sexually dimorphic plasma growth hormone profiles regulating expression of the rat sex-dependent hepatic CYP isoforms. *Drug metabolism and disposition, 25*(11), 1249-1256.

Alavijeh, M. S., & Palmer, A. M. (2004). The pivotal role of drug metabolism and pharmacokinetics in the discovery and development of new medicines. *Curr. Opin. Investig. Drugs*, *5*, 755-763.

Alqahtani, M. S., Kazi, M., Alsenaidy, M. A., & Ahmad, M. Z. (2021). Advances in oral drug delivery. *Frontiers in Pharmacology, 12,* 618411.

Asaoka, Y., Sakai, H., Sasaki, J., Goryo, M., Yanai, T., Masegi, T., & Okada, K. (2010). Changes in the gene expression and enzyme activity of hepatic cytochrome P450 in juvenile Sprague-Dawley rats. *Journal of Veterinary Medical Science*, 0912110096-0912110096.

Aueviriyavit, S., Kobayashi, K., & Chiba, K. (2010). Species differences in mechanism-based inactivation of CYP3A in humans, rats and mice. *Drug metabolism and pharmacokinetics, 25*(1), 93-100.

Barnaba, C., Yadav, J., Nagar, S., Korzekwa, K., & Jones, J. P. (2016). Mechanism-based inhibition of CYP3A4 by podophyllotoxin: aging of an intermediate is important for in vitro/in vivo correlations. *Molecular pharmaceutics, 13*(8), 2833-2843.

Barr, J. T., Flora, D. R., & Iwuchukwu, O. F. (2014). Case study 1. Practical considerations with experimental design and interpretation. In *Enzyme Kinetics in Drug Metabolism* (pp. 419-429): Springer.

Barr, J. T., & Iwuchukwu, O. F. (2021). Case Study 1: Practical Considerations with Experimental Design and Interpretation. In *Enzyme Kinetics in Drug Metabolism* (pp. 633-642): Springer.

Bass, L., Robinson, P., & Bracken, A. J. (1978). Hepatic elimination of flowing substrates: the distributed model. *Journal of theoretical biology, 72*(1), 161-184.

Beilstein, F., Carrière, V., Leturque, A., & Demignot, S. (2016). Characteristics and functions of lipid droplets and associated proteins in enterocytes. *Experimental cell research, 340*(2), 172-179.

Benet, L. Z., Broccatelli, F., & Oprea, T. I. (2011). BDDCS applied to over 900 drugs. *The AAPS journal, 13*(4), 519-547.

Benet, L. Z., & Cummins, C. L. (2001). The drug efflux–metabolism alliance: biochemical aspects. *Advanced drug delivery reviews, 50,* S3-S11.

Bioquest, A. Potassium Phosphate (pH 5.8 to 8.0) Preparation and Recipe. Retrieved from https://www.aatbio.com/resources/buffer-preparations-and-recipes/potassium-phosphate-ph-5-8-to-8-0

Bittermann, K., & Goss, K.-U. (2017). Predicting apparent passive permeability of Caco-2 and MDCK cell-monolayers: A mechanistic model. *PLoS One, 12*(12), e0190319.

Boxenbaum, H. (1982). Interspecies scaling, allometry, physiological time, and the ground plan of pharmacokinetics. *Journal of Pharmacokinetics and Biopharmaceutics, 10*(2), 201-227. doi:10.1007/BF01062336

Bruyere, A., Decleves, X., Bouzom, F., Ball, K., Marques, C., Treton, X., . . . Panis, Y. (2010). Effect of variations in the amounts of P-glycoprotein (ABCB1), BCRP (ABCG2) and CYP3A4 along the human small intestine on PBPK models for predicting intestinal first pass. *Molecular pharmaceutics, 7*(5), 1596-1607.

Burkina, V., Rasmussen, M. K., Pilipenko, N., & Zamaratskaia, G. (2017). Comparison of xenobiotic-metabolising human, porcine, rodent, and piscine cytochrome P450. *Toxicology, 375*, 10-27. doi:10.1016/j.tox.2016.11.014

Burt, H. J., Pertinez, H., Säll, C., Collins, C., Hyland, R., Houston, J. B., & Galetin, A. (2012). Progress curve mechanistic modeling approach for assessing time-dependent inhibition of CYP3A4. *Drug Metabolism and Disposition, 40*(9), 1658-1667.

Busse, D., Leandersson, S., Amberntsson, S., Darnell, M., & Hilgendorf, C. (2020). Industrial approach to determine the relative contribution of seven major UGT isoforms to hepatic glucuronidation. *Journal of pharmaceutical sciences, 109*(7), 2309-2320.

Buters, J. T. M., Korzekwa, K. R., Kunze, K. L., Omata, Y., Hardwick, J. P., & Gonzalez, F. J. (1994). cDNA-directed expression of human cytochrome P450 CYP3A4 using baculovirus. *Drug Metabolism and Disposition, 22*(5), 688-692.

Camenisch, G., Riede, J., Kunze, A., Huwyler, J., Poller, B., & Umehara, K. (2015). The extended clearance model and its use for the interpretation of hepatobiliary elimination data. *ADMET and DMPK, 3*(1.), 1-14.

Camenisch, G., & Umehara, K. i. (2012). Predicting human hepatic clearance from in vitro drug metabolism and transport data: a scientific and pharmaceutical perspective for assessing drug–drug interactions. *Biopharmaceutics & drug disposition, 33*(4), 179-194.

Cascorbi, I. (2012). Drug interactions—principles, examples and clinical consequences. *Deutsches Ärzteblatt International, 109*(33-34), 546.

Castillo-Garit, J. A., Marrero-Ponce, Y., Torrens, F., & García-Domenech, R. (2008). Estimation of ADME properties in drug discovery: predicting Caco-2 cell permeability using atom-based stochastic and non-stochastic linear indices. *Journal of pharmaceutical sciences, 97*(5), 1946-1976.

Chang, W. C., Huang, L. C. L., Wang, Y.-S., Peng, W.-P., Chang, H. C., Hsu, N. Y., . . . Chen, C. H. (2007). Matrix-assisted laser desorption/ionization (MALDI) mechanism revisited. *Analytica Chimica Acta, 582*(1), 1-9.

Chaurand, P., Luetzenkirchen, F., & Spengler, B. (1999). Peptide and protein identification by matrix-assisted laser desorption ionization (MALDI) and MALDI-post-source decay time-of-flight mass spectrometry. *Journal of the American Society for Mass Spectrometry, 10*(2), 91-103.

Chawla, G., & Bansal, A. (2003). A means to address regional variability in intestinal drug absorption. *Pharm tech, 27*(2), 50-68.

Chen, Q., Yan, G., Gao, M., & Zhang, X. (2015). Ultrasensitive proteome profiling for 100 living cells by direct cell injection, online digestion and nano-LC-MS/MS analysis. *Analytical chemistry, 87*(13), 6674-6680.

Chiba, M., Hensleigh, M., & Lin, J. H. (1997). Hepatic and intestinal metabolism of indinavir, an HIV protease inhibitor, in rat and human microsomes: major role of CYP3A. *Biochemical pharmacology, 53*(8), 1187-1195.

Chiba, M., Ishii, Y., & Sugiyama, Y. (2009). Prediction of hepatic clearance in human from in vitro data for successful drug development. *The AAPS journal, 11*(2), 262-276.

Choi, G.-W., Lee, Y.-B., & Cho, H.-Y. (2019). Interpretation of non-clinical data for prediction of human pharmacokinetic parameters: in vitro-in vivo extrapolation and allometric scaling. *Pharmaceutics, 11*(4), 168.

Choi, J.-S., Choi, B.-C., & Kang, K. W. (2009). Effect of resveratrol on the pharmacokinetics of oral and intravenous nicardipine in rats: possible role of P-glycoprotein inhibition by resveratrol. *Die Pharmazie-An International Journal of Pharmaceutical Sciences, 64*(1), 49-52.

Choi, J. S., Koh, Y. Y., Chung, J. H., Choi, D. H., & Han, H. K. (2008). Reduced prehepatic extraction of nicardipine in the presence of pioglitazone in rats. *Journal of Pharmacy and Pharmacology, 60*(10), 1403-1407.

Chovan, J. P., Ring, S. C., Yu, E., & Baldino, J. P. (2007). Cytochrome P450 probe substrate metabolism kinetics in Sprague Dawley rats. *Xenobiotica, 37*(5), 459-473.

Chow, S. C. (2014). Bioavailability and Bioequivalence in Drug Development. *Wiley Interdiscip Rev Comput Stat, 6*(4), 304-312. doi:10.1002/wics.1310

Christensen, H., Mathiesen, L., Postvoll, L. W., Winther, B., & Molden, E. (2009). Different enzyme kinetics of midazolam in recombinant CYP3A4 microsomes from human and insect sources. *Drug metabolism and pharmacokinetics, 24*(3), 261-268.

Cima-Cabal, M. D., Vazquez, F., los Toyos, J. R. d., & Mar García-Suárez, M. d. (2019). Protein expression analysis by western blot and protein–protein interactions. In *Streptococcus pneumoniae* (pp. 101-111): Springer.

Cory Kalvass, J., & Maurer, T. S. (2002). Influence of nonspecific brain and plasma binding on CNS exposure: implications for rational drug discovery. *Biopharmaceutics & drug disposition, 23*(8), 327-338.

Dahan, A., Miller, J. M., & Amidon, G. L. (2009). Prediction of solubility and permeability class membership: provisional BCS classification of the world's top oral drugs. *The AAPS journal, 11*(4), 740-746.

Dansette, P. M., Amar, C., Valadon, P., Pons, C., Beaune, P. H., & Mansuy, D. (1991). Hydroxylation and formation of electrophilic metabolites of tienilic acid and its isomer by human liver microsomes: catalysis by a cytochrome P450 IIC different from that responsible for mephenytoin hydroxylation. *Biochemical pharmacology, 41*(4), 553-560.

Darling, N. J., Mobbs, C. L., González-Hau, A. L., Freer, M., & Przyborski, S. (2020). Bioengineering novel in vitro co-culture models that represent the human intestinal mucosa with improved Caco-2 structure and barrier function. *Frontiers in Bioengineering and Biotechnology*, *8*, 992.

Daugherty, A. L., & Mrsny, R. J. (1999). Transcellular uptake mechanisms of the intestinal epithelial barrier Part one. *Pharmaceutical science & technology today, 2*(4), 144-151.

de Montellano, P. R. O. (2018). 1-Aminobenzotriazole: a mechanism-based cytochrome P450 inhibitor and probe of cytochrome P450 biology. *Medicinal chemistry, 8*(3).

De Montellano, P. R. O., & Mathews, J. M. (1981). Autocatalytic alkylation of the cytochrome P-450 prosthetic haem group by 1-aminobenzotriazole. Isolation of an NN-bridged benzyne-protoporphyrin IX adduct. *Biochemical Journal, 195*(3), 761.

Demignot, S., Beilstein, F., & Morel, E. (2014). Triglyceride-rich lipoproteins and cytosolic lipid droplets in enterocytes: key players in intestinal physiology and metabolic disorders. *Biochimie, 96*, 48-55.

DeSesso, J. M., & Jacobson, C. F. (2001). Anatomical and physiological parameters affecting gastrointestinal absorption in humans and rats. *Food and Chemical Toxicology, 39*(3), 209-228.

DeSesso, J. M., & Williams, A. L. (2008). Contrasting the gastrointestinal tracts of mammals: factors that influence absorption. *Annual reports in medicinal chemistry, 43*, 353-371.

Devadasu, V. R., Deb, P. K., Maheshwari, R., Sharma, P., & Tekade, R. K. (2018). Physicochemical, pharmaceutical, and biological considerations in GIT absorption of drugs. In *Dosage Form Design Considerations* (pp. 149-178): Elsevier.

Di, L., & Obach, R. S. (2015). Addressing the challenges of low clearance in drug research. *The AAPS journal, 17*(2), 352-357.

Doherty, M. M., & Charman, W. N. (2002). The mucosa of the small intestine. *Clinical pharmacokinetics, 41*(4), 235-253.

Dokoumetzidis, A., Kalantzi, L., & Fotaki, N. (2007). Predictive models for oral drug absorption: from in silico methods to integrated dynamical models. *Expert opinion on drug metabolism & toxicology, 3*(4), 491-505.

Donnarumma, F., & Murray, K. K. (2016). Laser ablation sample transfer for localized LC-MS/MS proteomic analysis of tissue. *Journal of Mass Spectrometry, 51*(4), 261-268.

Dou, L., Gavins, F. K. H., Mai, Y., Madla, C. M., Taherali, F., Orlu, M., . . . Basit, A. W. (2020). Effect of Food and an Animal's Sex on P-Glycoprotein Expression and Luminal Fluids in the Gastrointestinal Tract of Wistar Rats. *Pharmaceutics, 12*(4), 296.

Drugbank. Midazolam. Retrieved from https://go.drugbank.com/drugs/DB00683

DRUGBANK. Nicardipine. Retrieved from https://go.drugbank.com/drugs/DB00622

Einolf, H. J., Chen, L., Fahmi, O. A., Gibson, C. R., Obach, R. S., Shebley, M., . . . Zhang, L. (2014). Evaluation of various static and dynamic modeling methods to predict clinical CYP3A induction using in vitro CYP3A4 mRNA induction data. *Clinical Pharmacology & Therapeutics, 95*(2), 179-188.

Ernest, C. S., Hall, S. D., & Jones, D. R. (2005). Mechanism-based inactivation of CYP3A by HIV protease inhibitors. *Journal of pharmacology and experimental therapeutics, 312*(2), 583-591.

Fagerholm, U. (2007). Prediction of human pharmacokinetics—gut-wall metabolism. *Journal of Pharmacy and Pharmacology, 59*(10), 1335-1343.

Fahmi, O. A., Hurst, S., Plowchalk, D., Cook, J., Guo, F., Youdim, K., . . . Hyland, R. (2009). Comparison of different algorithms for predicting clinical drug-drug interactions, based on the use of CYP3A4 in vitro data: predictions of compounds as precipitants of interaction. *Drug Metabolism and Disposition, 37*(8), 1658-1666.

Fahmi, O. A., Maurer, T. S., Kish, M., Cardenas, E., Boldt, S., & Nettleton, D. (2008). A combined model for predicting CYP3A4 clinical net drug-drug interaction based on CYP3A4 inhibition, inactivation, and induction determined in vitro. *Drug Metabolism and Disposition, 36*(8), 1698-1708.

Fairman, D. A., Collins, C., & Chapple, S. (2007). Progress curve analysis of CYP1A2 inhibition: a more informative approach to the assessment of mechanism-based inactivation? *Drug metabolism and disposition, 35*(12), 2159-2165.

FDA. (2018). Bioanalytical Method

Validation

Guidance for Industry. Retrieved from

https://www.fda.gov/files/drugs/published/Bioanalytical-Method-Validation-Guidance-for-Industry.pdf

Fedi, A., Vitale, C., Ponschin, G., Ayehunie, S., Fato, M., & Scaglione, S. (2021). In vitro models replicating the human intestinal epithelium for absorption and metabolism studies: A systematic review. *Journal of Controlled Release, 335*, 247-268.

Ferl, G. Z., Theil, F. P., & Wong, H. (2016). Physiologically based pharmacokinetic models of small molecules and therapeutic antibodies: a mini-review on fundamental concepts and applications. *Biopharm Drug Dispos, 37*(2), 75-92. doi:10.1002/bdd.1994

Flaten, G. E., Dhanikula, A. B., Luthman, K., & Brandl, M. (2006). Drug permeability across a phospholipid vesicle based barrier: A novel approach for studying passive diffusion. *European journal of pharmaceutical sciences, 27*(1), 80-90.

Flaten, G. E., Palac, Z., Engesland, A., Filipović-Grčić, J., Vanić, Ž., & Škalko-Basnet, N. (2015). In vitro skin models as a tool in optimization of drug formulation. *European journal of pharmaceutical sciences, 75*, 10-24.

Forker, E. L., & Luxon, B. A. (1983). Albumin binding and hepatic uptake: the importance of model selection. *Journal of pharmaceutical sciences, 72*(10), 1232-1233.

Forker, E. L., & Luxon, B. A. (1985). Lumpers vs. distributers. In (Vol. 5, pp. 1236-1237): Wiley Online Library.

Galetin, A., Gertz, M., & Houston, J. B. (2008). Potential role of intestinal first-pass metabolism in the prediction of drug-drug interactions. *Expert Opin Drug Metab Toxicol, 4*(7), 909-922. doi:10.1517/17425255.4.7.909

Galetin, A., Gertz, M., & Houston, J. B. (2010). Contribution of intestinal cytochrome p450-mediated metabolism to drug-drug inhibition and induction interactions. *Drug Metab Pharmacokinet, 25*(1), 28-47. doi:10.2133/dmpk.25.28

Galetin, A., Hinton, L. K., Burt, H., Obach, R. S., & Houston, J. B. (2007). Maximal inhibition of intestinal first-pass metabolism as a pragmatic indicator of intestinal contribution to the drug-drug interactions for CYP3A4 cleared drugs. *Current drug metabolism, 8*(7), 685-693.

Galetin, A., & Houston, J. B. (2006). Intestinal and hepatic metabolic activity of five cytochrome P450 enzymes: impact on prediction of first-pass metabolism. *Journal of Pharmacology and Experimental Therapeutics, 318*(3), 1220-1229.

Gantzsch, S. P., Kann, B., Ofer-Glaessgen, M., Loos, P., Berchtold, H., Balbach, S., . . . Windbergs, M. (2014). Characterization and evaluation of a modified PVPA barrier in comparison to Caco-2 cell monolayers for combined dissolution and permeation testing. *Journal of Controlled Release, 175*, 79-86.

Garg, A., & Balthasar, J. P. (2007). Physiologically-based pharmacokinetic (PBPK) model to predict IgG tissue kinetics in wild-type and FcRn-knockout mice. *Journal of Pharmacokinetics and Pharmacodynamics, 34*(5), 687-709. doi:10.1007/s10928-007-9065-1

Gaspari, M., & Cuda, G. (2011). Nano LC–MS/MS: A robust setup for proteomic analysis. In *Nanoproteomics* (pp. 115-126): Springer.

Gertz, M., Harrison, A., Houston, J. B., & Galetin, A. (2010). Prediction of human intestinal first-pass metabolism of 25 CYP3A substrates from in vitro clearance and permeability data. *Drug Metabolism and Disposition, 38*(7), 1147-1158.

Ghanbari, F., Rowland-Yeo, K., Bloomer, J. C., Clarke, S. E., Lennard, M. S., Tucker, G. T., & Rostami-Hodjegan, A. (2006). A critical evaluation of the experimental design of studies of mechanism based enzyme inhibition, with implications for in vitro-in vivo extrapolation. *Current drug metabolism, 7*(3), 315-334.

Gibaldi, M., & Perrier, D. (1982). *Pharmacokinetics* (Vol. 15). New York: Marcel Dekkar, Inc.

Gobeau, N., Stringer, R., De Buck, S., Tuntland, T., & Faller, B. (2016). Evaluation of the GastroPlus™ advanced compartmental and transit (acat) model in early discovery. *Pharmaceutical research, 33*(9), 2126-2139.

Graham, D. J., Dow, R. J., Hall, D. J., Alexander, O. F., Mroszczak, E. J., & Freedman, D. (1985). The metabolism and pharmacokinetics of nicardipine hydrochloride in man. *British journal of clinical pharmacology, 20*(S1), 23S-28S.

Granvil, C. P., Yu, A.-M., Elizondo, G., Akiyama, T. E., Cheung, C., Feigenbaum, L., . . . Gonzalez, F. J. (2003). Expression of the human CYP3A4 gene in the small intestine of transgenic mice: in vitro metabolism and pharmacokinetics of midazolam. *Drug metabolism and disposition, 31*(5), 548-558.

Grimm, S. W., Einolf, H. J., Hall, S. D., He, K., Lim, H.-K., Ling, K.-H. J., . . . Skordos, K. W. (2009). The conduct of in vitro studies to address time-dependent inhibition of drug-metabolizing enzymes: a perspective of the pharmaceutical research and manufacturers of America. *Drug Metabolism and Disposition, 37*(7), 1355-1370.

Ha-Duong, N.-T., Dijols, S., Macherey, A.-C., Goldstein, J. A., Dansette, P. M., & Mansuy, D. (2001). Ticlopidine as a selective mechanism-based inhibitor of human cytochrome P450 2C19. *Biochemistry, 40*(40), 12112-12122.

Hallifax, D., Foster, J. A., & Houston, J. B. (2010). Prediction of human metabolic clearance from in vitro systems: retrospective analysis and prospective view. *Pharmaceutical research, 27*(10), 2150-2161.

Hallifax, D., & Houston, J. B. (2012). Evaluation of hepatic clearance prediction using in vitro data: emphasis on fraction unbound in plasma and drug ionisation using a database of 107 drugs. *Journal of pharmaceutical sciences, 101*(8), 2645-2652.

Harrison, R. K. (2016). Phase II and phase III failures: 2013–2015. *Nat Rev Drug Discov, 15*(12), 817-818.

Hayeshi, R., Hilgendorf, C., Artursson, P., Augustijns, P., Brodin, B., Dehertogh, P., . . . Korjamo, T. (2008). Comparison of drug transporter gene expression and functionality in Caco-2 cells from 10 different laboratories. *European Journal of Pharmaceutical Sciences, 35*(5), 383-396.

Hebel, R., & Stromberg, M. W. (1986). *Anatomy and embryology of the laboratory rat*: BioMed Verlag.

Hedaya, M. A. (2012). *Basic pharmacokinetics*: CRC Press.

Henne, K. R., Tran, T. B., VandenBrink, B. M., Rock, D. A., Aidasani, D. K., Subramanian, R., . . . Wong, S. G. (2012). Sequential metabolism of AMG 487, a novel CXCR3 antagonist, results in formation of quinone reactive metabolites that covalently modify CYP3A4 Cys239 and cause time-dependent inhibition of the enzyme. *Drug Metabolism and Disposition, 40*(7), 1429-1440.

Hidalgo, I. J., Raub, T. J., & Borchardt, R. T. (1989). Characterization of the human colon carcinoma cell line (Caco-2) as a model system for intestinal epithelial permeability. *Gastroenterology, 96*(2), 736-749.

Higuchi, S., & Shiobara, Y. (1980). Comparative pharmacokinetics of nicardipine hydrochloride, a new vasodilator, in various species. *Xenobiotica, 10*(6), 447-454.

Hollenberg, P. F., Kent, U. M., & Bumpus, N. N. (2008). Mechanism-based inactivation of human cytochromes p450s: experimental characterization, reactive intermediates, and clinical implications. *Chem Res Toxicol, 21*(1), 189-205. doi:10.1021/tx7002504

Holt, K., Ye, M., Nagar, S., & Korzekwa, K. (2019). Prediction of Tissue-Plasma Partition Coefficients Using Microsomal Partitioning: Incorporation into Physiologically based Pharmacokinetic Models and Steady-State Volume of Distribution Predictions. *Drug Metabolism and Disposition, 47*(10), 1050-1060.

Horspool, A. M., Wang, T., Scaringella, Y.-S., Taub, M. E., & Chan, T. S. (2020). Human liver microsomes immobilized on magnetizable beads: a novel approach to study in vitro drug metabolism. *Drug Metabolism and Disposition, 48*(8), 645-654.

Howgate, E. M., Rowland Yeo, K., Proctor, N. J., Tucker, G. T., & Rostami-Hodjegan, A. (2006). Prediction of in vivo drug clearance from in vitro data. I: impact of inter-individual variability. *Xenobiotica, 36*(6), 473-497.

Hu, M., Ling, J., Lin, H., & Chen, J. (2004). Use of Caco-2 cell monolayers to study drug absorption and metabolism. In *Optimization in drug discovery* (pp. 19-35): Springer.

Huang, W., Lee, S. L., & Lawrence, X. Y. (2009). Mechanistic approaches to predicting oral drug absorption. *The AAPS journal, 11*(2), 217-224.

Ingersoll, K. S., & Cohen, J. (2008). The impact of medication regimen factors on adherence to chronic treatment: a review of literature. *Journal of behavioral medicine, 31*(3), 213-224.

Ito, K., Hallifax, D., Obach, R. S., & Houston, J. B. (2005). Impact of parallel pathways of drug elimination and multiple cytochrome P450 involvement on drug-drug interactions: CYP2D6 paradigm. *Drug metabolism and disposition, 33*(6), 837-844.

Ito, K., & Houston, J. B. (2005). Prediction of human drug clearance from in vitro and preclinical data using physiologically based and empirical approaches. *Pharm Res, 22*(1), 103-112. doi:10.1007/s11095-004-9015-1

Jun-Shik, C., Sung-Il, H. A., & Dong-Hyun, C. (2010). Effects of atorvastatin on the pharmacokinetics of nicardipine after oral and intravenous administration in rats. *The Korean Society of Applied Pharmacology, 18*(2), 226-232.

Jung, Y. H., Heo, D. G., Lee, D. C., Kwon, Y. M., Seol, M. J., Zhang, D., . . . Kim, J. H. (2022). Effect of concomitant oral administration of ethanol on the pharmacokinetics of nicardipine in rats. *Biomedical Chromatography,* e5425.

Kachingwe, B. H., Uang, Y. S., Huang, T. J., Wang, L. H., & Lin, S. J. (2018). Development and validation of an LC-MS/MS method for quantification of NC-8 in rat plasma and its application to pharmacokinetic studies. *J Food Drug Anal, 26*(1), 401-408. doi:10.1016/j.jfda.2017.09.003

Kaminsky, L. S., & Zhang, Q.-Y. (2003). The small intestine as a xenobiotic-metabolizing organ. *Drug metabolism and disposition, 31*(12), 1520-1525.

Karjalainen, M. J., Neuvonen, P. J., & Backman, J. T. (2006). Rofecoxib is a potent, metabolism-dependent inhibitor of CYP1A2: implications for in vitro prediction of drug interactions. *Drug metabolism and disposition, 34*(12), 2091-2096.

Kato, M., Chiba, K., Hisaka, A., Ishigami, M., Kayama, M., Mizuno, N., . . . Ueda, K. (2003). The intestinal first-pass metabolism of substrates of CYP3A4 and P-glycoprotein—quantitative analysis based on information from the literature. *Drug metabolism and pharmacokinetics, 18*(6), 365-372.

Katoh, M., Nakajima, M., Yamazaki, H., & Yokoi, T. (2000). Inhibitory potencies of 1, 4-dihydropyridine calcium antagonists to P-glycoprotein-mediated transport: comparison with the effects on CYP3A4. *Pharmaceutical research, 17*(10), 1189-1197.

Kaufmann, R. (1995). Matrix-assisted laser desorption ionization (MALDI) mass spectrometry: a novel analytical tool in molecular biology and biotechnology. *Journal of biotechnology, 41*(2-3), 155-175.

Kaza, M., Karaźniewicz-Łada, M., Kosicka, K., Siemiątkowska, A., & Rudzki, P. J. (2019). Bioanalytical method validation: new FDA guidance vs. EMA guideline. Better or worse? *Journal of pharmaceutical and biomedical analysis, 165*, 381-385.

Keiding, S., & Andreasen, P. B. (1979). Hepatic clearance measurements and pharmacokinetics. *Pharmacology, 19*(3), 105-110.

Kim, T. H., Shin, S., & Shin, B. S. (2018). Model-based drug development: application of modeling and simulation in drug development. *Journal of Pharmaceutical Investigation, 48*(4), 431-441.

Klieber, S., Hugla, S., Ngo, R., Arabeyre-Fabre, C., Meunier, V., Sadoun, F., . . . Guillou, F. (2008). Contribution of the N-glucuronidation pathway to the overall in vitro metabolic clearance of midazolam in humans. *Drug metabolism and disposition, 36*(5), 851-862.

Klieber, S., Hugla, S., Ngo, R., Arabeyre-Fabre, C., Meunier, V., Sadoun, F., . . . Guillou, F. (2009). Contribution of the N-glucuronidation pathway to the overall in vitro metabolic clearance of midazolam in humans. *The FASEB Journal, 23*, 372-371.

Koenen, A., Kroemer, H. K., Grube, M., & Meyer zu Schwabedissen, H. E. (2011). Current understanding of hepatic and intestinal OATP-mediated drug–drug interactions. *Expert review of clinical pharmacology, 4*(6), 729-742.

Koenigs, L. L., Peter, R. M., Hunter, A. P., Haining, R. L., Rettie, A. E., Friedberg, T., . . . Trager, W. F. (1999). Electrospray ionization mass spectrometric analysis of intact cytochrome P450: identification of tienilic acid adducts to P450 2C9. *Biochemistry, 38*(8), 2312-2319.

Kola, I., & Landis, J. (2004). Can the pharmaceutical industry reduce attrition rates? *Nature reviews Drug discovery, 3*(8), 711-716.

Korzekwa, K. (2014). Enzyme kinetics of oxidative metabolism: cytochromes P450. In *Enzyme Kinetics in Drug Metabolism* (pp. 149-166): Springer.

Korzekwa, K., Tweedie, D., Argikar, U. A., Whitcher-Johnstone, A., Bell, L., Bickford, S., & Nagar, S. (2014). A numerical method for analysis of in vitro time-dependent inhibition data. Part 2. Application to experimental data. *Drug Metabolism and Disposition, 42*(9), 1587-1595.

Korzekwa, K. R., Krishnamachary, N., Shou, M., Ogai, A., Parise, R. A., Rettie, A. E., . . . Tracy, T. S. (1998). Evaluation of atypical cytochrome P450 kinetics with two-substrate models: evidence that multiple substrates can simultaneously bind to cytochrome P450 active sites. *Biochemistry, 37*(12), 4137-4147.

Kotegawa, T., Laurijssens, B. E., von Moltke, L. L., Cotreau, M. M., Perloff, M. D., Venkatakrishnan, K., . . . Greenblatt, D. J. (2002). In vitro, pharmacokinetic, and pharmacodynamic interactions of ketoconazole and midazolam in the rat. *Journal of Pharmacology and Experimental Therapeutics, 302*(3), 1228-1237.

Kuepfer, L., Niederalt, C., Wendl, T., Schlender, J. F., Willmann, S., Lippert, J., . . . Teutonico, D. (2016). Applied Concepts in PBPK Modeling: How to Build a PBPK/PD Model. *CPT Pharmacometrics Syst Pharmacol, 5*(10), 516-531. doi:10.1002/psp4.12134

Kulkarni, J. A., Witzigmann, D., Leung, J., van der Meel, R., Zaifman, J., Darjuan, M. M., . . . Cullis, P. R. (2019). Fusion-dependent formation of lipid nanoparticles containing macromolecular payloads. *Nanoscale, 11*(18), 9023-9031. doi:10.1039/c9nr02004g

Kulkarni, P. R., Youssef, A. S., & Argikar, A. A. (2021). Prediction of Drug Clearance from Enzyme and Transporter Kinetics. In *Enzyme Kinetics in Drug Metabolism* (pp. 369-417): Springer.

Label, F. Midazolam Injection, USP.

Lave, T., Coassolo, P., & Reigner, B. (1999). Prediction of hepatic metabolic clearance based on interspecies allometric scaling techniques and in vitro-in vivo correlations. *Clin Pharmacokinet, 36*(3), 211-231. doi:10.2165/00003088-199936030-00003

Lawrence, X. Y., & Amidon, G. L. (1999). A compartmental absorption and transit model for estimating oral drug absorption. *International journal of pharmaceutics, 186*(2), 119-125.

Lennernas, H., Nylander, S., & Ungell, A. L. (1997). Jejunal permeability: a comparison between the ussing chamber technique and the single-pass perfusion in humans. *Pharmaceutical research, 14*(5), 667.

Lennernäs, H., Ahrenstedt, Ö., Hällgren, R., Knutson, L., Ryde, M., & Paalzow, L. K. (1992). Regional jejunal perfusion, a new in vivo approach to study oral drug absorption in man. *Pharmaceutical research, 9*(10), 1243-1251.

Lentz, K. A., Polli, J. W., Wring, S. A., Humphreys, J. E., & Polli, J. E. (2000). Influence of passive permeability on apparent P-glycoprotein kinetics. *Pharmaceutical research, 17*(12), 1456-1460.

Li, J., Wu, J., Bao, X., Honea, N., Xie, Y., Kim, S., . . . Sanai, N. (2017). Quantitative and mechanistic understanding of AZD1775 penetration across human blood–brain barrier in glioblastoma patients using an IVIVE–PBPK modeling approach. *Clinical Cancer Research, 23*(24), 7454-7466.

Lightning, L. K., Jones, J. P., Friedberg, T., Pritchard, M. P., Shou, M., Rushmore, T. H., & Trager, W. F. (2000). Mechanism-based inactivation of cytochrome P450 3A4 by L-754,394. *Biochemistry, 39*(15), 4276-4287.

Lin, H.-l., Kent, U. M., & Hollenberg, P. F. (2002). Mechanism-based inactivation of cytochrome P450 3A4 by 17α-ethynylestradiol: evidence for heme destruction and covalent binding to protein. *Journal of Pharmacology and Experimental Therapeutics, 301*(1), 160-167.

Lin, H.-l., Zhang, H., & Hollenberg, P. F. (2018). Formation of both heme and apoprotein adducts contributes to the mechanism-based inactivation of human CYP2J2 by 17α-ethynylestradiol. *Drug Metabolism and Disposition, 46*(6), 813-822.

Lin, J. H. (1995). Species similarities and differences in pharmacokinetics. *Drug Metabolism and Disposition, 23*(10), 1008-1021.

Lin, J. H. (1998). Applications and limitations of interspecies scaling and in vitro extrapolation in pharmacokinetics. *Drug metabolism and disposition, 26*(12), 1202-1212.

Lin, J. H., Chiba, M., & Baillie, T. A. (1997). In vivo assessment of intestinal drug metabolism. *Drug metabolism and disposition, 25*(9), 1107-1109.

Lin, L., & Wong, H. (2017). Predicting oral drug absorption: mini review on physiologically-based pharmacokinetic models. *Pharmaceutics, 9*(4), 41.

Lindell, M., Lang, M., & Lennernäs, H. (2003). Expression of genes encoding for drug metabolising cytochrome P450 enzymes and P-glycoprotein in the rat small intestine; comparison to the liver. *European journal of drug metabolism and pharmacokinetics*, *28*(1), 41-48.

Lown, K. S., Ghosh, M., & Watkins, P. B. (1998). Sequences of intestinal and hepatic cytochrome P450 3A4 cDNAs are identical. *Drug metabolism and disposition, 26*(2), 185-187.

Lušin, T. T., Mrhar, A., Stieger, B., Kullak-Ublick, G. A., Marc, J., Ostanek, B., . . . Delić, K. (2012). Influence of hepatic and intestinal efflux transporters and their genetic variants on the pharmacokinetics and pharmacodynamics of raloxifene in osteoporosis treatment. *Translational research, 160*(4), 298-308.

Löbenberg, R., Amidon, G. L., Ferraz, H. G., & Bou-Chacra, N. (2013). Mechanism of gastrointestinal drug absorption and application in therapeutic drug delivery. In *Therapeutic Delivery Methods: A Concise Overview of Emerging Areas* (pp. 8-22): Future Science Ltd.

Löbenberg, R., Krämer, J., Shah, V. P., Amidon, G. L., & Dressman, J. B. (2000). Dissolution testing as a prognostic tool for oral drug absorption: dissolution behavior of glibenclamide. *Pharmaceutical research, 17*(4), 439-444.

Macedo, M. H., Araújo, F., Martínez, E., Barrias, C., & Sarmento, B. (2018). iPSC-derived enterocyte-like cells for drug absorption and metabolism studies. *Trends in molecular medicine, 24*(8), 696-708.

Mahmood, I., & Balian, J. D. (1999). The pharmacokinetic principles behind scaling from preclinical results to phase I protocols. *Clinical pharmacokinetics, 36*(1), 1-11.

Martignoni, M. (2006). *Species and strain differences in drug metabolism in liver and intestine*: University Library Groningen][Host].

Martignoni, M., de Kanter, R., Grossi, P., Mahnke, A., Saturno, G., & Monshouwer, M. (2004). An in vivo and in vitro comparison of CYP induction in rat liver and intestine using slices and quantitative RT-PCR. *Chemico-biological interactions, 151*(1), 1-11.

Martignoni, M., Groothuis, G. M. M., & de Kanter, R. (2006). Species differences between mouse, rat, dog, monkey and human CYP-mediated drug metabolism, inhibition and induction. *Expert opinion on drug metabolism & toxicology, 2*(6), 875-894.

Mayhew, B. S., Jones, D. R., & Hall, S. D. (2000). An in vitro model for predicting in vivo inhibition of cytochrome P450 3A4 by metabolic intermediate complex formation. *Drug Metabolism and Disposition, 28*(9), 1031-1037.

Mazhar, R., Qaiser, F., Zahra, S. A., Fatimad, S. K., & Khane, I. A Literature Review of the Physicochemical, Physiological and Pharmaceutical Considerations in GIT Absorption of Drugs.

McConn, D. J., Lin, Y. S., Allen, K., Kunze, K. L., & Thummel, K. E. (2004). Differences in the inhibition of cytochromes P450 3A4 and 3A5 by metabolite-inhibitor complex-forming drugs. *Drug Metabolism and Disposition, 32*(10), 1083-1091.

Mehvar, R. (2018). Clearance concepts: fundamentals and application to pharmacokinetic behavior of drugs.

Melchior, D. L., Sharom, F. J., Evers, R., Wright, G. E., Chu, J. W. K., Wright, S. E., . . . Yabut, J. (2012). Determining P-glycoprotein–drug interactions: evaluation of reconstituted P-glycoprotein in a liposomal system and LLC-MDR1 polarized cell monolayers. *Journal of pharmacological and toxicological methods, 65*(2), 64-74.

Michaelis, L., & Menten, M. L. (1913). Die kinetik der invertinwirkung. *Biochem. z, 49*(333-369), 352.

Michel, P. E., Crettaz, D., Morier, P., Heller, M., Gallot, D., Tissot, J. D., . . . Rossier, J. S. (2006). Proteome analysis of human plasma and amniotic fluid by Off-Gel™

isoelectric focusing followed by nano-LC-MS/MS. *Electrophoresis, 27*(5-6), 1169-1181.

Mizuma, T., Tsuji, A., & Hayashi, M. (2004). Does the well-stirred model assess the intestinal first-pass effect well? *Journal of pharmacy and pharmacology, 56*(12), 1597-1599.

Moein, M. M., El Beqqali, A., & Abdel-Rehim, M. (2017). Bioanalytical method development and validation: Critical concepts and strategies. *Journal of Chromatography B, 1043,* 3-11.

Mohutsky, M., & Hall, S. D. (2014). Irreversible enzyme inhibition kinetics and drug–drug interactions. In *Enzyme Kinetics in Drug Metabolism* (pp. 57-91): Springer.

Mooij, M. G., Schwarz, U. I., De Koning, B. A. E., Leeder, J. S., Gaedigk, R., Samsom, J. N., . . . Kim, R. B. (2014). Ontogeny of human hepatic and intestinal transporter gene expression during childhood: age matters. *Drug Metabolism and Disposition, 42*(8), 1268-1274.

Morgan, E. T., MacGeoch, C., & Gustafsson, J.-A. (1985). Hormonal and developmental regulation of expression of the hepatic microsomal steroid 16 alpha-hydroxylase cytochrome P-450 apoprotein in the rat. *Journal of Biological Chemistry, 260*(22), 11895-11898.

Mouly, S., & Paine, M. F. (2003). P-glycoprotein increases from proximal to distal regions of human small intestine. *Pharmaceutical research, 20*(10), 1595-1599.

Mugford, C. A., & Kedderis, G. L. (1998). Sex-dependent metabolism of xenobiotics. *Drug metabolism reviews, 30*(3), 441-498.

Naderkhani, E., Isaksson, J., Ryzhakov, A., & Flaten, G. E. (2014). Development of a biomimetic phospholipid vesicle-based permeation assay for the estimation of intestinal drug permeability. *Journal of Pharmaceutical Sciences, 103*(6), 1882-1890.

Nagar, S., Jones, J. P., & Korzekwa, K. (2014). A numerical method for analysis of in vitro time-dependent inhibition data. Part 1. Theoretical considerations. *Drug Metabolism and Disposition, 42*(9), 1575-1586.

Nagar, S., Korzekwa, R. C., & Korzekwa, K. (2017). Continuous Intestinal Absorption Model Based on the Convection–Diffusion Equation. *Molecular pharmaceutics, 14*(9), 3069-3086.

Nakamura, K., Ariyoshi, N., Iwatsubo, T., Fukunaga, Y., Higuchi, S., Itoh, K., . . . Yamamoto, K. (2005). Inhibitory effects of nicardipine to cytochrome P450 (CYP) in human liver microsomes. *Biological and Pharmaceutical Bulletin, 28*(5), 882-885.

Nakanishi, T., & Tamai, I. (2015). Interaction of Drug or Food with Drug Transporters in Intestine and Liver. *Curr Drug Metab, 16*(9), 753-764. doi:10.2174/1389200216091512011113537

Naritomi, Y., Terashita, S., Kimura, S., Suzuki, A., Kagayama, A., & Sugiyama, Y. (2001). Prediction of human hepatic clearance from in vivo animal experiments and in vitro metabolic studies with liver microsomes from animals and humans. *Drug metabolism and disposition, 29*(10), 1316-1324.

Nath, A., & Atkins, W. M. (2006). A theoretical validation of the substrate depletion approach to determining kinetic parameters. *Drug metabolism and disposition, 34*(9), 1433-1435.

Nelson, D. R. (2006). Cytochrome P450 Nomenclature, 2004. In *Cytochrome P450 protocols* (pp. 1-10): Springer.

Nelson, D. R., Zeldin, D. C., Hoffman, S. M. G., Maltais, L. J., Wain, H. M., & Nebert, D. W. (2004). Comparison of cytochrome P450 (CYP) genes from the mouse and human genomes, including nomenclature recommendations for genes, pseudogenes and alternative-splice variants. *Pharmacogenetics and Genomics, 14*(1), 1-18.

Nguyen, H. Q., Kimoto, E., Callegari, E., & Obach, R. S. (2016). Mechanistic modeling to predict midazolam metabolite exposure from in vitro data. *Drug Metabolism and Disposition, 44*(5), 781-791.

Ni, P. F., Ho, N. F. H., Fox, J. L., Leuenberger, H., & Higuchi, W. I. (1980). Theoretical model studies of intestinal drug absorption V. Non-steady-state fluid flow and absorption. *International Journal of Pharmaceutics, 5*(1), 33-47.

Nikolakakis, I., & Partheniadis, I. (2017). Self-Emulsifying Granules and Pellets: Composition and Formation Mechanisms for Instant or Controlled Release. *Pharmaceutics, 9*(4). doi:10.3390/pharmaceutics9040050

Nishiya, Y., Hagihara, K., Kurihara, A., Okudaira, N., Farid, N. A., Okazaki, O., & Ikeda, T. (2009). Comparison of mechanism-based inhibition of human cytochrome P450 2C19 by ticlopidine, clopidogrel, and prasugrel. *Xenobiotica, 39*(11), 836-843.

Nishiyama, Y., Nakayama, S. M. M., Watanabe, K. P., Kawai, Y. K., Ohno, M., Ikenaka, Y., & Ishizuka, M. (2016). Strain differences in cytochrome P450 mRNA and protein expression, and enzymatic activity among Sprague Dawley, Wistar, Brown Norway and Dark Agouti rats. *Journal of Veterinary Medical Science, 78*(4), 675-680.

Niwa, T., Murayama, N., & Yamazaki, H. (2010). Comparison of the contributions of cytochromes P450 3A4 and 3A5 in drug oxidation rates and substrate inhibition. *Journal of Health Science, 56*(3), 239-256.

Nordt, S. P., & Clark, R. F. (1997). Midazolam: a review of therapeutic uses and toxicity. *The Journal of emergency medicine, 15*(3), 357-365.

Obach, R. S. (1999). Prediction of human clearance of twenty-nine drugs from hepatic microsomal intrinsic clearance data: an examination of in vitro half-life approach and nonspecific binding to microsomes. *Drug Metabolism and Disposition, 27*(11), 1350-1359.

Obach, R. S., & Reed-Hagen, A. E. (2002). Measurement of Michaelis constants for cytochrome P450-mediated biotransformation reactions using a substrate depletion approach. *Drug Metabolism and Disposition, 30*(7), 831-837.

Offman, E., & Edginton, A. N. (2015). A PBPK workflow for first-in-human dose selection of a subcutaneously administered pegylated peptide. *J Pharmacokinet Pharmacodyn, 42*(2), 135-150. doi:10.1007/s10928-015-9406-4

Okumu, A., DiMaso, M., & Löbenberg, R. (2008). Dynamic dissolution testing to establish in vitro/in vivo correlations for montelukast sodium, a poorly soluble drug. *Pharmaceutical research, 25*(12), 2778-2785.

Olivares-Morales, A., Hatley, O. J., Turner, D., Galetin, A., Aarons, L., & Rostami-Hodjegan, A. (2014). The use of ROC analysis for the qualitative prediction of human oral bioavailability from animal data. *Pharm Res, 31*(3), 720-730. doi:10.1007/s11095-013-1193-2

Orr, S. T. M., Ripp, S. L., Ballard, T. E., Henderson, J. L., Scott, D. O., Obach, R. S., . . . Kalgutkar, A. S. (2012). Mechanism-based inactivation (MBI) of cytochrome P450 enzymes: structure–activity relationships and discovery strategies to mitigate drug–drug interaction risks. *Journal of medicinal chemistry, 55*(11), 4896-4933.

Paine, M. F., Khalighi, M., Fisher, J. M., Shen, D. D., Kunze, K. L., Marsh, C. L., . . . Thummel, K. E. (1997). Characterization of interintestinal and intraintestinal variations in human CYP3A-dependent metabolism. *Journal of Pharmacology and Experimental Therapeutics, 283*(3), 1552-1562.

Paine, M. F., Shen, D. D., Kunze, K. L., Perkins, J. D., Marsh, C. L., McVicar, J. P., . . . Thummel, K. E. (1996). First-pass metabolism of midazolam by the human intestine. *Clinical Pharmacology & Therapeutics, 60*(1), 14-24.

Pal, Y., Deb, P. K., Bandopadhyay, S., Bandyopadhyay, N., & Tekade, R. K. (2018). Role of Physicochemical Parameters on Drug Absorption and Their Implications in Pharmaceutical Product Development. In *Dosage Form Design Considerations* (pp. 85-116): Elsevier.

Palleria, C., Di Paolo, A., Giofrè, C., Caglioti, C., Leuzzi, G., Siniscalchi, A., . . . Gallelli, L. (2013). Pharmacokinetic drug-drug interaction and their implication in clinical management. *J Res Med Sci, 18*(7), 601-610.

Pang, K. S. (2003). Modeling of intestinal drug absorption: roles of transporters and metabolic enzymes (for the Gillette Review Series). *Drug metabolism and disposition, 31*(12), 1507-1519.

Paragas, E. M., Wang, Z., Korzekwa, K., & Nagar, S. (2021). Complex Cytochrome P450 kinetics due to multisubstrate binding and sequential metabolism. Part 2. Modeling of experimental data. *Drug Metabolism and Disposition, 49*(12), 1100-1108.

Park, G. R., Manara, A. R., & Dawling, S. (1989). Extra-hepatic metabolism of midazolam. *British journal of clinical pharmacology, 27*(5), 634-637.

Parmentier, Y., Pothier, C., Hewitt, N., Vincent, L., Caradec, F., Liu, J., . . . Bouaita, B. (2019). Direct and quantitative evaluation of the major human CYP contribution (fmCYP) to drug clearance using the in vitro Silensomes™ model. *Xenobiotica, 49*(1), 22-35.

Pałasz, A., Wiaderkiewicz, A., Wiaderkiewicz, R., Czekaj, P., Czajkowska, B., Lebda-Wyborny, T., . . . Bryzek, A. (2012). Age-related changes in the mRNA levels of CYP1A1, CYP2B1/2 and CYP3A1 isoforms in rat small intestine. *Genes & nutrition, 7*(2), 197-207.

Peters, S. A., Jones, C. R., Ungell, A.-L., & Hatley, O. J. D. (2016). Predicting drug extraction in the human gut wall: assessing contributions from drug metabolizing enzymes and transporter proteins using preclinical models. *Clinical pharmacokinetics, 55*(6), 673-696.

Plise, E. G., Tran, D., & Salphati, L. (2010). Semi-automated protein binding methodology using equilibrium dialysis and a novel mixed-matrix cassette approach. *Journal of pharmaceutical sciences, 99*(12), 5070-5078.

Poovi, G., & Damodharan, N. (2018). Lipid nanoparticles: A challenging approach for oral delivery of BCS Class-II drugs. *Future Journal of Pharmaceutical Sciences, 4*(2), 191-205.

Porat, D., & Dahan, A. (2018). Active intestinal drug absorption and the solubility-permeability interplay. *International journal of pharmaceutics, 537*(1-2), 84-93.

Prasad, V., De Jesús, K., & Mailankody, S. (2017). The high price of anticancer drugs: origins, implications, barriers, solutions. *Nature reviews Clinical oncology, 14*(6), 381-390.

Prentis, R. A., Lis, Y., & Walker, S. R. (1988). Pharmaceutical innovation by the seven UK-owned pharmaceutical companies (1964-1985). *British journal of clinical pharmacology, 25*(3), 387-396.

Qureshi, Z. P., Seoane-Vazquez, E., Rodriguez-Monguio, R., Stevenson, K. B., & Szeinbach, S. L. (2011). Market withdrawal of new molecular entities approved in the United States from 1980 to 2009. *Pharmacoepidemiol Drug Saf, 20*(7), 772-777. doi:10.1002/pds.2155

Radice, C., Korzekwa, K., & Nagar, S. (2022). Predicting impact of food and feeding time on oral absorption of drugs with a novel rat continuous intestinal absorption model. *Drug Metabolism and Disposition*.

Rane, A., Wilkinson, G. R., & Shand, D. G. (1977). Prediction of hepatic extraction ratio from in vitro measurement of intrinsic clearance. *Journal of Pharmacology and Experimental Therapeutics, 200*(2), 420-424.

Rautio, J., Kumpulainen, H., Heimbach, T., Oliyai, R., Oh, D., Järvinen, T., & Savolainen, J. (2008). Prodrugs: design and clinical applications. *Nature reviews Drug discovery, 7*(3), 255-270.

Reix, N., Guhmann, P., Bietiger, W., Pinget, M., Jeandidier, N., & Sigrist, S. (2012). Duodenum-specific drug delivery: in vivo assessment of a pharmaceutically developed enteric-coated capsule for a broad applicability in rat studies. *International journal of pharmaceutics, 422*(1-2), 338-340.

Riccardi, K., Cawley, S., Yates, P. D., Chang, C., Funk, C., Niosi, M., . . . Di, L. (2015). Plasma protein binding of challenging compounds. *Journal of pharmaceutical sciences, 104*(8), 2627-2636.

Riede, J., Poller, B., Umehara, K.-i., Huwyler, J., & Camenisch, G. (2016). New IVIVE method for the prediction of total human clearance and relative elimination pathway contributions from in vitro hepatocyte and microsome data. *European Journal of Pharmaceutical Sciences, 86*, 96-102.

Riedl, A. G., Watts, P. M., Douek, D. C., Edwards, R. J., Boobis, A. R., Rose, S., & Jenner, P. (2000). Expression and distribution of CYP2C enzymes in rat basal ganglia. *Synapse, 38*(4), 392-402.

Riley, R. J., Grime, K., & Weaver, R. (2007). Time-dependent CYP inhibition. *Expert opinion on drug metabolism & toxicology, 3*(1), 51-66.

Roberts, M. S., & Rowland, M. (1986a). A dispersion model of hepatic elimination: 1. Formulation of the model and bolus considerations. *Journal of pharmacokinetics and biopharmaceutics, 14*(3), 227-260.

Roberts, M. S., & Rowland, M. (1986b). A dispersion model of hepatic elimination: 2. Steady-state considerations-influence of hepatic blood flow, binding within blood, and hepatocellular enzyme activity. *Journal of pharmacokinetics and biopharmaceutics, 14*(3), 261-288.

Rowland, M. (1985). Physiologic pharmacokinetic models and interanimal species scaling. *Pharmacology & therapeutics, 29*(1), 49-68.

Rowland, M., Lesko, L. J., & Rostami-Hodjegan, A. (2015). Physiologically Based Pharmacokinetics Is Impacting Drug Development and Regulatory Decision Making. *CPT Pharmacometrics Syst Pharmacol, 4*(6), 313-315. doi:10.1002/psp4.52

Rowland, M., & Tozer, T. N. (2011). Clinical pharmacokinetics and pharmacodynamics: concepts and applications. 2011. In: Philadelphia: Wolters Kluwer Health/Lippincott William & Wilkins.

Rubbens, J., Mols, R., Brouwers, J., & Augustijns, P. (2018). Exploring gastric drug absorption in fasted and fed state rats. *International Journal of Pharmaceutics, 548*(1), 636-641.

Sager, J. E., Yu, J., Ragueneau-Majlessi, I., & Isoherranen, N. (2015). Physiologically Based Pharmacokinetic (PBPK) Modeling and Simulation Approaches: A Systematic Review of Published Models, Applications, and Model Verification. *Drug Metab Dispos, 43*(11), 1823-1837. doi:10.1124/dmd.115.065920

Sakamoto, Y., Ishiguro, M., & Kitagawa, G. (1986). Akaike information criterion statistics. *Dordrecht, The Netherlands: D. Reidel, 81*.

Salminen, K. A., Leppänen, J., Venäläinen, J. I., Pasanen, M., Auriola, S., Juvonen, R. O., & Raunio, H. (2011). Simple, direct, and informative method for the assessment of CYP2C19 enzyme inactivation kinetics. *Drug metabolism and disposition, 39*(3), 412-418.

Salminen, K. A., Meyer, A., Imming, P., & Raunio, H. (2011). CYP2C19 progress curve analysis and mechanism-based inactivation by three methylenedioxyphenyl compounds. *Drug metabolism and disposition, 39*(12), 2283-2289.

Sawada, Y., Sugiyama, Y., Miyamoto, Y., Iga, T., & Hanano, M. (1985). Hepatic drug clearance model: Comparison among the distributed, parallel-tube and well-stirred models. *Chemical and pharmaceutical bulletin, 33*(1), 319-326.

Scott Obach, R. (2011). Predicting clearance in humans from in vitro data. *Current topics in medicinal chemistry, 11*(4), 334-339.

Sedic, M., Senn, J. J., Lynn, A., Laska, M., Smith, M., Platz, S. J., . . . Smith, P. F. (2018). Safety Evaluation of Lipid Nanoparticle-Formulated Modified mRNA in the Sprague-Dawley Rat and Cynomolgus Monkey. *Vet Pathol, 55*(2), 341-354. doi:10.1177/0300985817738095

Shargel, L. (2013). Biopharmaceutics. In *Encyclopedia of Pharmaceutical Science and Technology, Fourth Edition* (pp. 195-210): CRC Press.

Sietsema, W. K. (1989). The absolute oral bioavailability of selected drugs. *Int J Clin Pharmacol Ther Toxicol, 27*(4), 179-211.

Silverman, R. B. (1995). [10] Mechanism-based enzyme inactivators. In *Methods in enzymology* (Vol. 249, pp. 240-283): Elsevier.

Smith, M. T., Eadie, M. J., & Brophy, T. R. (1981). The pharmacokinetics of midazolam in man. *European journal of clinical pharmacology, 19*(4), 271-278.

Snyder, W. S., Cook, M. J., Nasset, E. S., Karhausen, L. R., Howells, G. P., & Tipton, I. H. (1975). *Report of the task group on reference man* (Vol. 23): Pergamon Oxford.

Spencer, R. L., Kalman, B. A., Cotter, C. S., & Deak, T. (2000). Discrimination between changes in glucocorticoid receptor expression and activation in rat brain using western blot analysis. *Brain research, 868*(2), 275-286.

Stoll, B. R., Batycky, R. P., Leipold, H. R., Milstein, S., & Edwards, D. A. (2000). A theory of molecular absorption from the small intestine. *Chemical Engineering Science, 55*(3), 473-489.

Strelevitz, T. J., Foti, R. S., & Fisher, M. B. (2006). In vivo use of the P450 inactivator 1-aminobenzotriazole in the rat: varied dosing route to elucidate gut and liver contributions to first-pass and systemic clearance. *Journal of pharmaceutical sciences, 95*(6), 1334-1341.

Stringer, R. A., Strain-Damerell, C., Nicklin, P., & Houston, J. B. (2009). Evaluation of recombinant cytochrome P450 enzymes as an in vitro system for metabolic clearance predictions. *Drug Metabolism and Disposition, 37*(5), 1025-1034.

Sun, H., Chow, E. C. Y., Liu, S., Du, Y., & Pang, K. S. (2008). The Caco-2 cell monolayer: usefulness and limitations. *Expert opinion on drug metabolism & toxicology, 4*(4), 395-411.

Takenaka, T., Kazuki, K., Harada, N., Kuze, J., Chiba, M., Iwao, T., . . . Kazuki, Y. (2017). Development of Caco-2 cells co-expressing CYP3A4 and NADPH-cytochrome P450 reductase using a human artificial chromosome for the prediction of intestinal extraction ratio of CYP3A4 substrates. *Drug metabolism and pharmacokinetics, 32*(1), 61-68.

Tang, C., & Prueksaritanont, T. (2010). Use of in vivo animal models to assess pharmacokinetic drug-drug interactions. *Pharmaceutical research, 27*(9), 1772-1787.

Tanna, R. S., Tian, D.-D., Cech, N. B., Oberlies, N. H., Rettie, A. E., Thummel, K. E., & Paine, M. F. (2021). Refined prediction of pharmacokinetic kratom-drug interactions: time-dependent inhibition considerations. *Journal of Pharmacology and Experimental Therapeutics, 376*(1), 64-73.

Taxak, N., Desai, P. V., Patel, B., Mohutsky, M., Klimkowski, V. J., Gombar, V., & Bharatam, P. V. (2012). Metabolic-intermediate complex formation with cytochrome P450: Theoretical studies in elucidating the reaction pathway for the generation of reactive nitroso intermediate. *Journal of computational chemistry, 33*(21), 1740-1747.

Taylor, A. M., Storm, J., Soceneantu, L., Linton, K. J., Gabriel, M., Martin, C., . . . Callaghan, R. (2001). Detailed characterization of cysteine-less P-glycoprotein reveals subtle pharmacological differences in function from wild-type protein. *British journal of pharmacology, 134*(8), 1609-1618.

Taylor, S. C., Berkelman, T., Yadav, G., & Hammond, M. (2013). A defined methodology for reliable quantification of Western blot data. *Molecular biotechnology, 55*(3), 217-226.

Taylor, S. C., & Posch, A. (2014). The design of a quantitative western blot experiment. *BioMed research international, 2014*.

Tolle-Sander, S., Rautio, J., Wring, S., Polli, J. W., & Polli, J. E. (2003). Midazolam exhibits characteristics of a highly permeable P-glycoprotein substrate. *Pharmaceutical research, 20*(5), 757-764.

Toutain, P. L., & Bousquet-Mélou, A. (2004). Bioavailability and its assessment. *J Vet Pharmacol Ther, 27*(6), 455-466. doi:10.1111/j.1365-2885.2004.00604.x

Tracy, T. S. (2006). Atypical cytochrome P450 kinetics. *Drugs in R & D, 7*(6), 349-363.

Tsuchida, S., Umemura, H., & Nakayama, T. (2020). Current status of matrix-assisted laser desorption/ionization–time-of-flight mass spectrometry (MALDI-TOF MS) in clinical diagnostic microbiology. *Molecules, 25*(20), 4775.

Tubic, M., Wagner, D., Spahn-Langguth, H., Bolger, M. B., & Langguth, P. (2006). In silico modeling of non-linear drug absorption for the P-gp substrate talinolol and of consequences for the resulting pharmacodynamic effect. *Pharmaceutical research, 23*(8), 1712-1720.

Turpeinen, M., Jouko, U., Jorma, J., & Olavi, P. (2005). Multiple P450 substrates in a single run: rapid and comprehensive in vitro interaction assay. *European journal of pharmaceutical sciences, 24*(1), 123-132.

US-FDA. (2020). *In Vitro Drug Interaction Studies — Cytochrome P450 Enzyme- and Transporter-Mediated Drug Interactions*

Guidance for Industry. Center for Drug Evaluation and Research (CDER) Retrieved from https://www.fda.gov/Drugs/GuidanceComplianceRegulatoryInformation/Guidances/default.htm

Uvarova, N. E., Eremenko, N. N., Ramenskaya, G. V., Goryachev, D. V., & Smirnov, V. V. (2019). Comparison of FDA (2018) and EAEU Regulatory Requirements for Bioanalytical Method Validation. *Pharmaceutical Chemistry Journal, 53*(8), 759-765.

Vaessen, S. F. C., van Lipzig, M. M. H., Pieters, R. H. H., Krul, C. A. M., Wortelboer, H. M., & van de Steeg, E. (2017). Regional expression levels of drug transporters and metabolizing enzymes along the pig and human intestinal tract and comparison with Caco-2 cells. *Drug metabolism and disposition, 45*(4), 353-360.

van de Kerkhof, E. G., de Graaf, I. A. M., & Groothuis, G. M. M. (2007). In vitro methods to study intestinal drug metabolism. *Current drug metabolism, 8*(7), 658-675.

Vanstraelen, K., Wauters, J., De Loor, H., Vercammen, I., Annaert, P., Lagrou, K., & Spriet, I. (2014). Protein-binding characteristics of voriconazole determined by high-throughput equilibrium dialysis. *Journal of Pharmaceutical Sciences, 103*(8), 2565-2570.

Venkatakrishnan, K., von Moltke, L. L., Harmatz, J. S., Crespi, C. L., & Greenblatt, D. J. (2000). Comparison between cytochrome P450 (CYP) content and relative activity approaches to scaling from cDNA-expressed CYPs to human liver microsomes: ratios of accessory proteins as sources of discrepancies between the approaches. *Drug metabolism and disposition, 28*(12), 1493-1504.

Vertzoni, M., Augustijns, P., Grimm, M., Koziolek, M., Lemmens, G., Parrott, N., . . . Van Den Abeele, J. (2019). Impact of regional differences along the gastrointestinal tract of healthy adults on oral drug absorption: an UNGAP review. *European Journal of Pharmaceutical Sciences, 134*, 153-175.

Vieira, M. L. T., Kirby, B., Ragueneau-Majlessi, I., Galetin, A., Chien, J. Y. L., Einolf, H. J., . . . Grime, K. (2014). Evaluation of various static in vitro–in vivo extrapolation models for risk assessment of the CYP3A inhibition potential of an investigational drug. *Clinical Pharmacology & Therapeutics*, *95*(2), 189-198.

Vinarov, Z., Abdallah, M., Agundez, J. A. G., Allegaert, K., Basit, A. W., Braeckmans, M., . . . Grimm, M. (2021). Impact of gastrointestinal tract variability on oral drug absorption and pharmacokinetics: An UNGAP review. *European Journal of Pharmaceutical Sciences, 162*, 105812.

Wacher, V. J., Salphati, L., & Benet, L. Z. (2001). Active secretion and enterocytic drug metabolism barriers to drug absorption. *Advanced drug delivery reviews, 46*(1-3), 89-102.

Wagner, C., Zhao, P., Pan, Y., Hsu, V., Grillo, J., Huang, S. M., & Sinha, V. (2015). Application of physiologically based pharmacokinetic (PBPK) modeling to support dose selection: report of an FDA public workshop on PBPK. *CPT: pharmacometrics & systems pharmacology, 4*(4), 226-230.

Wandel, C., Böcker, R., Böhrer, H., Browne, A., Rügheimer, E., & Martin, E. (1994). Midazolam is metabolized by at least three different cytochrome P450 enzymes. *British Journal of Anaesthesia, 73*(5), 658-661.

Wang, J., & Urban, L. (2004). The impact of early ADME profiling on drug discovery and development strategy. *DDW Drug Discovery World, 5*(4), 73-86.

Wang, R. W., Cai, X. X., Tang, W., Edom, R. W., Didolkar, V., Stearns, R. A., & Evans, D. C. (2002). *Substrate-dependent drug interaction with CYP3A4 irreversible inactivators*.

Wang, Y.-H., Jones, D. R., & Hall, S. D. (2004). Prediction of cytochrome P450 3A inhibition by verapamil enantiomers and their metabolites. *Drug Metabolism and Disposition, 32*(2), 259-266.

Wang, Z., Paragas, E. M., Nagar, S., & Korzekwa, K. (2021). Complex Cytochrome P450 Kinetics Due to Multisubstrate Binding and Sequential Metabolism. Part 1. Theoretical Considerations. *Drug Metabolism and Disposition, 49*(12), 1090-1099.

Watkins, P. B. (1997). The barrier function of CYP3A4 and P-glycoprotein in the small bowel. *Advanced drug delivery reviews, 27*(2-3), 161-170.

Willmann, S., Lippert, J., Sevestre, M., Solodenko, J., Fois, F., & Schmitt, W. (2003). PK-Sim®: a physiologically based pharmacokinetic ‘whole-body’model. *Biosilico, 1*(4), 121-124.

Winter, H., Egizi, E., Erondu, N., Ginsberg, A., Rouse, D. J., Severynse-Stevens, D., . . . Everitt, D. (2013). Evaluation of pharmacokinetic interaction between PA-824 and midazolam in healthy adult subjects. *Antimicrobial agents and chemotherapy, 57*(8), 3699-3703.

Witherow, L. E., & Houston, J. B. (1999). Sigmoidal kinetics of CYP3A substrates: an approach for scaling dextromethorphan metabolism in hepatic microsomes and isolated hepatocytes to predict in vivo clearance in rat. *Journal of Pharmacology and Experimental Therapeutics, 290*(1), 58-65.

Wong, H., & Chow, T. W. (2017). Physiologically Based Pharmacokinetic Modeling of Therapeutic Proteins. *J Pharm Sci, 106*(9), 2270-2275. doi:10.1016/j.xphs.2017.03.038

Wu, C.-Y., & Benet, L. Z. (2005). Predicting drug disposition via application of BCS: transport/absorption/elimination interplay and development of a biopharmaceutics drug disposition classification system. *Pharmaceutical research, 22*(1), 11-23.

Xie, F., Ding, X., & Zhang, Q. Y. (2016). An update on the role of intestinal cytochrome P450 enzymes in drug disposition. *Acta Pharm Sin B, 6*(5), 374-383. doi:10.1016/j.apsb.2016.07.012

Yadav, J., Korzekwa, K., & Nagar, S. (2019). Impact of lipid partitioning on the design, analysis, and interpretation of microsomal time-dependent inactivation. *Drug Metabolism and Disposition, 47*(7), 732-742.

Yadav, J., Korzekwa, K., & Nagar, S. (2021). Numerical methods for modeling enzyme kinetics. In *Enzyme Kinetics in Drug Metabolism* (pp. 147-168): Springer.

Yadav, J., Paragas, E., Korzekwa, K., & Nagar, S. (2020). Time-dependent enzyme inactivation: Numerical analyses of in vitro data and prediction of drug-drug interactions. *Pharmacology & Therapeutics, 206*, 107449.

Yamaoka, K., Nakagawa, T., & Uno, T. (1978). Application of Akaike's information criterion (AIC) in the evaluation of linear pharmacokinetic equations. *Journal of pharmacokinetics and biopharmaceutics, 6*(2), 165-175.

Yamazaki, H., Niwa, T., Murayama, N., & Emoto, C. (2008). Comparison of kinetic parameters for drug oxidation rates and substrate inhibition potential mediated by cytochrome P450 3A4 and 3A5. *Current drug metabolism, 9*(1), 20-33.

Yau, E., Petersson, C., Dolgos, H., & Peters, S. A. (2017). A comparative evaluation of models to predict human intestinal metabolism from nonclinical data. *Biopharmaceutics & drug disposition, 38*(3), 163-186.

Yoshida, K., Maeda, K., & Sugiyama, Y. (2013). Hepatic and intestinal drug transporters: prediction of pharmacokinetic effects caused by drug-drug interactions and genetic polymorphisms. *Annual review of pharmacology and toxicology, 53*, 581-612.

Zhang, D., Luo, G., Ding, X., & Lu, C. (2012). Preclinical experimental models of drug metabolism and disposition in drug discovery and development. *Acta Pharmaceutica Sinica B, 2*(6), 549-561.

Zhang, H., Amunugama, H., Ney, S., Cooper, N., & Hollenberg, P. F. (2011). Mechanism-based inactivation of human cytochrome P450 2B6 by clopidogrel: involvement of both covalent modification of cysteinyl residue 475 and loss of heme. *Molecular pharmacology, 80*(5), 839-847.

Zhang, J., Shou, W. Z., Vath, M., Kieltyka, K., Maloney, J., Elvebak, L., . . . Weller, H. N. (2010). An integrated bioanalytical platform for supporting high-throughput serum protein binding screening. *Rapid Communications in Mass Spectrometry, 24*(24), 3593-3601.

Zhang, Z.-Y., & Wong, Y. N. (2005). Enzyme kinetics for clinically relevant CYP inhibition. *Current drug metabolism, 6*(3), 241-257.

Zhao, P., Rowland, M., & Huang, S. M. (2012). Best practice in the use of physiologically based pharmacokinetic modeling and simulation to address clinical pharmacology regulatory questions. *Clinical pharmacology & therapeutics*, *92*(1), 17-20.

Zhao, P., Zhang, L., Grillo, J. A., Liu, Q., Bullock, J. M., Moon, Y. J., . . . Huang, S. M. (2011). Applications of physiologically based pharmacokinetic (PBPK) modeling and simulation during regulatory review. *Clin Pharmacol Ther, 89*(2), 259-267. doi:10.1038/clpt.2010.298

Zhou, S., Chan, S. Y., Goh, B. C., Chan, E., Duan, W., Huang, M., & McLeod, H. L. (2005). Mechanism-based inhibition of cytochrome P450 3A4 by therapeutic drugs. *Clinical pharmacokinetics*, *44*(3), 279-304.

Zhou, S., Yung Chan, S., Cher Goh, B., Chan, E., Duan, W., Huang, M., & McLeod, H. L. (2005). Mechanism-based inhibition of cytochrome P450 3A4 by therapeutic drugs. *Clin Pharmacokinet, 44*(3), 279-304. doi:10.2165/00003088-200544030-00005

Zhou, S.-F., Xue, C. C., Yu, X.-Q., Li, C., & Wang, G. (2007). Clinically important drug interactions potentially involving mechanism-based inhibition of cytochrome P450 3A4 and the role of therapeutic drug monitoring. *Therapeutic drug monitoring*, *29*(6), 687-710.

Zhou, S. F. (2008). Drugs behave as substrates, inhibitors and inducers of human cytochrome P450 3A4. *Curr Drug Metab, 9*(4), 310-322. doi:10.2174/138920008784220664

Zhou, S. F., Liu, J. P., & Chowbay, B. (2009). Polymorphism of human cytochrome P450 enzymes and its clinical impact. *Drug Metab Rev, 41*(2), 89-295. doi:10.1080/03602530902843483

Zhou, Z.-W., & Zhou, S.-F. (2009). Application of mechanism-based CYP inhibition for predicting drug–drug interactions. *Expert opinion on drug metabolism & toxicology*, *5*(6), 579-605.

Zhuang, X., & Lu, C. (2016). PBPK modeling and simulation in drug research and development. *Acta Pharm Sin B, 6*(5), 430-440. doi:10.1016/j.apsb.2016.04.004

Zimmerman, C. L., Wen, Y., & Remmel, R. P. (2000). First-pass disposition of (−)-6-aminocarbovir in rats: II. Inhibition of intestinal first-pass metabolism. *Drug Metabolism and Disposition, 28*(6), 672-679.

Zöllner, A., Buchheit, D., Meyer, M. R., Maurer, H. H., Peters, F. T., & Bureik, M. (2010). Production of human phase 1 and 2 metabolites by whole-cell biotransformation with recombinant microbes. *Bioanalysis, 2*(7), 1277-1290.

APPENDIX A: EQUIIBRIUM DIALYSIS OF NICARDIPINE ADDING DRUG IN THE RECEIVER COMPARTMENT

The method described in chapter 3 was followed to repeat the equilibrium dialysis of NCD but adding the drug in the receiver compartment. The HIM concentration was 0.1 mg/mL and the incubation time was 12 hours. The rpm was 100 and the incubation was maintained at 37.5 °C temperature with at least 5% carbon dioxide. This was done to decide if that the equilibrium was actually reached. Table A1 is the results of equilibrium dialysis of NCD:

Table A1: Equilibrium dialysis of NCD (Repeat experiment)

	Adding drug in the donor compartment Mean (SD)	Adding drug in the receiver compartment Mean (SD)
Diluted f_{um} at 0.1mg/mL HIM	0.59 (0.0075)	0.67 (0.032)
Scaled f_{um} at 1 mg/mL	0.13 (0.0042)	0.17 (0.026)

The f_{um} rose from 0.13 to 0.17 when NCD was added to the receiver compartment, which is a clear sign that the equilibrium was not reached in the prior experiment. However, it may be reasonable to estimate that the NCD f_{um} ranges between 0.12 to 0.17 plus or minus the related standard error. To precisely identify the f_{um}, more investigation may be required. This might involve increasing the incubation period, lowering the microsomal protein content, or perhaps doing both.